Title	Study of Hemispherical Electrostatic Analyzers and Its Application to Rocket and Satellite Observations of Low Energy Electrons(Dissertation_)
Author(s)	Mukai, Toshifumi
Citation	Kyoto University ( )
Issue Date	1986-09-24
URL	http://dx.doi.org/10.14989/doctor.r6030
Right	
Type	Thesis or Dissertation
Textversion	author

STUDY OF HEMISPHERICAL ELECTROSTATIC ANALYZERS
AND ITS APPLICATION TO ROCKET
AND SATELLITE OBSERVATIONS OF LOW ENERGY ELECTRONS

by

Toshifumi MUKAI

May 1986

STUDY OF HEMISPHERICAL ELECTROSTATIC ANALYZERS

AND ITS APPLICATION TO ROCKET

AND SATELLITE OBSERVATIONS OF LOW ENERGY ELECTRONS

BY

Toshifumi MUKAI

May 1986

The Institute of Space and Astronautical Science

6-1, Komaba 4-chome, Meguro-ku, Tokyo 153, Japan

Acknowledgements

The author wishes to express his sincere thanks to Emeritus
Professor Kunio Hirao of the Institute of Space and Astronautical
Science (ISAS), now Professor of Tokai University, for his
valuable suggestions and guidance throughout the present work,
and careful reading of the manuscript. The author also wishes
to express his deep appreciation to Professor Iwane Kimura of
Kyoto University for his careful reading of the manuscript,
helpful advice and encouragement. In particular, the correlation
study of waves and particles in Section 3 of Chapter V was
carried out under his stimulating supervision.

The author also wishes to express his grateful thanks to
Professors Tomizo Itoh, Tatsuzo Obayashi, Atsuhiro Nishida of
ISAS, Hiroshi Oya of Tohoku University, Nobuki Kawashima of ISAS,
and Susumu Kato of Kyoto University for their continual advice
and encouragement.

The author also wishes to express his hearty appreciation to
Professor Hiroshi Matsumoto of Kyoto University for his useful
advice, encouragement and careful reading of the manuscript, and
in particular, for his collaborative research on correlation
study of waves and particles.

The author is greatly indebted to Professors Kazuo Takayanagi
of ISAS, (late) Takao Tohmatsu and Toshihiro Ogawa of University
of Tokyo, and Dr. Osamu Ashihara of ISAS for many useful sugges-
tions and comments on study of ionospheric photoelectrons. The
author also is grateful to Dr. Koh-ichiro Oyama of ISAS for his
useful comments on the energy distribution of very low energy
electrons in the ionosphere, to Dr. Haruya Kubo of ISAS for his

Within the last two decades, there has been a considerable
progress in our knowledge of the physical properties of the
extraterrestrial environment of the earth.   It is well known
that the earth is surrounded by the ionized gas; plasma.   Early
efforts for investigation of the plasma environment were concen-
trated to obtain macroscopic properties, such as density and
temperature under the assumption of thermal equilibrium.
However, the plasmas in space are neither uniform nor homogeneous
at all, but there are various plasma domains around the earth.
Any adjacent plasma domains may be, more or less, coupled with
each other through various transport processes being accompanied
with either acceleration or degradation of particles which has
not yet been fully understood.   As a result of these processes,
the energy distribution of plasma particles is deviated from a
simple Maxwellian.   Therefore the measurement of the energy
distributions of plasma particles is essential for understanding
of the dynamical behavior of the plasma.   Even in the ionosphere
where electrons may be recognized to be well thermalized, photo-
electrons play an important role in the energetics of the thermo-
sphere in spite of their very low abundance ratio to the thermal
electrons.

The thesis is concerned with the study of low energy electron
spectrometers and its application to the rocket and satellite
observations.   A hemispherical electrostatic analyzer is adopted
as an energy analyzer.   The primary attraction of this instrument
is a high energy resolution over a wide energy range from a few
eV to several tens of keV.   It has inherently a double-focusing

property due to the spherical symmetry and therefore has a good particle transmission. In Chapter II, transmission properties of the hemispherical analyzer are investigated theoretically, keeping in mind the application to space use, and the design parameters are derived. Transmission properties of an electron-optical system are also investigated theoretically for design of the inlet collimator in the rocket-borne electron spectrometer.

Based on the calculated results, the electron spectrometers have been designed and constructed in order to measure the ionospheric photoelectrons by rockets, as described in Chapter III. Emphasis in the design is laid on the high energy resolution to resolve fine structures in the energy spectrum. A sophisticated inlet collimator which can constitute electron lenses is added for flexible operation of the analyzer, that enables to make measurements of very low energy electrons. It should be noted that careful considerations must be taken for a reliable measurement of low energy electrons by rockets. Those considerations arise from the basic nature of low energy electrons susceptible to the electric and magnetic field on a rocket, and also from the possible coexistence of spurious electrons in the same energy range as that of the right electrons to be measured. Characteristics of the instrument necessary for reduction of the flight data must be also calibrated carefully by the pre-flight experiment in the laboratory. Instrumental performance in flight has been refined through the experience of the flight experiments, by which more and more adequate procedures mentioned above have been attained.

The scientific results obtained by the rocket observations are discussed in Chapter IV. The observed results have revealed

several prominent features in the energy spectrum and their
altitudinal variation, which are discussed in terms of theoretical
interpretation.   A remarkable coincidence between the observed
spectrum and the calculated one is obtained, indicating the high
energy resolution capability and high reliability of our electron
spectrometer.

Chapter V is devoted to description of the application to
the satellite observations of auroral electrons by KYOKKO , of
inner-magnetospheric electrons by JIKIKEN, and of ionospheric
photoelectrons and auroral particles by OHZORA.   The KYOKKO
observation has revealed the local-time dependence, the substorm
phase variation and the spatial structure of the inverted-V
precipitation, and characteristics of the upgoing electrons in
the auroral region, including a new finding of the localized
region of intense upgoing electrons.   The JIKIKEN observation
has provided us with valuable data of wave-particle interactions.
A peculiar feature of the high pitch angle anisotropy in electron
distributions, which plays a role in amplification of the VLF
signals artificially transmitted from the ground Siple station,
has been newly found out in the equatorial region around a local
time of noon.   The OHZORA observation has also provided us with
valuable data of the global distribution of the charged particles
in space.

We hope that these observations will contribute to progress
of the ionospheric and magnetospheric physics, and that the
experimental techniques developed during the present study will
be utilized in future explorations of the plasma environment
around the earth and other planets.

CONTENTS

Chapter I. General Introduction

    As a general introduction of the present thesis, we begin
this chapter with a short review of the material of the investiga-
tion.   The thesis is concerned with the study of low-energy
electron spectrometers using hemispherical electrostatic analyzers
and the application to the rocket and satellite observations in
space.

    The plasma environment in the earth's neighborhood is first
briefly reviewed as a background.   Early plasma measurements
were concentrated to obtain macroscopic parameters such as plasma
density and temperature under the assumption of thermal equilibrium,
but any space plasma generally contains suprathermal particles
which play important roles in the energetics and dynamics of the
plasma.   Ionospheric photoelectrons, auroral electrons and
inner-magnetospheric electrons are just the object of the investi-
gation in this thesis and are reviewed in section 2.   Particular
attentions have to be paid for the design, construction and
calibration of the measuring instruments and for data analysis of
these electrons.   In section 3, existing techniques for the
measurements of low energy electrons are reviewed.   Finally, the
contribution of the present thesis is described.

§1. Overview of Plasma characteristics in the Earth's Neighborhood

    It is well known that the earth is surrounded by ionized
gases, plasmas, the region of which may be divided largely into two;
ionosphere and magnetosphere.   Plasma characteristics are quite

different between these two regions. Generally, the ionospheric plasma is cold and dense, while the magnetospheric plasma is hot and tenuous. These characteristics are determined by production and loss of the plasma including various transport processes.

The ionosphere is formed by the ionization of the upper atmosphere, the density of which decays roughly exponentially with altitude. The most significant ionizing source is the solar x-ray and EUV (extreme ultra-violet) radiation. The photoionization and photoabsorption of the atmosphere and also the chemical and dynamical processes result in the layered structure of the ionosphere above altitudes of ∿60 km. Examples of electron density and temperature in the daytime ionoshere at a middle latitude are shown in Fig. 1.1(a) and (b), respectively. The density profile shows a layered structure, named as D-, E-, F1- and F2-regions. It should be noted that the ionosphere exhibits significant variation with altitude, local time, latitude, season, solar cycle and geomagnetic activity.

The additional ionizing sources are hydrogen Lyman-α and -β radiation from the geocorona and energetic electrons precipitating from the magnetosphere. The additional sources become important at night-time when the solar radiation cannot contribute to the ionosphere formation. The precipitating electrons are especially significant in the high-latitude ionosphere which can be magnetical-ly linked to the distant magnetosphere. Therefore the high-latitude ionosphere is strongly influenced by the magnetospheric activity.

The magnetosphere is a confined region where the earth's magnetic field dominates. The region outside of the magnetosphere is the interplanetary space where the supersonic magnetized plasma (so-called a solar wind) is flowing out from the solar corona.

(a)

(b)
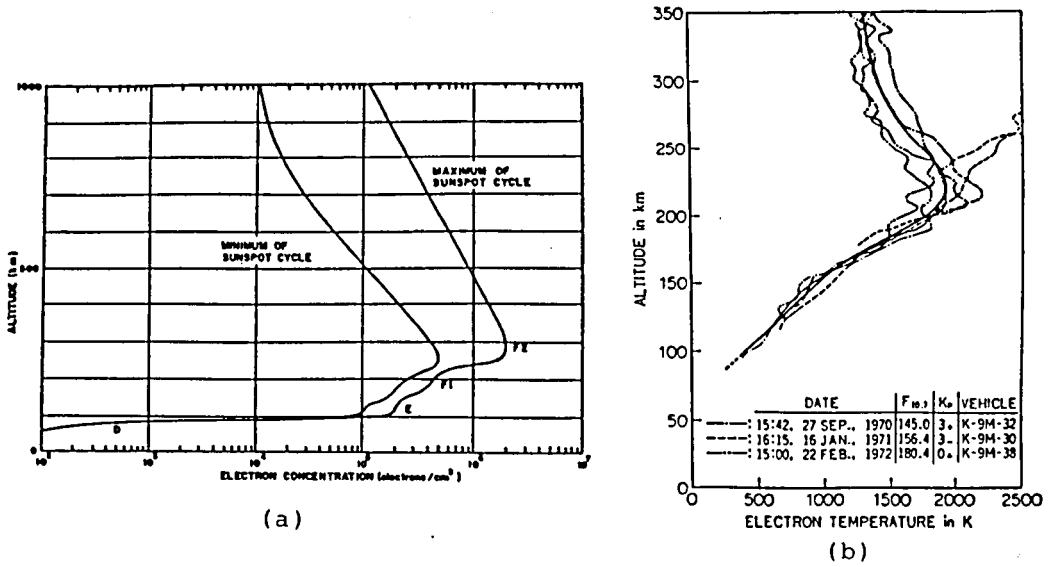
Fig. 1.1 Profiles of electron density and temperature in the daytime
          ionosphere at a middle latitude.
          (a) electron density (after W. B. Hanson, 1965)
          (b) electron temperature (after K. -I. Oyama, 1975)
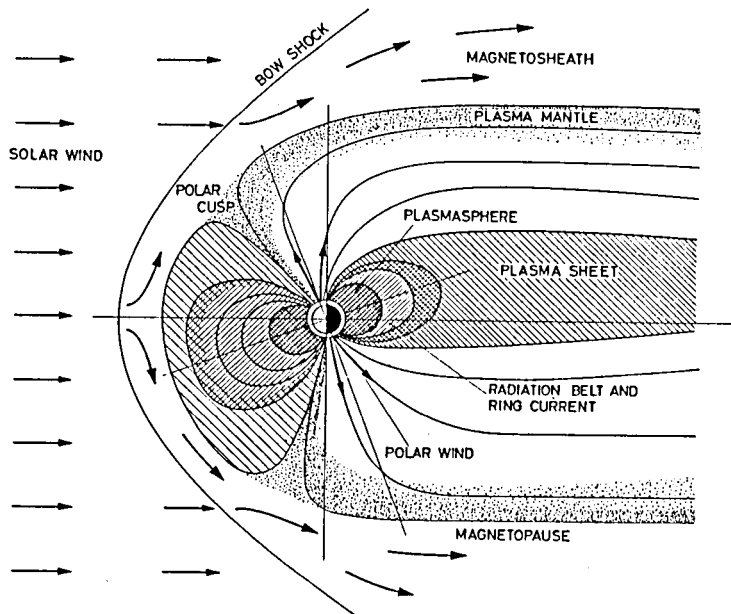
Fig. 1.2 Noon-midnight cross section of the magnetospheric plasma
          domains. (after H. Rosenbauer et al., 1975)

Since the intrinsic magnetic field of the earth represents a hard obstable to the supersonic solar wind, strong bow shock is formed to deflect the bulk of the incident flow around the earth. The domain where the earth's magnetic field dominates is therefore confined to a limited region. Figure 1.2 shows schematically the bow shock and the magnetosphere. In the downstream of the bow shock, the solar wind is diverted around the hard obstacle in a region called the magnetosheath. After being decelerated by the bow shock the heated solar wind is accelerated again from subsonic to supersonic flow. The interaction of this magneto-sheath plasma flow with the geomagnetic field is considered to produce an open magnetotail that is stretched out to several hundred earth radii in the antisolar direction. The magneto-sphere thus formed is populated by thermal plasma and energetic charged particles of both solar wind and ionospheric origin.

Owing to the interaction of the solar wind and the magneto-sphere, there are several plasma domains as shown in Fig. 1.2. On the dayside the polar cusp is a singular region where reconnec-tion of the magnetic field lines between the earth and the interplanetary space is considered to occur. The geomagnetic field lines at lower-latitude side of this region are closed on the dayside, whereas those lines at higher latitudes (polar cap) are flown away toward the magnetotail and are considered to reconnect the interplanetary magnetic field lines eventually. The solar wind plasma in the magnetosheath has a direct access to the ionoshere in the vicinity of the polar cusp.

The plasma sheet are primarily composed of magnetosheath plasma which has been transported into the magnetosphere, though including sometimes significant fraction of ionospheric origin.

The plasma density in the plasma sheet is two or three orders of magnitude lower than that of the magnetosheath plasma, while the average energy is 10 times higher. Due to the interaction of the solar wind and the magnetosphere, an electric potential difference of several ten kV is generated across the magnetotail, the resulting electric field pointing from dawn to dusk. The behavior of the plasma sheet particles is influenced by the electric field[*] and (of course) the tail magnetic field.

The radiation belt is in part the earthward extension of the plasma sheet. It is composed of trapped energetic ions and electrons which encircle the earth due to the gradient-B drift in opposite directions, causing a ring current around the earth.

The plasmasphere is a torus-shaped region that surrounds the earth and contains a relatively cool, high-density plasma of ionospheric origin. The plasma in this region corotates with the earth, but it can also flow along the geomagnetic field lines from one hemisphere to the other. Profiles of the plasma density in the equatorial plane are shown in Fig. 1.3. The outer boundary of the plasmasphere, called the plasmapause, is marked by a sharp decrease in plasma density. The plasmapause is essentially the boundary between plasma that corotates with the earth and plasma that does not.

(*) Since the geomagnetic field lines are usually equipotentials due to the high electrical conductivity along the field lines, this electric field is mapped into the high-latitude ionosphere and, therefore, has a direct influence on the ionospheric plasma, too.
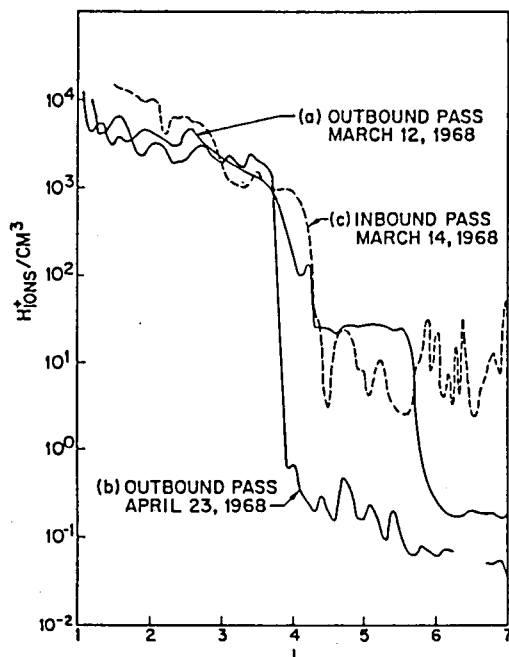
Fig. 1.3 L-dependence of hydrogen ion concentration: a composite of several typical plasmapause crossings in different levels of magnetic activity. (after C. R. Chappell et al., 1970)

Any adjacent plasma domains may be, more or less, coupled with each other through various processes by plasma transport, acceleration and degradation which have not yet been fully established. As a result of these processes, the energy distribution of plasma particles is more or less deviated from a simple Maxwellian. This provides a free energy source for plasma instability and wave generation. Therefore, the in-situ measurement of the particle distribution function is essential for understanding the dynamical behavior of the plasma.

§2. Review of Suprathermal Electrons in the Ionosphere and
    Magnetosphere

2.1.   Ionospheric Photoelectrons

2.1.1. Theoretical Background

   Photoelectrons are produced through the ionization of the
neutral particles (atoms and molecules) in the upper atmosphere
by the solar EUV radiation.   Primary photoelectrons produced
initially have an average energy of 10-20 eV which is much higher
than the mean kinetic energy of the ambient particles [Tohmatsu
et al., 1965].   These electrons therefore lose their energy
through collisions with ambient particles, until they are therma-
lized and eventually disappear by recombination with positive ions
or by negative-ion formation.   Through these processes, photo-
electrons play important roles in the energetics of the thermo-
sphere.   The details of elementary photoelectron processes were
reviewed by Takayanagi and Itikawa [1970].
   Figure 1.4 is a crude schematic diagram of the process
involved in the breakdown of solar EUV energy, reviewed by
Stolarski [1976].   The width of each arrow shows approximately
the amount of energy involved in each channel.   The absorbed
solar EUV energy is split initially between photoelectron and ion
pair production that becomes stored chemical energy.   Most of
energy of a primary photoelectron is lost through inelastic
collisions with neutral species which may contribute to the
excitation of day airglow [Dargarno et al., 1969].   About 10 %
(1 - 3 eV) of the photoelectron energy goes to heating of thermal
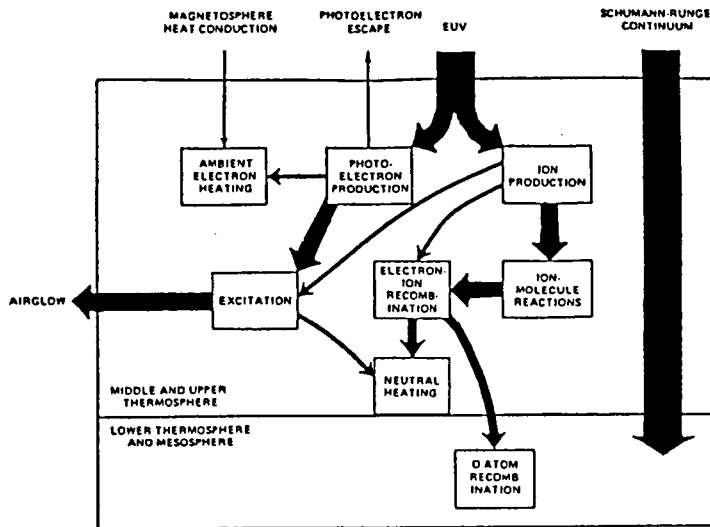
Fig. 1.4   Schematic of EUV energy flow in thermosphere.
          (after R. S. Stolarski, 1976)

electrons, which may maintain an electron temperature exceeding

the corresponding temperatures for ions and neutrals.   The

knowledge of the spatial and energy distribution of photoelectrons

has been recognized to be essential for quantitative understanding

of their important roles and has been the object of extensive

theoretical calculations.

At lower altitudes ($\leq$ 250 km), it is valid to assume that

the photoelectron energy distribution is determined by local

production and loss.   This assumption is called as a local

approximation.   There are two ways in treatment of energy loss;

continuous slowing down and discrete energy loss.   The continuous

slowing-down assumption is valid when the fractional energy loss

is much less than unity in most collisions.   Early works were

carried out under this assumption [Hoegy et al., 1965; Dargarno

et al., 1969; Shea et al., 1968].   Although these calculations

gave roughly reasonable results, the discrete energy-loss procedure

is expected to be more accurate in the photoelectron energy region where a considerable fraction of the electron energy is lost by inelastic collisions with neutral particles. This procedure has been applied by Ogawa [1971], Myers et al. [1975], Victor et al. [1976] and others. Ogawa [1971] has given a comparison of the continuous slowing-down solution with the discrete energy-loss solution, as shown in Fig. 1.5. The discrete energy-loss solution shows fine structures in the energy spectrum; e.g., a hump in the energy range of 20-30 eV and a steep decrease at 60 eV. These characteristics are attributed to the production spectrum of the primary photoelectron. A deep dip at 2.5 eV is due to the resonant vibrational excitation of nitrogen molecules.
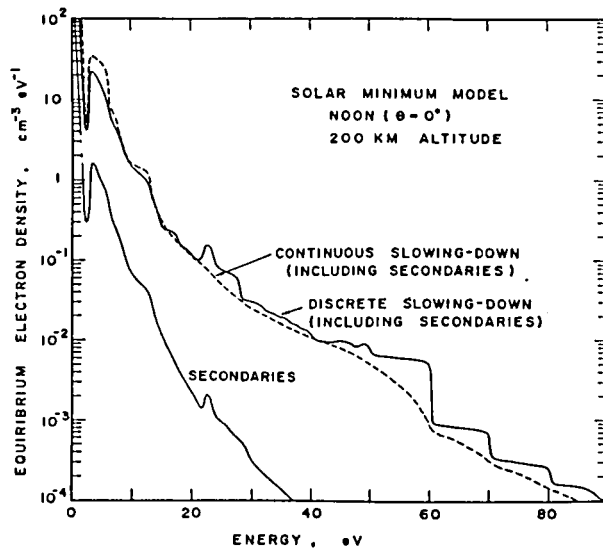
Fig. 1.5 Steady-state energy spectrum f(E) of the nonthermal electrons. Comparison of the continuous slowing-down solution and the discrete energy-loss solution. (after T. Ogawa, 1971)

The assumption of energy loss itself may not be valid in the
very low-energy part of the electron distribution function,
especially in the transition from the non-thermal to the thermal
regions. Ashihara and Takayanagi [1974] have solved the Boltzmann
equation to obtain the electron distribution function, taking
into account all the relevant atomic collision processes.

At higher altitudes where the mean free path associated with
(fast) electron-neutral collisions exceeds the neutral scale
height, fast photoelectrons can travel a considerable distance
before being degraded locally [Hanson, 1963].   Under suitable
conditions this distance can be so large that photoelectrons are
capable of escaping from the ionosphere where they are produced,
and of travelling along the geomagnetic field lines to the
conjugate ionosphere through the magnetosphere (plasmasphere).
During travelling through the plasmasphere, the escaping photo-
electrons lose their energies through collisions with ambient
thermal electrons, which may contribute to the heat source of
plasmaspheric electrons.   The precipitation of the photoelectrons
onto the dark upper atmosphere from the sunlit conjugate ionosphere
is now recognized to be important cause of predawn enhancement of
630 nm airglow [Duboin et al., 1968; Noxon and Johanson, 1970;
Thuillier et al., 1976] and of predawn increase in electron
temperature [Carlson, 1966; Wrenn and Shepherd, 1969].

A variety of approaches have been devised to treat the
complexities introduced by transport, including models based on
the Monte Carlo technique [Cicerone and Bowhill, 1971; Schlegel,
1974], the diffusion theory [Nisbet, 1968; Swartz and Nisbet,
1972; Swartz et al., 1975], and the two-stream approximation in
the flux-continuity equation [Nagy and Banks, 1970; Banks and

Nagy, 1970]. Cicerone et al. [1973] have carried out a compara-
tive study of these three methods and found a reasonable agreement
among them. Stolarski [1972] and Prather et al. [1978] have
developed the methods based on the radiative transfer theory.
Mantas [1975] and Mantas and Bowhill [1975] have developed a
unified theory including the discrete energy-loss procedure and
the transport effects, where the effects of elastic collisions
and pitch angle variation on transport have been taken into
account. Those approaches have given only the escape flux of
the photoelectron. In order to describe photoelectron transport
along a field line from one hemisphere to another, one has to
take into account other effects, e.g., angular diffusions due to
the long-range coulomb scattering and wave-particle interactions.
Lejeune and Wormser [1976] have taken into account the angular
diffusion due to electron-electron collision, and have found that
the angular diffusion may cause field-line trapping of photo-
electrons and thus decrease transmission of the photoelectron
between the conjugate points.

2.1.2 Observations of Ionospheric Photoelectrons by Other
     Investigators

    There have been very few rocket measurements of ionospheric
photoelectrons, although Doering et al. [1975, 1976] and Lee et
al. [1980a, 1980b] have recently made extensive measurements of
the photoelectrons by the AE-C and AE-E satellites. Satellite
measurements provide the data with global coverage under different
levels of solar activity, while rocket measurements have advantage

of obtaining the data on the vertical dependence of electron spectra under a constant geophysical and solar activity. The coverage of the altitudes is generally lower than satellite altitudes.

Early results on the experimental photoelectron flux were obtained by means of the incoherent scatter radar [Ungvesson and Perkins, 1968; Evans and Gastman, 1970], but their results did not show any characteristic features on the photoelectron spectra. There have been several earlier rocket and satellite measurements [Wrenn, 1974 for review] which have also provided only coarsely resolved energy spectra of photoelectrons. Rao and Donley [1969], Knudsen [1972], and Knudsen and Sharp [1972] used retarding potential analyzers which are susceptible to undesired backgrounds and are lack of fine energy and angular resolution.

Doering et al. [1970] have used a hemispherical electrostatic analyzer, but did not take into account all the necessary considerations for the measurements of low energy electrons; e.g., no shielding of the external magnetic field and no quantitative consideration for the shadowing effect (see Section 3 in Chapter III). However, Hays and Sharp [1973] used a hyperbolic arrangement of electrostatic analyzer with adequate considerations and obtained the photoelectron spectra at dusk (solar zenith angle - 90°) showing the valley like structure around 2.5 eV. McMahon and Heroux [1978], who used a cylindrical electrostatic analyser, measured relative values of photoelectron energy spectra in the daytime and obtained an altitudinal variation of the valley like structure around 2.5 eV. There have been no rocket measurements of the conjugate photoelectrons at predawn in winter by other investigators.

2.2 Auroral Electrons

2.2.1 Polar Aurora and Electron Precipitation

It is well known that polar auroras are caused by energetic
particles, mainly electrons, precipitating into the upper atmos-
phere at high latitudes along the magnetic field lines from the
distant magnetosphere.   Auroral phenomena are closely related
with local and global dynamical behavior of the magnetosphere.
Early works in auroral research were based on ground-based
observations of visual auroras and magnetograms.   Feldstein
[1966] first established the configuration of the auroral oval.
Akasofu [1964] first defined the auroral substorm, the onset of
which was the sudden brightening of an equatorward aurora near
midnight.   The auroral substorm is, now, one of various manifes-
tations of a magnetospheric substorm; a transient process initiated
on the nightside of the earth, in which a significant amount of
energy derived from the solar-wind magnetosphere interaction is
deposited in the auroral ionosphere and in the magnetosphere
[Akasofu and Kamide, 1980].
    Various types of auroras have been recognized to exist;
their characteristics on a global scale are shown schematically
in Fig. 1.6.   It is seen that the auroral oval consists of
diffuse auroras and of discrete auroras located poleward of
diffuse auroras.   The highest-latitudinal region around noon is
a singular region; that is, a cusp where the magnetosheath plasma
may make direct access to the polar ionosphere [e.g., Frank,
1971; Winningham, 1972; Doering et al., 1976].
    Characteristics of auroral electrons have been studied
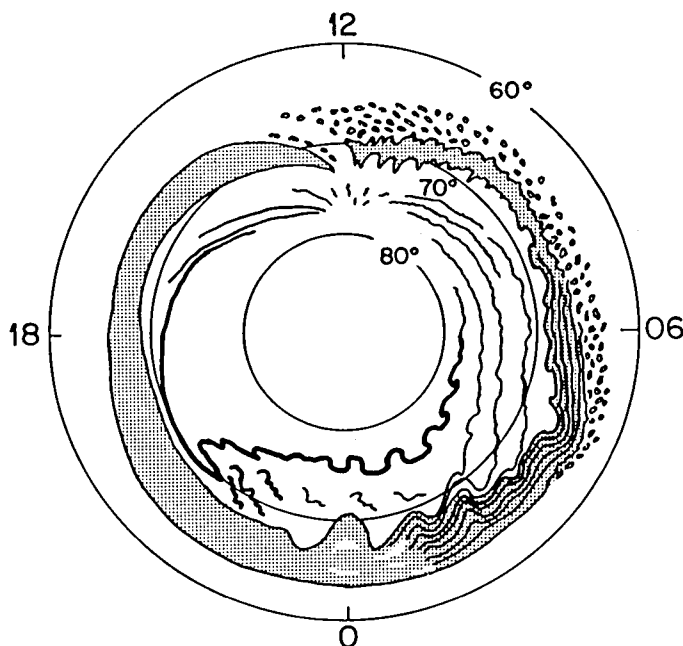
Fig. 1.6 Schematic diagram showing the main characteristics of auroras
during an auroral substorm in dipole-MLT coordinates.
Discrete arcs are indicated by lines and the diffuse auroral
regions are shaded. (after S. -I. Akasofu, 1977)

extensively by rocket and satellite observations [Meng, 1978 for

review].   Winningham et al. [1975] classified the precipitation

region in the nightside into three latitudinal zones connected to

parts of the magnetotail as source regions; Van Allen belt, CPS

(central plasma sheet) and BPS (boundary plasma sheet) from lower

to higher latitudes.   BPS electrons are highly variable according

to the substorm phases.   Lui et al. [1977] and Meng [1978] found

that diffuse aurora is caused by the CPS electrons with a Maxwellian

energy spectrum and the discrete aurora by the BPS electrons

which are energized to have monoenergetic peaks in the 1 to 10

keV energy range.   This energization of precipitating electrons

is one of the major problems in the magnetospheric and auroral

physics and will be described in the next subsections.

Field-aligned currents, called sometimes the Birkeland currents, have been considered to play important roles in coupling the magnetosphere with the auroral ionosphere electrically. Figure 1.7 shows a summary of the spatial distribution and flow directions of the large scale Birkeland currents determined from magnetic-field measurements on the TRIAD satellite [Iijima and Potemra, 1978]. However, the identification of the charge carriers for these currents has not been well resolved. Most of the charge carriers of upward currents seem to be precipitating low-energy electrons with energies below a few hundred eV [Saflekos et al., 1977], while it has been suggested that the downward currents are carried by ionospheric thermal electrons flowing upwards [Potemra, 1979]. This, however, has not been confirmed.
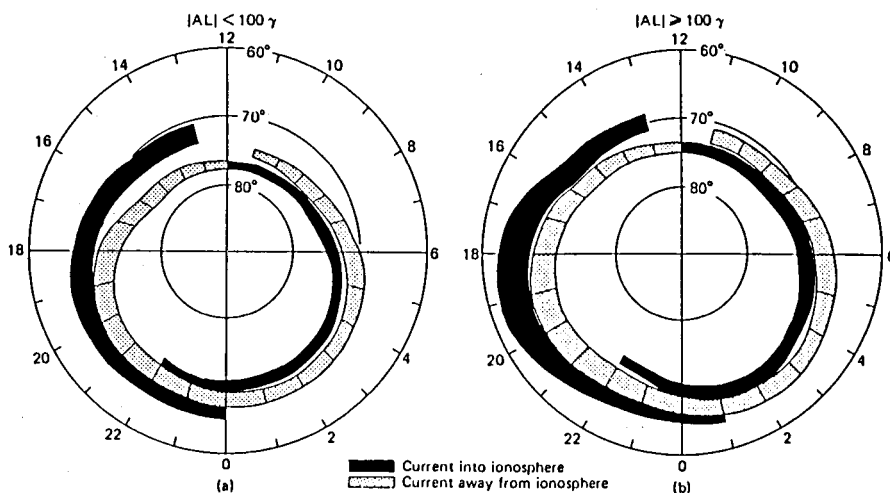
Fig. 1.7 A summary of the distribution and flow directions of large-scale Birkeland currents determined from (a) data obtained from 439 passes of TRIAD during weakly disturbed conditions and (b) data obtained from 366 TRIAD passes during active periods. (after T. Iijima and T. A. Potemra, 1978)

2.2.2 Acceleration of Auroral Electrons

Acceleration of auroral electrons to the keV-energy range is
one of the major problems in the magnetospheric and auroral
physics.   Theoretical models for electron acceleration by the
electric field parallel to the magnetic field lines have been
proposed; double layer [Block, 1972, 1975], oblique electrostatic
shock [Swift, 1978], anomalous resistivity [Paradopoulos, 1977].
Developments toward a unified theory have been reviewed by Kan
[1982].   Various rocket and satellite observations [e.g.,
Arnoldy et al., 1974, Lui et al., 1977; Meng, 1978] have shown
that the energy spectra of precipitating electrons which produce
discrete auroral arcs have monoenergetic peaks in the 1 to 10 keV
energy range.   The peak energy has been found to show an inverted-
V variation in the energy-time spectrogram [Frank and Ackerson,
1971].   In addition, Frank and Gurnett [1971] have suggested
that the inverted-V precipitation in the dusk auroral region is
produced by direct electrostatic acceleration of magnetosheath
electrons.   Burch et al. [1976] also have suggested that the
electron distribution functions in the inverted-V events in the
1200-1800 MLT quadrant are well described by Maxwellian primary
electron beams which have been accelerated through an electrostatic
potential and that these events occur in the regions magnetically
connected to the plasma sheet as well as to the magnetosheath.
Lin and Hoffman [1979] have found that inverted-V events occur at
all local times in the auroral as well as the polar cap latitudes
and that most of the energy and pitch angle features can be
interpreted as electrons accelerated by an electrostatic field
which is created by anomalous resistivity.   Recent particle and

field observations from the S3-3 satellite [Mizera and Fennell, 1977; Cladis and Sharp, 1979; Mozer et al., 1980a] and the near-conjugate observations of precipitating electrons by the DE-1 and DE-2 satellites [Lin et al., 1985] have suggested a possibility that such parallel electric fields for particle acceleration exist at altitudes of several thousand km above the auroral ionosphere.

Most observations of auroral electrons described above and also in the preceding subsections have been made from polar-orbiting satellites, and thus have shown only latitudinal patterns of precipitation. In contrast, observations from the KYOKKO satellite to be described in Section 2 of Chapter V have provided us with interesting patterns which show longitudinal as well as latitudinal variations.

2.3 Suprathermal Electrons in the Inner Magnetosphere

An enhanced dawn-dusk electric field across the magnetotail convects quickly the plasma sheet particles earthward by the E x B drift. The convecting particles experience betatron and Fermi acceleration as they are transported by the enhanced electric field, until their motion is influenced by the force of gradient-B and curvature drift to form the ring current (Van Allen belt). This simple picture is complicated by interactions between these hot plasmas and the cold dense plasmasphere via a variety of wave-particle interactions around the plasmapause.

Observations from the geostationary satellites (e.g., ATS, SCATHA and GEOS-2) revealed the dynamical behavior of substorm-

associated plasma injection at nearly constant L of 6.6 in the
equatorial region, while highly eccentric satellite (e.g., OGO-5,
S3-A, ISEE-1, GEOS-1) observed the ring current evolution and
decay.   Ejiri [1978] have developed a quantitative convection
model to exlain the so-called nose feature of the proton dynamics
observed by the S3-A satellite.

    There have been few simultaneous observations of wave
spectra and electron distribution functions in the inner magneto-
sphere.   Anderson and Maeda [1978] observed VLF emissions
associated with enhancements of low energy electrons during
periods of geomagnetic disturbances.   Wrenn et al. [1979]
observed 'pancake' distributions of low-energy electrons correlated
with electron-cyclotron harmonic waves.   Koons and Fennell
[1983] observed correlations between wave emissions and hardening
and anisotropy of electron spectra in the inner edge of the
plasma sheet.   The JIKIKEN observation (see Section 3 in Chapter
V) has shown a unique feature of the high pitch angle anisotropy
in electron distributions around the plasmapause, in association
with amplification of the VLF signals artificially transmitted
from the ground Siple station [Kimura et al., 1983].

§3. Review of Existing Methods for Measurement of Low Energy

    Electrons

    There are a wide range of techniques available that can be
used for the energy measurement of charged particles.   In
general, both electric and magnetic fields in various geometrical
shapes will give energy separation, but magnetic devices are

unsuitable for measuring low-energy electrons because of the difficulties in controlling low magnetic fields. A review of various types of energy analyzers in general is given by Stecklmacher [1973]. Here we briefly review two basic types of instruments which have been used to measure low-energy electrons in space plasma; retarding potential analyzers and electrostatic analyzers.

3.1 Retarding Potential Analyzers (RPA's)

RPA's, sometimes called Faraday Cups, have been used for a long time on both rockets and satellites. Figure 1.8 shows a schematic diagram of a retarding potential analyzer used for measuring ionospheric photoelectrons by Knudsen and Sharp [1972].
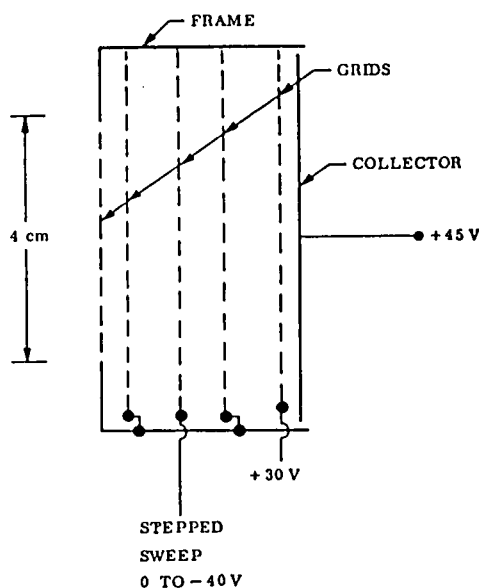
Fig. 1.8 Schematic diagram of a retarding potential analyzer.
(after W. C. Knudsen and G. W. Sharp, 1972)

This is a typical example of an RPA used also by others.   It
consists of a circular current collector behind several high-
transparency grids.   The essential part for the energy analysis
is, in this case, the third grid to which a swept retarding
voltage is applied.   Electrons which can just surmount the
height of this potential barrier can reach the collector.
Therefore the current to the collector, which is usually detected
with a logarithmic electrometer, is a measure of the integral
electron flux with energy above this threshold.   Additional
grids are used to shield the electric fields, repel positive ions
and suppress the secondary emission.

      Advantages of the RPA's are that they have a simple structure
with small dimensions and that the electrometers are stable
detectors and can be calibrated accurately in flight.   On the
other hand, the RPA's suffer from several shortcomings.

      First, the experimental curve must be differentiated in
order to obtain the energy spectrum of electrons being analyzed,
but this is not a simple procedure because the transmission is a
complex function involving energy and angle.   Let the nominal
retarding potential and the incident angle be V_o and θ, respective-
ly.   Then the particle energy reaching the collector, E, must
satisfy the following equation.

$$E > eV_o \sec^2\theta, \tag{1.1}$$

where e is the electronic charge.   Since the RPA collects over a
large solid angle, the shape of energy and angular distributions,
which is the object of measurement, must be assumed in order to
derive the energy spectrum.   The angular distribution is usually

assumed isotropic, but this is not always correct. In addition,
there are parasitic effects due to the interactions between
electrons and grids. After all, high energy and angular resolu-
tion cannot be achieved with the RPA's.

Next, since high-energy particles and solar EUV radiation
can strike the current collector directly, spurious effects due
to their secondary emissions cannot be fully rejected. A
suppressor grid with some negative potential relative to the
collector is usually used for this protection, but secondary
electrons from grids can reach the collector, being accelerated.
These spurious effects due to high-energy particles and solar EUV
radiation may be, more or less, inevitable in any type of the
plasma analyzer for space use, but the rejection of data including
these effects is very difficult especially in the RPA, since the
current collector can look space straightforward and collect over
a large view angle.

The modulated Faraday cup have been used in order to overcome
the above shortcomings, in which an alternating potential,
usually in the form of a square wave, is applied to the modulator
grid instead of a steady retarding potential. These Faraday
cups have been successfully used to measure positive ions
[Vasyliunas, 1970]. However, it is inevitable that the upper
most energy of measurement is limited because of high voltage
breakdown and also of insufficiency of the incoming fluxes in
high energies.

3.2 Electrostatic Analyzers

An electrostatic analyzer consists of a pair of electrostatic

deflection plates.   Various geometries for deflectors, as

reviewed by Afanas'ev and Yavor [1976], have been developed for

the energy measurements of charged particles over a wide range of

energy from a few eV up to several tens of keV.   The common

features are listed below:

 (1)   The applied voltage on the analyzer plate is a linear

function of particle energy where relativistic effects can be

neglected.   The ratio of the applied voltage to the particle

energy is usually much smaller than unity.   Therefore, it can be

applicable for measurements of higher energy particles than those

by RPA's, because a possibility of high voltage breakdown is less

than RPA's.

 (2)   These analyzers have well-defined fields of view and can

give differential energy spectra with far higher resolution than

is possible with RPA's.   The relative energy resolution $\Delta E/E_0$ is

constant over a wide energy range.

 (3)   On the other hand, since the sensitivity/geometrical factor

cannot be so large as those of RPA's, they must be usually used

together with electron multipliers as detectors rather than the

current collectors.   The developments of small channel electron

multipliers, which is reviewed in next subsection, have considera-

bly increased the availability of electrostatic analyzers in

space.

     The most popular analyzers are cylindrical and spherical

electrostatic analyzers.   Figure 1.9 shows a schematic diagram

of a cylindrical analyzer, in which some voltage is applied

across the inner and outer plates.   Then, since the electric

field is radial, the trajectory of particles entering the analyzer

with normal incidence will be circular in the analyzer if the
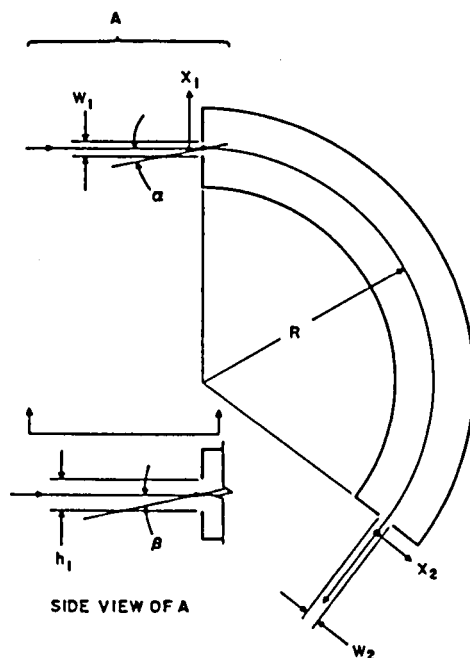
Fig. 1.9 Highly schematic diagram of an electrostatic energy analyzer.
(after C. E. Kuyatt, 1968)

electric field is balanced against the centrifugal force of the
particles with the same center of curvature; i.e.,

$$mv_o{}^2/R = qE_r \ ,$$

(1.2)

where R is the radius of the particle trajectory, E_r is the
strength of the radial electric field, and m, v_o and q are mass,
velocity and charge of the particle, respectively.   Optimum
focusing action is obtained when the particle beam is deflected
through $127°17'$ [Hughes and Rojansky, 1929].   The radial position
X_2 at the exit plane of particles with energy (Eo + ΔE) entering
the analyzer at the radial position X_1 can be given in the

first-order approximation [Kuyatt, 1968] by

$$X_2/R = -X_1/R + \Delta E/E_o - 4\alpha^2/3 - \beta^2 \; , \qquad (1.3)$$

where $E_o = mv_o^2/2$, and α and β are the incident angles relative to the normal of the entrance plane in the radial and tangential planes, respectively. The corresponding relationship for the spherical analyzer giving after 180° deflection [Purcell, 1938] is

$$X_2/R = -X_1/R + 2\Delta E/E_o - 2\alpha^2 \; . \qquad (1.4)$$

Both types give second-order focusing in the radial plane, but the hemispherical analyzers (i.e., 180° spherical deflection) give perfect focusing in the tangential (β) plane due to the spherical symmetry. The above equations are useful for design of the analyzer especially for laboratory use where the paraxial particle beams are treated. The more accurate calculations of the particle trajectory have to be carried out for space use where the source particles are diffuse ambient particles.

Other geometries of electrostatic analyzers that have been used for measurements of charged particles in space are LEPEDEA by Frank [1967], SPS by Heikilla et al. [1970], and HARP by Hays and Sharp [1973]. The LEPEDEA consists of three cylindrical 43° section plates which make two gaps for analyzers; one is for ion measurements and another for electrons. The SPS consists of two diverging systems; one for electrons and another for ions. The HARP is a hyperbolic arrangement retarding potential analyzer which gives differential energy spectra and has been used for the measurement of ionospheric photoelectrons.

3.3 Electron Multipliers

There are various types of electron multipliers; discrete and continuous.   Continuous channel electron multipliers are one of the most useful detectors which have been used frequently together with electrostatic analyzers.   Figure 1.10 shows a schematic diagram of a channel electron multiplier to explain multiplication of secondary electrons.   It is made of a curved glass-tube and its inside wall is of a semiconductor material which has a large coefficient for secondary-electron emission. It is sensitive to charged particles, photons and other energetic particles capable of emitting secondary electrons from the surface of the material.   Some high voltage (typically $\sim$ 3 kV) is applied across the inlet and exit of the multiplier so as to accelerate electrons toward the exit.   Secondary electrons which are emitted from the inside wall by an incident particle are accelerated through the tube and strike the wall to emit a few secondary electrons additionally.   The number of electrons
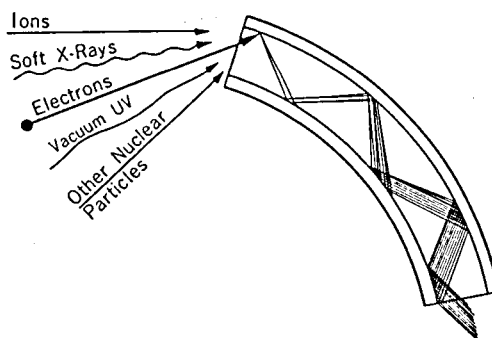
Principle of Electron Multiplication

Fig. 1.10 Schematic drawing of a channel electron multiplier.

increases through repeating this process, until it reaches some

saturation level of $10^{7 \sim 8}$ due to the space charge effect. The

number of electrons produced from the exit for one incident

electron is called 'gain' of the multiplier. Since it is

produced as a charge pulse from the exit, the output charge can

be converted into a voltage pulse by a particular electronic

circuit; e.g., a charge-sensitive amplifier, and can be counted

digitally. The advantage of this method is that the obtained

data (counts) are insensitive to the gain variation if the output

pulse is sufficiently higher than a noise level. The problem,

however, is variability of the detection efficiency which is a

probability for producing the output pulse by incidence of the

particle, as shown in Fig. 1.11.

Some channel electron multipliers have funnels or cones at

the inlet to increase sensitive areas, but caution must be paid

for usage because the detection efficiency is not necessarily

uniform over the inlet area [Baumgartner and Huber,1976].
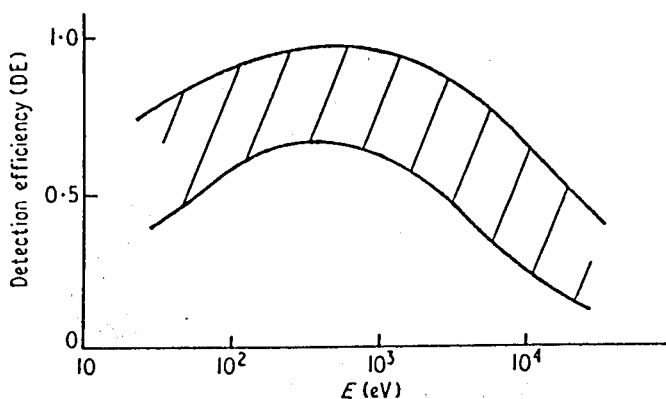
Fig. 1.11 Absolute detection efficiency of continuous channel electron
multipliers against energy E of electrons.
(after W. E. Baumgartner and W. K. Huber, 1976)

§4. Contribution of the Present Work

As reviewed in the preceding sections, suprathermal electrons play important roles in the ionospheric and magnetospheric plasma, and to date, many measurements have been made by means of various energy analyzers on board rockets and satellites. However, full understanding has not yet been established, since these measurements were not complete.

The choice of instrument is essential. We adopt a hemispherical electrostatic type as an energy analyzer. The transmission properties of charged particles through this analyzer will be examined in detail in the next chapter. The primary attraction of this instrument is high energy resolution over a wide energy range from a few eV to several tens of keV. It has inherently a double focusing property due to the spherical symmetry and therefore gives a good transmission. In addition, there is less chance of unwanted particles reaching the detector than in other types of energy analyzers, because the particle trajectories are long and curved. This feature is especially important for the measurement of low energy electrons, since most instrumental secondaries are produced at low energies and become a cause for background noise. In addition, we add a high-energy particle trap on the outer hemispherical plate for suppression of the background noise. For measurements of ionospheric photoelectrons in the very low energy, a sophisticated inlet collimator which constitutes electron lenses is developed. By accelerating or decelerating electrons through the electron lenses, the energy of electrons entering the analyzer can be kept constant during the energy scanning; i.e., the measured energy is scanned by changing

the acceleration/deceleration voltage. Thus, since the condition
of electron transmission through the analyzer is kept constant,
the energy bandwidth can be kept constant (ΔE = constant) over
the measured energy range. Instead, the transmission function
of the collimator must be well known and will be described in the
next chapter.

Chapter III is devoted to the description of instrumentation
for measurement of the photoelectrons in the ionosphere [Mukai
and Hirao, 1973a, 1974, 1975; Mukai et al., 1979]. At first the
design principle is given, based upon the study in Chapter II.
In order to operate the spectrometer well for the measurement of
low energy electrons on rockets, various cautions should be paid
for the design, construction and calibration of the spectrometer.
They arise basically from the nature of low energy electrons
susceptible to the electric and magnetic field and from the
surface physics that high energy particles and solar EUV photons
eject electrons from the material in the same energy range as
that of the ionospheric photoelectrons to be measured.

The scientific results obtained by the rocket experiments
are discussed in Chapter IV [Mukai and Hirao, 1973a, 1973b, 1974,
1975; Mukai et al., 1979]. The six rocket experiments were
carried out successfully; four experiments in the daytime and two
at predawn. In spite of careful design and construction of the
electron spectrometer, it is actually inevitable that the raw
data contain spurious ones to some extent. Removal of these
spurious data is carried out to give reliable results. The
observed spectra in the daytime condition are discussed in terms
of theoretical interpretation. A remarkable coincidence between
observation and calculation is attained, indicating a high

resolution capability and high reliability of our instrument. The predawn experiments in winter have also revealed interesting characteristics of the conjugate photoelectrons, which are discussed in comparison with calculated results.

Based on the result of developments of the rocket-borne instruments, electron spectrometers are designed for satellite payloads and discussed in Chapter V. Three satellite observations will be described; observations of auroral electrons by the KYOKKO satellite [Mukai and Hirao, 1978, 1979a, 1979b, 1981, 1982], of inner-magnetospheric electrons by the JIKIKEN satellite [Mukai et al., 1979; Kubo et al., 1979, 1981; Matsumoto et al., 1979, 1981; Kimura et al., 1983], and of auroral particles and ionospheric photoelectrons by the OHZORA satellite [Mukai et al., 1985a, 1985b; Kaya et al., 1985]. The limitations of weight, power, bit rate and other environmental conditions are much severer in satellite instrumentation than in rocket payloads. We have designed and constructed the instruments to obtain as more scientific results as possible under the allowed resources, taking into account the orbit and the attitude control system of the satellite. The observed results have revealed various characteristics of the dynamical behaviors of charged particles in the ionosphere and magnetosphere and are discussed in terms of the relating physical processes.

Chapter II. Theory and Calculations of Transmission Properties of
        Hemispherical Electron Spectrometers

§1. Introduction

     As mentioned in Section 4 of Chapter I, we have adopted a
hemisherical electrostatic analyzer for measuring low-energy
electrons in the ionosphere and magnetosphere.   For the rocket
observations of ionospheric photoelectrons, we have also used an
inlet collimator which consists of a three-electrode electron
lens.   In this chapter, we are concerned with theoretical
studies of basic transmission properties of these analysing
elements.   The results obtained in this chapter will be applied
to design of electron spectrometers on board rockets and satel-
lites in subsequent chapters.
     Spherical electrostatic analyzers have been used for many
years in the laboratory and their instrumental functions have
been reported by many authors [Purcell, 1938; Pogers, 1951;
Kuyatt and Simpson, 1967; Roy and Carette, 1971].   In the
laboratory the particle source is discrete, and the most important
properties of the spectrometer are the energy resolution and
focusing action. On the other hand, for space use the source
particles are diffuse, extended and have a wide range of energies.
The most important parameter is the energy-geometric factor, in
addition to the energy resolution and angular acceptance.
General consideration for space use is given in the next section.
     In section 3 the properties of hemispherical electrostatic
analyzers are calculated theoretically for the diffuse particle
source.   Other authors also have described methods of calculating

the properties of spherical electrostatic analyzers for the diffuse particle source. Paolini and Theodoridis [1967] have presented the method for obtaining the energy-geometric factor under the assumption that all the particle trajectories are approximated by circular arcs and that the effects of the fringing field was neglected. Chase [1973] have calculated the properties of hemispherical electrostatic analyzers with large plate separation numerically, taking the fringing field into account. Gosling et al. [1978] have reported effects of a long entrance aperture upon the azimuthal response of spherical electrostatic analyzers. We present a numerical method for calculating the energy and angular responses and the energy-geometric factor of hemispherical electrostatic analyzers by using the exact particle trajectories under the assumption that the effect of the fringing field can be neglected.

Section 4 is devoted to calculations of transmission properties of a three-electrode electrostatic electron lens. The important properties of an electron lens are generally the focal length and the aberration, but our purpose is to calculate the geometric factor for the diffuse source. Firstly, we present a method for calculating the geometric factor by using a paraxial-ray approximation. Then, the more accurate values are calculated by using a Monte-Carlo method (full treatment) and are compared with the results obtained by the paraxial-ray approximation.

§2. General Consideration

What we want to know in measurements is the differential particle flux f(E) at energy E. The value of the velocity

distribution function F(v) can be related with the differential

flux f, as follows.

$$F = [(m/e)^2 f/2E] \times 10^{-2}, \qquad (2.1)$$

where F is expressed in $s^3 m^{-6}$, f is in $(cm^2 \ s \ sr \ keV)^{-1}$, E is the

particle energy in keV, and m and e are the particle mass and

charge in MKS units, respectively.   More conveniently, the above

relations for electron and proton, respectively, are given below.

For electron,

$$F = 1.616 \times 10^{-25} (f/E). \qquad (2.2)$$

For proton,

$$F = 5.449 \times 10^{-19} (f/E). \qquad (2.3)$$

The counting rate C, in units of sec^{-1}, of an instrument

measuring differential energy spectra of particles in this

distribution at $t = t_0$ is given by

$$C(E_0, t_0) = \frac{1}{\tau} \int_{t_0 - \tau/2}^{t_0 + \tau/2} dt \int_S \mathbf{r} \cdot d\mathbf{a} \int_\Omega d\boldsymbol{\omega} \int_0^\infty dE \ f(E, \mathbf{a}, \boldsymbol{\omega}, t) \ p(E_0, E, \mathbf{a}, \boldsymbol{\omega}) \ \eta(E),$$
$$\qquad (2.4)$$

where E=particle energy, E_0=tuned energy of the instrument,

τ=sampling period, $\mathbf{r}$=unit vector in direction $\boldsymbol{\omega}$, d$\mathbf{a}$=surface

element of the instrument entrance aperture S, and Ω=solid angle,

respectively.   The function p has the value unity for values E_0,

E, $\mathbf{a}$, $\boldsymbol{\omega}$ corresponding to trajectories which transmit through the

analyzer and zero otherwise.   The function η is the detection

efficiency of a detector, which is usually a slowly-varying

function of particle energy.

The following assumptions are usually used to simplify the

above integral equation; (a) the particle flux is constant over

the sample period, the entrance aperture and the energy bandwidth
of the instrument; and (b) the particle flux is isotropic over
the instrument field of view.   Then the equation (2.4) can be
expressed as

$$C(E_0,t_0) = f(E_0,t_0)\ g(E_0)\ \eta(E_0),\tag{2.5}$$

where

$$g(E_0) = \int_S \mathbf{r} \cdot d\mathbf{a} \int_\Omega d\omega \int_0^\infty dE\ p(E_0,E,\mathbf{a},\omega).\tag{2.6}$$

$g(E_0)$ is, so called, an energy-geometric factor and is usually
expressed in units of $(cm^2 sr\ eV)$ or $(cm^2 sr\ keV)$.   The energy
dependent geometrical factor $G(E_0,E)$ is defined by

$$G(E_0,E) = \int_S \mathbf{r} \cdot d\mathbf{a} \int_\Omega d\omega\ p(E_0,E,\mathbf{a},\omega)\tag{2.7}$$

in units of $(cm^2 sr)$, and then, the equation (2.6) can be re-
written as

$$g(E_0) = \int_0^\infty G(E_0,E)\ dE.\tag{2.8}$$

Both quantities, $G(E_0,E)$ and $g(E_0)$, are functions of the
geometry of the analyzer/detector only.   From $G(E_0,E)$, the
energy resolution ΔE, defined to be the full width at half-maximum,
can be found as shown in Fig. 2.1.   If the functional shape of
$G(E_0,E)$ can be approximated to be triangular, then the equation
(2.4) can be rewritten as

$$C(E_0,t_0) = \Delta E\ G_0\ \eta(E_0)\ f(E_0)\ .\tag{2.9}$$

where $G_0 = G(E_0,E_0)$.
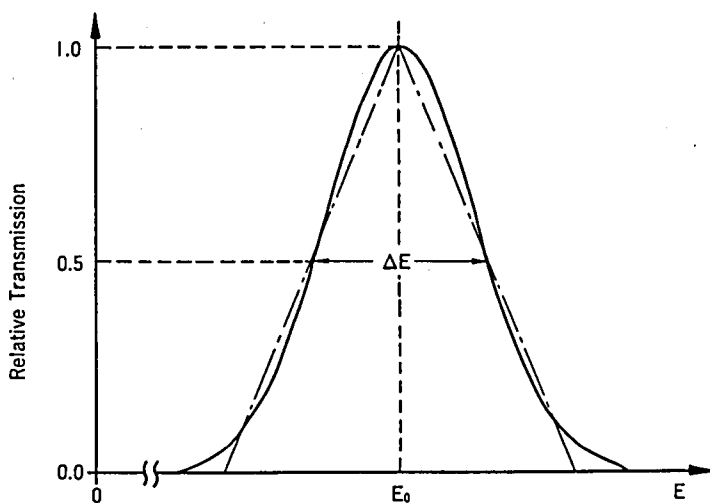
Fig. 2.1 Transmission function of an energy analyzer of differential type. ΔE is the full width at half maximum.
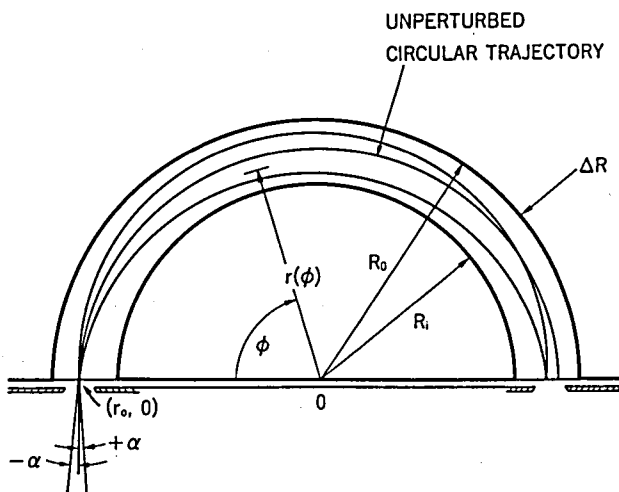
Fig. 2.2 Schematic representation of particle trajectories in a hemispherical electrostatic analyzer.

§3. Charged Particle Transmission through Hemispherical

  Electrostatic Analyzers

 3.1. Electric Potential

    The geometry of a hemispherical electrostatic analyzer
consists of two concentric hemispherical plates with slits in the
entrance and exit planes, as schematically shown in Fig. 2.2.
R_i and R_o are the radii of the inner and outer plates, and V_i and
V_o are the electric potentials of the inner and outer plates,
respectively. If the potentials of the inlet and exit slit
electrodes are zero and the gap between the slit electrode and
the spherical plate can be neglected, then the electric potential
$\Phi(r,\phi)$ in the analyzer can be expressed exactly as

$$\Phi(r,\phi) = \sum_{\substack{n \\ (odd)}} \frac{2n+1}{2} (-1)^{\frac{n-1}{2}} \frac{(n-2)!!}{(n+1)!!} \frac{P_n(\sin \phi)}{(R_o^{2n+1} - R_i^{2n+1})}$$

$$\times [r^n(V_o R_o^{n+1} - V_i R_i^{n+1}) + r^{-(n+1)}(V_i R_i^{n+1} R_o^{2n+1}$$

$$- V_o R_o^{n+1} R_i^{2n+1})] , \qquad\qquad (2.10)$$

where r and ϕ are the coordinates of the point as shown in Fig.
2.2.   The function $P_n(\sin\phi)$ is the n-th order Legendre polynomial
and the sum is carried out over odd integer values of n.

    Equation (2.10) is identical to the following expression
except near the edges;

$$\Phi(r) = -K/r + \Phi_\infty , \qquad\qquad (2.11)$$

where　　$K = VR_oR_i/\Delta R$,

　　　　$\Phi_\infty = (V_oR_o - V_iR_i)/\Delta R$,

　　　　$V = V_o - V_i$,

　　　　$\Delta R = R_o - R_i$.

3.2　Particle Trajectories

　　According to Eq. (2.11), the electrostatic force on a
charged particle in the electric field between two concentric
hemispherical plates is radial with respect to the common center
of the plates.　Then, neglecting the effect of the fringing
field, the particle trajectory is given by the solution of the
usual central-force problem (Goldstein, 1959) as

　　　　$1/r = A [1 + \varepsilon\cos(\phi-\phi')]$,　　　　　　　　　　　(2.12)

　where　$A = mqK / L^2$,

　　　　$L^2 = 2mr_0^2 E(r_0) \cos^2\alpha$; angular momentum,

　　　　$\varepsilon = \sqrt{1+(2\Psi L^2/mq^2K^2)}$; eccentricity,

　　　　$\Psi = E_\infty - q\Phi_\infty = E(r)-qK/r$; energy relative to the spheres

　　　　$E(r)$; kinetic energy of the particle at point (r,ϕ),

　　　　α　; incident angle of the particle at the entrance

　　　　　　point (r_0) as shown in Fig. 2.2,

　　　　E_∞　; kinetic energy of the particle at infinity, or more

　　　　　　practically just outside the entrance slit.

　　　　m ; mass of the particle,

　　　and q ; charge of the particle, respectively.

ϕ', the angle of the apsides, is determined by the initial conditions at $\phi=0$ which are $r=r_0$ and $(dr/d\phi)= r_0 \tan\alpha$, and is given by

$$\phi' = \tan^{-1} (r_0 \sin\alpha \cos\alpha/(c-r_0\cos^2\alpha)), \qquad (2.13)$$

where the parameter c is given by $c=qK/2E(r_0)$.

The particle trajectory can be determined only if the initial condition r_0, α, q and $E(r_0)$ of the particle are known for given analyzer parameters R_i, R_o, V_i and V_o. As noted above, $E(r_0)$ is related to E_∞ as

$$E(r_0) = E_\infty - q\phi(r_0). \qquad (2.14)$$

This relationship is important since the particle flux at some energy E_∞ is what we want to measure. It should be noted that the trajectory is independent of mass m, and therefore the analyzer can be used to measure heavy particles. It can be also found out that the trajectories of particles entering at angles of $+\alpha$ and $-\alpha$ intersect and therefore are focused after the 180° deflection (hemispherical analyzer). On the other hand, all the orbit planes which are in planes of great circles intersect with each other at the 180° deflection due to spherical symmetry. Therefore, a hemispheric electrostatic analyzer has a double-focusing property.

For a particle to be transmitted through the analyzer, $T < 0$ and the trajectory is an ellipse. In addition the following conditions must be satisfied;

$$|r_0 - \bar{R}| < w_i/2, \qquad\qquad\qquad (2.15)$$

$$|r_\pi - \bar{R}| < w_o/2, \qquad\qquad\qquad (2.16)$$

and $R_i < r_{min}$ and/or $r_{max} < R_o$, $\qquad\qquad (2.17)$

where $\bar{R}$ is the mean radius of the analyzer $(R_i + R_o)/2$, r_π the radius of the trajectory at $\phi = \pi$, and w_i and w_o the widths of the inlet and exit slits, respectively. Condition (2.17) comes from $R_i < r(\phi) < R_o$ for $0 < \phi < \pi$, and can be rewritten more concretely as

$$A(1-\varepsilon) > 1/R_o \qquad \text{for } \alpha > 0, \qquad\qquad (2.17a)$$

$$\text{or} \quad A(1+\varepsilon) < 1/R_i \qquad \text{for } \alpha < 0. \qquad\qquad (2.17b)$$

Next we consider a case for the circular trajectory at $r_0 = \bar{R}$. Then, $\varepsilon = 0$ and $\alpha = 0$, and therefore

$$E(\bar{R}) = qVR_oR_i \,/\, (R_o^2 - R_i^2). \qquad\qquad (2.18)$$

It should be noted that the product of q and V must be positive; i.e., V < 0 for the measurement of electron. From Eqs. (2.11), (2.14) and (2.18),

$$E_0 \equiv E_{\infty 0} = E(\bar{R}) + \phi(\bar{R})$$
$$= q(V_o R_o^2 - V_i R_i^2) \,/\, (R_o^2 - R_i^2). \qquad\qquad (2.19)$$

The particle energy E_0 is the mean analyzer energy for the given analyzer parameters. If the analyzer parameters satisfy the condition as

$$R_o V_o = -R_i V_i, \qquad\qquad\qquad (2.20)$$

then $\Phi(\bar{R}) = 0$ and therefore $E_0 = E(\bar{R})$. This is the case when a particle entering the center of the inlet slit does not experience a change in potential or in kinetic energy, and hence the case when the particle trajectory is least affected by the fringing field. If $\Delta R \ll \bar{R}$ and $V_i = -V_0$, then the equation (2.19) can be rewritten as

$$E_0 \simeq qV(\bar{R}/2\Delta R). \tag{2.19a}$$

The equation (2.19) or (2.19a) is important since the applied voltages on the analyzer plates can be related directly with the kinetic energy of the particle to be measured.

3.3   Energy-Angle Response

For given analyzer parameters R_i, R_o, V_i, V_o, w_i and w_o, whether the particle trajectory is transmittable through the analyzer can be easily judged by using Eqs. (2.15) $\sim$ (2.17) under initial conditions E_∞, α and r_0; i.e., the function p in Eq. (2.4) can be evaluated. The energy-angle response is obtained by integration of the function p over the inlet slit. Figure 2.3 shows the calculated range of energies E_∞ and incident angles α transmitted through a hemispherical electrostatic analyzer, where Eq. (2.20) is adopted as the analyzer condition, and $\delta E = E_\infty - E_0$. The transmission is zero beyond the outermost envelope, and the 100 % transmission means that all the particles entering any position in the inlet slit with some energy and angle of incidence can be transmitted through the analyzer. The calcu-

w/R

w/2R

$\delta E/E_0$

0

$-w/2R$

$-w/R$

$-\Delta R/R$ $-\Delta R/2R$ 0 $\Delta R/2R$ $\Delta R/R$

α

T=0

T=1/2

$R_i = 21.5$
$R_0 = 28.5$
$w_i = 6.0$
$w_0 = 6.0$

(b)

w/R

w/2R

$\delta E/E_0$

0

$-w/2R$

$-w/R$

$-\Delta R/R$ $-\Delta R/2R$ 0 $\Delta R/2R$ $\Delta R/R$

α

T=0

T=1/2

$R_i = 21.5$
$R_0 = 28.5$
$w_i = 2.0$
$w_0 = 2.0$
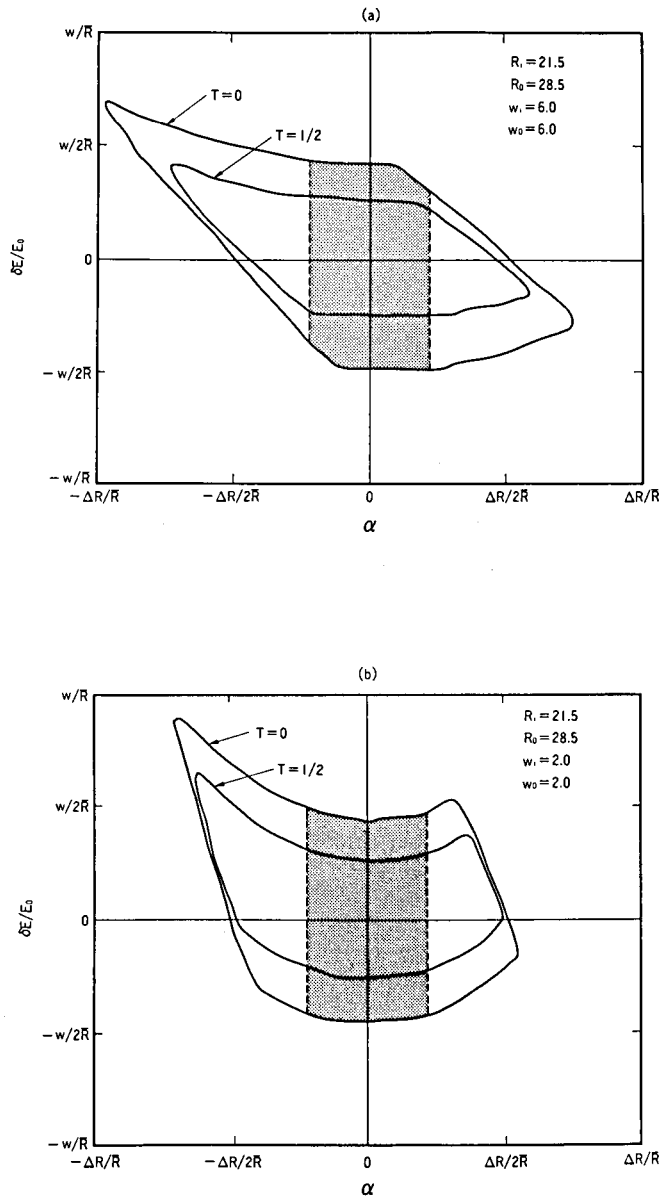
Fig. 2.3   Energy-angle transmission diagrams for a hemispherical
electrostatic analyzer for different slit widths.   Shaded area
represents transmission for a limited angular acceptance.
(a) $R_i = 21.5$ $R_0 = 28.5$ $w = w_i = w_0 = 6.0$
(b) $R_i = 21.5$ $R_0 = 28.5$ $w = w_i = w_0 = 2.0$

lations are made in two cases of slit widths for studying the effect of the slit width.   Here, the width of the exit slit is equal to that of the inlet slit; $w = w_i = w_o$.   The calculated response is not symmetric about either $\alpha=0$ or $\delta E/E_0 = 0$, and therefore it is difficult to define energy and angular resolution separately.   However, it can be said that the angular responses scale as $\Delta R/\bar{R}$ while the energy responses scale as $w/\bar{R}$.   If we adopt a limit of α, such as the shaded area in Fig. 2.3, then the transmission contours approach to be of rectangular shape, in which the energy and angular resolution can be well-defined separately.

Figure 2.4 shows angular responses which is integrated in energy response.   The angular response has a plateau around $\alpha=0$. The full width at half-maximum (FWHM) is nearly independent of the slit width and can be determined as $\Delta R/R$.

Figure 2.5 shows energy responses integrated in angular dimension, in which the angular widths in integration are shown as parameters.   The energy resolution can be obtained as

$$\Delta E/E_0 \simeq w/2\bar{R}, \qquad\qquad (2.21)$$

where ΔE is the full width at half maximum (FWHM).

3.4   Energy-Geometric Factor

Transmission properties discussed above represent an essential part of the analyzer properties, but the energy-geometric factor which is expressed by Eq.(2.6) is the most important for measuring
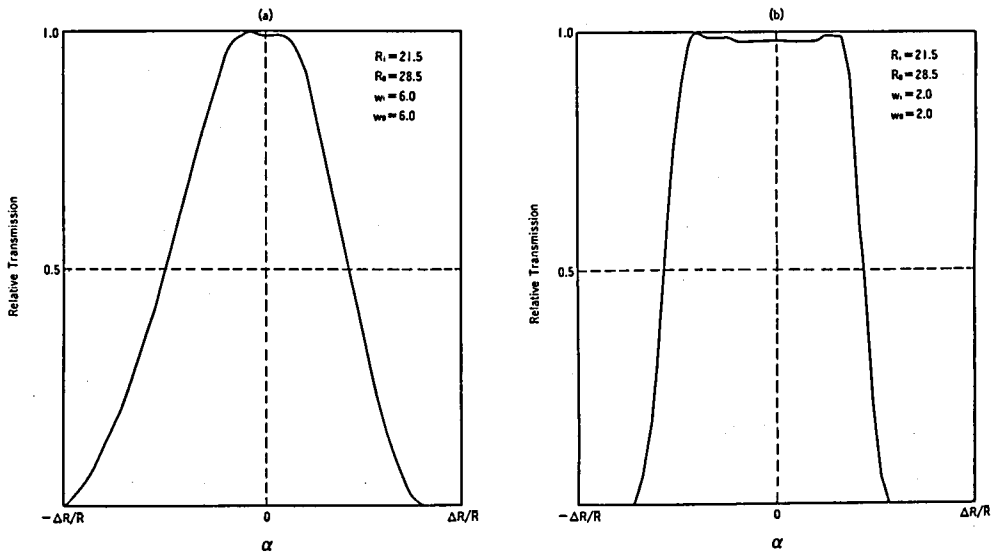
Fig. 2.4 Angular responses integrated in energy for the cases same
as Fig. 2.3.
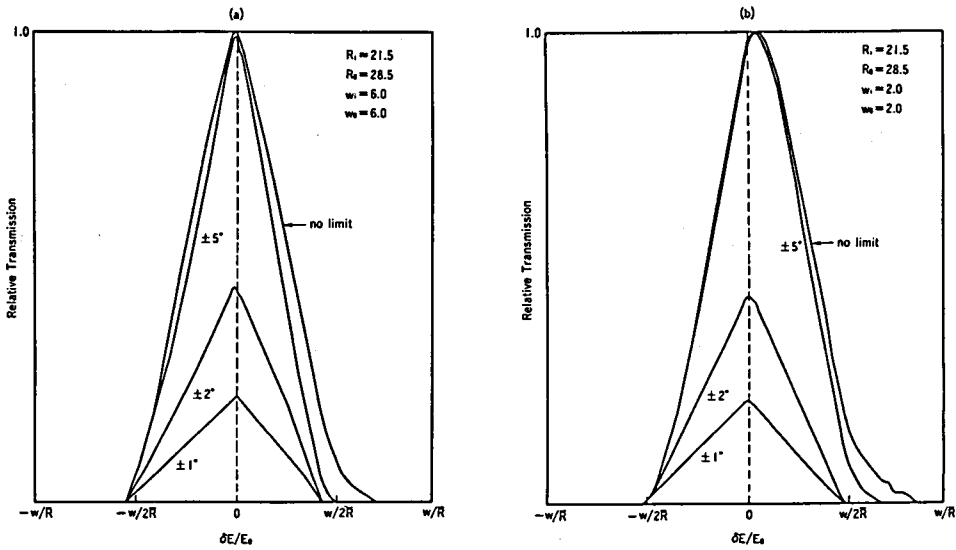
Fig. 2.5 Energy responses integrated in angular dimension for the
cases same as Fig. 2.3. Several graphs correspond to the
different integration widths in angular dimension.

ambient particles.

Figure 2.6(b) shows an example of the energy response for
the collimator-analyzer configuration as shown in Fig. 2.6(a).
This response can be obtained by integration of Eq.(2.7) over
four variables (i.e., two positional and two angular variables)
at each energy by means of a Monte-Carlo method with quasi-random
numbers.   The energy-geometric factor $\langle G \Delta E \rangle$ ($\equiv g(E_0)$; Eq.
(2.6)) can be obtained by integration of the energy response
curve and is shown in the same figure.   The energy response is
similar to that obtained in the previous section (i.e., Fig. 2.5)
and the peak value is nearly equal to the geometric factor G_0 of
the collimator only.   In this case $\langle G \Delta E \rangle$ may be obtained by the
product of G_0 and ΔE where ΔE can be obtained from Eq.(2.21).
More generally, the crude estimate of $\langle G \Delta E \rangle$ is given by

$$\langle G \Delta E \rangle = G_0 \Delta E \xi, \qquad\qquad (2.22)$$

where ξ is a non-dimensional factor which means transmission
efficiency of the analyzer.   The factor ξ depends on the shape
of the energy-angle response contour.   It becomes unity if the
contour shape is rectangular within the angular acceptance of the
collimator.   Eq. (2.22) is useful for quick design of the
analyzer, assuming a reasonable value of $\xi \simeq 0.8$ for instance.
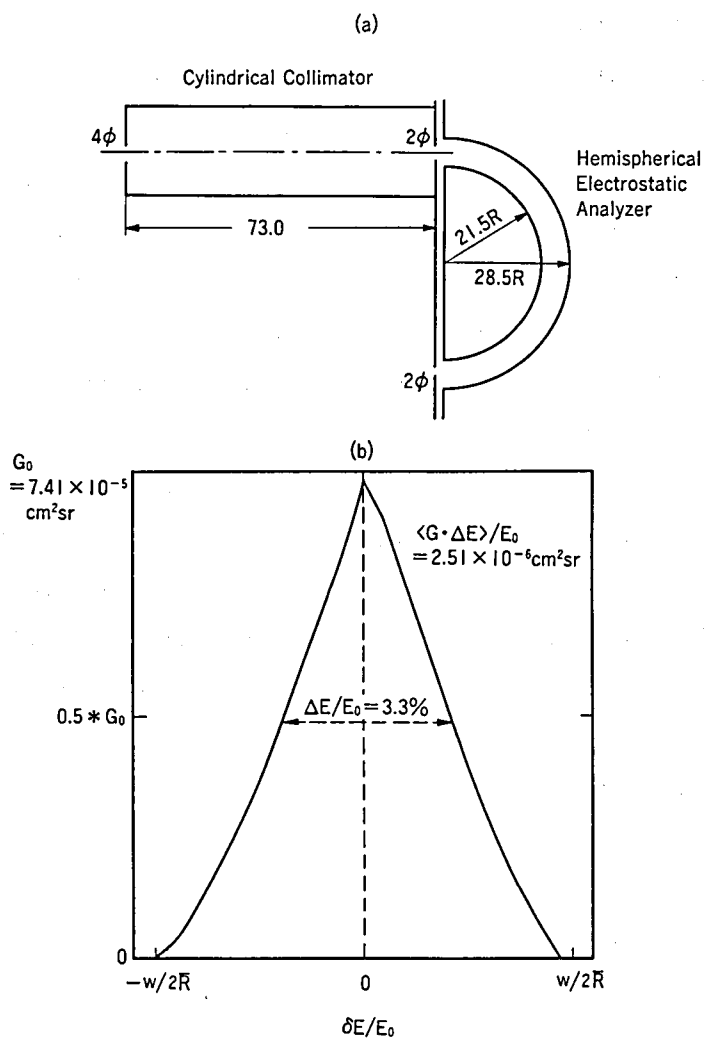
Fig. 2.6 (a) Geometry of a hemispherical electrostatic analyzer
with an inlet collimator.
(b) Energy response obtained by integration Eq. (2.7).

§4. Calculation of Transmission Properties of

Electrostatic Electron Lenses

4.1 Basic Consideration

In this section we are concerned with the geometric factor
of a collimator. At first we consider, as the simplest case,
the circular collimator defined by two infinitely thin, plane,
coaxial parallel areas with known separation. Figure 2.7
shows the relevant geometry. The geometrical factor G_0 can be
expressed exactly (Heristchi, 1967; Thomas and Willis, 1972) as

$$G_0 = \frac{1}{2} \pi^2 \left(R_1{}^2 + R_2{}^2 + L^2 - \left[(R_1{}^2 + R_2{}^2 + L^2)^2 - 4R_1{}^2 R_2{}^2\right]^{1/2}\right) , \qquad (2.23)$$

where R_1 and R_2 are the radii of the inlet and exit apertures,
respectively, and L is the separation between the apertures.
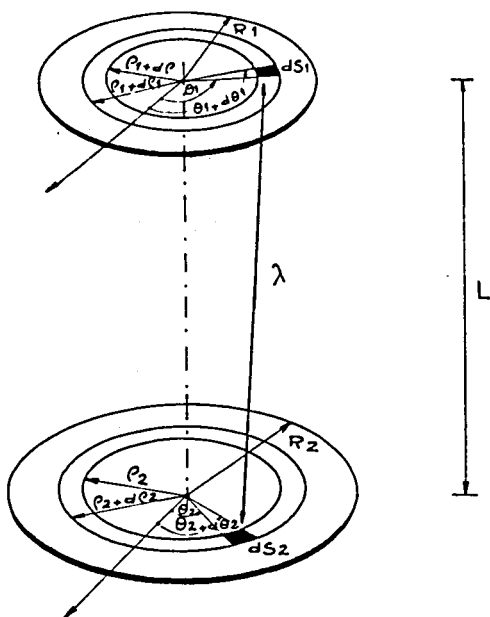
Fig. 2.7
Geometry of a circular collimator.
The Geometrical factor G_o can be
given by
$$G_0 = \int_0^{R_1} d\rho_1 \int_0^{R_2} d\rho_2 \int_0^{2\pi} d\theta_1 \int_0^{2\pi} d\theta_2 \; L^2 \rho_1 \rho_2 / \lambda^4$$

(after Dj. Heristchi, 1967)

In the limiting case $R_1{}^2$, $R_2{}^2 \ll L^2$ the above equation reduces to
the form

$$G_0 \simeq \pi^2 R_1{}^2 R_2{}^2 / L^2.\qquad\qquad\qquad(2.24)$$

Similarly the geometrical factor of a rectangular collimator,
which consists of two rectangular areas having sides of X_1, Y_1
and X_2, Y_2 with separation of L can be expressed approximately as

$$G_0 \simeq X_1 Y_1 X_2 Y_2 / L^2,\qquad\qquad\qquad(2.25)$$

where $X_1{}^2, Y_1{}^2, X_2{}^2, Y_2{}^2 \ll L^2$.   The exact expression has also
been given by Thomas and Willis (1972).

     Next we consider the case that the electric potential of the
exit slit is different from that of the entrance slit; i.e.,
charged particles are accelerated/or decelerated by the amount of
the potential difference between the entrance and exit slits of
the collimator.   In this case the particle trajectory for
oblique incidence is not a simple straight line in the collimator,
but is curved by the electric field.   The degree of deformation
depends on the incidence angle as well as on the ratio of the
particle energy to the acceleration (or deceleration) potential.
In addition, an intermediate electrode may be inserted between
the entrance and exit slits in order to control the particle
transmission through the collimator, constituting electrostatic
lenses.   In the following we calculate the geometric factor of
axially-symmetric electrostatic electron lenses, the geometry of
which is shown in Fig. 2.8.
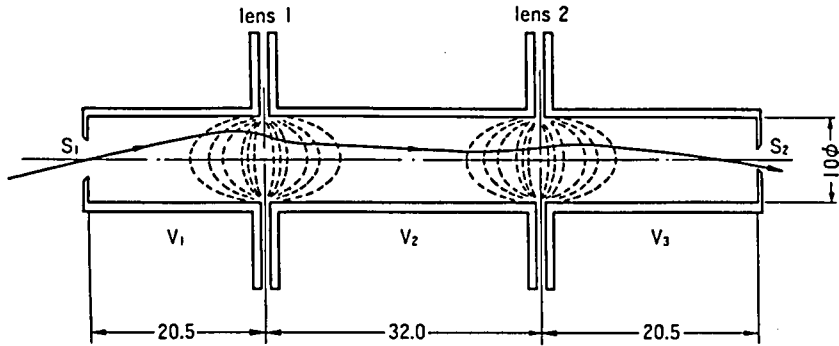
Fig. 2.8 Geometry of axially-symmetric electrostatic electron lenses. V_1, V_2 and V_3 are the electric potentials corresponding to the electron energies. Schematic drawings of equi-potential contours (dashed lines) and an electron trajectory are also shown.

4.2 Calculation of the Geometric Factor with a Paraxial-Ray Approximation

For paraxial and near-axial particle paths, the equation of particle motion in the axially-symmetric electric field is given in the cylindrical coordinate as follows.[*]

$$\frac{d^2r}{dz^2} + \frac{1}{2U_0(z)} \frac{dU_0(z)}{dz} \frac{dr}{dz} + \frac{1}{4U_0(z)} \frac{d^2U_0(z)}{dz^2} r = 0 , \qquad (2.26)$$

where U_0 is an electric potential along the central axis. Here the zero-point of the potential corresponds to the place where the kinetic energy of the particle is zero, and thus the electric potential is identical to the particle energy. This equation is

[*] This equation can be reduced from the exact equation (2.29).

known as the geometric optics equation and has frequently been
used to obtain electron-optical properties such as focal lengths.

Since Eq.(2.26) is a linear second-order differential
equation, the final state $\begin{pmatrix} r_f \\ r_f' \end{pmatrix}$ can be related to the initial state
$\begin{pmatrix} r_i \\ r_i' \end{pmatrix}$ as follows.

$$\begin{pmatrix} r_f \\ r_f' \end{pmatrix} = \begin{pmatrix} d_{11} & d_{12} \\ d_{21} & d_{22} \end{pmatrix} \begin{pmatrix} r_i \\ r_i' \end{pmatrix}, \qquad (2.27)$$

where the prime denotes the derivative with respect to z.   The
matrix elements can be obtained by considering the geometric
optics for two particular paths, if the focal lengths of each
two-tube lens which constitutes the geometry as shown in Fig. 2.8
are known.   Now, we consider a virtual slit with radius of R_i
which is the image of the exit slit at the distance of L in front
of the entrance slit, as shown in Fig. 2.9.   Then, the geometric
factor of the real collimator (X-Y) is equal to that of the
virtual collimator (I-X).   Since the virtual collimator is a
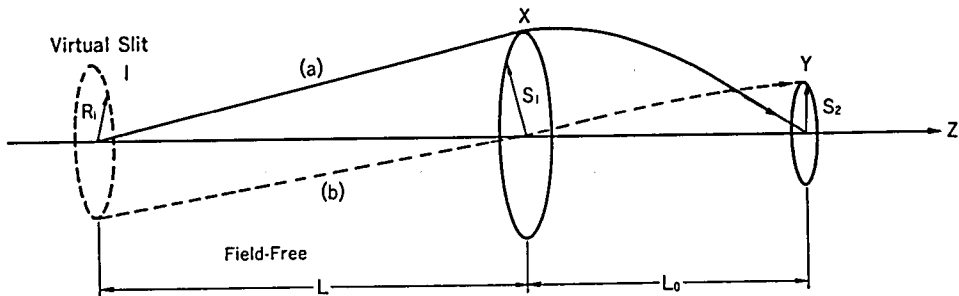
Fig. 2.9   Concept of a virtual slit I with radius of R_i. The slits X
(radius: s_1) and Y (radius: s_2) are real ones.
Paths (a) and (b) are the limiting trajectories as

(a) $r_i = s_1$ $r_i' = s_1/L$ $r_f = 0$

(b) $r_i = 0$ $r_i' = R_i/L$ $r_f = s_2$

field-free simple collimator, Eq.(2.23) or (2.24) can be applied for estimation of the geometric factor if R_i and L are known. By using Eq.(2.27) for paths (a) and (b) in Fig. 2.9, we can obtain $L = -d_{12}/d_{11}$ and $R_i = -s_2/d_{11}$. Therefore, the geometric factor G_0 can be calculated roughly as

$$G_0 \simeq \pi^2 s_1^2 s_2^2 \ / \ d_{12}^2. \tag{2.28}$$

Comparing this equation with Eq.(2.24), d_{12} is the effective length of the electron-lens collimator.

Figure 2.10 shows the geometric factor calculated by the method mentioned above. Here we have used the approximate formulas for the focal lengths of a two-tube lens derived by Grivet (1965). In the figure, each contour line shows an equal geometric factor, and the dashed line corresponds to the focusing condition (i.e., $L=0$). The shape of a contour line does not depend on the slit radius, but depends on $Z_1/R, Z_2/R$ and Z_3/R, where Z_1, Z_2 and Z_3 are tube lengths and R is the radius of the tube. Figure 2.10 is very useful for design of the electron lenses shown in Fig. 2.8, but it should be noted that the geometric factor thus calculated may include a significant error especially in case of a large value of the geometric factor because the paraxial-ray approximation may not hold for such a case (i.e., large angle of acceptance).
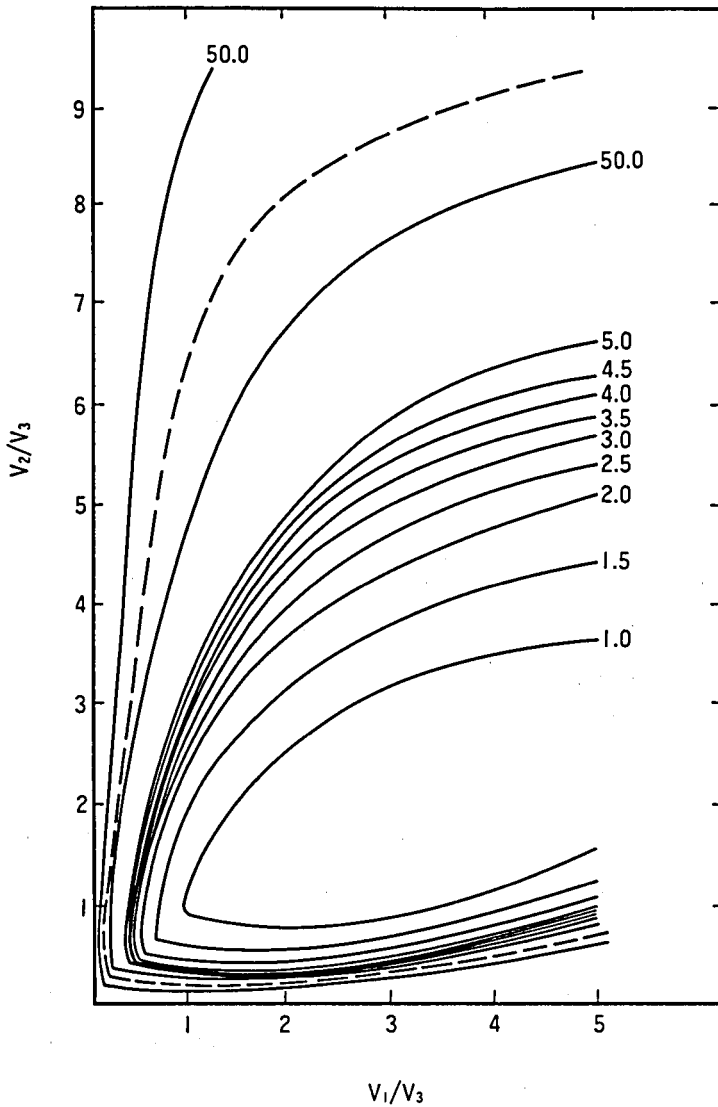
Fig. 2.10 Contour plot of calculated geometric factors.
Values corresponding to contour lines are normalized by the
geometric factor G in the field-free case.   The dashed
line corresponds to the focusing condition.

4.3 Calculation of the Geometric Factor by Monte Carlo Simulation

The paraxial-ray approximation has been applied easily for calculation of the geometric factor and is very useful for design of the lens potential, but an actual particle path may be more or less different from the approximated ray. In this subsection the geometric factor is calculated with least approximation and is compared with the result obtained by the paraxial-ray approximation.

4.3.1 Particle Trajectory in an Axially-Symmetric Electrostatic Field

In cylindrical coordinates the trajectory equation of a charged particle motion in an axially-symmetric field electrostatic ($E_\phi=0$, $B=0$) can be expressed exactly (Paszkowski, 1968) as

$$\frac{d^2r}{dz^2} - \frac{1 + (dr/dz)^2 + r^2(d\phi/dz)^2}{2\,U(z,r)} \left[\frac{\partial\phi(z,r)}{\partial r} - \frac{dr}{dz}\frac{\partial\phi(z,r)}{\partial r} \right] = 0 \tag{2.29}$$

and

$$\frac{d\phi}{dz} = \frac{1}{r^2}\sqrt{\frac{H}{\Phi(z,r)}\left[1 + (\frac{dr}{dz})^2\right]} \tag{2.30}$$

Here, $\Phi(z,r) = U(z,r) - H/r^2$, $\tag{2.31}$

and H is the constant which is determined from the initial condi-

tion (see Fig. 2.11) as

$$H = r_i^2 \, V_1 \, (\sin \theta_i \, \sin\psi_i)^2. \qquad\qquad (2.32)$$

$U(z,r)$ is the electric potential corresponding to the particle energy at a point (z,r), and $V_1 = U(0,0)$.

The geometric electron optics equation, Eq.(2.26), can be obtained from Eq.(2.29) for paraxial and near-axial particle paths, using the approximation that $(dr/dz)^2 = 0, \partial U/\partial z = dU_0(z)/dz$ and $\partial U/\partial r = (r/2)(dU_0(z)/dz)$ and that the quantity H can be selected to be zero; e.g., $\psi_i = 0$.
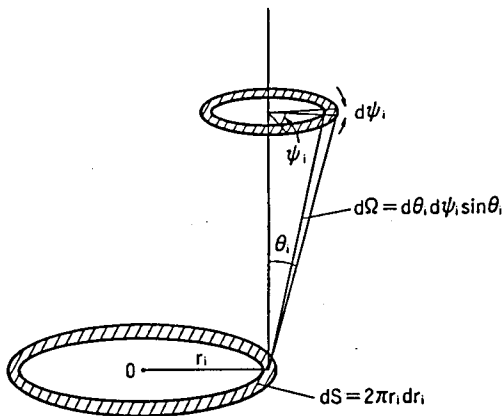
Fig. 2.11
Definition of the coordinate
system for an initial condition
of particle incidence.

4.3.2 Distribution of the Electric Potential

The potential distribution $U(z,r)$ in the tube lens having a zero gap can be expressed exactly (e.g., Grivet, 1965) as

$$U(z,r) = \frac{1}{2}(V_1 + V_2) + \frac{1}{2}(V_1 - V_2)$$

$$\times \ (1 - 2 \sum_n [J_0(\mu_n r) \exp(-\mu_n |z|)] \ / \ [\mu_n \ J_1(\mu_n)]), \qquad (2.33)$$

for $z < 0$ (V_1-side), where z in this equation is measured from the gap center, μ_n is the root of $J_0(\mu) = 0$, J_0 and J_1 are the Bessel functions, and all distances are measured in unit of the cylinder radius. The distribution for the V_2-side can be obtained by interchange of V_1 and V_2 in Eq.(2.33). The above expression can be applied with good approximation for estimation of the electric potential in the electron lens shown in Fig. 2.8, although our lens has a small gap. The derivatives $\partial U/\partial z$ and $\partial U/\partial r$ can be obtained by a numerical differentiation method.

4.3.3 Geometric Factor

For the coordinate of the initial condition of particle incidence defined in Fig. 2.11, the geometric factor G can be expressed as

$$G = 2\pi \int_0^{s_i} dr_i \int_0^{\theta_0} d\theta_i \int_0^{2\pi} d\psi_i \ \ p(r_i, \theta_i, \psi_i) \ r_i \ \sin\theta_i, \qquad (2.34)$$

where the function p has the value unity for r_i, θ_i and ψ_i corresponding to a trajectory of electrons which transmit through the collimator and zero otherwise. The integration limit θ_0 is selected to be a reasonable value for saving the computation time.

In evaluating Eq. (2.34), we have used a Monte Carlo method

using quasi-random numbers for r_i, Θ_i and ψ_i; the ray tracing of Eqs. (2.29) and (2.30) has been done for various values of r_i, Θ_i and ψ_i. Several examples of the calculated results are shown in Figs. 2.12 $\sim$ 2.16, where the results by the paraxial ray approximation are also presented for comparison. The parameters V_1, V_2, V_3 and s_1 have been chosen for application of the results to the rocket experiment (see next chapter), and not for the extreme case such as the focusing condition. None the less it is quite remarkable that in each figure the result obtained by the paraxial ray approximation shows a good agreement with that obtained by a Monte Carlo simulation in spite of the non-negligible inlet slit radius ($s_1/R = 0.8$). The difference between both results is within 10 % in most cases. The larger difference of 30 % in Fig. 2.16 occurs in the case of a larger value.
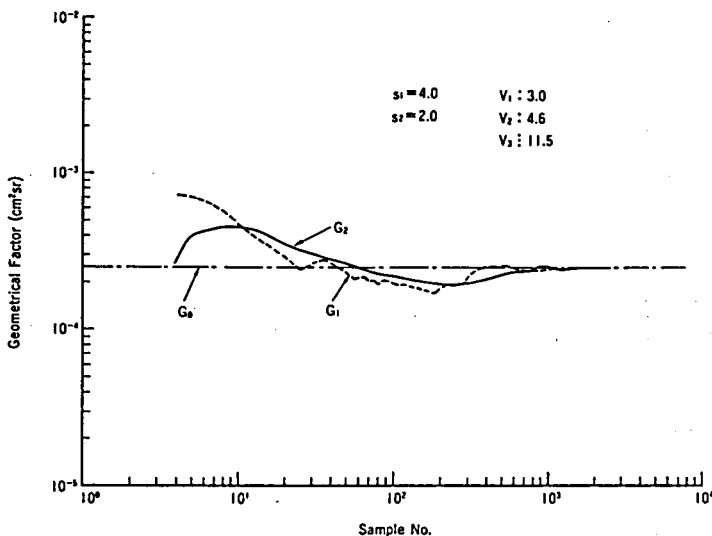
Fig. 2.12 Geometric factors G_1 and G_2 calculated by Monte-Carlo the method with quasi-random numbers.
G_0 is the value obtained by a paraxial-ray approximation.
The lens condition is given in the figure;
s_1 = 4.0, s_2 = 2.0, V_1 = 3.0, V_2 = 4.6, and V_3 = 11.5
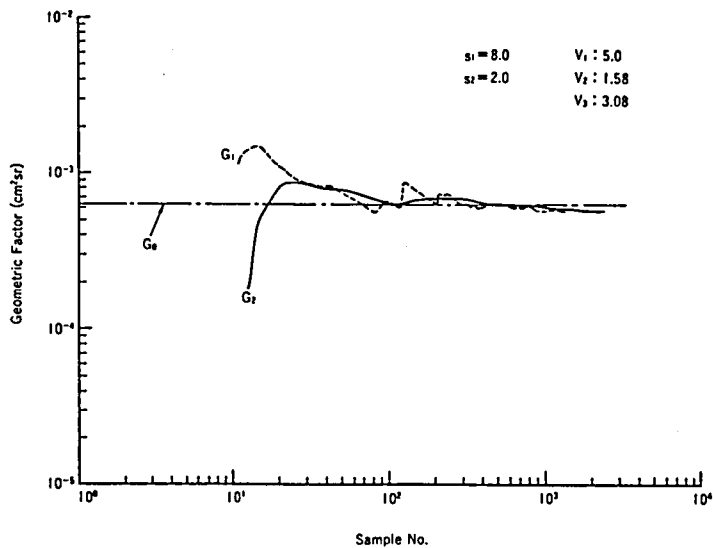
Fig. 2.13　Same as Fig.2.12.
　　　　　The lens condition is given in the figure;
　　　　　$s_1 = 8.0$, $s_2 = 2.0$, $V_1 = 5.0$, $V_2 = 1.58$, and $V_3 = 3.08$
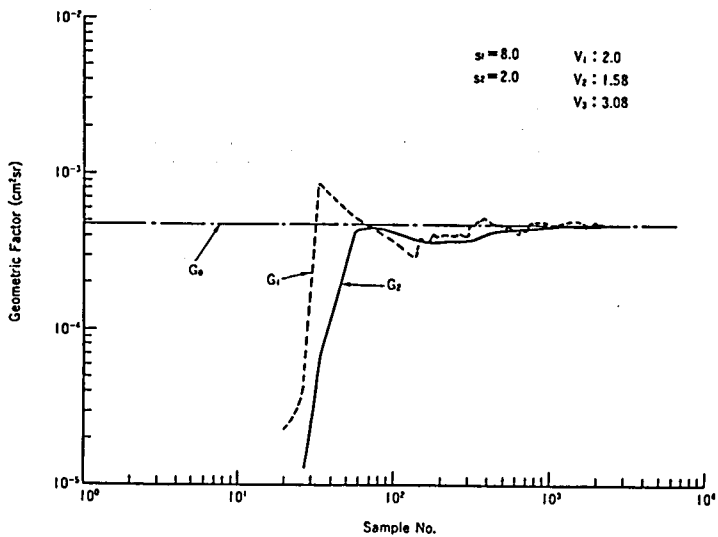
Fig. 2.14　Same as Fig.2.12.
　　　　　The lens condition is given in the figure;
　　　　　$s_1 = 8.0$, $s_2 = 2.0$, $V_1 = 2.0$, $V_2 = 1.58$, and $V_3 = 3.08$
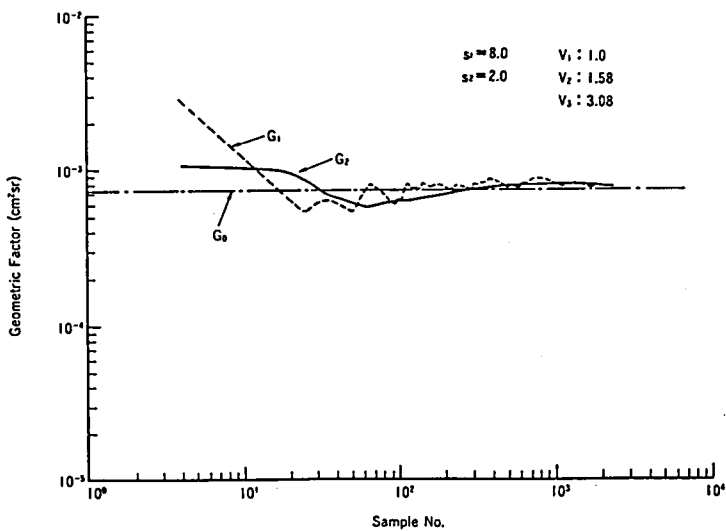
Fig. 2.15   Same as Fig.2.12.
            The lens condition is given in the figure;
            s_1 = 8.0, s_2 = 2.0, V_1 = 1.0, V_2 = 1.58, and V_3 = 3.08
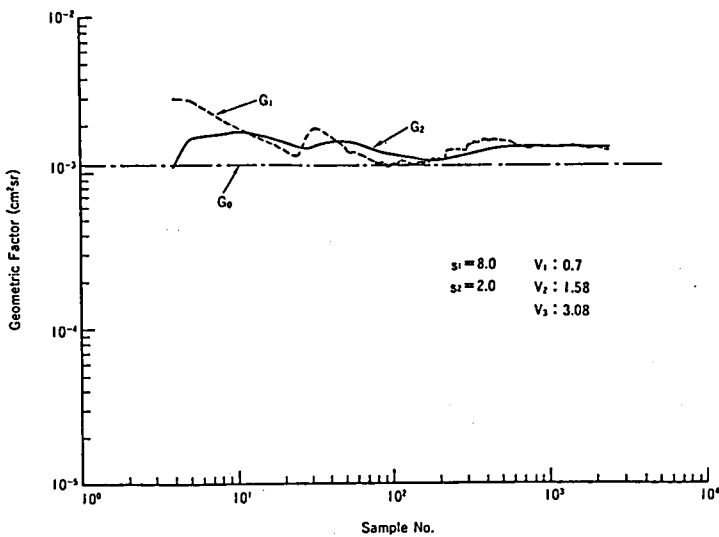
Fig. 2.16   Same as Fig.2.12.
            The lens condition is given in the figure;
            s_1 = 8.0, s_2 = 2.0, V_1 = 0.7, V_2 = 1.58, and V_3 = 3.08

§5. Concluding Remarks

In this chapter we have investigated theoretically the
fundamental properties of particle transmission through hemi-
spherical electrostatic analyzers and collimators, respectively.
The most important property of a particle spectrometer for space
use is an energy-geometric factor relating the output count rate
to the ambient particle flux, which is defined by Eq. (2.6) in
Section 2. The energy resolution and angular acceptance are
also important for discussion of the data obtained by the spectro-
meter. Numerical integration for a given geometry must be
carried out in order to know these important properties, since
the transmission function is not known explicitly.

In Section 3 the transmission properties of a hemispherical
electrostatic analyzer have been derived by using the exact
particle trajectories under the assumption that the effect of the
fringing field can be neglected. The analyzer of this type
gives inherently a differential energy spectrum of charged
particles with a limited range of energy and angle around the
center. The center energy can be determined by Eq. (2.19) or
(2.19a) which means that the center energy is proportional to the
applied voltage across the spherical plates with the constant of
proportionality determined by the geometrical dimension. The
energy resolution can be estimated by Eq. (2.21), and the angular
acceptance (α-angle) is roughly equal to $\Delta R/\bar{R}$, although the
transmission curves are not symmetric in the E-α plane. If we
adopt an inlet collimator with a suitable field stop of view, the
transmission curve approaches to be of rectangular shape. Then
the energy-geometric factor can be obtained by the product of G_0

and ΔE, where G_0 is the geometric factor of the collimator only and ΔE is the energy width (FWHM) of the analyzer.   More general expression for the crude estimate of the energy-geometric factor is given by Eq. (2.22) which is useful for quick design of the spectrometer.   The energy-geometric factor is proportional to the measured energy, since the energy width ΔE is proportional to E_0 ($\Delta E/E_0 =$ const.).   The constant of proportionality is determined by the geometric dimension of the spectrometer configuration.

If we adopt an electron-lens system for the inlet collimator, then the geometric factor and the energy width can be controlled separately with flexibility.   In other words, if we adopt pre-acceleration or pre-deceleration V of particles before entering the analyzer, the energy width ΔE can be selectable by adjusting the energy E_a in the analyzer, where the measured energy is equal to $E_a + qV$.   The geometric factor G_0 can be controlled by the electron-optical property of the collimator which is determined by the voltages applied to the lens-electrodes.   In Section 4 we have presented two kinds of methods for calculating the geometric factor of the electrostatic electron lenses.   One is a paraxial approximation and another is a Monte Carlo simulation of ray tracing with least approximation.   Figure 2.10 shows a useful result for design of the lens potential, which has been calculated by means of paraxial approximation.   The result has been confirmed in several examples by the latter method which is much more time-consuming than the paraxial approximation.

Chapter III. Development of Rocket-Borne Electron Spectrometers

for Measurement of the Ionospheric Photoelectrons

§1. Introduction

This chapter is devoted to the description of instrumentation for the _in-situ_ measurement of the photoelectrons in the ionosphere.   It is anticipated theoretically that the photoelectrons have characteristic fine structures in the energy spectrum which are determined by the processes of production, energy-loss and transport, although earlier rocket measurements did not necessarily resolve them.   Therefore, emphasis has been laid on the high energy resolution in our spectrometer.   Principle of the spectrometer design, which is based on the results obtained in the previous chapter, is given in Section 2.

The energy of interest in the measurement of the ionospheric photoelectrons is in the range from sub-eV to several tens of eV. There are several difficulties to be overcome in order to make the electron spectrometer work well in this low-energy range. There are additional problems peculiar to the rocket experiment to be solved.   These considerations are discussed in Section 3.

In practice, however, the problems accompanied with the rocket experiment are difficult to be solved completely by the laboratory experiment.   Some of the difficulties have been overcome through the experience of the flight experiments; four for the measurement of daytime photoelectrons and two of conjugate photoelectrons at predawn in winter.   Section 4 is devoted to the description of these practical payloads on board the sounding rockets.

In Section 5 we discuss the experimental performance of the electron spectrometer which has been calibrated in the laboratory. Since the calculations of particle trajectories for design of the spectrometer include more or less approximations for the practical one, the pre-flight calibration of the spectrometer is essential for analysis of the data obtained from the rocket experiment.

Concluding remarks in this chapter are given in Section 6.

§2. Principle of the Spectrometer Design

The first step of the spectrometer design starts from selection of what type of energy analyzer is most suitable for the objective, and we have already adopted a hemispherical electrostatic analyzer. Basic transmission properties of the analyzer of this type have been discussed in the previous chapter and are used for the design of the practical electron spectrometer.

As mentioned in Section 1, emphasis is laid on the high energy resolution in our spectrometer. However, the energy resolution attained practically is a result of compromise with the design of the energy-geometric factor. The energy-geometric factor should be designed to have a reasonable value for obtaining the statistically meaningful output, taking into account that a channel electron multiplier (see Section 3.3 in Chapter I) is available as a detector for counting the output electrons of the analyzer. The above considerations and the compatibility of the size with the rocket dimension have resulted in $\bar{R} = 25.0$ mm and $w = 2.0$ mm as the analyzer dimension, and $\Delta R = 7.0$ mm have been selected for obtaining an ideal energy-angle response of the analyzer. The

calculated response is shown in Fig. 2.3 in Chapter II, and the energy resolution, $\Delta E/E_a$ is estimated to be $\sim$5 %, which results in the energy width of $\sim$0.5 eV at the analyzer energy of 10 eV.

The absolute value of the energy width is important to resolve fine structures of the energy spectrum rather than the relative energy resolution, $\Delta E/E$, and it is desirable to keep the energy width constant during the energy scanning.   Figure 3.1 shows a schematic diagram of the electron spectrometer on board the K-9M-40 rocket which was the first experiment for us.   The details will be described in Section 4.1, but the principle is described in this section.

The essential part of the electron spectrometer consists of a collimator, a hemispherical electrostatic analyzer and a channel electron multiplier.   The collimator consists of cylindrical
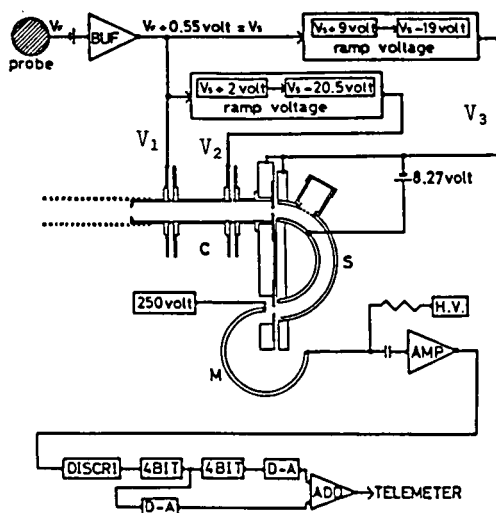
Fig. 3.1 A schematic diagram of the electron spectrometer
on board K-9M-40.
C: collimator,   S: hemispherical electrostatic analyzer,
M: channel electron multiplier.

electron lenses, the transmission properties of which have been
calculated in Section 4 in Chapter II.   All electrodes of the
spectrometer are isolated electrically.   The measured energy E_0
is expressed by Eq. (2.19) and can be rewritten as follows.

$$E_0/e = k \cdot \Delta V - V_3 \, , \tag{3.1}$$

where e is the electronic charge (1.602×10^{-19} Coulomb), $\Delta V =$
$V_i - V_o$, V_3 is the electric potential of the third electrode of
the collimator relative to the plasma potential, and k is deter-
mined by the geometric dimension of the analyzer and the method
of voltage supply to the analyzer plates; e.g.,

$$k = R_i^2 / (R_o^2 - R_i^2) \qquad ; \text{ for } V_o = V_3 ,$$
$$k = R_o R_i / (R_o^2 - R_i^2) \qquad ; \text{ for } R_o(V_o - V_3) + R_i(V_i - V_3) = 0 ,$$
$$k = (R_o^2 + R_i^2) / (R_o^2 - R_i^2); \text{ for } V_o + V_i = 2 V_3 .$$

The value of $k \cdot \Delta V$ corresponds to the energy of electrons at the
third electrode of the collimator just before entering the
analyzer, which can be transmitted through the analyzer.   The
energy, E_0 can be scanned either by varying ΔV with a constant
value of V_3 or by varying V_3 with a constant value of ΔV, if the
value k is kept constant.   The former method of energy scanning
is used commonly in usual analyzers with $V_3 \simeq 0$, while the latter
method is a special feature in our spectrometer.   The latter
method of energy scanning leads to the constant analyzer energy
and hence the constant energy width.   The potential of the
second electrode of the collimator can be varied simultaneously
in order to keep the geometric factor as unchanged as possible

during the energy scanning. In this method, therefore, both the geometric factor and the energy width can be kept constant during the energy scanning.

Possibility of flexible operation of our spectrometer leads to additional advantages. For example, it is expected that very low energy electrons can be measured in our spectrometer by pre-accelerating electrons before entering the hemispherical analyzer, since it is usually difficult to operate the analyzer in the very low energy range (e.g. $\leq$ 2 $\sim$ 3 eV).

§3. Rocket-Instrument Considerations

3.1 Shielding of the Spectrometer from the External Magnetic Field

The Larmor radius, r_L of a charged particle encircling around a magnetic-field line is given by

$$r_L = mv_\perp \ / \ qB, \qquad\qquad (3.2)$$

where m and q are mass and charge of the particle, $v_\perp$ is the particle velocity perpendicular to the magnetic field line, and B is the strength of the magnetic field, respectively. More practically for an electron, Eq. (3.2) can be rewritten as

$$r_L = 3.37 \ \sqrt{E} \ \sin\alpha \ / \ B, \qquad\qquad (3.2a)$$

where r_L is in cm, E is the electron energy in eV, α is the pitch

angle of the electron with respect to the magnetic field line,
and B is in G(gauss).   Since the geomagnetic field is 0.3 ∿ 0.4
G in strength at the ionospheric height, the Larmor radius of an
electron with an energy of 1 ∿ 100 eV can be calculated to be an
order of 10 cm, which is a comparable scale to the size of the
spectrometer.

Figure 3.2 shows a simple geometry of an electron trajectory
deviated from the straight line due to the magnetic field.   The
deviation d can be expressed as

$$d \sim a^2 / 2 r_L, \tag{3.3}$$

and the angle of deflection θ can be expressed as

$$\theta \sim a / r_L, \tag{3.4}$$
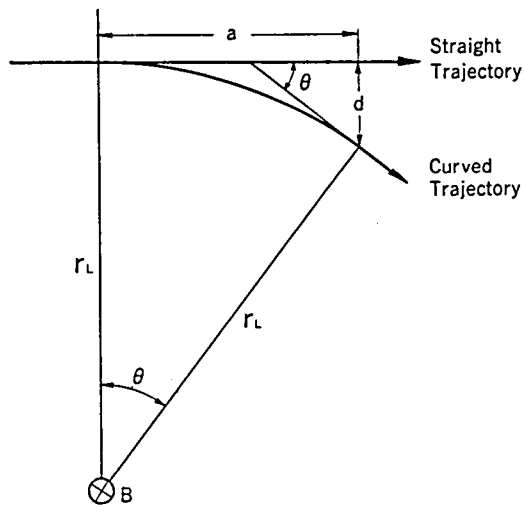
Fig. 3.2   Deviation of an electron trajectory due to the
magnetic field.

where a is the length of the electron trajectory. If a = 10 cm
and d ≤ 0.2 mm (i.e. 10 % of the slit size in our spectrometer),
then the strength of the magnetic field in the spectrometer should
be reduced to be less than 1 mG in order to measure electrons with
an energy of 1 eV. This simple calculation shows the necessity
of shielding the electron spectrometer from the external magnetic
field as well as the necessity of careful selection of non-magnetic
materials used for construction of the spectrometer.

3.2 Potential Difference between the Rocket and the Ambient Plasma

The electric potential of a floating body in a plasma is
generally different from the plasma potential because of the
difference between electron and ion velocities. The floating
potential, V_F, can be determined under the condition that the net
current flowing to the body is zero.

$$-V_F = (\kappa T_e \ / \ 2e) \ \ln(T_e m_i \ / \ T_i m_i) \ , \tag{3.5}$$

where κ is the Boltzmann constant, T_e and T_i are the electron and
ion temperatures, and m_e and m_i are the electron and ion masses,
respectively. In the ionosphere above the altitude of 200 km, T_e
and T_i are $\sim1500^{\circ}$K and $\sim1000^{\circ}$K, respectively, and the main ion
species is O^+, that yield the floating potential of ~ -0.55 volt.
In case of a rocket the situation is much more complicated than in
a laboratory plasma, because the rocket moves at a supersonic speed
and also because it is exposed to solar EUV radiation and high

energy particles which can eject secondary electrons from the rocket surface. This problem is not discussed here in detail, but we discuss only the effect in the measurement of charged particles due to the potential difference between the rocket and the ambient plasma.

Figure 3.3 shows schematically a situation that the rocket potential is V_R relative to the plasma potential. If a charged particle of energy E_1 and angle α_1 in the plasma enters the spectrometer on the rocket, then the energy E_2 and angle α_2 of the particle at the entrance of the spectrometer can be obtained as follows;

$$E_2 = E_1 + qV_R, \tag{3.6}$$

and

$$\sqrt{E_2}\, \sin\alpha_2 = \sqrt{E_1}\, \sin\alpha_1. \tag{3.7}$$
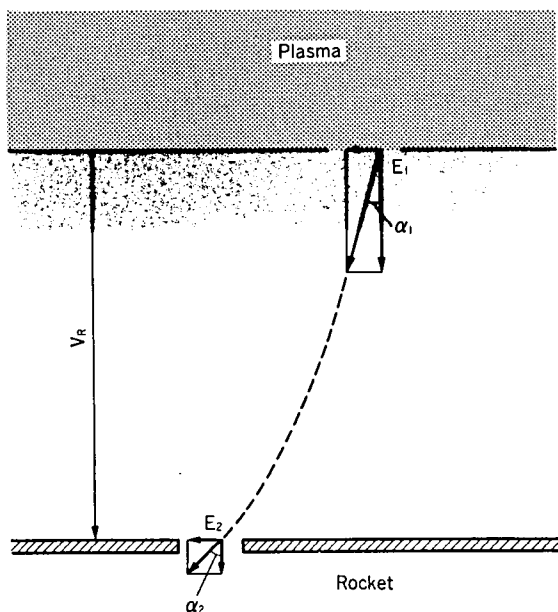
Fig. 3.3 Deviation of an electron trajectory due to the potential
difference between the ambient plasma and the rocket.

The above equations show the effect not only on an energy shift but also on angular change, which leads to change of the geometric factor. The rocket potential is usually 1 ∿ 2 V below the plasma potential. Therefore, the effect is serious in case of measuring low-energy electrons of eV-order. Methods for correction of the potential difference will be discussed in Section 4 in conjunction with the description of the actual payloads.

3.3 Shadowing Effect by the Rocket Body

It may happen that an electron trajectory entering the spectrometer is intersected by the rocket body or the extended booms, because the Larmor radius of an electron with an energy of 1 ∿ 100 eV is a comparable scale to the size of the rocket radius, and also because a mean collision time for such an electron in the ionosphere is much longer than a gyration time of spiraling motion of the electron. We call this effect 'shadowing'. The spectrometer must be oriented so as to avoid shadowing in the field of view. The effort for minimizing this effect must be carried out not only in the design of the payload arrangement on board the rocket, but also in processing the obtained data. In order to remove the shadowing effect, it is necessary to trace back the electron trajectories entering the rocket-borne spectrometer, taking into account the spiral motion around the magnetic field line. It is noted that, in judging the shadowing, the sizes of the rocket and the extended booms must be regarded as larger by the sheath thickness than the actual ones.

3.4 Photoelectrons Produced inside the Spectrometer and from the

   Rocket Surface

   One of the most serious problems in measuring the photo-

electrons in the ionosphere is to remove the spurious data

contaminated by direct or scattered solar EUV radiation.   It

should be pointed out that the spectrum of photoelectrons ejected

from metallic surfaces are indistinguishable from the spectrum of

the ionospheric photoelectrons.   Figure 3.4 shows a comparison

between both spectra for the case of normal incidence on the

aluminum plate [Hays and Sharp; 1973].

   In our spectrometer, the inlet slit has been placed inside

the collimator tube so as to decrease solar illumination on the

inlet slit.   In addition, the sun sensor has been installed
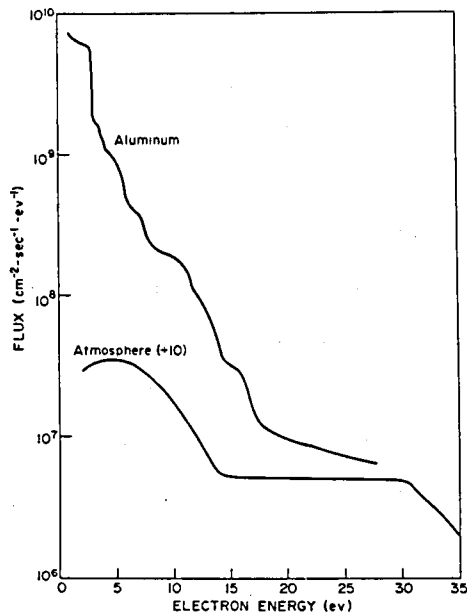
Fig. 3.4 Photoelectron energy spectrum of aluminum and the earth's
          atmosphere (reduced by a factor of 10).
          (after P. B. Hays and W. E. Sharp, 1973).

with the same orientation as the collimator axis in order to check the effect of the direct entry of sunlight into the collimator. In data processing, we have eliminated those data which were obtained at a timing of the high-level output of the sun sensor.

It may happen that the photoelectrons ejected from the rocket body or the extended booms enter the spectrometer because of the same reason as the shadowing effect as mentioned in the former subsection. Therefore, the shadowing effect does not necessarily decrease the output count rate; the output may not be decreased if the part of the rocket which shadows the field of view is illuminated by the sunlight. These spurious photo-electrons are indistinguishable from the ambient photoelectrons, as mentioned above, but should be removed in order to obtain a reliable result. The algorithm to remove the shadowing effect is useful for this purpose.

3.5 Others

A channel electron multiplier has been frequently used for a charged particle detector and is used also in our electron spectrometer. The advantages of this type of detector are its small size, light weight, low power consumption and high sensitiv-ity with a stable gain, while as a drawback a high voltage, typical 3 kV, must be applied between the input and output terminals of the multiplier. One of the serious problems in a rocket experiment is high-voltage breakdown which may cause an irreversible damage for the rocket experiment. In addition, the input area of the channel electron multiplier must be shielded for stray electrons;

the shielding leads to low conductance of air evacuation. For protection of high-voltage breakdown, our electron spectrometer is put in the vacuum-sealed vessel, the cap of which is opened at an altitude above 100 km. Other advantages of the vacuum seal are that the surface of the spectrometer electrode can be kept clean, which is essential for the measurement of charged particles, and that the channel electron multiplier can be operated stably [Timothy, 1973].

Another problem in the measurement of low-energy electrons in space is rejection of background noise which is caused

  (a) by solar EUV radiation,

  (b) by stray electrons, and

  (c) by high-energy particles including cosmic-rays.

Item (a) has already been discussed in section 3.4. The channel electron multiplier must be shielded from stray electrons (item (b)) and also from cosmic-ray backgrounds (item (c)). In our spectrometer, in addition, a trap for rejection of high-energy particles and EUV photons is placed behind the outer hemispherical plate at the position where high-energy particles and photons transmitted through the collimator will impinge onto the outer hemisphere. Nevertheless, some background counts are inevitable practically and must be subtracted from the signal in data processing.

Finally, it should be noted as a matter of course that the instrument must be compatible with the electrical and mechanical interface on the rocket, and the environmental condition such as shock and vibration at the rocket flight.

§4. Description of the Actual Payloads

We have carried out six rocket experiments at KSC (Kagoshima Space Center of ISAS), Uchinoura, Japan (31°15'N, 131°05'E geographic; 20.0°N geomagnetic) to measure photoelectron flux in the ionosphere; four flights in the daytime and two at predawn.

4.1 K-9M-40 Experiment

The first experiment was carried out in the daytime by the K-9M-40 rocket. A schematic diagram of the electron spectrometer on board the rocket is shown in Fig. 3.1 (p. 61). As described in section 2, the main part of the electron spectrometer consisted of a collimator, a hemispherical electrostatic analyzer and a channel electron multiplier (Galileo CEM 4010 type). The collimator was composed of three cylindrical electrodes forming the electron lens which determines the geometric factor. The inner diameter of all the collimator electrodes was 10.0 mm, while the inlet slit was 4.0 mm in diameter. The exit slit of the collimator which also served the inlet slit of the electrostatic analyzer was 2.0 mm in diameter. The potential of the collimator inlet had to be kept at the potential of the ambient ionospheric plasma, V_s. In this K-9M-40 experiment the potential of the collimator inlet was kept 0.55 volt above the floating potential of a plane probe placed in the vicinity of the inlet, based upon the simple assumption, Eq. (3.5). The energy was scanned by sweeping V_3 (see Eq. (3.1)) linearly from 9 to -19 volt with respect to V_s as shown in Fig. 3.1, where V_s was expected to be the potential of the ambient ionospheric plasma as is discussed above. The

analyzer voltage was kept constant (ΔV = 8.27 volt, as shown in Fig. 3.1), and therefore, the spectrometer was operated in the mode of constant energy width which was calibrated to be 0.34 eV. The value k in Eq. (3.1) was also calibrated to be 1.39 that resulted in k·ΔV of 11.5 volt. Thus, the energy range of measurement is from 2.5 to 30.5 eV as calculated by Eq. (3.1). The potential of the second electrode of the collimator was also swept as

$$E_2 = 0.2 \, E_0 + 4 \, , \qquad\qquad\qquad (3.8)$$

where E_2 is an electron energy in the second electrode of the collimator and E_0 is given by Eq. (3.1), respectively. Figure 3.5 shows the energy dependence of the geometric factor of the collimator calculated by the method discussed in section 4 in chapter II. The geometric factor is kept nearly constant (about 1×10^{-4} cm^2 sr) above an energy of 5 eV. Electrons transmitted
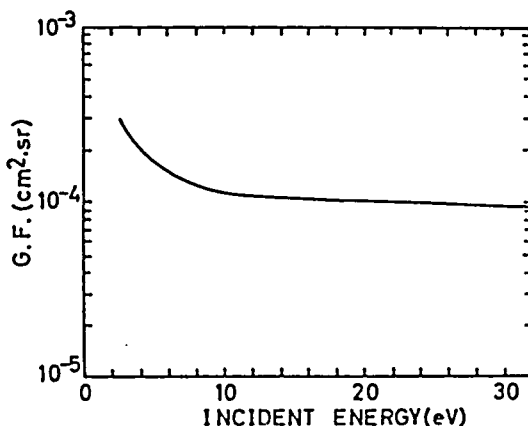
Fig. 3.5 Energy dependence of the collimator transmission.
G.F. = geometrical factor

through both the collimator and the electrostatic analyzer was accelerated by 250 eV, impinging onto the entrance of the channel electron multiplier. Therefore, the detection efficiency would be nearly constant irrespective of electron energy (see Fig. 1.11). The output pulse of the channel electron multiplier is amplified, discriminated and shaped, and is converted to the analog signal (D/A conversion) through the step-counter method, as shown in Fig. 3.1.

Although it is not shown in Fig. 3.1, the sun sensor was also installed with the same orientation as the collimator axis in order to check the effect of the direct entry of sunlight into the collimator. The essential part of the spectrometer was constructed of non-magnetic material and was surrounded by a high-μ metal so as to shield the spectrometer from the external magnetic field; a few mG inside the high-μ metal. In addition, the spectrometer, together with the high-μ metal, was put in the
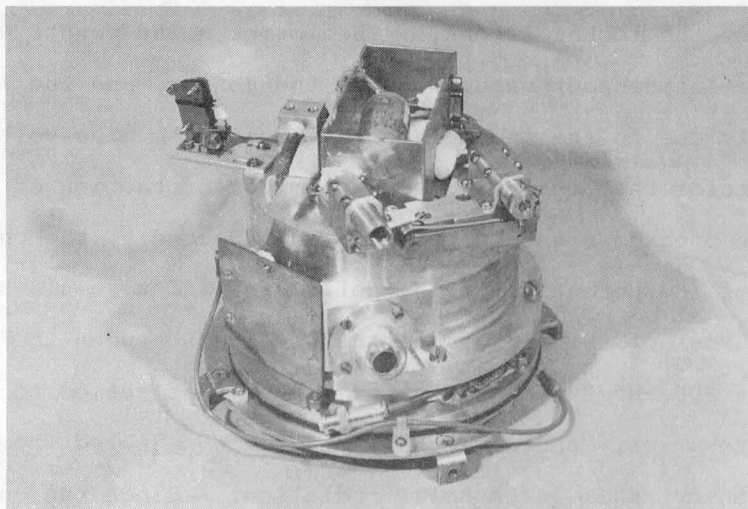
Fig. 3.6 Photograph of the sensor (vacuum vessel) on board K-9M-40.

vacuum vessel, the cap of which was opened at an altitude of
about 100 km. Figure 3.6 shows a photograph of the main part of
the sensor.

Leaving the details of observation in the subsequent chapter,
we briefly discuss performance of the instrument in flight which
is related with modifications made in the next K-9M-45 experiment.
The high-resolution capability of the electron spectrometer with
the adequate design leads to a new finding of fine structures in
the photoelectron energy spectrum, as will be discussed in the
subsequent chapter. It was also found that the instrument might
include a few problems to be overcome. Firstly, the instrument
was operated only during the altitude range from 160 to 315 km in
the ascent leg of the rocket flight. The high-voltage power
supply was switched on at an altitude of about 120 km (10 sec.
after the cap open of the vacuum vessel). The noise counts were
greater than the signal for a while, followed by a normal opera-
tion. However, the noise counts again increased suddenly near
the apogee of the rocket flight. The former noise counts were
possibly due to the poor vacuum inside the sensor, and the latter
were probably due to the incomplete potting of the high-voltage
terminal outside the sensor. The system for protection of
high-voltage breakdown should be improved. Secondly, the on-board
correction of the potential of the collimator inlet should be
improved. Most of the energy spectra obtained between the
altitudes of 200 and 300 km contained a peak that seemed to
correspond to primary photoelectrons of 27.2 eV ejected from
atomic oxygen by He II 304-$\overset{o}{A}$ solar radiation. Since the on-board
correction of the potential of the collimator inlet was not
highly accurate, the zero point of the energy scale was adjusted

so that this peak appeared at 27.2 eV. The required energy
shift was about 0.8 eV at the 200-km level. Finally, there
remained some concern about the perfect elimination of the solar
EUV contamination and the shadowing effect by the rocket body.
The instrumental arrangement of the rocket payload must be made
carefully so as to avoid these spurious effects.

4.2 K-9M-45 Experiment

The electron spectrometer on board the K-9M-45 rocket was
essentially identical with that used in the previous K-9M-40
rocket experiment, except several modifications to improve the
instrumental performance. Figure 3.7 shows a schematic diagram
of the electron spectrometer together with the voltages applied
to the electrodes. As shown in Fig. 3.7(b), three modes of
energy scanning A, B and C were prepared for measurement of the
photoelectron spectrum in the energy range from thermal up to 48
eV as well as the pause mode in between the sweep cycles. The
A-mode was a special mode aiming at detecting the space potential.
The B-mode was essentially the same as that used in the previous
K-9M-40 experiment, i.e., the mode of constant transmission and
constant energy width during the energy scanning ranging from
thermal up to 30 eV, where the analyzer voltage $\Delta V(=V_4-V_3)$ was
kept at a constant value of 4.02 volt in order to improve the
energy resolution (0.22 eV; calibrated in the pre-flight experi-
ment). In the C-mode where V_1, V_2 and V_3 were kept at a
constant equal value, the analyzer voltage V_4 was swept to measure
photoelectrons over the energy range from thermal up to 48 eV.
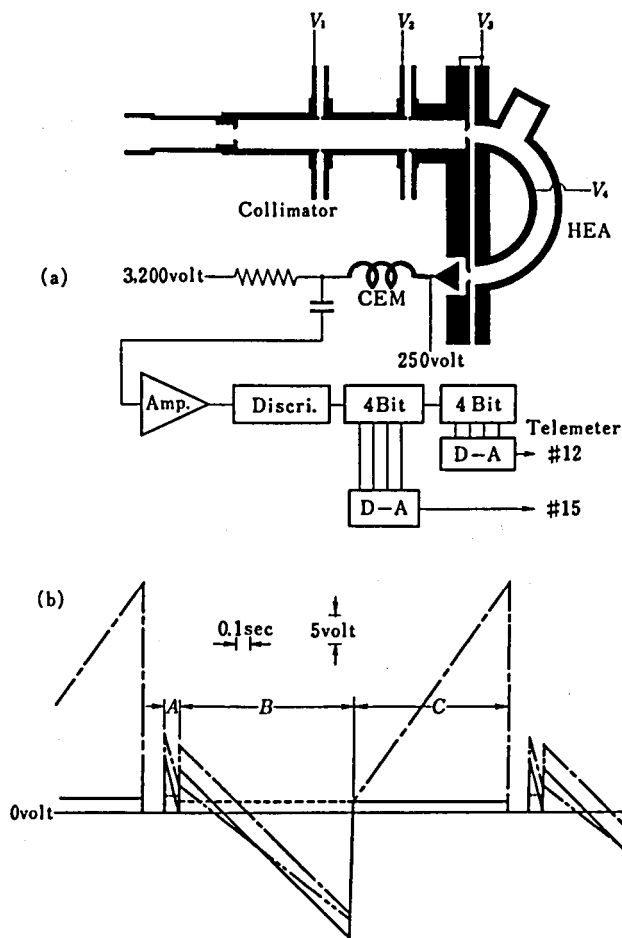
Fig. 3.7(a) The schematic diagram of the electron spectrometer on board
the sounding rocket K-9M-45;
HEA: hemispherical electrostatic analyzer,
CEM: channel electron multiplier (Galileo 4039 type).
(b) The voltages of the electrodes shown in (a):
－ － － －: V_1, ——··——··——: V_2,
——————: V_3, ——·——·——·: V_4.
'0 volt' means the rocket potential.
A, B, and C show the energy-scanning modes.

In this mode the counting statistics would be improved at the sacrifice of energy resolution in the higher energy where the electron flux would be decreased, since the energy width was proportional to the analyzer energy (i.e., $\Delta E/E$ = constant). The overlapping of the energy range between the B and C modes was designed in order to check the instrumental performance that both modes would give the same energy spectrum of photoelectrons in the overlapped energy range. In both the B and C modes, V_1 was kept at +2.0 volt with respect to the rocket potential so as to maintain the potential of the collimator inlet near the space potential, while it was 3.0 volt in the A-mode. The collimator inlet was extruded at $\sim$10 mm outside the vacuum vessel after opening the cap of the vessel. The pause mode was for checking the background count rates, where all the electrode voltages but those applied to the channel electron multiplier were set at zero volt.

Figure 3.8 shows a schematic drawing of the sensor. The main part of the sensor was shielded by a high-μ metal and put in the vacuum vessel, the cap of which was opened at the altitude of 120 km. In addition, a part of electronics including the high-voltage power supply was sealed at an air-tight vessel for protection of high-voltage breakdown. In order to minimize spurious effects due to the sunlight contamination and the shadowing effect by the rocket body, the sensor assembly was placed at the top of the rocket payloads so as to look upward in parallel with the spin axis of the rocket. The sun sensor was also installed in order to check the effect of the direct entry of sunlight into the collimator. Figure 3.9 shows a photograph of the sensor assembly, where four probes for TED (thermal
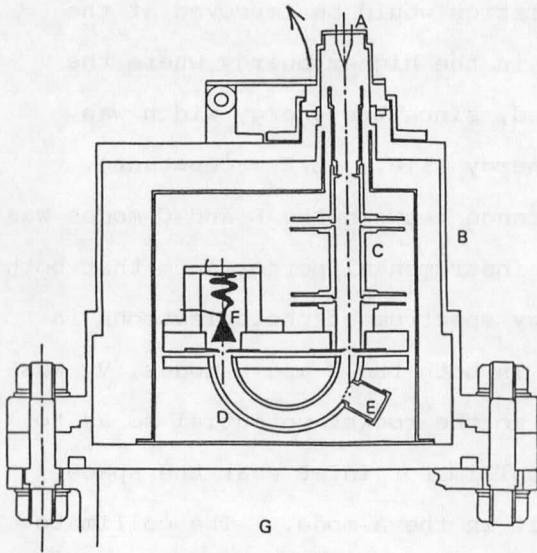
Fig. 3.8

Schematic of the electron
spectrometer on board
K-9M-45.
A : ejectable cap
B : vacuum vessel
C : collimator composed
    of three cylindrical
    electrodes
D : hemispherical electro-
    static analyzer
E : high-energy particle
    and photon trap
F : channel electron
    multiplier
    (Galileo; 4039-type)
G : air-tight electronics
    including high-voltage
    power supply and pre-amp.
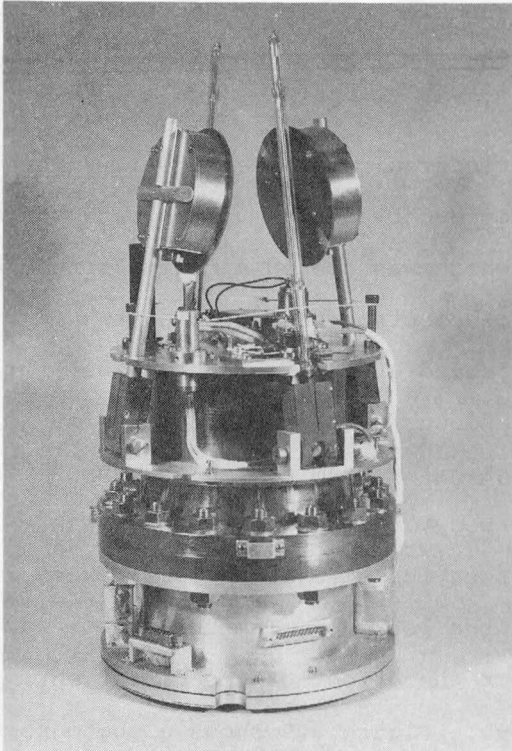
Fig. 3.9

A photograph of the sensor
part of the electron
spectrometer
and four probes for TED
and TEL.

electron distribution) and TEL (electron temperature) instruments
would be deployed after opening the nose-cone of the rocket.

The instrumental performance in this flight was much better
than in the previous K-9M-40 experiment; i.e., no problem in
protection of high-voltage breakdown and elimination of the
sunlight contamination and the shadowing effect by the rocket
body, but there still remained a problem in correction of the
potential of the collimator inlet.   In both the A and B modes,
the analyzer voltage ΔV was kept at a constant value of 4.02
volt, and thus the center energy of electrons which could be
transmitted through the hemispherical analyzer was kept at a
constant value of 4.89 eV just before entering the analyzer,
since the value of k in Eq. (3.1) was calibrated to be 1.217 in
the pre-flight experiment.   In the B-mode, V_3 was swept from +6
down to -25 volt with respect to V_1; that resulted in scanning of
the electron energy from -1.1 to 29.9 eV.   Then the output
counts from the channel electron multiplier was expected to be
zero in the negative value of electron energy and to rise up from
the zero point of energy.   Thus the plasma potential could be
expected to be determined from this information.   The A-mode, in
which V_1 was 3.0 volt with respect to the rocket potential, was
also to serve to such a purpose.   In practice, however, the
count rate showed a significant value in the negative energy
range, while a dip was detected at an electron energy which
seemed to be zero.   This might be because the potential of the
collimator inlet was higher than the plasma potential.   This
result was consistent with the pre-flight experiment, the details
of which will be discussed in Section 5.3 in this chapter.
The plasma potential obtained by the above method was 0.4 $\sim$ 0.7

volt with respect to the rocket potential, while the data obtained by TED showed the plasma potential of 1.5 volt [Oyama, private communication]. This inconsistency would be explained in part by the difference of the work function between the spectrometer electrodes and the TED probe, but it was not solved completely. The electron flux, therefore, would be unreliable below energy of ~2 eV, since the potential of the collimator inlet was much higher than the plasma potential.

4.3 K-9M-47 Experiment

The modifications made in the K-9M-47 experiment were (i) the method of energy scanning, (ii) the change of the view direction of the sensor and (iii) refinement of the vacuum seal, as described below.

The energy of measurement was scanned stepwise in order to make processing of the obtained data simple. Table 3.1 shows various modes of energy scanning, which is composed of three modes; LE (low energy) mode, HE (high energy) mode and BG (background) mode. The LE mode, which was a special feature in our electron spectrometer, was here limited to measure photoelectrons in the very low energy range below ~5 eV with constant transmission and constant energy width; $G \simeq 1.5 \times 10^{-4}$ $cm^2 \cdot sr$ and $\Delta E \simeq 0.09$ eV. The difference between A and B in the LE mode was that the potential of the collimator inlet in the A mode was 1.48 volt with respect to the rocket potential, while it was 1.98 volt in the B mode. The experimental purpose was to investigate how much the energy spectrum of electrons would be affected by the

Table 3.1 Energy scanning modes in the K-9M-47 experiment

	A	B	C	D	E
step numbers	32	32	64	1	1
ΔE (eV)	~ 0.2	~ 0.2	~ 0.9	–	–
step width (msec)	20	20	20	80	80
energy range (eV)	$-1.8 \to 4.6$	$-2.2 \to 4.1$	$0.5 \to 58$	–	–
V_1 (volt)	1.48	1.98	1.48	1.98	0
energy scanning method	ΔV constant		ΔV scannd	$V_2 \sim V_5 : 0$	
		LE	HE		BG

V_1 = Potential of the collimator inlet relative to the rocket.

$\Delta V = V_o - V_i$

potential of the collimator inlet. In both modes the energy of measurement was scanned from the negative range in order to obtain the information about the space potential by the same way as that used in the previous K-9M-45 experiment. In the HE mode, which is essentially the same as the B mode in the previous K-9M-45 experiment, the analyzer voltage $\Delta V(=V_i-V_o)$ was scanned to measure electrons with 64 points of energy from 0.5 to 58 eV. In both the LE mode and HE mode, the potentials of the hemispherical plates were scanned with holding the following relationship in order to minimize the effect of the fringing field.

$$R_i(V_i - V_3) + R_o(V_o - V_3) = 0. \qquad (3.9)$$

In this K-9M-47 experiment, the sensor was installed at the second top position on the rocket, and the view direction of the sensor was inclined at 40° from the spin axis of the rocket in

order to investigate the pitch angle distribution of the photo-electrons. Instead the shadowing effect due to the rocket body and the extended plasma probes was carefully checked by the trajectory tracing of electrons entering the spectrometer in both stages of design of the payload arrangement on the rocket and of processing of the obtained data. Figure 3.10 shows a photograph of the electron spectrometer on this rocket.

A vacuum-seal system, keeping the main part of the sensor in high vacuum, was refined in this K-9M-47 experiment; the vacuum vessel was made of stainless steel (SUS-316) with the main sealing by a metal gasket, and the high-voltage terminals outside the vessel was sealed by potting of a kind of silicon compound (RTV-11). Thus the system for protection of high-voltage breakdown was completed in this experiment.
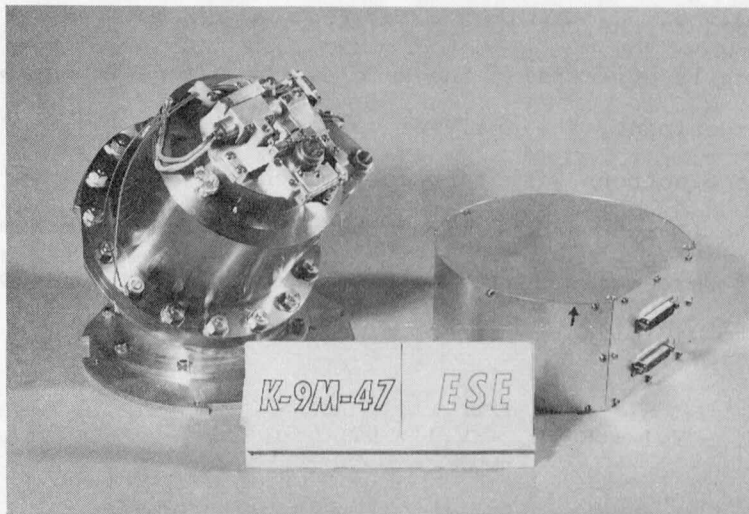
Fig. 3.10 Photograph of the sensor (left-hand) and the electronics (right-hand) of the electron spectrometer on board K-9M-47.

The instrumental performance in flight was complete.   It revealed interesting structures in the energy spectrum of photo-electrons in the energy range from 1 to 60 eV, as will be discussed in the subsequent chapter.

4.4 K-9M-54 Experiment

This experiment was carried out under the predawn condition in order to measure the photoelectrons transported from the conjugate ionosphere through the magnetosphere along the geo-magnetic field lines.   The electron spectrometer was nearly the same as those used in our previous experiments and was designed to measure the 96 point, linearly spaced, spectrum of photo-electrons over the energy range of 1 to 70 eV.   The modifications made in this experiment were (i) enlargement of the diameter of the input slit of the collimator from 4.0 to 8.0 mm, and (ii) the potential of the collimator inlet.   The former item resulted in the increased geometrical factor G of 3×10^{-4} cm^2 sr, while the energy resolution $\Delta E/E$ was 0.04, the same as that of the previous experiment, since the slit diameter of the hemispherical analyzer was not changed from the previous experiments.   The potential of the collimator inlet was kept at 1.0 volt relative to the rocket potential during the energy scanning, since the potential of the collimator inlet of 1.5 volt was somewhat higher than the ambient plasma potential from the results of previous rocket experiments. The collimator orientation was upward 30° with respect to the rocket axis in this K-9M-54 experiment.

The instrument itself worked very well in flight, but the LE

mode could not give reliable electron flux due to the unexpectedly large fluctuation of the rocket potential during the flight which seemed to be caused by the leakage of high voltage used in other instrument on board the same rocket. Nevertheless, we could observe the vertical profiles of the conjugate photoelectron energy spectra for the first time in the world, as will be discussed in the subsequent chapter.

4.5 K-9M-72 Experiment

The purpose of this experiment was a technical performance test of the EXOS-C low-energy particle experiment which consists of two electron sensors and one ion sensor, as will be discussed in Section 4 of Chapter IV. Two types of electron spectrometers were installed on board the K-9M-72 rocket. One was nearly the same as those used in our previous rocket experiments and was designed to measure the 96 point, linearly spaced, spectrum of photoelectrons over the energy range from 1 to 90 eV. The modification made in this experiment was insertion of a mesh just before the channel electron multiplier in order to suppress secondary electrons produced inside the analyzer by applying the mesh voltage V_M as

$$V_M = V_o - 5 \text{ volt.} \tag{3.10}$$

This mesh potential did not affect the detection of electrons which could be transmitted through the hemispherical electrostatic analyzer, but would suppress secondary electrons effectively.

Another electron spectrometer was a quadrispherical electro-static analyzer which was designed to measure electrons over the energy range from 10 eV to 10 keV. The energy spectra observed by both spectrometer showed a good coincidence in the overlapped energy range from 10 to 90 eV, as shown in Section 3 of Chapter IV.

4.6 K-9M-76 Experiment

This experiment was carried out under the predawn condition for the same purpose as the K-9M-54 experiment. The electron spectrometer was completely the same as the K-9M-72 experiment and gave the vertical profiles of the conjugate photoelectron energy spectra over the energy range from 1 to 90 eV.

§5. Pre-Flight Experiments in the Laboratory

5.1 Experiment with a Monoenergetic Electron Beam

The important properties in our electron spectrometer are energy resolution and linearity between the analyzer voltage and the measured energy. These properties should be calibrated by a monoenergetic beam with an energy width being much narrower than that of the spectrometer. Since electrons produced by an electron gun with a heated cathode have an energy spread corresponding to the cathode temperature plus the voltage drop across the cathode, they have usually the energy width of 0.2 ∿ 0.5 eV, which is comparable to, or larger than that of our electron spectrometer. Therefore, a simple electron gun cannot be used

for calibration of our instrument in a low energy range below about 10 eV.   Although the calibration can be carried out in nigh energy without the above argument, performance of the instrument should be tested in a low energy range, where an electron spectrometer is generally susceptible to spurious effects due to the magnetic field, charge-up and stray electrons. Thus we have adopted an electron monochromator to produce a monoenergetic, fine, electron beam in a low energy, as shown in Fig. 3.11.   The electron monochromator is composed of a low-energy electron gun, an energy selector and an electron-optical lens. Only a limited part of electrons produced by the electron gun can be transmitted through the energy selector which comprises a
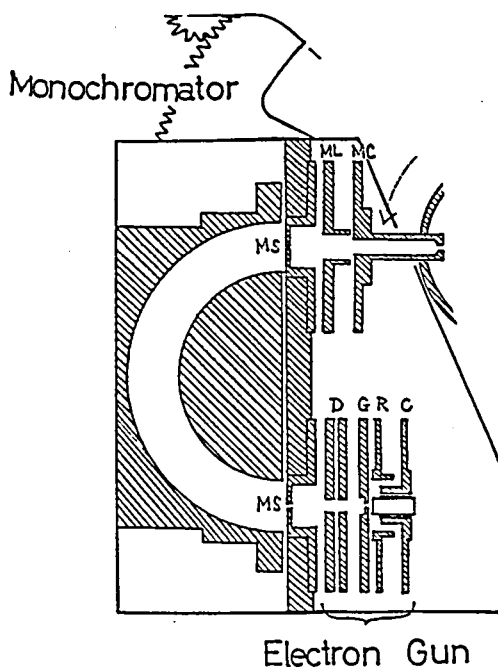
Fig. 3.11   Schematic of an electron monochromator.
       C : cathode   R : repeller   G : grid   D : deflector
       MS : monochromator slit   ML : monochromator lens
       MC : monochromator collimator

hemispherical electrostatic analyzer of the inner and outer radii
of 24.0 mm and 36.mm, respectively, with the identical input and
output circular slits of 0.5 mm in diameter.   The energy spread
of the output electron beam, which is typically as narrow as 60
meV, can be determined by the energy selector.   Electrons
ejected from the energy selector are accelerated (or decelerated)
to the final energy through the electron lens.   The monochromator
assembly shown in Fig. 3.11 is surrounded by a high-μ metal to
shield the external magnetic field.

Figure 3.12 shows the experimental data of transmission pro-
perties of the electron spectrometer on board the K-9M-40 rocket.
Panel (a) shows an example of the obtained energy spectrum, from
which the center energy, the energy width ΔE and the peak height
are measured.   Panels (b) shows a good linearity between the
analyzer voltage $\Delta V_A (=V_i - V_o)$, and the center energy.   Panel (c)
shows the observed energy spread, which also has a linear
relationship with the analyzer voltage if the source electron
beam would be completely monoenergetic.   In practice the source
beam has a finite energy width defined by the energy selector in
the monochromator, and then the resultant energy spread becomes a
result of convolutional integral of transmission functions
between the energy selector for the source beam and the spectro-
meter to be calibrated.   It can be expressed by a following
equation under the reasonable assumption that both the selector
and the analyzer have transmission property of Gaussian shape in
energy.

$$\Delta E/e = \sqrt{(k_M \cdot \Delta V_M)^2 + (k_A \cdot \Delta V_A)^2}, \qquad\qquad (3.11)$$

Fig. 3.12
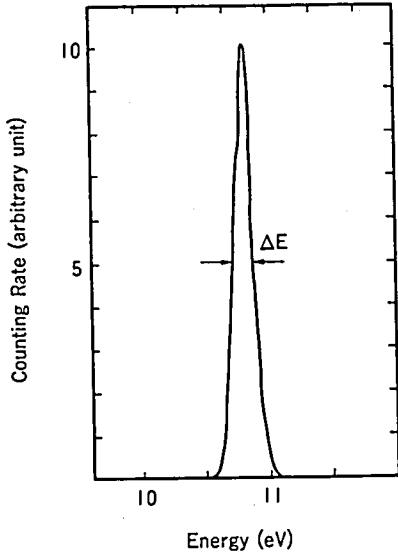
Transmission properties of the electron spectrometer obtained by means of a monoenergetic electron beam.
(a) example of the energy profile
(b) relationship between the analyzer voltage and the center energy
(c) relationship between the analyzer voltage and the energy spread
(d) angular response

(a) example of the energy profile

$\Delta V_A = 0.715E$
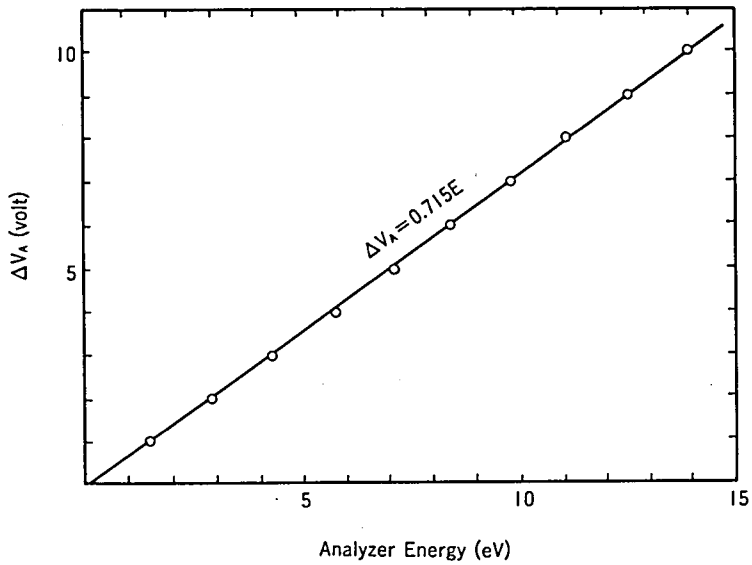
(b) relationship between the analyzer voltage and the center energy
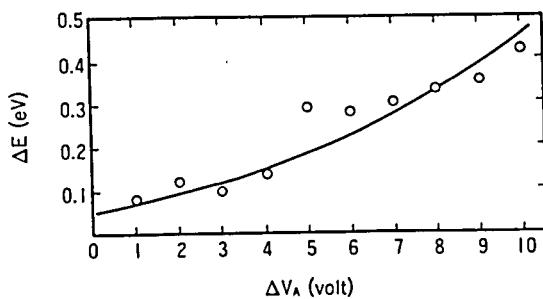
(c) relationship between the analyzer voltage
    and the energy spread
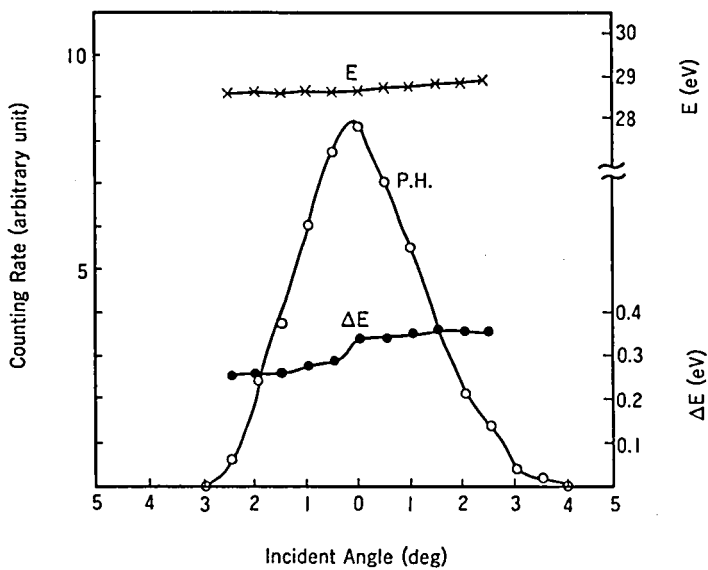
(d) angular response

where ΔE is the observed energy spread, and ΔV_M and ΔV_A are the voltages applied to the selector and to the analyzer, respectively. The constants k_M and k_A can be obtained by the least squares fit of the data shown in Panel (c) where V_M = 5.364 volt, as follows.

$$k_M = 0.012 \text{ , and}$$
$$k_A = 0.041 \text{ .} \qquad\qquad (3.12)$$

Thus the energy width of the source beam $(k_M \cdot \Delta V_M)$ is determined to be 0.064 eV, and that of the rocket-borne spectrometer $(k_A \cdot \Delta V_A)$ is 0.34 eV for the analyzer voltage ΔV_A of 8.27 volt (see Section 4.1). Panel (d) shows angular response of the rocket-borne spectrometer, in which FWHM can be found out to be about 3.6°.

Calibration experiments of the electron spectrometers on board the K-9M-45 and K-9M-47 rockets have been carried out similarly. It has, thus, been established that our electron spectrometer on board the rocket is well suitable for the measurement of very low energy electrons.

5.2 Experiment with a Diffuse Electron Beam

The monoenergetic, fine, electron beam mentioned above is useful for calibration of the transmission properties of the energy analyzer, but laborious experiments must be carried out for studying the transmission property of the collimator which is composed of electron lenses; i.e., angle, position and energy of particle incidence must be varied for various electrode potentials. A simpler experiment using a diffuse electron beam is more

suitable for such a purpose.   The diffuse electron beam, which

has a wide range of area and angular spread, can be easily

produced by a simple filament cathode placed just in front of the

collimator inlet.   Figure 3.13 shows an example of the trans-

mission properties of the collimator lens, where the theoretical

geometrical factor calculated by a paraxial-ray approximation is

also shown for comparison.   The experimental curve is normalized

at the point encircled in the figure.   Both curves generally

coincide with each other, while larger errors can be seen at

larger values of the geometrical factor, probably because of the

breakdown of the paraxial-ray approximation.   The potential of

the intermediate electrode designed for the practical instrument

is chosen so that the geometrical factor has a moderate value in
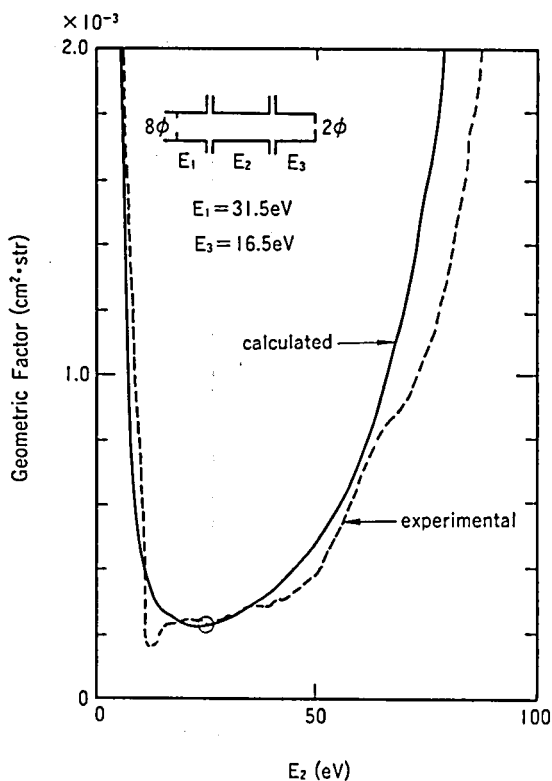
Fig. 3.13

Transmission property
of the collimator

which the agreement between experiment and calculation is attained.
We would like to note here again that the geometrical factor
calculated by the paraxial-ray approximation has a good agreement
with the result obtained by the particle simulation; see Section
4.3 in Chapter II. Thus it was confirmed that the geometrical
factor estimated by the paraxial-ray approximation is useful for
processing of the data obtained in flight of the rocket.

The analyzer characteristics similar to those as shown in
Fig. 3.12 can be obtained also by the diffuse electron beam.
Figure 3.14 shows such an example in which the energy resolution
$\Delta E/E$ can be determined to be 3.9 % in a good agreement with the
theoretical estimate by Eq. (2.21). It should be, however,
noted that the minimum energy spread in this experiment is about
0.4 eV and therefore it is unknown from these data whether the
linearity between the energy width and the analyzer energy may
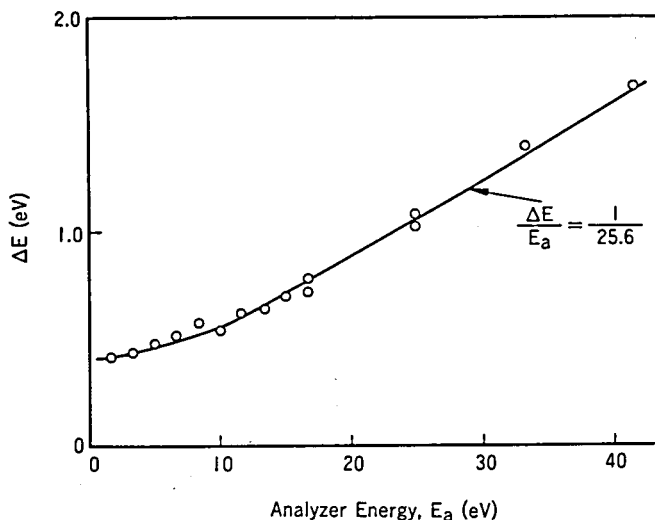
Fig. 3.14 Experimental data for energy resolution of the hemispherical
electrostatic analyzer obtained by means of a diffuse beam.

hold even in the low energy range.   We have already confirmed
this linearity in the very low energy range by using the mono-
energetic electron beam.

5.3 Measurement of Thermal Electrons in a Space Plasma Chamber

Although it has been designed to measure non-thermal photo-
electrons with higher energy, our electron spectrometer may be,
in principle, applicable to the measurement of thermal electrons.
An experiment for this challenge was carried out in the space
plasma chamber, which was equipped with a plasma source of back-
diffusion type.   The electron spectrometer which had been
fabricated for the K-9M-45 experiment was placed in the middle of
the plasma chamber, as shown in Fig. 3.15.

a: spherical probe
b: electron spectrometer
c: collimator inlet

TO PUMP

d: plasma source
e: table for
   spectrometer
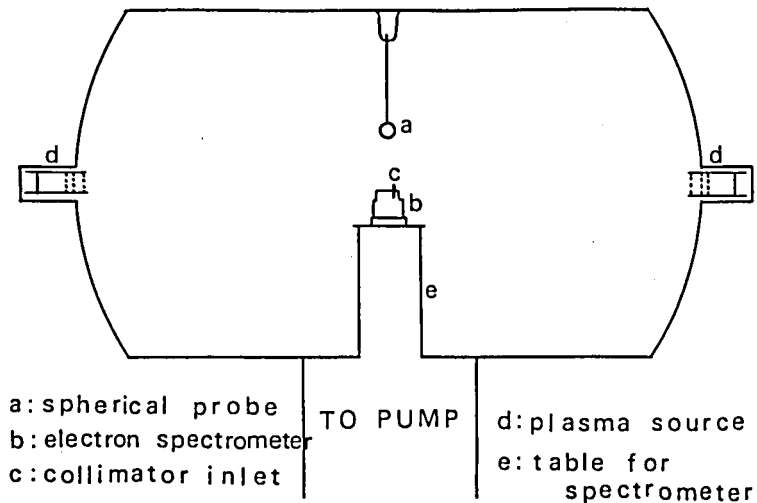
Fig. 3.15 Experimental setup in a large space plasma chamber.

A technical problem for the measurement of thermal electrons
is the determination of the plasma potential, since the potential
of the collimator inlet must be made equal to that potential as
mentioned in Section 3.2 of this chapter.   Now, let the potential
of the collimator inlet be higher than that of the ambient plasma,
and let the energy of measurement be scanned in a range from
negative to positive by the same way as the A-mode in the K-9M-45
experiment (see section 4.2 in this chapter).   Then the output
signal from the spectrometer will be zero in the negative energy
range and rise up from the zero point of energy owing to contri-
bution of thermal electrons.   Thus we may expect that the plasma
potential can be determined from the rising point.   In practice,
however, the experimental result was much more complex, as shown
in Fig. 3.16.   It can be seen that the rising point shifted
according to the change of the potential of the collimator inlet,
while a dip was detected at a fixed point irrespective of the
potential of the collimator inlet.   This dip appeared in case of
the potential of the collimator inlet higher than 1.5 volt, and
was most likely to correspond to the plasma potential.   One
possible cause for the dip might be due to heavy saturation of
the channel electron multiplier in detecting the very high flux
of thermal electrons.   The derived plasma potential was about
1.2 volt, the accuracy of which would be the order of electron
temperature.   All the energy distributions above the plasma
potential were of a similar shape irrespective of the potential
of the collimator inlet and were likely to show the energy
distribution of thermal electrons.   Then, what was the source
for electrons in the negative energy range ?   Clearly those
particles were not positive ions, since the hemispherical
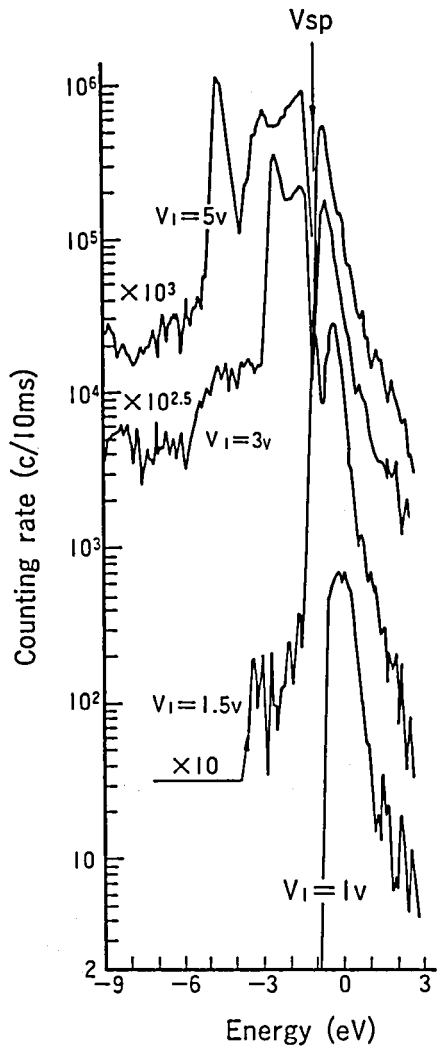
Fig. 3.16 Obtained energy profiles of very low energy electrons.
Energy of the abscissa is referred to the electric potential
of the chamber wall.   Several spectra with different
potentials of the collimator are presented. V_{sp} is the
plasma potential inferred from the obtained energy profiles.

electrostatic analyzer used in our spectrometer could transmit
electrons only.   Thermal electrons had too low energies to
produce secondary electrons, even if they were accelerated by
the potential of the collimator inlet.   Those particles might be
electrons inelastically-scattered from the electrode surface of
the collimator inlet.

Figure 3.17 shows a comparison of the energy distributions of
thermal electrons obtained by two different methods in the plasma
chamber.   One set of the data which contain the main part of
thermal electrons was obtained by means of a spherical Langmuir
probe with the second-harmonic method [Oyama, private communica-
tion].   Another set of the data containing the high-energy tail
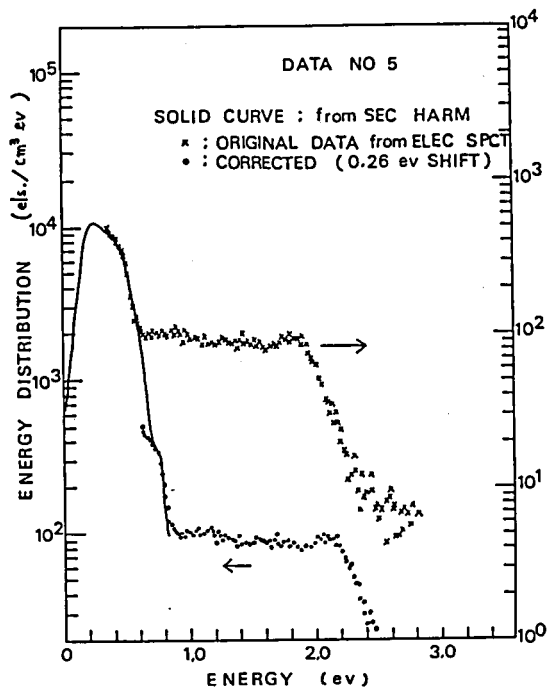
Fig. 3.17   Comparison of the energy distribution of thermal electrons
          obtained by means of the electron spectrometer with that
          by the spherical Langmuir probe using the second harmonic
          method.

was obtained by means of our electron spectrometer, in which the
potential of the collimator inlet was kept at the potential derived
by the above-mentioned method.   It is noted that the vertical
measure in the probe data is relative and adjustable with the
spectrometer data.   Here we discuss the shape of the energy
distribution only qualitatively.   The vertical measure was first
adjusted without energy shift, as shown in the upper part (right-
hand scale) of the figure so that the energy distribution of the
Maxwellian part might be fitted with the probe data.   However the
spectrometer data show a plateau in the high-energy tail, which is
contradictory to the probe data showing a simple Maxwellian
distribution.   The plateau possibly represents the remnant of
fresh electrons before being well thermalized; those electrons
would have an energy spread corresponding to the voltage drop
(1-2 volt) across the source cathode in addition to the thermal
spread.   On the other hand the spectrometer data might be saturat-
ed in the main part of the Maxwellian distribution, since the
electron spectrometer was designed to measure much lower fluxes of
photoelectrons.   In addition, it is not unreasonable that the
plasma potential derived by the electron spectrometer is different
from that of the probe data because of the difference between the
work functions of the electrode surfaces.   Although both of the
electrodes of the spectrometer and the spherical Langmuir probe
were gold-plated, the procedures of fabrication and handling were
different in between.   Therefore, both data could be better
fitted as shown in the lower part (left-hand scale) of Fig. 3.17,
by shifting the energy as well as the vertical measure.   The
required energy shift was 0.26 eV.   It is noted that the electron
temperatures derived from the shape of the Maxwellian part by both

methods yielded nearly identical values.

After all, our electron spectrometer might be applicable to measure the energy distribution of thermal electrons if the potential of the collimator inlet could be kept at the plasma potential. It is at least capable of determining the plasma potential from the measured energy spectra of thermal electrons. The instrumental performance in measuring thermal electrons would be improved with a suitable geometric factor for such a purpose.

5.4 Effect of the Suppressor Grid in Front of the Channel Electron Multiplier

In the K-9M-72 experiment, a mesh was inserted in front of the channel electron multiplier in order to suppress secondary electrons produced inside the hemispherical electrostatic analyzer. We call it a suppressor grid. The used mesh was made of 150-mesh molibdenum with a geometric transmission of 65 %. The mesh potential should be so negative as to reject spurious secondaries, but on the other hand the electric field around the mesh should not much affect the trajectory of the right electrons to be detected. Here we are concerned with the pre-flight experiments, by which the optimum mesh potential was determined.

Generally a hemispherical electrostatic analyzer is intrinsically almost free from the background due to secondary electrons produced inside the analyzer, and hence, can provide a good energy resolution. Figure 3.18 shows an energy spectrum obtained by means of the electron spectrometer on board the K-9M-72 rocket, when a diffuse electron beam with energy of ~300 eV was intro-

duced into the collimator inlet of the spectrometer. The energy
profile of the main peak seemed to be not contaminated at all by
secondary electrons, and the energy peak and the width could be
clearly defined. Most of the energy profile obtained through the
calibration experiment (see Section 5.1 and 5.2) could have
beautiful shapes similar to that in Fig. 3.18. On the other
hand, there is an argument that a low-energy electron spectrometer
may be suffered more or less from instrumental secondaries. A
very small peak in low energies (see the data multiplied by 20 in
Fig. 3.18) might be caused by such contamination. Through varius
experiments with change of the electrode potential, we found that
most of these electrons were not produced inside the electrostatic
analyzer but were created around the collimator inlet, and that
these were indistinguishable from natural ambient electrons.
However, contribution due to these secondaries is usually negligi-
bly small in our electron spectrometer, as shown in Fig. 3.18.
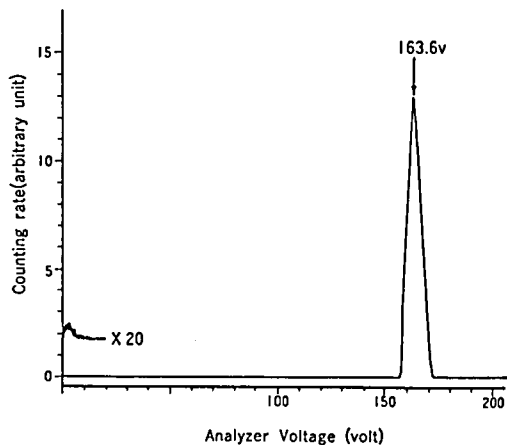
Fig. 3.18 An example of the energy profile obtained in the
calibration experiment.

Thus the experiment using a strong EUV source was carried out in order to investigate how much secondary electrons produced inside the electrostatic analyzer might contribute to the output signal, and to investigate the effectiveness of the suppressor grid in rejection of these electrons. A D_2-lamp with a MgF_2-window [Hamamatsu Photonics, Co.] which produced strong EUV radiation with a wavelength longer than 1200 Å was placed at ∿15 cm in front of the collimator inlet of our electron spectrometer. Figure 3.19 shows variation of output signals versus the mesh potential, indicating the effectiveness of the mesh in suppression of photoelectrons created inside the electrostatic analyzer. With the mesh potential sufficiently negative, the output counting rate of the spectrometer is at a low level which is independent of the analyzer voltage and seems to be caused by multipli-scattered EUV photons entering the channel electron multiplier. With the mesh potential of a small negative value, the signal is at a significantly high level which is caused by photoelectrons ejected from the analyzer electrode. The high electric field in the analyzer would prevent them from being transmitted through the hemispherical analyzer. The cut-off potential, which is shown by the arrows in Fig. 3.19, depends on the analyzer voltage, and can be determined experimentally as

$$V_M = V_o - 5 \text{ (volt)}, \tag{3.13}$$

where V_M is the cut-off mesh potential. This relation means that the upper-most energy of these spurious photoelectrons is determined by the potential of the outer hemispherical plates and that the ejection energy is about 5 eV at highest. The latter
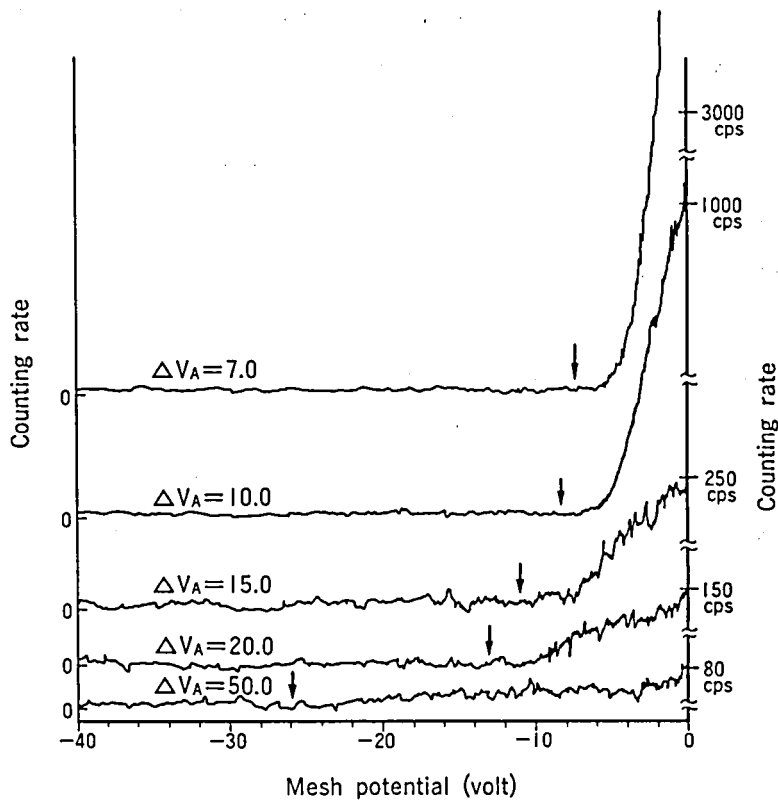
Fig. 3.19   Suppression of EUV background due to mesh potential.
The potentials of all the collimator electrodes were kept at
ground (0-volt).   The parameters for several curves are the
analyzer voltages.   See text for arrows.

might be due to the upper-most energy of the incident photons,

but generally the secondary electrons ejected from the metal

surface due to the incidence of high energy particles have a peak

at an energy below 5 eV; e.g., see Fig. 3.18.

Next the experiment was conducted to investigate the effect

of the mesh potential on detecting the right electrons.   Figure

3.20 shows several examples of electron energy spectra with

various incident beam energies. In this experiment, one pair of

spectra were obtained with the mesh potential equal to that of the

analyzer slit and with the potential expressed by Eq. (3.13),

respectively. There are only slight differences in both the

count peak and the energy width between both cases, except for a

large deformation of the spectrum B at 4 eV which indicates that

this corresponds to the lowest-energy limit for the case B.

Figure 3.21 shows a summary of relative transmission of the mesh

referred to the value with the mesh potential equal to the slit.

This effect is caused by the electric field between the exit

slit of the analyzer and the mesh, which affects trajectories

of electrons to be detected.
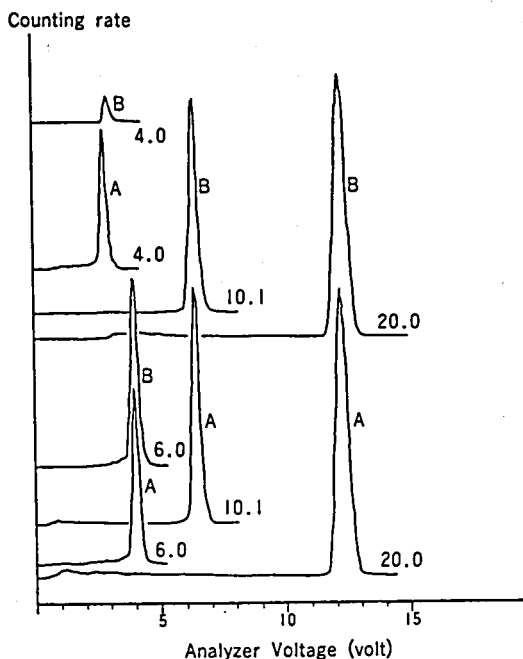
Fig. 3.20 Examples of the energy spectra showing a small effect of the mesh potential on the electron detection. The numeral in each spectrum represents the incident electron energy. The data denoted as A and B correspond to the cases of $V_M = V_s$ (slit potential) and $V_M = V_o - 5$ (volt), respectively.
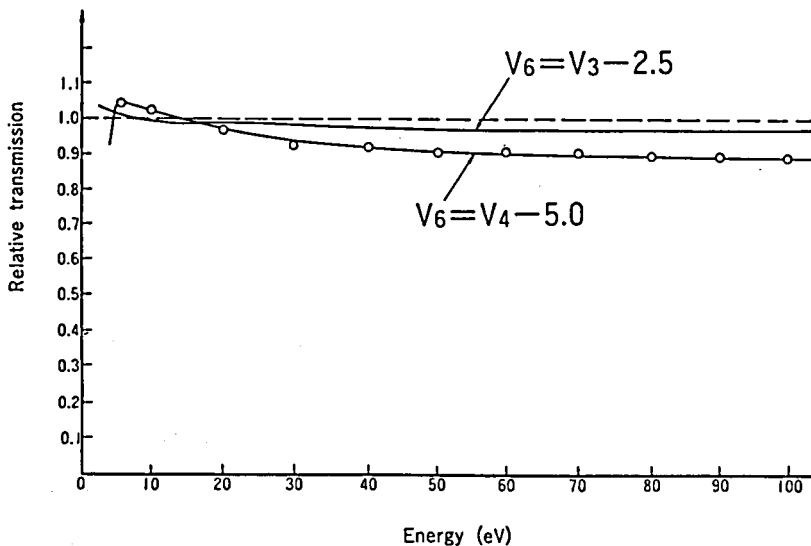
Fig. 3.21   Effect of the mesh potential deduced from the data shown
in Fig. 3.20.   Unity corresponds to the case that the
potential of the mesh is equal to that of the slit.

§6. Concluding Remarks

In this chapter we have described the design, construction
and the pre-flight experiments of the electron spectrometer for
the in-situ measurement of the photoelectrons in the ionosphere.
Table 3.2 shows a summary of experimental parameters of our
electron spectrometers which were successfully carried on the
sounding rockets.   All the electron spectrometers flown were
essentially of the same configuration which consists of a colli-
mator, a hemispherical electrostatic analyzer and a channel
electron multiplier.   A special feature in our spectrometers is
that the collimator is composed of three cylindrical electrodes

which can form an electron lens.   This has allowed us for flexible
operation of the electron spectrometer, e.g., with a constant
energy width during the energy scanning.   The first experiment
was carried out by the K-9M-40 rocket.   In this experiment the
measured energy was scanned with constant energy width in a
limited energy range from 2.5 to 30.5 eV.   Although the obser-
vation provided us with a new finding of the fine structures in
the energy range from 20 to 30 eV, as will be discussed in the
subsequent chapter, it was also found that there might be a few
problems in the design of the actual rocket payload.   These
problems have been overcome through the followed experiments on
board the K-9M-45 and K-9M-47 experiments.   In these experiments,
the measured energy range has been extended toward both lower and
higher energies, and the observation has been refined.   As will
be discussed in the subsequent chapter, the observational results
have revealed the high-resolution capability of our electron
spectrometer and also the adequate design considerations to
measure the photoelectron energy spectra in the daytime ionosphere.
The experiment was also carried out at the predawn conditions by
the K-9M-54 and the K-9M-76 rockets in order to measure conjugate
photoelectrons.   The K-9M-72 experiment was carried out as a
preliminary test of the EXOS-C low-energy particle experiment.
Thus we have accomplished the development of the rocket-borne
electron spectrometer to obtain the high-resolution energy
spectra of the ionospheric photoelectrons.

    Finally it should be emphasized that careful considerations
described in Section 3 are important for design and construction
of the electron spectrometer to make a reliable measurement of
low-energy electrons on board the rocket.

Table 3.2   Summary of experimental parameters

Rocket	K-9M-40	K-9M-45	K-9M-47
Launch(JST)	14:00, 20 Sept. 1972	11:00, 16 Jan. 1974	11:00, 19 Sept. 1974
Altitude range of data	160-315 km	117-360 km	112-315 km
Rocket spin rate	2.44 Hz	1.85 Hz	2.08 Hz
Energy range (design)	2-30 eV	1-48 eV	1-58 eV
Energy range (data)	5-30 eV	2-48 eV	1-58 eV
Period of energy scan	10 s	2.8 s	2.8 s
Method of energy scan	Continuous	Continuous	Stepwise (80 points)
Energy resolution	$\Delta E=0.34$ eV (constant)	$\Delta E/E=0.22$ eV $\Delta E/E=0.05$	$\Delta E/E=0.04$
Angular acceptance	3.6° cone	3.2° cone	3.2° cone
Geometrical factor	1×10^{-4} cm^2 sr	1×10^{-4} cm^2 sr	7.6×10^{-5} cm^2 sr

Table 3.2 (continued)

K-9M-54	K-9M-72	K-9M-76
06:00, 17 Jan. 1976	11:00, 13 Feb. 1982	05:40, 15 Jan. 1983
200-366 km	116-327 km	125-349 km
2.32 Hz	2.50 Hz	2.50 Hz
1-70 eV	1-90 eV	1-90 eV
6-70 eV	1-90 eV	1-90 eV
2.8 s	2.84 s	2.74 s
Stepwise (96 points)	Stepwise	Stepwise
$\Delta E/E=0.04$	$\Delta E/E=0.04$	$\Delta E/E=0.04$
6.3°cone	6.3°cone	6.3°cone
3×10^{-4} cm^2 sr	3×10^{-4} cm^2 sr	3×10^{-4} cm^2 sr

Chapter IV. Rocket Observations of the Photoelectrons

in the Ionosphere

§1. Introduction

This chapter deals with the scientific results and discussions of the ionospheric photoelectrons observed by means of the rocket-borne low-energy electron spectrometers. Their details have been described in the preceding chapter. We have carried out six rocket experiments ; four flights in the daytime and two at predawn in winter. The geophysical conditions during these observations are summarized in Table 4.1. The next section gives the method for data reduction. In order to convert the raw data into the physical quantities, we must know the instrumental characteristics, the details of which have already been described in chapters II and III. Therefore the next section is a summary of the items necessary for data reduction.

The purpose of the daytime experiments is to study the energy spectra of "local" photoelectrons in the upper atmosphere, whereas that at predawn is to study those of "conjugate" photoelectrons under a condition of little local production by the solar EUV radiation. Therefore, we will discuss both observations separately. Section 3 describes the daytime experiments on board the K-9M-40, the K-9M-45, the K-9M-47 and the K-9M-72 rockets. It is reported there that the energy spectrum of the photoelectrons has several features which can be related with the elementary processes of production and loss. The experimental results are discussed also in terms of the theoretical calculation.

In Section 4 the predawn experiments, the K-9M-54 and the

Table 4.1
Geophysical conditions at the rocket experiments

	Launch (JST)	solar zenith angle	$F_{10.7}$ (*)	K_p
K-9M-40	14:00 20 Sept. 1972	43°	113	2
K-9M-45	11:00 16 Jan. 1974	54°	90	3
K-9M-47	11:00 19 Sept. 1974	34°	92	6_-
K-9M-54	06:00 17 Jan. 1976	105° 95° (conjugate point)	77	4_-
K-9M-72	11:00 13 Feb. 1982	51°	204	5_+
K-9M-76	05:40 15 Jan. 1983	92° (conjugate point)	141	2

(*) solar flux at 2800 MHz in 10^{-22} W m^{-2} Hz^{-1}

K-9M-76 observations, are discussed in comparison with the daytime observation. These observations are the sole ones which have ever measured the conjugate photoelectrons by rockets. The remarkable feature found out is an altitude profile of the electron flux, which was quite different from the daytime observation and which seemed to indicate that electrons were transported from a height above the apogee, probably from the conjugate sunlit ionosphere. The electron fluxes observed below the apogee height are also compared to the calculated ones in order to investigate the interaction of electrons with the atmospheric species during the passage in the ionosphere.

§2. Method for Data Reduction

    The raw data consist of counts per sample time in time
sequence of the energy scanning.   What we want to know is an
ambient electron flux at the energy of measurement.

    The measured energy at a certain time can be determined by
the analyzer constant and the electric potentials applied to the
spectrometer electrodes, as expressed by Eq. (3.1).   The analyzer
constant calibrated by the pre-flight experiment has already been
shown in Table 3.2.   Although the monitors of the applied
voltages were included in the telemetry data, they had insuf-
ficient accuracies to deduce the energy of measurement.   We have
used them only as time marker of the energy scanning.   Instead
we have used the values of the applied voltages calibrated on the
ground in order to deduce the measured energy.

    The ambient electron flux, $f(E)$, can be related with the raw
count data, C, by Eq. (2.4) generally, which can be rewritten in
our electron spectrometer as follows.

    $$f = C \ / \ (G_0 \cdot \Delta E \cdot \eta \cdot \tau),\qquad\qquad\qquad (4.1)$$

where G_0 is the geometric factor, ΔE is the energy width, η is
the detection efficiency of the channel electron multiplier, and
τ is the sample time, respectively.   The quantity 'C/τ' gives the
counting rate (counts per second).   The values G_0 and ΔE have
also already been shown in Table 3.2.   The value η was assumed to
be unity irrespective of the measured energy, since it was designed
for the electrons to be accelerated by 250 eV before entering the
channel electron multiplier.

Although our electron spectrometers flown were carefully designed and constructed taking into account all the relevant auxiliary items described in Section 3 of the preceding chapter, a part of the raw data might be contaminated inevitably by the spurious effects. Those items which should be corrected in processing the obtained data are

     (a) rejection of the data contaminated by the photoelectrons produced in the instrument by the solar EUV radiation,

     (b) rejection of the data contaminated by the shadowing effect due to the rocket body and the extended booms,

     (c) subtraction of the background noise, and

     (d) correction of the rocket potential.

Although the first item (a) could be carried out easily by the sun sensor signal and also an anomalous high count rate, the methods with respect to other items are closely related with each instrumentation. These were refined successively through the flight experiences, and therefore, will be described in the respective experiment.

§3. Observations of the Daytime Photoelectrons

3.1 Results

3.1.1 K-9M-40 Experiment

In this first experiment, the energy was scanned linearly from 2.5 to 30 eV. The period of the energy scanning was about 10 sec, whereas the rocket spin period was about 0.41 sec. The

collimator was oriented perpendicular to the rocket axis by the requirement of the payload arrangement. The angle between the directions of the collimator and the geomagnetic field line varied from $55°±5°$ to $125°±5°$ during one spin of the rocket. When this angle was between $70°$ and $110°$, the trajectory of the measured electrons spiraling around the geomagnetic field lines intersected the rocket body. In this case the obtained data were excluded from the analysis in order to avoid the contamination by photoelectrons ejected from the rocket body as well as the shadowing effect. The photoelectron counting rates were 10 $\sim 10^5$ counts/sec, whereas the background count rates were usually less than a few tens of counts per second and were subtracted from the data in the analysis. The count rates were read out as the data points in every 20 msec, which corresponded to the energy interval of about 60 meV. We have averaged the count rates over one spin of the rocket so as to eliminate the effects related to the rocket spin and have further taken the average over several consecutive scans. Thus the data represent the average spectrum over the vertical range of $\sim$30 km. The spectrum, originally read at 60 meV intervals, was smoothed again by the filtration corresponding to the energy resolution (0.34 ev). We think that the fluxes thus obtained are reliable within a factor of 2. Most of the spectra obtained between the altitudes of 200 and 300 km contain a peak that seems to correspond to primary photoelectrons of 27.2 eV ejected from atomic oxygen by He II 304-Å solar radiation. Since our on-board correction of the potential of the collimator inlet (see Section 4.1 in Chapter III) is not very accurate, the zero point of the energy scale is adjusted so that this peak appears at 27.2 eV. The required

energy shift is about 0.8 eV at the 200-km level.

The energy spectra of photoelectrons thus obtained are shown in Fig. 4.1 for several altitudes. Below about 5 eV the observed electron flux would not be reliable because the estimate of the transmission function of the spectrometer may include errors below about 5 eV and also because the on-board correction of the potential of the collimator inlet may not be perfect. Figure 4.2 compares the present result with the theoretical calculation by Ogawa [1971] and other experimental results [Doering et al., 1970; Knudsen and Sharp, 1972; Hays and Sharp, 1973] at the ∿ 200 km level (Table 4.2).

The general shape of our spectrum is in fairly good agreement with that theoretically computed by Ogawa [1971] in the energy
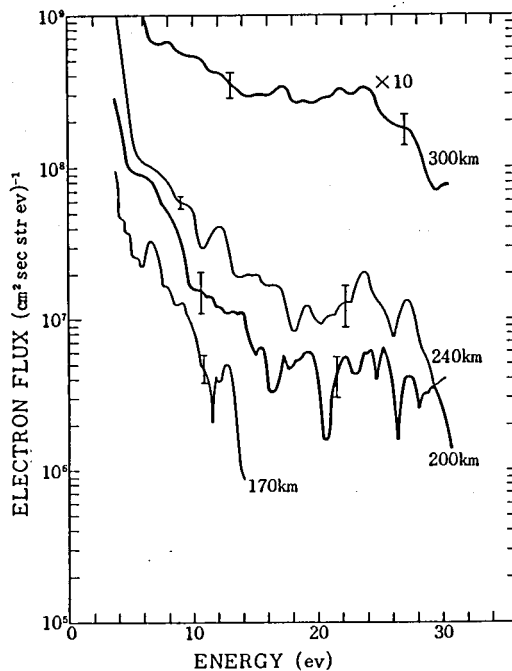
Fig. 4.1 Energy spectra of the photoelectron flux. Each spectrum represents an average over the vertical distance of ∿30 km. Error bars represent ±1 standard deviation in the electron flux.
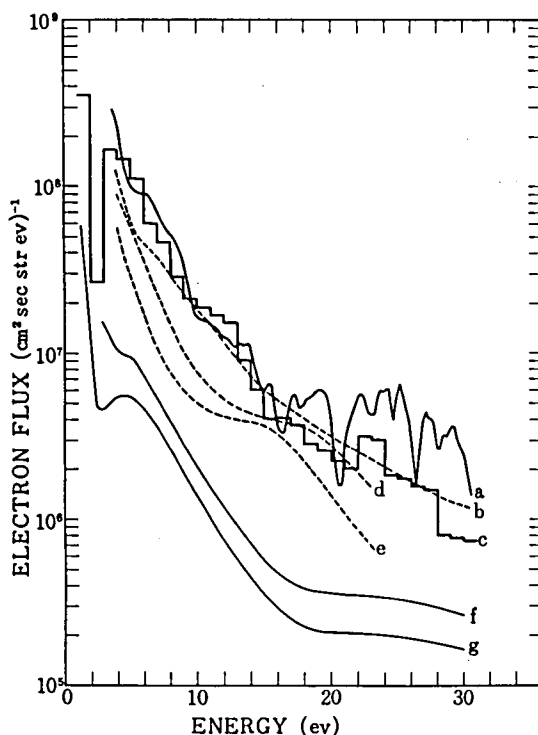
Fig. 4. 2 Comparison of the present result with other observational
and theoretical spectra at the ∿200-km level:
a, present study; b, Knudsen et al. [1970]; c, Ogawa [1971];
d, Doering et al. [1970]; e, Doering et al. [1970]; f, Hays
and Sharp [1973]; and g, Hays and Sharp [1973].   See Table
4.2 for solar zenith angles and altitude.   Spectra f and g
have been multiplied by the factor 1/4π.

Table 4. 2 Comparison of the Present Study with Other Spectra at the
∿200-km Level

Study	Solar Zenith Angle, degrees	Altitude, km
Present study*	43	200
Knudsen and Sharp [1972]*	47	180
Ogawa [1971]†	60	200
Doering et al. [1970]*	60	200 down-leg
Doering et al. [1970]*	60	200 up-leg
Hays and Sharp [1973]*	90	202 down-leg
Hays and Sharp [1973]*	90	202 up-leg

* Observation.
† Theory.

—113—

range 5-16 eV at an altitude of 200 km; i.e., our spectrum shows shoulders (i.e., relatively steep declines) at 6 and 13 eV, which correspond to discontinuities in the energy loss function [Ogawa, 1971]. However, above ∿16 eV our observed spectrum shows peaks that are higher and finer than those seen in Ogawa's spectrum. These peaks are not evident in the observed spectrum of Hays and Sharp [1973] either, but they seem to reflect the primary photo-electrons ejected from atomic oxygen and molecular nitrogen through the ionization by He II 304 Å. We discuss below whether these peaks in our observed spectrum are physically significant.

Figure 4.3 shows a comparison of our observed spectrum with the theoretical estimate[*] of the production rate of photo-electrons in the energy range 20-30 eV at ∿200 km (Table 4.3). The atmospheric composition is taken from Jacchia [1971] at the exospheric temperature of $900^\circ K$. The solar flux is taken from Hinteregger [1970], and the attenuation by the upper-lying atmosphere is neglected. The photoionization cross sections for various electronic states are taken from Shoen [1969] for molecular nitrogen and Henry [1967] for atomic oxygen. At ∿200 km the photoelectron yielded from molecular oxygen is relatively insig-nificant. One can see in Fig. 4.3 that the peaks of our observed spectrum agree reasonably well with the peaks in the primary photoelectron yield due to the ionization of atomic oxygen and molecular nitrogen by He II 304-Å solar radiation, particularly at the 200-km level, where the observed spectral peaks are seen at energies of about 22.2, 23.8, or 23.9, 25.2, and 27.2 eV, as is expected theoretically. At the 240-km level, the intense

---

[*] see Eq. (4.4) in Section 3.2.1.
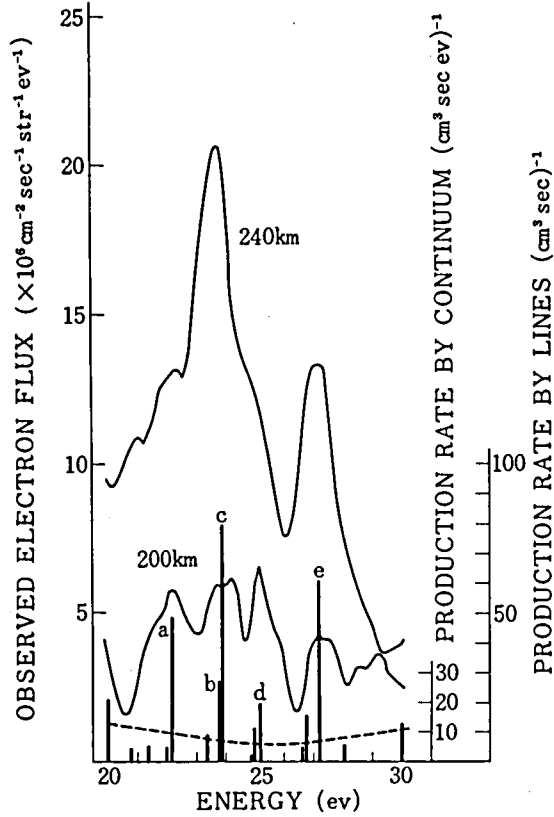
Fig. 4. 3 Comparison of the present result with the theoretical estimate
of the production rate of primary photoelectrons in the energy
range 20-30 eV. The solid curves are observed values,
the dashed curve is the production rate by continuum, and
vertical lines a-e are the production rates by lines
(see Table 4.3). The attenuation of the solar flux by the
upper atmosphere above 200 km is neglected.

Table 4.3 Comparison of Photoelectron Production Rates by Lines.

He II Line in Figure 3	Produced Ion	Energy of Ejected Photoelectrons, ev
Line a	$O^+(^2P)$	22.2
Line b	$N_2^+(A)$	23.8
Line c	$O^+(^2D)$	23.9
Line d	$N_2(X)$	25.2
Line e	$O^+(^4S)$	27.2

peaks are seen at energies of 23.9 and 27.2 eV, and a small peak is seen at 22.2 eV, corresponding to the peaks of the primary photoelectron yield due to the ionization of atomic oxygen by He II 304 Å.

Thus the peaks found in our spectrum seem to be physically meaningful. Many of these peaks are lost in the steady state spectrum calculated by Ogawa, probably because of the smearing effect by the various kinds of slowing-down processes assumed there. Another possible cause of difference would be in the data adopted by Ogawa (e.g., cross sections and an atmospheric model) and also in the usage of the digitized energy width of 1 eV.

As the altitude becomes higher (e.g., 300 km), the peaks mentioned above become less marked, and the energy spectrum becomes rather smooth and flat. This tendency appears reasonable, since at higher altitudes (above 260 km) the elastic collision with ambient electrons makes a large contribution of the slowing-down mechanism of photoelectrons and leads to the flattening of the energy spectrum [Ogawa, 1971].

3.1.2 K-9M-45 Experiment

In this experiment the instrument was installed at the top of the rocket payload, and looked upward in parallel with the rocket axis. Therefore we have no concern about the shadowing effect or the wake problem caused by the rocket body. The energy scanning and also the correction of the rocket potential are referred to Section 4.2 in the preceding chapter.

The count rates were read out at first as the data points in every 10 msec. For statistical significance, if the counts in the raw data (counts per 10 msec) were less than ten, next count data were added to these data until the sum of the data were over ten and were averaged over the summed period. Then, the data were reconstructed as the data points in every 0.25 eV in the B mode of energy scanning and in every 0.5 eV in the C mode, respectively. Background count rates, which could be obtained from the counts at zero electrode voltage, were subtracted from the data. The energy spectra in each mode of the energy scanning have been obtained in this way. There were, however, some systematic differences of the obtained spectra between the B mode and the C mode. Since the difference was in general trend (slope) of the spectra rather than the existence of fine structures, we considered that it was caused by the estimation error of the geometric factor in the B mode (the voltage applied to the second electrode of the collimator was not monitored unfortunately in this experiment). Thus the correction factor in the B-mode data was determined by the ratio of the <u>smoothed</u>[*] spectrum in the B mode to that in the C mode after averaging <u>all</u> the data in each mode obtained during the rocket flight. It was within a factor of two in the worst case.

The energy spectra of the photoelectron flux obtained thus around an altitude of $\sim$230 km are shown in Fig. 4.4, where each spectrum was obtained by averaging several consecutive scans.

---

[*] since the energy resolution was different in between the B mode and the C mode, all the fine structures observed have been smoothed out for the purpose of ratio calculation.
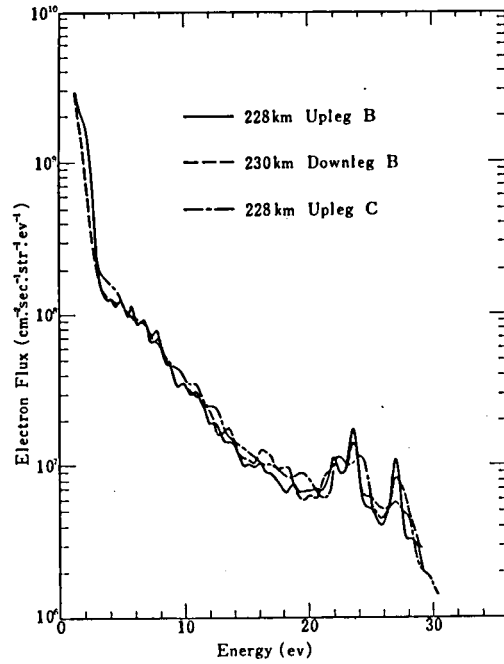
Fig. 4.4 Energy spectra of the photoelectron flux from the upleg data
(B-mode and C-mode) and the downleg data (B-mode) at
∿230-km altitude.
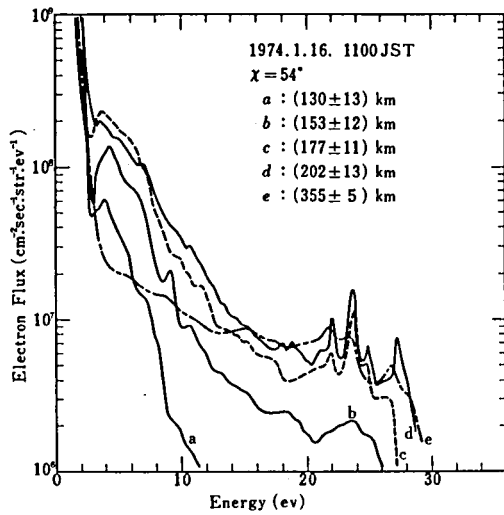
Fig. 4.5 Energy spectra of the photoelectron flux at different altitudes.

It is remarkable that the B-mode upleg data agreed very well even in the shape of the fine structure from 20 to 30 eV with the C mode data in spite of the rough method of estimation of the correction factor mentioned above. It is also reasonable that the B mode spectrum shows higher energy resolution with respect to the shape of the fine structure than the C mode spectrum. A very good coincidence between the upleg data and the downleg ones is also remarkable, since a factor of two difference between both data was common even in the most reliable observations by others; see the differences between the curves d and e, and also between f and g in Fig. 4.2. This fact does indicate much higher reliability of our data than others.

Figure 4.5 shows energy spectra of the photoelectron flux at various altitude regions. Only the B-mode data are presented in this figure, because they revealed higher energy resolution than the C-mode data. Part of the C-mode data will be presented in conjunction with those obtained by the K-9M-47 experiment. The spectra "b" through "e" are obtained from both upleg and downleg data because of good coincidence of both data, whereas the spectrum "a" is only from the downleg data because of absence of upleg data below ∿140-km altitude. The energy spectra at altitudes between "d" and "e" are not included in this figure, because the spectrum at ∿230-km altitude has already been shown in Fig. 4.4, and also because the altitude dependence of the photoelectron flux is gradual especially above an energy of 15 eV; see Fig. 4.7. Comparison of the present data with other observational and theoretical spectra at ∿200-km altitude is shown in Fig. 4.6. The general shape of the present spectrum is in fairly good agreement with our previous data by the K-9M-40
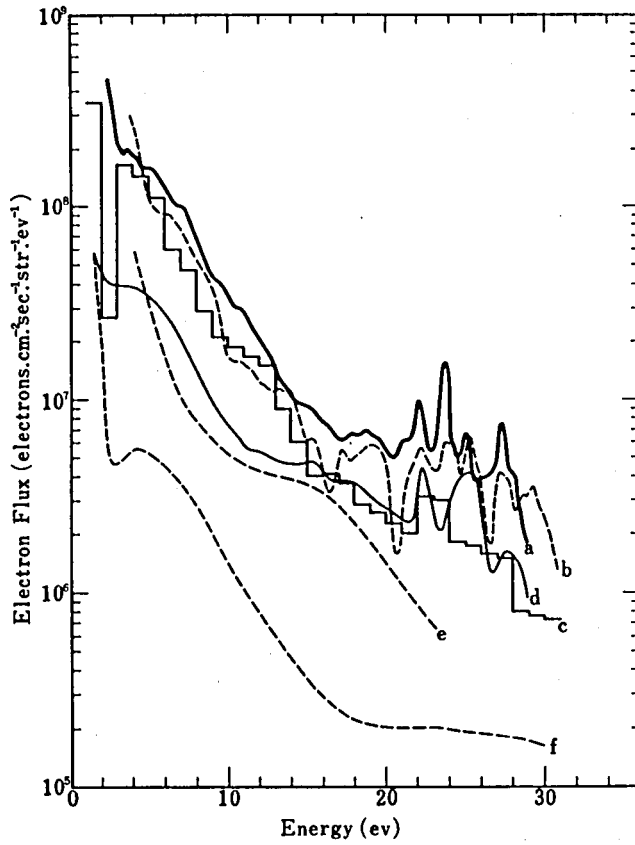
Fig. 4.6   Comparison of the present data with other observational and
theoretical spectra at ∿200-km altitude;

(a) Present data[*] (K-9M-45), χ = 54°, 202 km

(b) Previous data[*] (K-9M-40), χ = 43°, 202 km

(c) Ogawa [1971][†] , χ = 60°, 200 km

(d) Mantas and Bowhill [1975][†], χ = 0°, 179 km

(e) Doering et al. [1970][*], χ = 60°, 200 km upleg

(f) Hays and Sharp [1970][*], χ = 90°, 202 km upleg

   *: Observation   †: Theory

Spectra f have been multiplied by the factor 1/(4π).

experiment and hence with the theoretical spectrum calculated by
Ogawa [1971], although the present data show somewhat higher
level of the photoelectron flux.   This slight difference might
be attributed to the differences among the geophysical conditions
of the individual data and also to the experimental inaccuracies.

It can be seen that the data obtained by this experiment
have much better quality than the previous ones shown in Fig.
4.1.   The spectral shape of the fine structure in an energy
range from 20 to 30 eV and its dependence on altitude are
seen much more clearly.   The theoretical spectrum by Ogawa
[1971] has shown a hump at energies of 22 ∿ 24 eV and a shoulder
at 27 eV, while that calculated by Mantas and Bowhill [1975] has
revealed a few peaks in the energy range from 20 to 30 eV.   The
existence of this fine structure was newly found out in the
K-9M-40 experiment and was reconfirmed clearly by this experiment,
although other previous observations had not shown the existence.
The fine structure is most evident at the altitude of ∿200 km.
It might be explained qualitatively by a combination of the
abundances of atmospheric species and the atmospheric attenuation
of He II 304 $\overset{\circ}{A}$ solar radiation; the abundance ratio of N_2 to O
decreases with height, the intensity of solar EUV radiation
decreases at lower altitudes due to the atmospheric absorption,
and the higher density of neutral particles leads to the quick
degradation of photoelectrons at lower altitudes.   It is because
of prevalence of the elastic collision with ambient thermal
electrons, as discussed in the preceding subsections, that the
peaks become less marked at higher altitudes.

A dip, which seems to indicate the theoretically well-known
one caused by the resonant vibrational excitation of nitrogen

molecules, can be found around an energy of 3 eV in the spectra at low altitudes; "a", "b" and "c" in Fig. 4.5.   Although the collision cross section has the largest value at an energy of 2.3 eV [Schulz, 1964], Hoegy et al.[1965] argued that the dip would shift to a somewhat higher energy owing to the Maxwellian tail of thermal electrons.   Hays and Sharp [1973] observed the dip at an energy of 2.7 eV, which has been the sole observation so far. Our observation, in which a dip is detected around 3 eV, might be affected possibly by the high electric potential of the collimator relative to the ambient plasma potential.

Figure 4.7 shows altitude profiles of the electron fluxes at several selected energies.   The height for the maximum electron flux, which exists in a range from 180 to 230 km, tends to be lowered with decreasing energy of the photoelectron.   This result is consistent with the altitude profile of the electron temperature
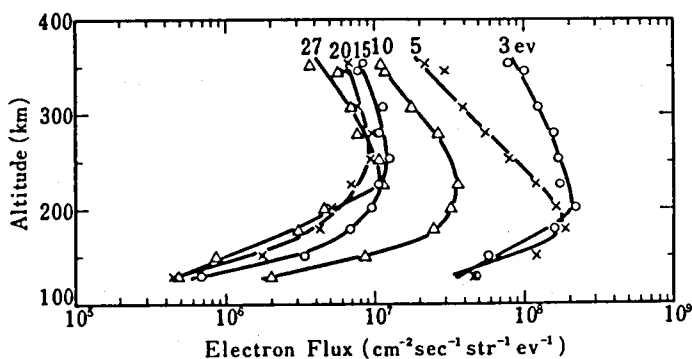
Fig. 4.7 Altitude distribution of electron flux for several
          discrete energies.

observed simultaneously by Oyama [private communication, 1974].

Figure 4.8 shows comparison of the energy distribution function in a very low energy range obtained by our electron spectrometer with the thermal electron distribution function measured simultaneously by a Langmuir probe with the second-harmonic method [Oyama, 1976].   It should be noted that the spectrometer data marked by the triangles were affected by saturation of the detection system above 10^2 els/cm^3 eV, since our electron spectrometer was designed to measure lower flux of the photoelectron at higher energies.   Taking into account this effect, it can be said that at higher altitudes the extention of the Maxwellian tail of thermal electrons is in good agreement with the lowest-energy part of the spectrometer data in case of the lower electron temperature.   On the other hand, the discrepancy between both data can be clearly found at lower altitudes. Ashihara and Takayanagi [1974] has calculated the distribution function of ionosheric electrons in the same energy range as that shown in Fig. 4.8 and argued that the resonant vibrational excitation of molecular oxygen causes a plateau-like structure with a slight wriggle at around 1 eV in the velocity distribution function in the case of 120 km-altitude.   Recently, Oyama and Hirao [1985] have observed a plateau with several peaks in an energy range from 0.5 to 2 eV at altitudes below 150 km, which were identified as due to the super-elastic collisions with excited neutral particles.   The discrepancy seen at lower altitudes in Fig. 4.8 might be attributed in part to these processes, and also possibly to the high electric potential of the collimator inlet referred to the ambient plasma.
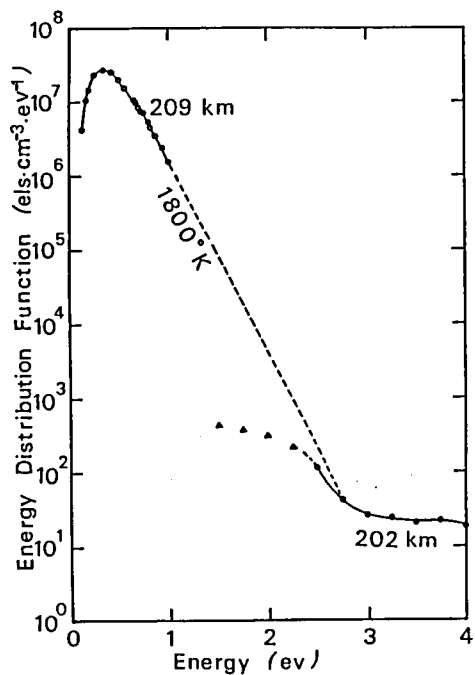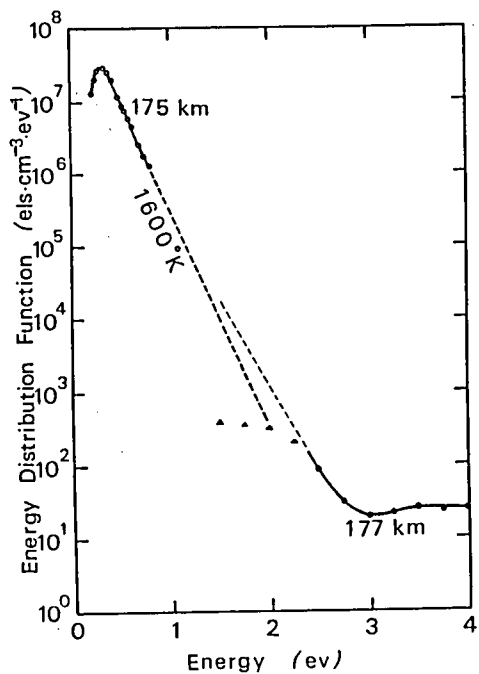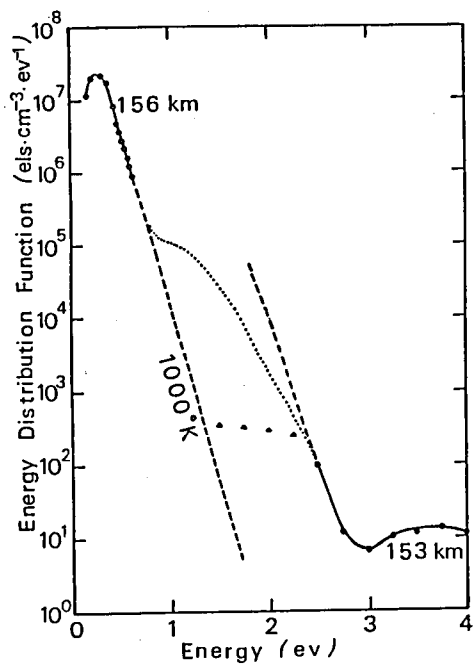
Fig. 4.8

Comparison of the energy distribution functions obtained by the electron spectrometer with those obtained by the second harmonic method [Oyama, 1976] at various altitude.
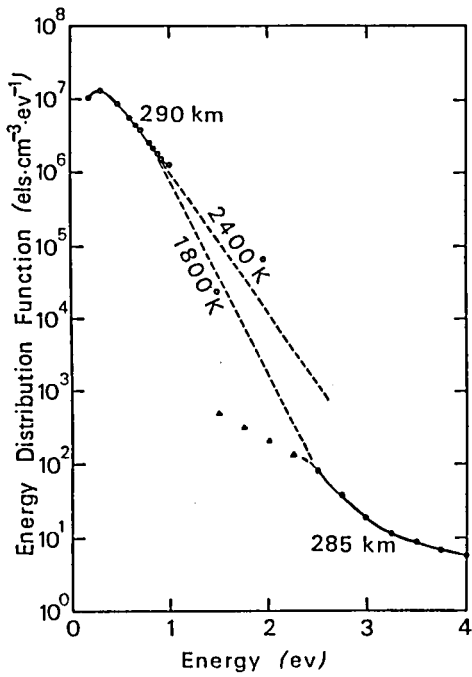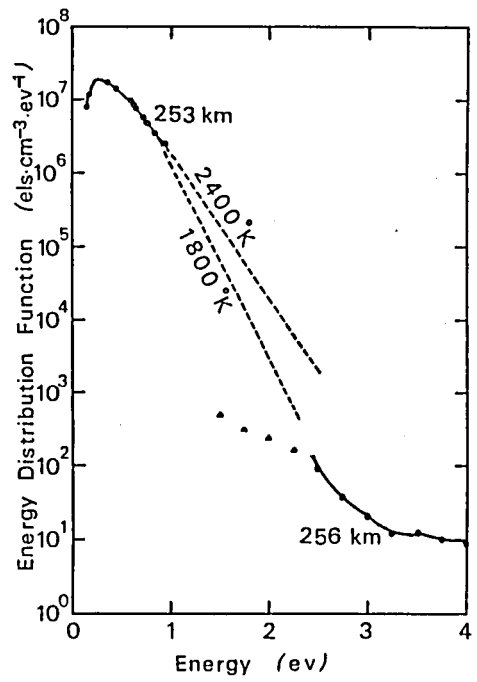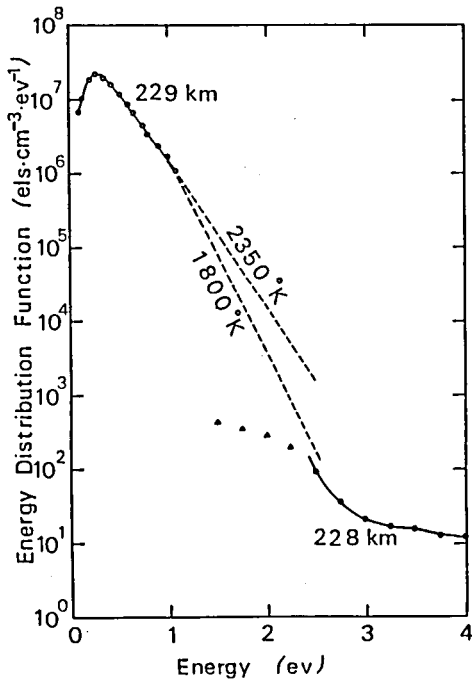
Fig. 4.8 (continued)

3.1.3 K-9M-47 Experiment

Since the measured energy was scanned stepwise, the correspondence between the count data and the measured energies is defined clearly in this experiment.   The method for correction of the energy scale is same as that used in the K-9M-45 rocket.   The background noise, which is estimated from the counts in the E-mode (see Table 3.1), is also subtracted from the count data.   In this experiment, the instrument was placed at the second top position in the arrangement of the rocket payload, and the collimator orientation was upward $40°$ relative to the rocket axis.   In order to remove the shadowing effect, we have checked the trajectories of electrons entering the spectrometer at every point of the data, taking into account the spiral motion of electrons along the magnetic field line, and discarded those data corresponding to the shadowing caused by the rocket and the extended probes.

Figure 4.9 shows the pitch angle distributions of the photoelectron fluxes at several energies which were obtained from the data above 285-km altitude.   The flux was nearly isotropic in the measured pitch angle range from $5°$ to $85°$, although the minimum seemed to appear at a pitch angle from $20°$ to $40°$.   At altitudes above 300 km, the measured photoelectron flux might include, in part, the non-local photoelectron flux coming from the conjugate ionosphere along the geomagnetic field line, because the instrument measured the downward flux of electrons.   Enhancement of the electron flux at the smallest pitch angle might arise from this.   A theory [Mantas and Bowhill, 1975] has predicted isotropy of the photoelectron flux at altitudes below 330 km.

Figure 4.10 shows a good coincidence between the energy
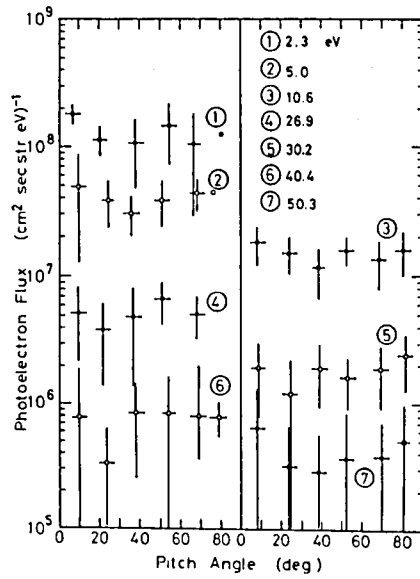
Fig. 4.9 Pitch angle distributions of the photoelectron flux
at several energies.
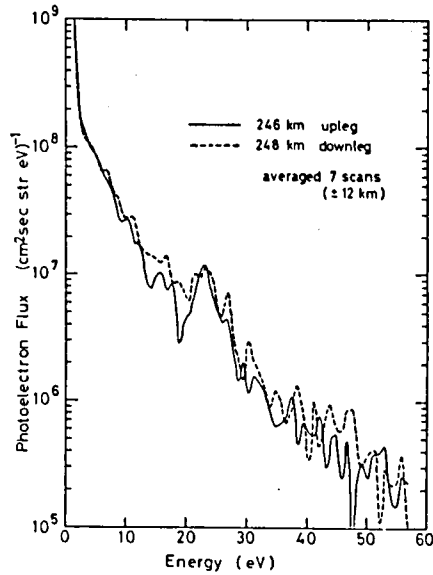
Fig. 4.10 Comparison between the upleg data and the downleg ones.

spectra obtained in the ascent and the decent of the rocket flight, similarly to the previous K-9M-45 experiment; see Fig. 4.4. Figure 4.11 shows energy spectra of the photoelectron flux at several selected altitudes. In this experiment in which the measured uppermost energy was extended up to 58 eV, we observed a sharp cut-off of the photoelectron flux at around 50 eV, above ∿180-km altitude, in addition to other features similar to those measured in the previous K-9M-45 rocket.

Figure 4.12 shows a comparison of the photoelectron energy spectra among the present data, the previous K-9M-45 data and the result calculated theoretically by Mantas and Bowhill [1975] at
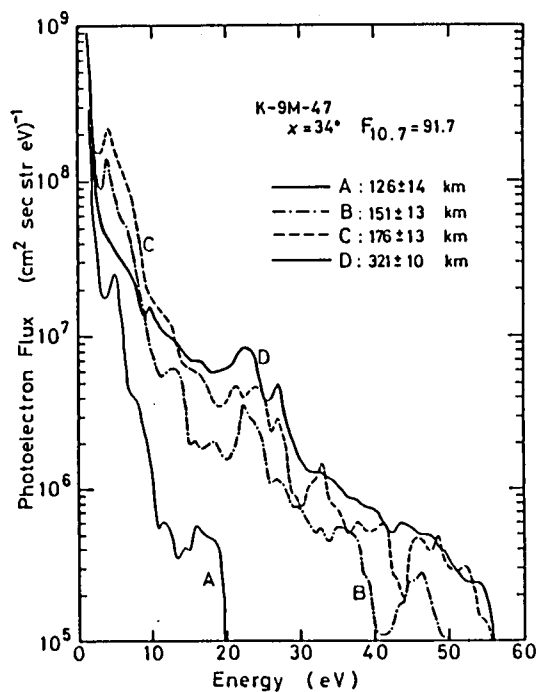
Fig. 4.11 Energy spectra of the photoelectron flux at various altitudes.

two different altitudes. In the K-9M-45 data, the energy

spectra below 30 eV are taken from the B-mode data and connected

with the C-mode data. A good coincidence is remarkable among

three energy spectra, especially at higher altitudes as shown in

Fig. 4.12(a). There can, however, be found some discrepancy

between the experimental results and the theoretical calculation

at a low altitude; see Fig. 4.12(b). This point will be discuss-

ed in the next subsection 3.2. It is because of the lack of the

energy resolution in this experiment that the K-9M-45 spectrum

has sharper peaks in an energy range from 20 to 30 eV than the

present K-9M-47 one. In the present experiment, the high-

resolution modes A and B were designed to be limited only to the

(a)   (b)
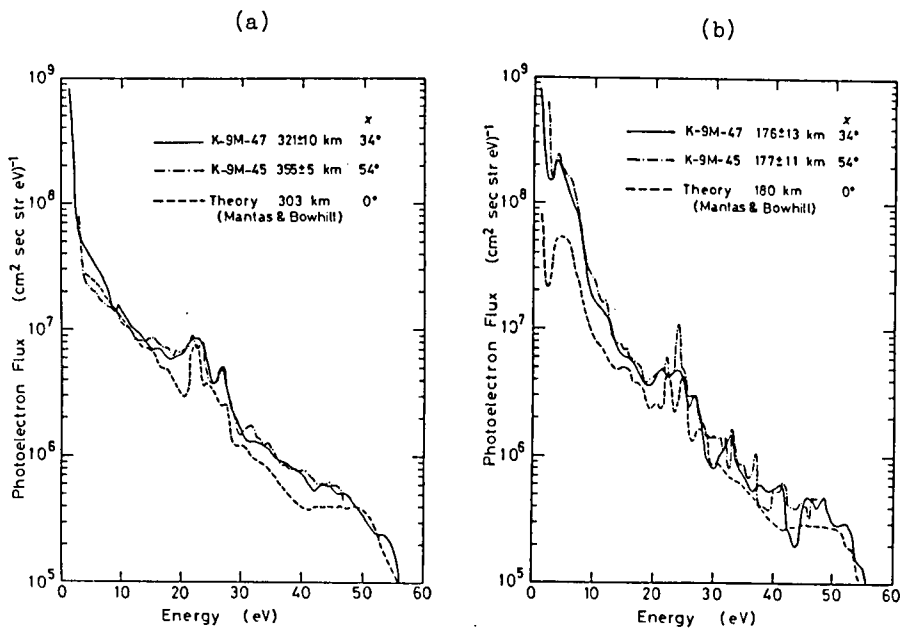
Fig. 4.12 Comparison of the photoelectron energy spectra among
the present data, the precious K-9M-45 data and
theoretical calculation by Mantas and Bowhill [1975]
at two altitude regions; (a) 300-355 km and (b) 180 km.

low energy range, which resulted from a compromise among time
resolution, energy resolution and energy range.

It is interesting to discuss about a dip at around 3 eV
observed at altitudes below ∿ 200 km (see curves A, B and C in
Fig. 4.11), since the modes A and B of the energy scanning in the
present experiment first provided us with the detailed energy
spectra in the low energy range.   The observed result obtained
at two selected altitudes is shown in Fig. 4.13, in which the
theoretical spectrum calculated by Mantas and Bowhill [1975] is
also shown together with the spectra observed at ∿180-km altitude.
The theoretical flux is multiplied by five times, since there
exists a great difference of the electron fluxes between obser-
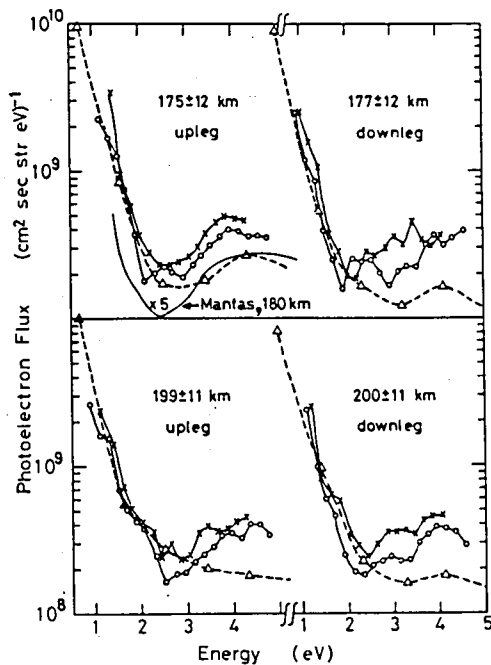
Fig. 4.13   Detailed energy spectra of the photoelectron flux
            in low energies.

vation and calculation in this low-energy range; see Fig. 4.12(b).

The higher electron flux in the B-mode spectrum than the A-mode

spectrum may arise from the high electric potential of the

collimator inlet in the B-mode.   This dip corresponds most

probably to the well-known which arises from the resonant vibration-

al excitation of nitrogen molecules.   Observations which have

been successful in detecting this dip have been only those by

Hays and Sharp [1973], by the previous K-9M-45 and by the present

experiment.   Although Hays and Sharp [1973] could not detect it

in the descent of the rocket flight, we have observed the dip in

both the ascent and the descent of the rocket.   Hays and Sharp

[1973] argued that the dip was shallower and was detected at

somewhat higher energy than theoretical prediction.   Figures 4.6

and 4.12 show a similar tendency.   One explanation is that the

Maxwellian tail of thermal electrons might tend to fill the dip

and shift the dip energy to slightly higher energies [Hoegy et

al. 1965], but the contribution of the thermal electrons would be

small with the measured electron temperature in the K-9M-45 case,

as shown in Fig. 4.8.   Another possibility is a plasma instabili-

ty as discussed by Bloomberg [1975] who suggested that an electro-

static electron instability has a possibility to smooth out the

energy distribution at altitudes of 150 to 200 km.   On the other

hand, the upper panel in Fig. 4.13 shows that the shape of the

energy spectra obtained by the high-resolution modes, A and B, is

relatively in good agreement with the Mantas spectrum.   The

conclusion is not definite now, and more refined measurements and

theoretical works should be made in future.

Figure 4.14 shows an altitude profile of the photoelectron

fluxes at several selected energies.   The electron flux in low

energies has a maximum at altitudes from 180 to 220 km, which is
similar to our previous data shown in Fig. 4.7, but the flux
tends to increase slightly with height in higher energies.
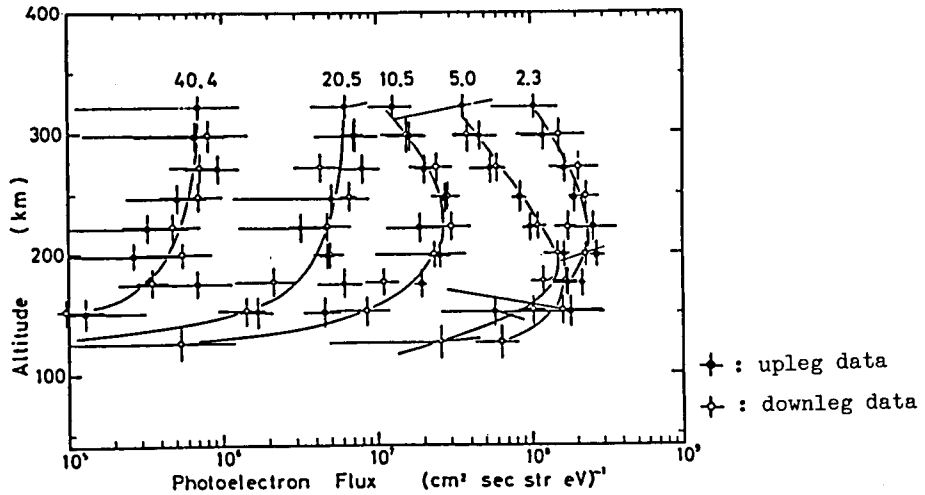
Fig. 4.14   Altitude profile of the photoelectron flux at several
energies as indicated.

3.1.4   K-9M-72 Experiment

This experiment, which consisted of two sensors, LE (low
energy) and HE (high energy), was carried out as a technical
performance test of the OHZORA low-energy particle experiment.
The observed result with respect to the ionospheric photoelectrons
is quite consistent with the previous ones described so far and
has nothing to be discussed any more.   Here we concentrate on
technical discussions of the experimental purpose.   The method
of processing of the obtained data is essentially the same as

that used in the previous experiment.

One of the experimental purpose was an in-flight test of the effect of the mesh which was newly placed just before the channel electron multiplier in order to suppress secondary electrons produced inside the hemispherical electrostatic analyzer. An incidental problem caused by the use of this mesh is the effect of the electric field around the mesh to the trajectories of the right electrons which should be detected normally. The mesh potential was determined by the pre-flight experiment (see Section 5.4 in Chapter III), so that this effect might be
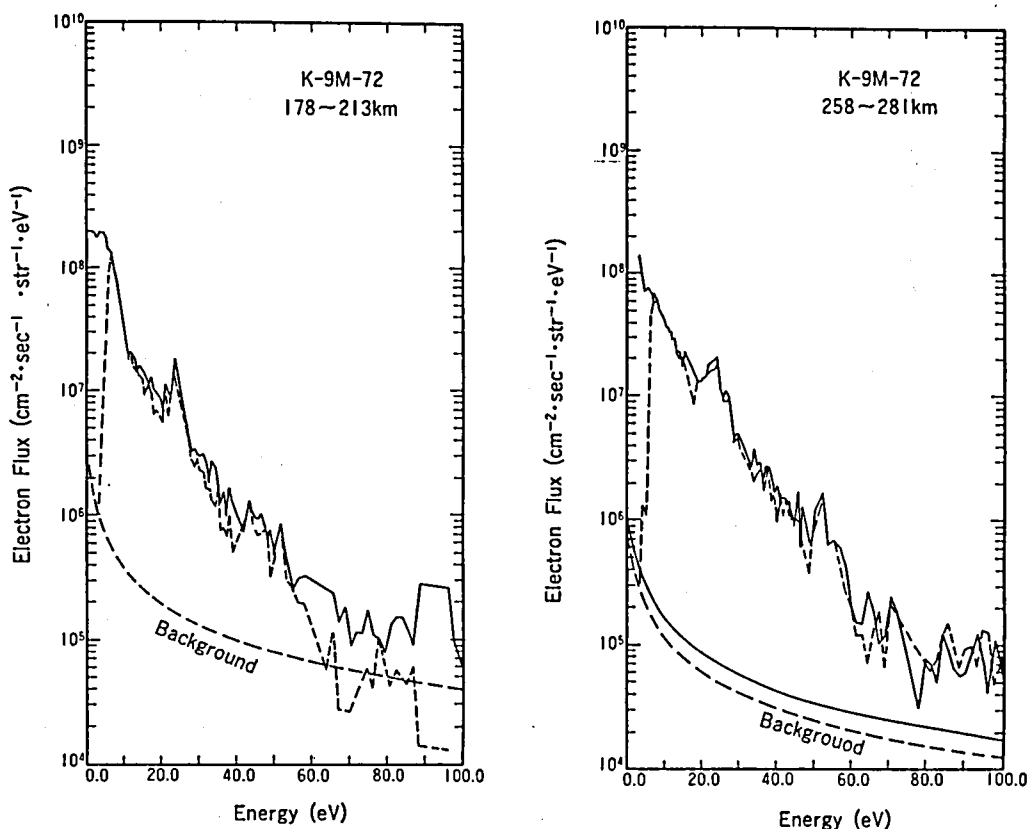
Fig. 4.15 Comparison between the photoelectron energy spectra obtained with different mesh potentials ($V_M = V_3$ for solid curves, and $V_M = V_o - 5$ for dashed curves) at three representative altitudes. (see also next page)

minimum.   Figure 4.15 shows examples of the data comparison at various altitudes.   The solid curves correspond to the case $V_M = V_3$, where V_M is the mesh potential and V_3 is the potential of the inlet and exit slit of the analyzer which is equal to that of the third electrode of the collimator, respectively.   The dashed curves correspond to the case $V_M = V_O - 5$ volt, where V_O is the potential applied to the outer spherical plate of the analyzer. The background fluxes are also shown in each panel.   The observed spectra are quite consistent with the previous results.   There can be also found a very good agreement between the energy spectra obtained with the different mesh potentials, except for the lowest energy range where the retarding potential applied to the mesh could suppress the electrons to be detected. This result indicates a negligible effect of the mesh potential as well as the capability of suppressing unwanted electrons, as expected from the pre-flight experiment.
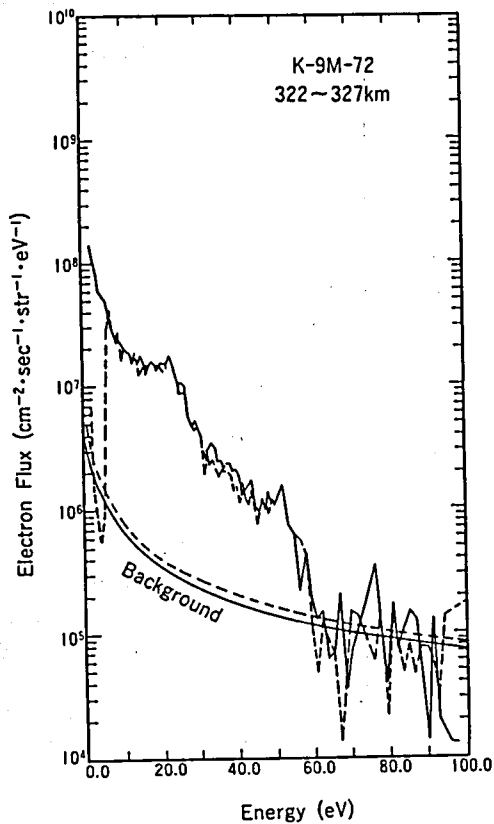
Figure 4.16 shows the result of another experimental purpose which compares the energy spectra obtained by our electron spectrometer (LE sensor) with those obtained by a quadrispherical electrostatic

Fig. 4.15 (continued)
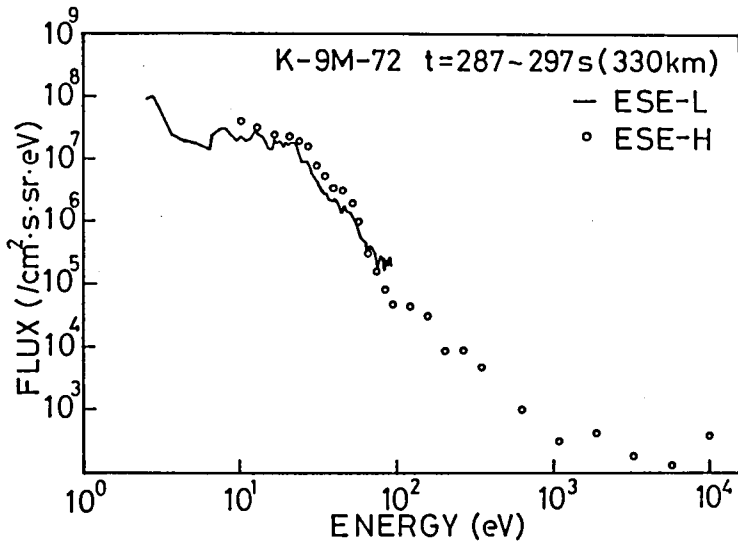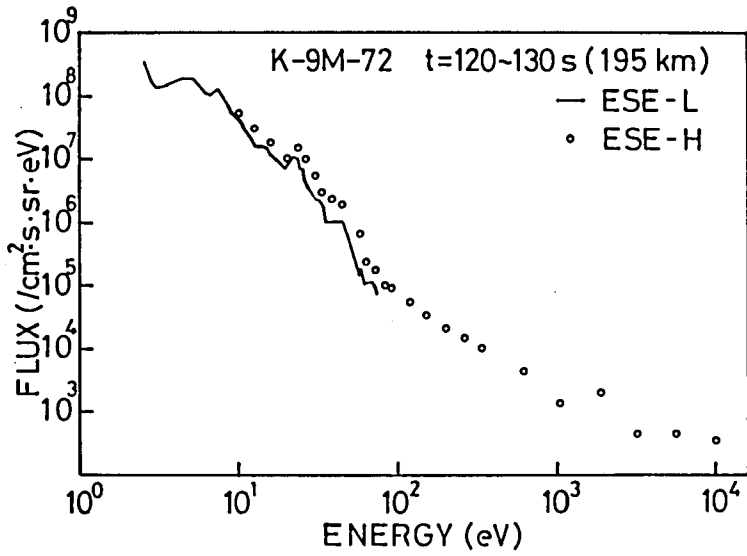
Fig. 4.16 Comparison of the LE spectrum with the HE spectrum.

analyzer (HE sensor).   The HE sensor in this experiment measured

energy spectra of the electron flux in an energy range from 10 eV

to 10 keV in three pitch angles.   The data shown in Fig. 4.16

were obtained in the same view direction as that of the LE

sensor.   There can be seen a fairly good agreement between both

spectra in the overlapped energy range from 10 to 90 eV, although

the LE data reveal somewhat finer spectrum reasonably.   This

result indicates reliability of the energy spectra obtained by

both sensors.

3.2 Calculation of the Photoelectron Flux and Comparison

     with the Experimental Result

The experimental energy spectra of the photoelectron flux in

the ionosphere have been presented so far and discussed in

comparison with those calculated theoretically by other research-

ers.   The observed features have been qualitatively consistent

with theory, but the absolute flux of photoelectrons shows some

discrepancy between the observation and the theory (see Fig.

4.12(b)), which might arise from a difference of the geophysical

condition between both spectra, and from inaccuracies in the

experimental spectra and also in the input data used for calcu-

lation; the solar EUV flux and the cross sections of various

elementary processes.

In this section we calculate the photoelectron energy spectra

under the same geophysical condition as that of the K-9M-47

observation, in which the energy spectra of the photoelectron flux

were observed completely.   Then we discuss the reliability of our

observations and also various characteristic features seen in the energy spectra by a comparison between both spectra.

3.2.1 Method of Calculation

We use the discrete energy-loss procedure under the assumption of local production and loss, and more practically, follow the method developed by Ogawa [1971]. This method seems to be valid under the observational conditions of altitudes and energy range; see Section 2.1.1 in Chapter I. The energy distribution f(E) in a steady state can be expressed [Takayanagi and Itikawa, 1970] as

$$f(E) = (\int_{E}^{\infty} f(E')P(E',E)dE' + q(E)) \Big/ \int_{0}^{E} P(E,E')dE', \qquad (4.2)$$

where P(E,E')dE' is the probability for an electron with the energy E to suffer a collision within a unit time interval where its energy changes to a new value in the energy range (E', E'+dE'), and q(E) is the source function which consists of the production of primary photoelectrons in the ionization of atmospheric constituents by the solar EUV radiation and the production of secondary electrons in the collisional ionization by primary photoelectrons. In practice, we put the upper-most energy of 100 eV for calculation of f(E) and divide the energy range of 0-100 eV into 100 energy bins by a 1-eV step. The calculation at each altitude is started from the highest energy bin, where the numerator in Eq. (4.2) could be contributed only by the production of primary photoelectrons. Then the distribution in the lower-energy bin could be calculated successively. The

result obtained by Eq. (4.2) is not the electron flux, but it is
the distribution in unit of els./cm^3 eV. Therefore we convert
it into the electron flux under the isotropic assumption.

The probability $P(E,E')dE'$ is the composite of those for
various elementary processes and can be expressed by

$$P(E,E')dE' = \sum_i \sum_\alpha \sigma_\alpha \, n(i,z) \, v_e \, , \qquad (4.3)$$

where σ_α is the cross section of an elementary process α, $n(i,z)$
is the number density of an atmospheric constituent i at an
altitude z, and v_e is the electron velocity at an energy E. The
data sources of cross sections will be presented in the following
subsection, but it should be noted here that we adopted the
stopping cross sections themselves for elastic collisions and
also vibrational excitations of molecules, assuming that the mean
energy loss per collision is equal to the energy bin of calculation
which is 1 eV.

The production rate, q, of primary photoelectrons due to the
photoionization of atmospheric constituents by the solar EUV
radiation can be given [Tohmatsu et al., 1965] by

$$q(i,j,\lambda,z,\chi) = \sigma_{ion}(i,\lambda) \, R_{ij} \, n(i,z) \, F_o(\lambda) \, \exp[-\tau(\lambda,z,\chi)], \quad (4.4)$$

where $\sigma_{ion}(i,\lambda)$ is the ionization cross section of an atmospheric
constituent i due to the EUV radiation with a wavelength λ, P_{ij}
is the branching ratio of the ionized state j in the photoioni-
zation, $F_o(\lambda)$ is the solar EUV spectrum at the top of the
atmosphere, and τ is the optical depth. The energy of the
produced photoelectron is given by

$$E_{prim} = hc/\lambda - I_{ij} \, ,\qquad\qquad\qquad (4.5)$$

where hc/λ gives the photon energy (h:Planck constant and c:light speed) and I_{ij} is the ionization potential of the ionized state j of a neutral particle i, respectively.   The optical depth is given by

$$\tau = \sum_{i} \sigma_{abs}(i,\lambda) \int_{z}^{\infty} n(i,z)ds \, ,\qquad\qquad (4.6)$$

where σ_{abs} is the absorption cross section of the EUV radiation with a wavelength λ by an atmospheric constituent i.   It should be noted that integration in Eq. (4.6) is carried out along the path line from the point z toward the solar direction, and hence that τ is a function of the solar zenith angle.

Finally, the density $[e_{th,k}]$ of thermal electrons in the energy bin k is given [Myers et al., 1975] by

$$[e_{th,k}] = \left(\alpha(y_k) - \alpha(y_{k-1})\right) N_e,\qquad\qquad (4.7)$$
where
$$\alpha(x) = erf(\sqrt{x}) - \frac{2}{\sqrt{\pi}} \sqrt{x} \, e^{-x},\qquad\qquad (4.8)$$

erf(z) is the error function, $y_k = W_k/\kappa T_e$ where W_k is the upper edge energy of the bin k, κ is the Boltzmann constant, T_e is the electron temperature, and N_e is the electron density.   The final energy distribution of electrons is given by adding of the distribution given by Eq.(4.7) to that given by Eq.(4.2).

3.2.2 Data Sources

(a) Geophysical parameters and data

The observation in the flight of the K-9M-47 rocket was carried out under the goephysical condition shown in Table 4.1. The atmospheric model was taken from Jacchia [1971] with the exospheric temperature of $900^{O}K$, which is deduced from the geophysical conditions as $\bar{F}_{10.7} = 90.9$, $F_{10.7}$(previous day) = 100.0, the local time 1100, and $K_p = 3_{-}$. The electron density and temperature are adopted from the measured values given by Watanabe [private communication] and by Oyama [private communication], respectively.

(b) $F_o(\lambda)$

The values of unattenuated solar EUV fluxes is taken from Hinteregger [1970] by using the factor FACT expressed as

$$FACT = (F_{10.7,obs.}/144 - 1) \times 0.75 + 1. \qquad (4.9)$$

The values in Table II in his paper are also normalized to those for the same condition of $F_{10.7} = 144$ as for the other tables by using Eq. (4.9). The wavelength range from 1027 to 40 $\overset{o}{A}$ is divided into 72 intervals.

(c) Cross sections

The data sources for the cross sections of various elementary processes are given in Table 4.4.

Table 4.4   Data sources of the cross sections of
various elementary processes

photo absorption photo ionization branching ratio		Stolarski and Johnson [1972]
electric excitation		Green and Stolarski [1972]
Ionization energy distribution of secondary electrons	N_2 O_2	Green and Sawada [1972]
	O	Peterson et al. [1969]
Vivrational excitation	N_2	Fig. 9 of Takayanagi and Itikawa [1970]
elastic collisions with neutrals	N_2	Engelhardt et al. [1964]
$S = \dfrac{2me}{M} \cdot E \cdot \sigma_m$ $\sigma_m = 10^{-15} cm^2$	O O_2	Sunshine et al. [1967]
elastic collisions with thermal electrons		Swartz et al. [1971]

3.2.3   Result and Discussion

The calculated energy spectra of the photoelectron fluxes at
two different altitudes are compared with the measured spectra in
Fig. 4.17, in which the calculated production spectra of primary
photoelectrons are also shown for comparison with the steady-state
spectra.   It should be noted that the fluctuation in the measured
flux below 10^6-level at a lower altitude might arise from the
worse statistics of counting in fewer averaging of energy scans
than at a higher altitude.   The general result is in better
agreement between the calculated and measured spectra than in
Fig. 4.12.   This implies a high reliability of the photoelectron
flux measured by us, and that a larger discrepancy seen at a
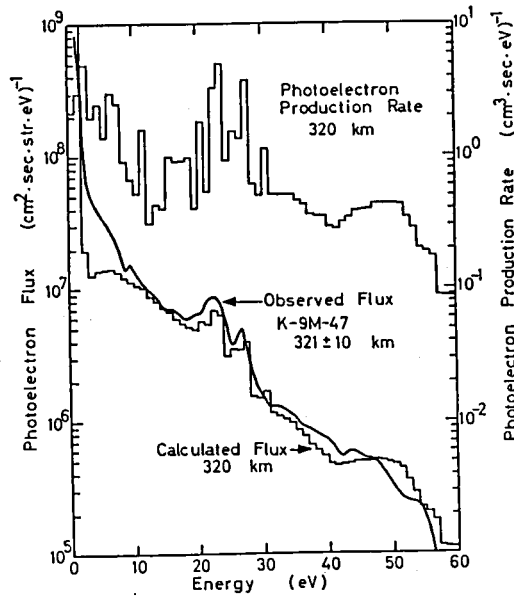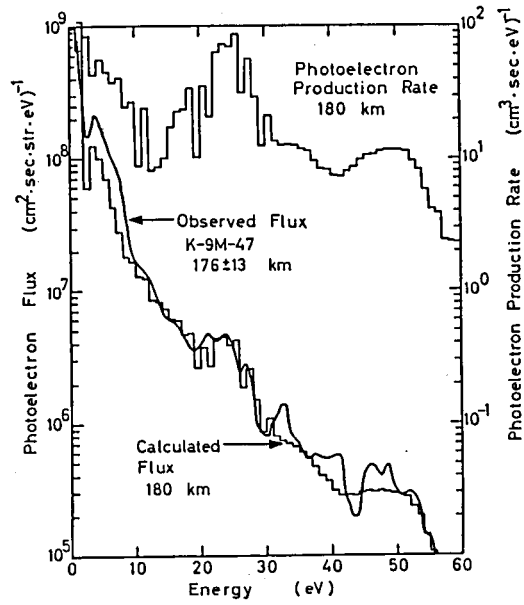
Fig. 4.17 Calculated and Measured energy spectra of the photoelectron
fluxes for altitudes of 180 km (upper panel) and 320 km (lower
panel). The production spectra of primary photoelectrons are
also shown for comparison with the steady-state spectra.

lower altitude in Fig. 4.12 might be attributed to the difference
of the geophysical conditions between the calculation and the
observation, and/or to the difference between the input data
adopted in the present calculation and those by Mantas and
Bowhill [1975].   There can be seen still some discrepancy below
about 10 eV between the calculated and measured flux in Fig. 4.17.
A good agreement in higher energies may exclude a possibility of
errors in the atmospheric model and also the solar EUV photon
flux for the discrepancy, although several investigators [e.g.,
Swartz and Nisbet, 1973; Roble and Dickinson, 1973; Cicerone et
al., 1973] have argued that the Hinteregger values of the solar
EUV flux should be doubled.   We consider that the discrepancy
may arise from possible errors in the cross sections and/or in
the measurement.   The high electric potential of the collimator
inlet account only qualitatively for the higher value of the
measured flux.

     There are several prominent features in the energy spectra
of the photoelectron flux.   The characteristics of these features
can be divided into two categories; production and energy-loss
features.   At first we discuss the energy-loss features.   The
existence of a dip at an energy of 2 ∿ 3 eV is the well-known
feature which arises from the resonant vibrational excitation of
molecular nitrogen, as already discussed in the preceding subsec-
tion.   The shoulders (i.e., relatively steep declines) at 6 and
13 eV in a lower altitude, which have also been discussed in
conjunction with the K-9M-40 experiment (see Fig. 4.2), correspond
to discontinuities in the energy-loss function due to the neutral
particles.   These features are more evident at lower altitudes,
where the photoelectrons lose their energies mainly by the

inelastic collisions with the neutral species. At higher

altitudes, the energy spectrum becomes rather smooth and flat

because of the main contribution of the elastic collision with

ambient electrons.

One of the prominent features found in the production

spectrum of primary photoelectrons is the existence of several

peaks in an energy range from 20 to 30 eV, which arise from the

photoionization yield of O and N_2 by the He II solar line at 304

Å. The remnants of these peaks can be found in both the calcu-

lated steady-state spectra and the measured energy spectra,

although the features have become smeared. The identification

of these peaks corresponding to the electronic states of O^+ and

N_2^+ has already been made in Section 3.3.1; see Fig. 4.3 and

Table 4.3. It should be noted here again that the energy

spectra measured by the K-9M-47 experiment were obtained with the

low energy resolution, that the calculation was carried out with

a 1-eV step consistent with the observation, and that the high-

resolution spectra measured by both the K-9M-40 and K-9M-45

experiment have shown the peaks more clearly; see Figs. 4.3 and

4.6.

The steady-state spectrum above 40 eV is quite similar to

the production spectrum of primary photoelectrons; i.e., a ledge

from 40 to 50 eV and a cut-off from 50 to 60 eV. This ledge

arises from the photoionization of O and N_2 by the solar photon

flux in a wavelength range from 200 to 150 Å. The cut-off of

the photoelectron flux above 55 eV also corresponds to the lack

of the solar photon flux below about 150 Å.

Generally, the characteristics seen in higher energies are

related with the production of primary photoelectrons, while

those seen in lower energies can be determined by the energy-loss
processes.   The boundary energy between both characteristics
seems to lie at around 20 eV.

§4. Observations of Conjugate Photoelectrons in the Predawn
     Ionosphere

4.1 K-9M-54 Experiment

4.1.1 Results

    In this experiment the collimator orientation was upward 30°
relative to the rocket axis.   There arised, however, no problem
in deducing the photoelectron flux from the raw data, except for
the correction of the rocket potential.   Although the lower
energy flux (thermal electron) measurements were utilized to
obtain the rocket potential in the previous experiments (see
Section 4.2 in Chapter III), in the present experiment, this
method could not be used owing to the unexpectedly large fluctua-
tion of the rocket potential during the flight.   The fluxes
observed show a peak in the energy range of 20 to 30 eV and a
rapid fall-off around 60 eV, corresponding to those which also
appear in the daytime photoelectron fluxes.   Under the assumption
of those correspondences, the energy axis of the electron spectrum
has been determined.   This assumption is equivalent to the
neglect of the energy shift of the 20-30 eV peaks which may have
occurred during the energy loss of electrons in the atmosphere.
The rocket potential relative to the ambient plasma potential
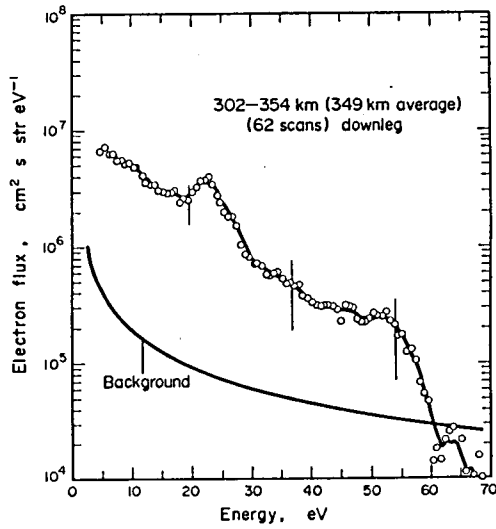
Fig. 4.18 Observed energy spectrum near the apogee. The bars in the
figure represent ±1 standard deviation in electron flux.
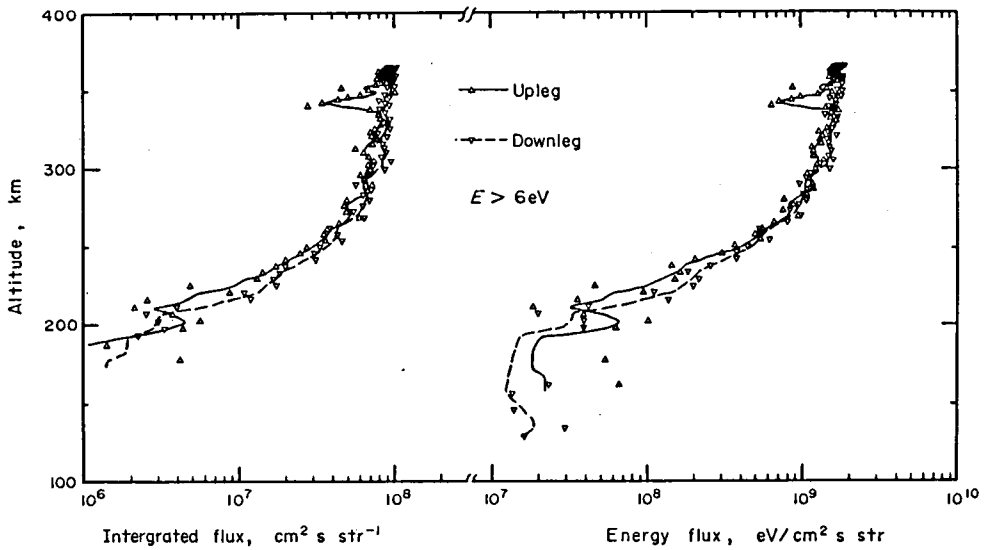
Fig. 4.19 Altitude profiles of the observed integrated flux and
energy flux.

(i.e., the opposite of the energy corrected by this method) was
-2.2 $\sim$ -5.4 volt which changed with time and height.   In the
downleg it is -2.2 volt irrespective of altitudes in accordance
with the result of the Langmuir probe which was also flown simul-
taneously [Oyama, private communication].   Since the data below
5 eV have shown irregular variations due to the change of the
rocket potential, this section will present photoelectron data in
the energy range of 6 to 70 eV.   As an example, the average flux
of 62 scans near the apogee obtained in this way is shown in Fig.
4.18.   The bars in the figure indicate the standard deviation of
the data.   The counts at zero electrode potential, which arise
from cosmic ray and stray electrons, are represented as background
flux.   The flux at each energy in the figure has been obtained by
subtracting the background from the total counts at that energy.
It is noted that at 60 eV the background flux becomes comparable
to the photoelectron flux.   Subtraction of the background from
total counts will thus cause large errors at higher energies.

The observed altitude profiles of the integrated flux above 6
eV ($\int_{6\ eV} f(E)dE$) and energy flux ($\int_{6\ eV} E \cdot f(E)dE$) are shown in
Fig. 4.19.   Below 200 km, fluxes are lower than detectable values
and rapidly increase at 220-280 km reaching almost constant values
(10^8 $cm^{-2}s^{-1}str^{-1}$) above 300 km.   The minimum around 340 km at
upleg seems to arise from the change of the potential of the
rocket body to large negative values.   This profile is quite
different from the daytime observational results which show the
maximum of the flux at 180-220 km.   This profile, together with
the condition of the solar zenith angle, seems to indicate that
electrons were not produced locally but transported from above
the apogee, probably from the conjugate sunlit ionosphere.

Pitch angle distribution (PAD) has been obtained near the apogee (Fig. 4.18) for the electrons with energies of 6-55 eV and is shown in Fig. 4.20. The PAD is normalized by the electron flux with the pitch angle of 20-30 degrees. The flux is nearly isotropic in the downward hemisphere, decreasing gradually with pitch angle. This is easily explained considering that the energy loss rate of an electron transported through the plasmasphere increases with the path length which is proportional to sec α, where α is the pitch angle of the electron. The PAD is considered to become more isotropic at the lower altitudes where collision frequency is enhanced, though it is difficult to obtain PAD below 300 km accurately since the electron flux varied rapidly below that altitude.

Energy distributions of the fluxes observed at different altitudes are shown in Figs. 4.21 and 4.22 for the upleg and downleg, respectively. Each spectrum is the average of the fluxes obtained within the altitude interval of 30-40 km. Photoelectron flux observed in the daytime (at a solar zenith angle of 34°) at 321 km is also depicted in Fig. 4.22 as a reference. It is larger by about a factor of 2 than that obtained at the apogee under the predawn condition.

The fluxes at the energies of 15 and 30 eV are 3×10^6 and 1×10^6 $(cm^2 \ s \ str \ eV)^{-1}$ respectively at the apogee and decrease at lower altitudes. Our observed values at 250 km (curve B in Figs. 4.21 and 4.22) can be compared with the satellite observation of the conjugate photoelectron fluxes by Peterson et al. [1977] at about the same altitude and solar zenith angles, though the conjugate solar zenith angles are somewhat smaller for their observations (73°- 93°). The absolute values of the two measure-
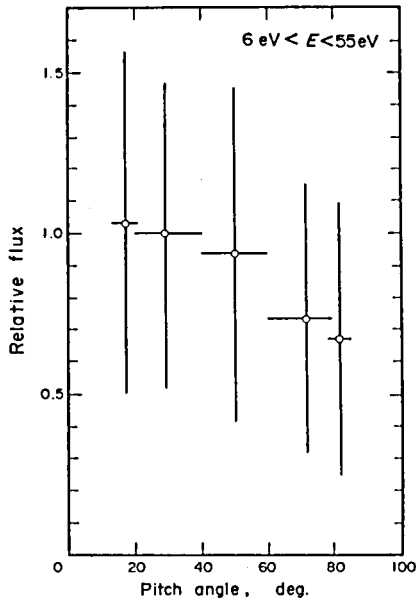
Fig. 4.20

Observed pitch angle distribution for electrons with energies of 6-55 eV at the apogee. Error bars represent ±1 standard deviation in the average.
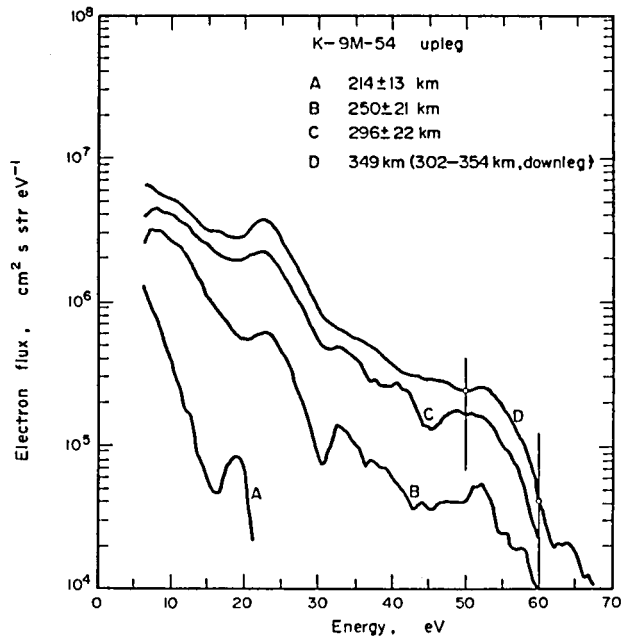
Fig. 4.21 Observed energy spectra of electron fluxes during upleg at various altitudes. The bars in the figure represent ±1 standard deviation at 50 and 60 eV.
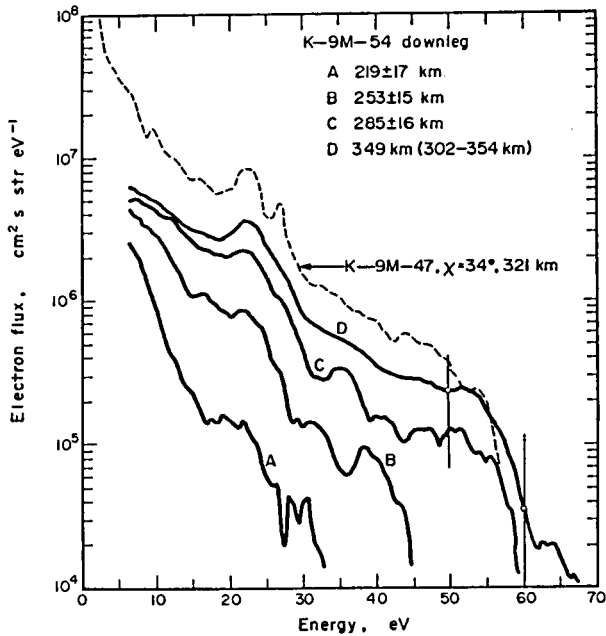
Fig. 4.22 Observed energy spectra of electron fluxes during downleg.
Dashed line represents the observed daytime electron flux at
a solar zenith angle of 34° and at a height of 341 km.
The bars are the same as in Fig. 4.21.

ments are in good agreement especially above 15 eV; both photo-
electron fluxes are about 1×10^6 and 1×10^5 $(cm^2 \ s \ str \ eV)^{-1}$ at
15 and 30 eV respectively.   Below 15 eV our measured values
become slightly larger.

In addition it is noted that the theoretical estimate of the
630 nm airglow emission, using the observed photoelectron fluxes,
is also in fairly good agreement with the simultaneously observed
630 nm airglow intensity.   Details of the results of the airglow
observation are referred to Shepherd et al. [1977].

As mentioned earlier, there appears a rapid fall-off of the
flux at energies of 55-60 eV caused by the rapid decrease of the
production rate of primary photoelectrons at these energies
[Tohmatsu et al., 1965].   The structure at 20-30 eV is obscure

compared to that observed in the daytime around 200 km when they were split into a few peaks. The peak is produced by the ionization of O and N_2 by He II 304 $\overset{o}{A}$ radiation. The above mentioned observation by Peterson et al. [1977] of the fluxes at 250-260 km show no such structure. They speculate that the peak is smoothed by Coulomb scattering in the plasmasphere. The invariant latitudes for their observation were larger than 30°, whereas it is lower (20°) in this case. Reduced frequencies of the Coulomb scattering in the plasmasphere owing to the less total plasma contents along magnetic tubes may explain the apparent discrepancy.

4.1.2   Calculation of the Photoelectron Flux and the
        Comparison with the Measurement

A lot of calculations for the daytime ionospheric photo-electrons have been carried out and compared with those measured. The uncertainties of the solar EUV flux data associated with these calculations can be excluded under the predawn condition when the local photoelectron production is negligibly small. So it is of interest to calculate the vertical profile of the impinging photoelectron flux and compare it with the observed one as it serves to check the theory concerning the collision processes in the upper atmosphere. The steps of the calculation are as follows. Firstly the measured flux near the apogee (350 km) is adopted as an initial flux f_∞ whose pitch angle distribution is assumed to be isotropic in the downward hemisphere in accordance with the observation.

Secondly the differential fluxes $f_i(Z)$ of electrons with
pitch angle α_i (α_i = 15, 30, 45, 60, and 75 degs.) are calculated
from f_∞ by using a continuous slowing-down approximation.
Details of the method of the calculation are referred to Kondo
and Ogawa [1976].   The pitch angle α_i is assumed to be constant
from the apogee to lower altitudes; i.e. the change of the pitch
angle which may occur both in elastic and inelastic collisions is
not included in the calculation.   Intervals of height and energy
in the calculation are 0.5 km and 1 eV, respectively.   The
densities of O, O_2, and N_2 have been taken from Jacchia [1971]
model for the exospheric temperature 680^OK which coincides with
the temperature at the time of the observation.   It has easily
been found in the course of calculation that the electron fluxes
at lower altitude can be determined by only the energy-loss
processes, as pointed out by Nagy et al. [1973].   Therefore the
production of electrons by secondary ionization of electrons with
energies higher than the ionization potentials of atmospheric
molecules is completely neglected in this case.   The electron
mostly loses its energy through the collisions with atomic oxygen
in the altitude region concerned.

Finally, $f_i(Z)$ calculated are summed by weighting with the
geometric factor sin α_i for comparison with the observation;
i.e.,

$$f(Z) = \Sigma \ f_i(Z) \cdot \sin\alpha_i \ / \ \Sigma \ \sin\alpha_i \ , \tag{4.10}$$
$$\alpha_i = 15, \ 30, \ 45, \ 60, \ \text{and} \ 75 \ \text{degs.}$$

$f(Z)$ thus obtained at 285, 250 and 220 km are shown in Fig. 4.23
together with the observed values at the downleg of the K-9M-54
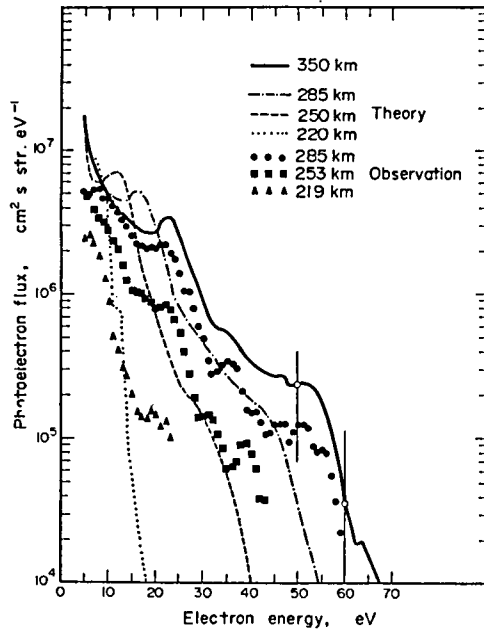
Fig. 4.23 Comparison of the calculated fluxes with the observation at
various altitudes. Circles, squares, and triangles show
the observed values at 285, 253 and 219 km respectively.
The bars are the same at Fig. 4.21.

rocket. Small ripples which appear in calculated f(Z) profiles

have been smoothed, since they are considered to disappear as the

number of $f_i(Z)$ is increased; i.e. as angular increments become

smaller. It is seen that f(Z) roughly coincides with the measure-

ments at all altitudes.   However it is also noticed that the

calculation always under-estimates the fluxes in the higher energy

region where they become smaller than 10^5 $(cm^2$ s str eV$)^{-1}$ and

theoretical values exceed, by a factor of 2 or 3, those measured

at the lower energy region where fluxes are larger than 10^6.   In

considering the reason for these disagreements it should be noted

first that the initial flux at the apogee has been obtained from

measurements and may contain experimental errors.   It is expected

from Fig. 4.23 that if a larger flux above about 55 eV is assumed

for the initial flux, the theory will satisfactorily predict the measured values at the lower altitudes at higher energy. As background counts, which have been subtracted from total counts, become relatively larger above 55 eV, experimental accuracy is reduced there. The standard deviations of the measured fluxes at 50 and 60 eV at the apogee are shown in Figs. 4.21 $\sim$ 4.23.

On the other hand experimental errors due to the background counts are reduced at lower energies. The electric field between the ambient plasma and the rocket body would affect the trajectories of electrons entering the sensor and therefore would vary the angular response that resulted in the change of the conversion factor. This effect is roughly estimated as $F'/F \simeq E/(E+eV)$, where E is the electron energy in the ambient plasma, e is the electronic charge, V is the rocket potential relative to the plasma, F is the flux in the undisturbed (i.e. field-free) condition and F' is the flux obtained by using the conversion factor which would be modified by the electric field, respectively; e.g. $F'/F \simeq 1.3$ at V = -2.2 volt and E = 10 eV. This effect thus cannot account for the discrepancy. The discrepancy at lower energies may be interpreted through the energy loss of the electron in the theory being too small at the lower energy region of about 10 to 15 eV. The collisions which contribute to the energy loss in this energy region is the excitation of atomic oxygen from ^3P to $^3S^0$ and $^5S^0$. In this calculation the experimental data by Stone and Zipf [1974] have been adopted. Larger values of these cross-sections may account for the discrepancy.

4.2 K-9M-76 Experiment

This experiment was carried out under the predawn condition similar to the previous K-9M-54 experiment, but with slightly larger solar-zenith angles, so that the local production of photoelectrons might be neglected more definitely. The measured energy range in this experiment was extended to higher energies; from 1 to 90 eV, since there had been some concern about the significant electron fluxes above 70 eV (i.e., upper-most measured energy in the previous K-9M-54 experiment) from the comparison between the observation and the calculation. Since there was no irregular change of the rocket potential in this experiment, we could use the data-reduction procedure established in the K-9M-47 experiment.
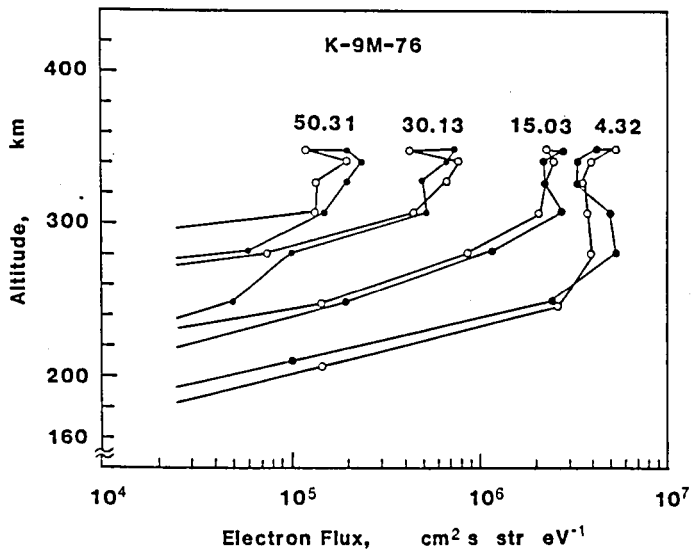
Fig. 4.24 Altitude profiles of the electron fluxes at four selected energies observed by the K-9M-76 experiment. Open and solid circles show the upleg data and the downleg data, respectively.

Figure 4.24 shows the altitude profiles of the observed electron fluxes at four selected energies. The general tendency is quite similar to that seen in Fig. 4.19, but in addition, Figure 4.24 shows the energy dependence clearly. At higher energies, the electron flux increased with height and the downleg data showed slightly higher fluxes than the upleg data, which is consistent with the variation of the solar zenith angle during the rocket flight. At lower energies, on the other hand, the electron fluxes were nearly constant above the altitude depending on the electron energy; 300 km at 15 eV and 280 km at 4.3 eV. The electron flux at 4.3 eV seemed to have a hump at an altitude of around 280 km. This tendency in the lower-energy electron flux may be exlained by the contribution due to the degraded electrons and also the secondary electrons produced through the precipitation of higher-energy electrons.

The observed energy spectra of the electron fluxes at various altitudes are shown in Fig. 4.25, where the upleg and downleg data are presented separately. It should be noted that the present data show the energy spectra in the complete energy range from 1 to 90 eV, compared to the energy range of 6 to 70 eV in the previous K-9M-54 rocket. The spectral features observed in the present experiment are quite similar to those seen in the previous one; compare Fig. 4.25 with Figs. 4.21 and 4.22. However, the structure in an energy range of 20 to 30 eV becomes much more smeared out, which is consistent with the satellite observation by Peterson et al. [1977]. This may imply a slight contamination of local photoelectrons in the previous K-9M-54 experiment. With respect to the previous discussion on the discrepancy between the calculation and the observation (see Fig.
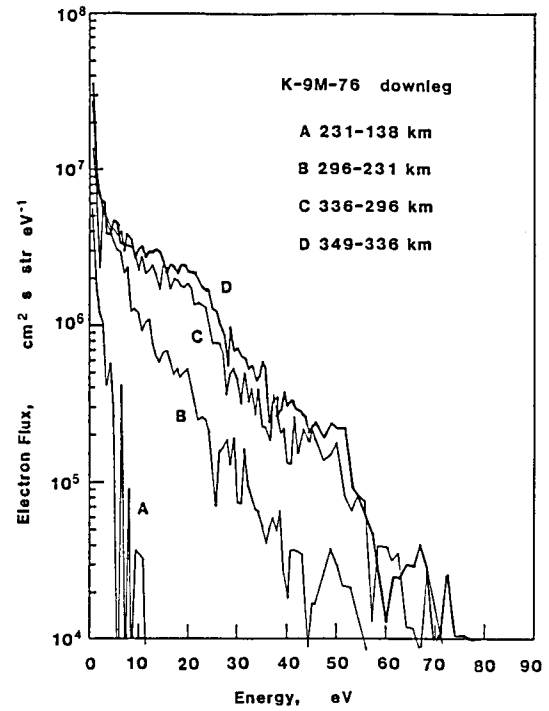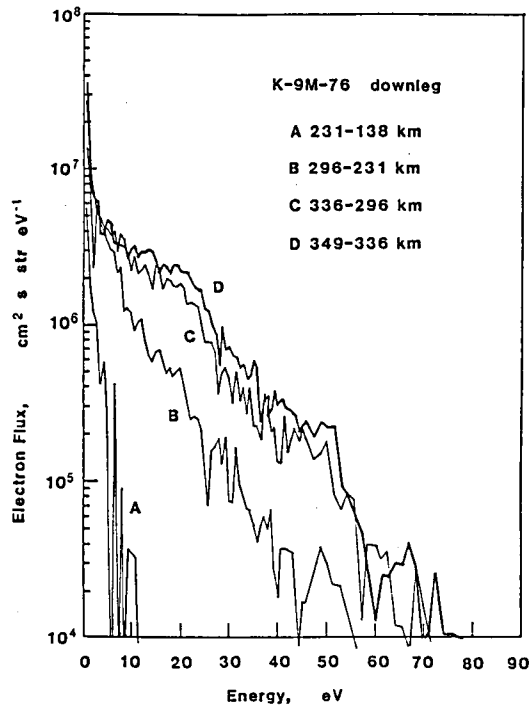
Fig. 4.25 Observed energy spectra of the electron fluxes at various altitudes
during the upleg and the downleg of the rocket flight.

4.23), there were no significant electron fluxes above 60 eV.
The spectral feature above 50 eV in the present experiment is
quite similar to that found in the previous K-9M-54 experiment,
and also consistent with the spectra observed in the daytime,
although bad statistics in this energy range cannot be denied.
The general agreement between the present result and the previous
K-9M-54 one indicates a high reliability of the data in spite of
the large fluctuation of the rocket potential in the previous
experiment.

§5. Concluding Remarks

In this chapter we have presented and discussed the charac-
teristics of the photoelectron flux in the ionosphere observed by
means of the electron spectrometers on the sounding rockets.
Various prominent features in the energy spectrum of the photo-
electron flux, which are consistent with theory, have been
revealed in the daytime observations, which indicate high-
resolution capability and high reliability of our electron
spectrometer.

The K-9M-40 experiment first revealed a prominent fine
structure of the daytime photoelectron spectrum in the energy
range of 20 to 30 eV, which had not been reported in the earlier
rocket observations by others.   Several peaks observed were
identified to correspond to the ground and excited states of
N_2^+ and O^+ produced in the photo-ionization by the solar 304 $\overset{\circ}{A}$
photon flux.   This result was confirmed and refined by the
followed experiments on the K-9M-45 and K-9M-47 rockets.   The

K-9M-47 observation provided us with complete energy spectra, including additionally a dip at around 2.5 eV and also a steep decline (cut-off of the photoelectron flux) at 50 $\sim$ 60 eV. The K-9M-47 observation also revealed a nearly isotropic distribution of the photoelectron flux and also an altitude profile which showed a maximum of the photoelectron flux at altitudes of 180 $\sim$ 220 km. The observed results were discussed in terms of the comparison with the calculated spectra. It was found that the characteristics seen in higher energies are related with the production of primary photoelectrons, while those seen in lower energies are with the energy-loss processes. The peculiar features summarized above become obscure at higher altitudes ($\geq$ 300 km) owing to the elastic collision with ambient electrons.

The predawn experiments, K-9M-54 and K-9M-76, showed the characteristics of the conjugate photoelectrons which were different from those of the daytime photoelectrons. The energy spectra of the photoelectron flux observed at the apogee ($\sim$350 km) were similar to those of the daytime photoelectron flux at altitudes above 300 km, but the peculiar features were more obscure, probably due to Coulomb scattering in the plasmasphere during the transportation from the conjugate-point ionoshere. The altitude profile of the photoelectron flux, which was quite different from that of the daytime flux, revealed the degradation process of the precipitating low-energy electrons.

Although the observed results are quite reasonable, our experiment may include some problems in measuring very low energy electrons to be overcome in the future. One is the not-yet-clear conclusion of the difference of the 2.5-eV dip between the observation and theory. The other is the discrepancy in the transition

spectrum from thermal to suprathermal energy between the spectro-meter and the Langmuir-probe data.   The design principle of our electron spectrometer will be useful in resolving such problems: The geometric factor and the energy resolution must be re-designed to have suitable values for measuring the high flux of very low energy electrons.   Most important is the on-board correction of the rocket potential.   The electric potential of the material around the collimator inlet should be kept at the same potential as that of the collimator inlet.

Chapter V   Satellite Observations of Low-Energy Electrons in the
            Ionosphere and Magnetosphere

§1. Introduction

     In this chapter we are concerned with the application of our
spectrometer to the satellite observations of low-energy charged-
particles, mainly electrons, in the ionosphere and magnetosphere.
Included in this chapter are observations of auroral electrons by
KYOKKO satellite (Section 2), of wave-particle interactions around
the plasmapause by JIKIKEN satellite (Section 3), and of auroral
particles and ionospheric photoelectrons by OHZORA satellite
(Section 4).   It has been well recognized that these observations
are essential for the understanding of the ionospheric and magneto-
spheric physics.   Most of the data obtained by the above satel-
lites are generally consistent with those obtained previously by
other researchers, but they have led us to more detailed studies
and also new findings of some peculiar phenomena.   For example,
the KYOKKO observation has revealed detailed characteristics of
the inverted-V precipitation as well as an existence of localized
intense fluxes of upgoing electrons which may suggest the upward
acceleration of electrons below a few thousands of km.   The
JIKIKEN observation has found out a strong pitch angle anisotropy
(pancake distribution) of low energy electrons which may amplify
VLF signals transmitted from the Siple station.   The OHZORA
observation also has observed some peculiar features in global
distributions of electrons and ions.   The details will be
described in each section.
     The charged-particle detectors on board these satellites were

designed to have basically the same configuration as the rocket-borne electron spectrometers; each of them consisted basically of a collimator, a spherical electrostatic analyzer and (a) channel electron multiplier(s).   It should be noted, however, that the satellite-borne instrument must be designed and constructed under much severer constraints.   It must be as light weight, small size and low power-consuming as possible, and meet the compatibility with environmental conditions of vibration, shock and operation temperature in high vacuum.   The energy coverage and the time resolution of the charged-particle observation must meet the scientific objectives under a given restricted PCM telemetry data rate.

§2. Observations of Auroral Electrons by KYOKKO Satellite

KYOKKO (EXOS-A) was launched on February 4, 1978 into a semi-polar orbit with inclination of 65.3° and with the initial apogee and perigee of 3978 km and 641 km respectively.   Because of the orbital property, the high-latitude part of the satellite track grazed nearly constant L-shells, scanning a wide range of magnetic local time (MLT).   In addition the satellite remained in the northern auroral region for a long time (30-40 minutes in the orbital period of 134 minutes), since the apogee latitude was in the northern hemisphere.   The main axis of the satellite was controlled so as to be aligned along the magnetic field line by means of a pair of permanent magnets at the tips of 2-m booms.

2.1 Instrumentation

The electron spectrometer was installed on the satellite to measure simultaneously both upward and downward electron fluxes along the geomagnetic field line in the energy range from several eV to $\sim$ 10 keV. It consisted of two identical sensors (sensor 1 and sensor 2) and common electronics for control and processing of the data. Figure 5.1 shows a schematic drawing of the sensor box, in which some electronic circuitry including the high voltage power supplies was contained. The main part of the sensor, which was surrounded by a high-μ metal in order to shield the sensor from the external magnetic field, was composed of a fan-shaped collimator, an electrostatic energy analyzer and a channel electron multiplier. The energy analyzer was hemispherical with the inner and outer radii of 28 mm and 32 mm, respectively, and has inlet and exit slits of 2 mm $\times$ 4 mm. As shown in Fig. 5.1, a cylindrical trap was placed at the outer hemisphere behind the inlet slit in order to absorb high-energy particles, but did not disturb the electric field in the analyzer. The analyzer was operated by the balanced voltages; i.e., the positive and negative voltages with equal amplitudes were applied to the inner and outer hemispherical plates, respectively. Charged particles entering the analyzer through the collimator are deflected by the electric field, and only those electrons with an appropriate energy can pass through the analyzer and impinge onto the channel electron multiplier. A high voltage of 2.5 $\sim$ 4.0 kV was applied to the output terminal of the channel electron multiplier, while about 10 % of that voltage was applied to the inlet of the multiplier so as to accelerate the electrons entering the multiplier. The level of the high voltage
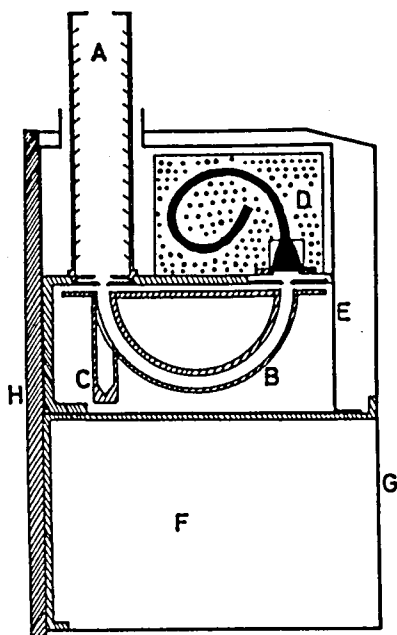
Fig. 5.1 A schematic drawing of the sensor box of the electron
          spectrometer on board the KYOKKO satellite.
          A: collimator
          B: hemispherical electrostatic analyzer
          C: higher-energy particle trap
          D: channel electron multiplier (CEM)
          E: high-permeability metal
          F: electronic circuitry including sweep-voltage power supply
             for the analyzer, high-voltage power supply for CEM,
             charge sensitive amplifier, discriminator and pulse shaper.
          G: case
          H: plate for installation on the spacecraft

was selectable by command in 4 steps with a space of 0.5 kV.

The output charge pulses from the multiplier were converted

by a charge sensitive amplifier into the voltage pulses, which

were then discriminated from noise, shaped and transmitted to the

main electronics-box of the instrument.   The field of view was

about 4° x 14°, and its central direction was parallel to the main

axis of the satellite which was within 10° to the ambient magnetic
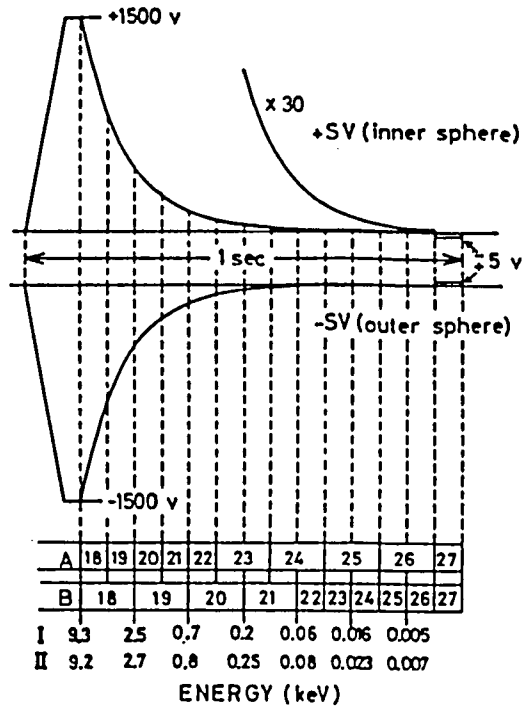
Fig. 5.2 Waveforms of the analyzer voltages and their
relationship with the data sampling. The
correspondence of the count data with the
allocated words in the PCM telemetry are also
shown. Some of the measured energies at the
boundary between the data samplings in sensor-1
and sensor-2 are shown in the bottom rows,
respectively.

field by means of the attitude control system mentioned above.

Since the view directions of two sensors were anti-parallel with

each other, the instrument measured simultaneously both

upward and downward electron fluxes along the magnetic field

line.

The energy scanning was performed by applying the voltages

of exponentially-decaying waveform to the analyzer plates, as

shown in Fig. 5.2. The repetition rate was 1 Hz at high bit

rate or 0.25 Hz at low bit rate. These voltages were swept

simultaneously in both sensors, so that two sensors measured electron fluxes of nearly identical energies simultaneously, as shown in the bottom rows of Fig. 5.2. One cycle of energy scanning takes 1 sec, including the rise time of 125 msec and the time for the reversed polarity of 62.5 msec. When the polarities of the analyzer voltages are reversed, only low energy ions can pass through the analyzer, but they will be reflected by the high electric potential barrier at the entrance of the channel electron multiplier. Thus, the data during that time accounts only for the background. Therefore the effective time for energy scanning is 812.5 msec, in which the output pulses from the sensor are counted continuously every 62.5 msec or 125 msec by a 15-bit counter. These count data are compressed to 8-bit data, stored temporarily in the buffer memory and then transmitted to the ground through the allocated words (sensor-1 data in the even frame number and sensor-2 data in the odd frame number) of the PCM telemetry. The relationship between the compressed data and the original 15-bit data is given by

$$C = 2^{11-S} (D+16), \qquad\qquad (5.1)$$

where C is the original data, and D and S are the decimal values of the upper and lower 4 bits of the compressed data, respectively.

Since we had only 9 words for the effective count data, we prepared two modes for selection of the sampling time; A and B, as shown in Fig. 5.2. The A-mode yielded 4 data in the keV-range, while the B-mode did 4 data below 60 eV, and both modes gave a 9-point energy distribution in the whole energy range. Most measurements in the auroral region were carried out in the A-mode.

The instrumental status and the monitors of the analyzer voltages were also included in the PCM telemetry words.

Characteristics of the sensors which were calibrated in a pre-flight experiment using an electron gun are summarized below.

(a) Relationship of the analyzer voltages with the measured energy:

$$E = e(3.82 \ V_o - 2.82 \ V_i) \quad \text{for sensor - 1,}$$

and $$(5.2)$$

$$E = e(3.76 \ V_o - 2.76 \ V_i) \quad \text{for sensor - 2,}$$

where E is the measured energy in eV, e is the electronic charge ($e = -1.602 \times 10^{-19}$ Coulomb), and V_o and V_i are the voltages applied to the outer and inner hemispherical plates, respectively.

(b) The energy resolution $\Delta E/E$:

$$\Delta E/E = 0.039 \quad \text{for sensor-1,}$$

and $$(5.3)$$

$$\Delta E/E = 0.047 \quad \text{for sensor-2.}$$

(c) The angular acceptance : $4^{\circ} \times 14^{\circ}$

The longer dimension of the field-of-view was 14.1° in both sensors, which was very close to the designed value of 14°. The shorter dimension was a calculated value.

(d) The relative sensitivity between both sensors

The sensitivity of the sensor-2 was unexpectedly worse than that of the sensor-1 especially in low-energy.   The relative

sensitivity was determined experimentally as

$$R = 0.14 \exp(0.021\sqrt{E}),\qquad\qquad\qquad (5.4)$$

where R is the ratio of the sensor-2 sensitivity to that of the sensor-1, and E is the measured energy in eV.

2.2 Method of Data Reduction

The PCM 8-bit data are converted to the original count data, C, by using Eq.(5.1). Then the sensor-2 data are corrected by using Eq. (5.4). As described earlier, it was expected at the design stage of the instrument to obtain the background count from the PCM Word-27 data obtained in the reversed polarity of the analyzer voltages (see Fig. 5.2), but it happened in practice that the background data deduced from Word-27 exceeded sometimes the data of Word-18 ∿ Word-26, especially in the radiation belt. Therefore, the Word-27 data cannot be regarded simply as a background, though they certainly gave a background information, and no background correction is made on the data presented here. However it may yield only a small effect for discussion of the data obtained in the auroral region, where the Word-27 data were usually much less than the data of Word-18 ∿ Word-26. It should be noted here that we have no necessity for correction of the shadowing effect, since the instrument measured only the field-aligned electron fluxes, and that the solar EUV contamination can be easily found by the sun-sensor data and also by anomalous counts, and discarded from the data analysis.

The differential electron flux $f(E)$, els./cm^2 sec sr eV, is deduced from the observed count data C by the relation

$$f(E) = C / (\langle G \cdot \Delta E \rangle \, \eta \, \tau),$$ (5.5)

where $\langle G \cdot \Delta E \rangle$ is an energy-geometric factor of the analyzer, η is a detection efficiency of the channel electron multiplier, and τ is the sampling time, respectively. Since the energy resolution $\Delta E/E$ is constant in an electrostatic analyzer, $\langle G \cdot \Delta E \rangle$ is proportional to the measured energy and may be roughly estimated as

$$\langle G \cdot \Delta E \rangle \simeq G_0 (\Delta E/E) E ,$$ (5.6)

where G_0 is a geometric factor of the collimator. Here we use the calculated value of 1.5×10^{-3} cm^2 sr for G_0, and the experimental value given by Eq.(5.3) for $\Delta E/E$, respectively. It should be noted that as the measured energy was varied considerably in the exponential waveform during the i-th data, we use the mean energy $\bar{E}_i$ which is given by

$$\bar{E}_i = \sqrt{E_i E_{i+1}} ,$$ (5.7)

where E_i is the boundary energy between the (i-1)-th and the i-th data. The boundary energy E_i is obtained by using Eq.(5.2) from the analyzer voltages. The detection efficiency η is assumed to be 0.3 irrespective of energy in the sensor-1, since the electrons entering the channel electron multiplier was accelerated by the inlet voltage of $\sim$ 250 V; see Fig. 1.11.

The total energy flux, which is an important quantity in the

auroral physics, is given by

$$EF = \int_0^{Em} E \cdot f(E) \ dE$$

$$= \sum_i \bar{E}_i \cdot f(\bar{E}_i) \cdot \Delta E_i \ , \tag{5.8}$$

where Em is the upper-most energy of the measurement, and $\Delta E_i = E_{i-1} - E_i$, respectively. If the significant electron flux is observed at the upper-most energy, the evaluation of Eq.(5.8) may be underestimated.

The data studied here were obtained over the northern auroral region at altitudes of 2500-4000 km for 486 passes during the periods of March to April 1978 and of September 1978 to January 1979, where the data of sensor-1 and sensor-2 corresponded to the downward and upward electron fluxes, respectively. We primarily use an energy-time spectrogram with the corresponding energy flux for analysis of the data. An example of the data presentation is given in Fig. 5.3. The data include several typical features of auroral electrons, which will be discussed later. Here, only the explanation of the data format is noted. The upper two and lower two panels show an energy-time spectrogram and the corresponding energy flux of the sensor-2 and sensor-1 data, respectively. In the energy-time spectrogram the ordinate is the electron energy and the abscissa is the universal time, UT. The detector response is represented as intensity, the scale of which is shown in the upper-right corner. The detector response has a physical meaning that the count rate is proportional to the differential energy flux; i.e., the following relation is deduced from Eqs. (5.5) and (5.6), since the energy resolution $\Delta E/E$ is constant.
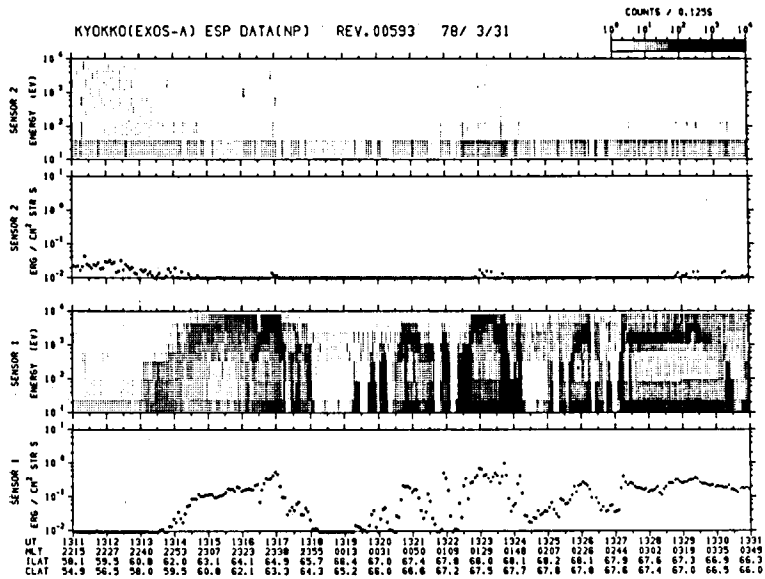
Fig. 5.3 Typical example of the data presentation format,
which comprises the energy-time spectrograms with
the energy fluxes for the sensor-1 (lower two panels)
and sensor-2 (upper two panels), respectively.
The bottom three rows are the dipole magnetic local
time, the invariant latitude and the geomagnetic
latitude at the geomagnetic sub-satellite point.

$$C/\tau = G_0 \; \eta \; (\Delta E/E) \; E \; f(E)$$

$$\propto E \; f(E). \tag{5.9}$$

2.3 General Features of the Precipitation Pattern of Auroral

Electrons ——Local-Time Dependence

A summary of the electron precipitation zone is shown in
Fig. 5.4 which is constructed by overlaying the precipitation
region observed along the orbital track of the satellite. It
should be noted here that the KYOKKO satellite could not attain
an invariant latitude higher than 79°. The observation times

KYOKKO

Spatial Distribution of Electron Precipitation

Kp ≳ 3-   Kp ≲ 2+
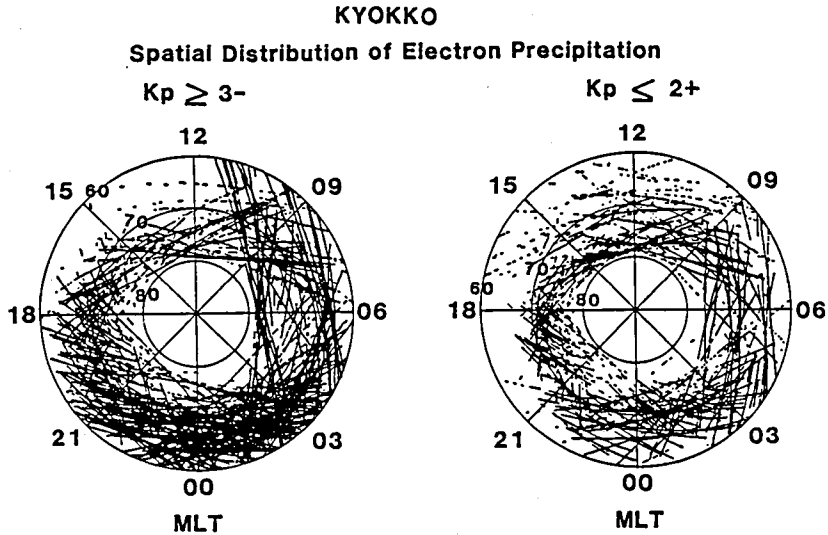
Fig. 5.4 Spatial distribution of precipitating electrons for the
geomagnetic conditions of $K_p \geq 3_-$ and $K_p \leq 2_+$.
Magnetic local time (MLT) and circles of constant
invariant latitude are shown for reference.

for these data are distributed almost equally in magnetic local
time and also in the geomagnetic conditions between $K_p \geq 3_-$ and
$Kp \leq 2_+$.   The precipitation occurs at all local times, but most
frequently on the night side under the disturbed condition.   The
low-latitude boundary tends to be higher under relatively quiet
conditions ($K_p \leq 2_+$) than disturbed conditions ($K_p \geq 3_-$).
Moreover it is highest in the early afternoon hours.

     A general field-line morphology of the magnetosphere indicates
that the high-latitude ionosphere is linked to the various
regions of the distant magnetosphere depending on the local time;
e.g., the night-side auroral region to the plasma sheet, and the
high-latitude part of the dayside region to the cusp.   Various
processes of electron precipitation including acceleration along
the magnetic field line may modify the precipitation pattern

substantially.   Therefore it is interesting to investigate the
local-time dependence of the electron precipitation pattern.

Figure 5.3 (p. 171) shows an example of the data obtained at
Rev. 593, in which the satellite traversed the auroral region in
magnetic local times from 2230 to 0350 MLT; the highest invariant
latitude of 68.2° at 1325 UT (0207 MLT).   This example includes
various typical features observed on the night side.   The
geomagnetic condition during this observation was that the values
of K_p-index and ΣK_p were 2 and 15-, respectively [Solar Geophysi-
cal Data, No. 406].   According to Boulder Geomagnetic Substorm
Log, the onset of substorm occurred at 1300 UT just before the
time of this observation.   The data of sensor 1 show precipita-
tion while those of sensor 2 show upward flux (secondary electrons,
degraded primary electrons and/or backscattered primaries).   A
complex precipitation pattern can be seen in the data of sensor
1, whereas the data of sensor 2 show negligible upward electron
flux except at lower latitudes.   Characteristics of the precipi-
tation pattern are listed as follows.

(i)   Structured precipitation characterized by low-energy bursts
or inverted-V events can be seen at higher latitudes, whereas
stable/or diffuse precipitation can be seen at lower latitudes.
This feature is generally consistent with earlier observations by
Winningham et al. [1975], who have suggested that the diffuse
precipitation is linked to the central plasma sheet, while the
structured one comes from the boundary plasma sheet.

(ii)   In the inverted-V event the electron energy for peak
differential intensities increases to the maximum energy of

kev-range and subsequently decreases with time. One of the features of the inverted-V event observed by KYOKKO is that the peak energy for the differential intensities often remains at the maximum energy for a while in contrast with the previous results [Frank and Ackerson, 1971], and therefore this structure looks like an inverted "U" (see the figure around 1323 UT), although the ordinary inverted "V" event can be seen around 1322 UT. The width of this structure around 1323 UT is $\sim$ 400 km, with a small change of only 0.1^O in invariant latitude from 67.9^O to 68.0^O. Another long structure can be seen from 1327 UT to 1329 UT in the post-midnight. Energy spectra of the electron flux during this structure have a very stable peak at around 2 keV, as shown in Fig. 5.5. The situation of this type occurs near the highest invariant latitudes, where the satellite grazes nearly constant invariant latitudes scanning a wide range of magnetic local times; the satellite traverses obliquely, almost along the auroral arc. In other words, it may be said from the KYOKKO data that the electron energy for the beam-like precipitation is nearly constant along the auroral arc.

(iii) The diffuse precipitation pattern of the pre-midnight data is different from that of the morning-side data, although the energy-flux profile at premidnight is quite similar to that in the morning side. The energy distributions of precipitating electrons become harder with increasing latitudes at pre-midnight, whereas those on the morning side tend to be so with decreasing latitudes. The difference of the precipitation patterns between the evening and morning hours is most evident in the progress of the magnetic substorm, as will be discussed in the next subsection.
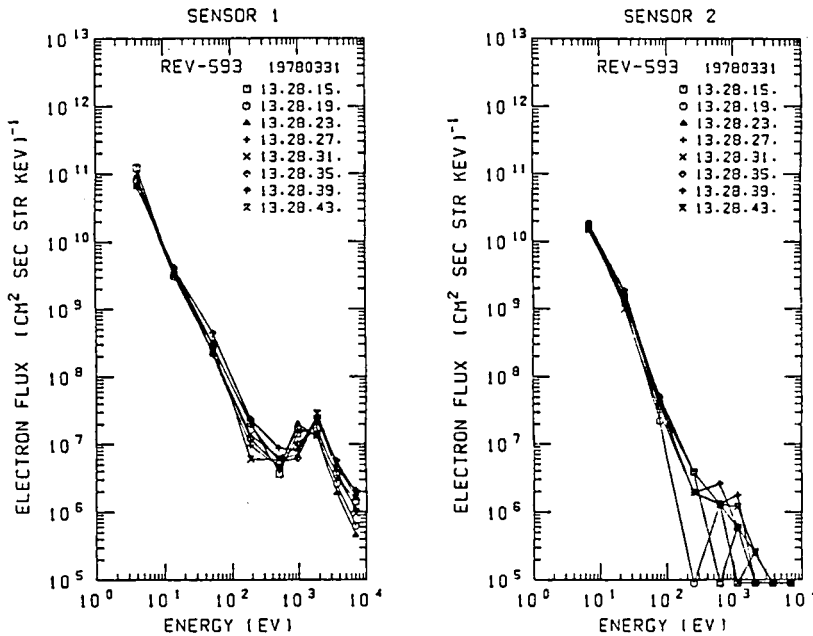
Fig. 5.5 Energy spectra of the electron flux obtained during the inverted-U structure at Rev. 593.

Figure 5.6 shows a typical example of the precipitation pattern in the morning hours. The satellite started to detect diffuse precipitation at 13:43 UT ($\sim$62° invariant latitude, 0543 MLT), then observed three inverted-V events at higher latitudes and entered a polar cap, until it observed intense, but sporadic, precipitation of soft electrons from 1000 to 1230 MLT at invariant latitudes of 78.8° to 76°. The left part of the pattern shows a latitudinal profile in the morning hours, since the satellite traversed toward higher latitudes with only a one-hour change of magnetic local times. Hardening of the precipitation at lower latitudes, as discussed above, is clearly seen. Those electrons may have precipitated from the inner edge of the plasma sheet
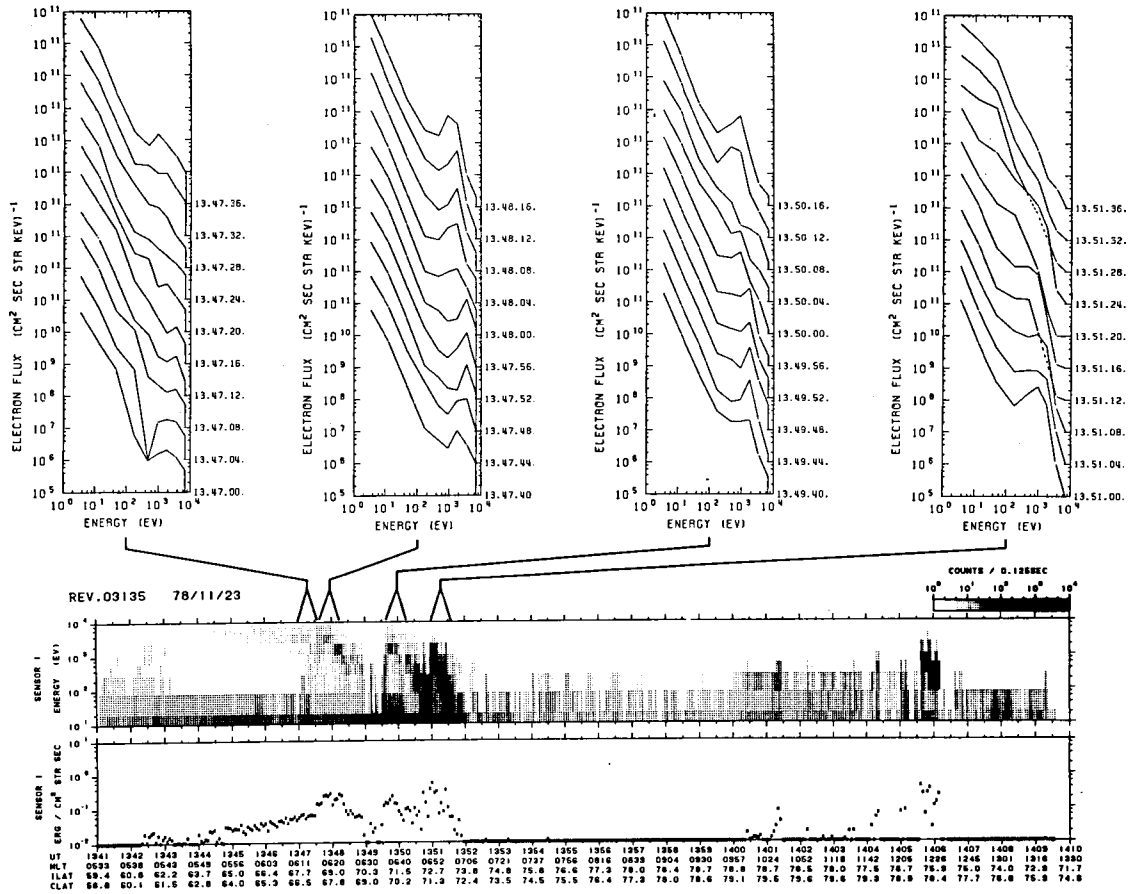
Fig. 5.6   Electron precipitation pattern in the morning hours.   Energy spectra during several periods of time are also shown in the upper panel.

in which the plasma particles are energized by the increasing

magnetic field during the E × B convective motion. The energy

spectra in the inverted-V events which are shown in the upper

panels show a peak clearly and its variation with time/space.

Intense, but sporadic, precipitation in the late morning hours is

a typical feature observed frequently at a high latitude region in

the dayside. This pattern may be related with the injection

mechanism of the magnetosheath plasma into the magnetosphere at

the source region, probably the distant cusp or the dayside

boundary layer. This is a problem to be solved in future, since

it is a big problem; which of the reconnection mechanism and the

viscous-like interaction is more important for plasma entry from

the magnetosheath into the magnetosphere.

An example of the precipitation pattern in the early after-

noon is shown in Fig. 5.7. The precipitation characteristics are

similar to those seen around noon in Fig. 5.6, but have a long

duration with changing energy, in which latitudinal change is

however only 2°. This long-duration feature is again typical in

the KYOKKO observation; the satellite would move along the auroral

arc owing to the semipolar orbit. Important features in the

early afternoon are that the precipitation generally occurs at

higher latitudes than any other local time, that the stable

diffuse precipitation is hardly observed in the early afternoon,

and that the energy of a peak in the spectrum is typically ≤ 1

keV, generally lower than that observed on the night-side

inverted-V event.

Figure 5.8 shows an example of the precipitation pattern in

the evening, in which the satellite traversed from the early

afternoon to the evening hours. The early-afternoon features as
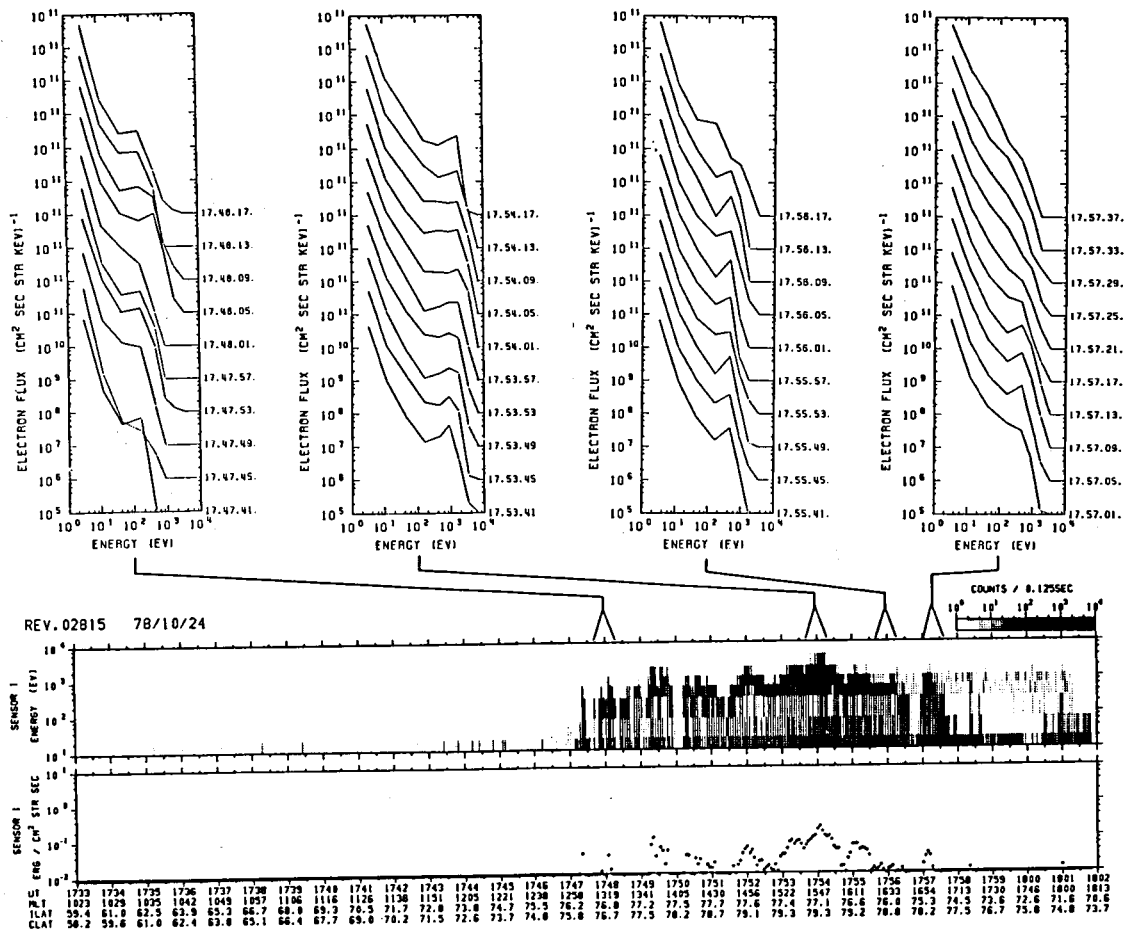
Fig. 5.7　Electron precipitation pattern in the early afternoon.
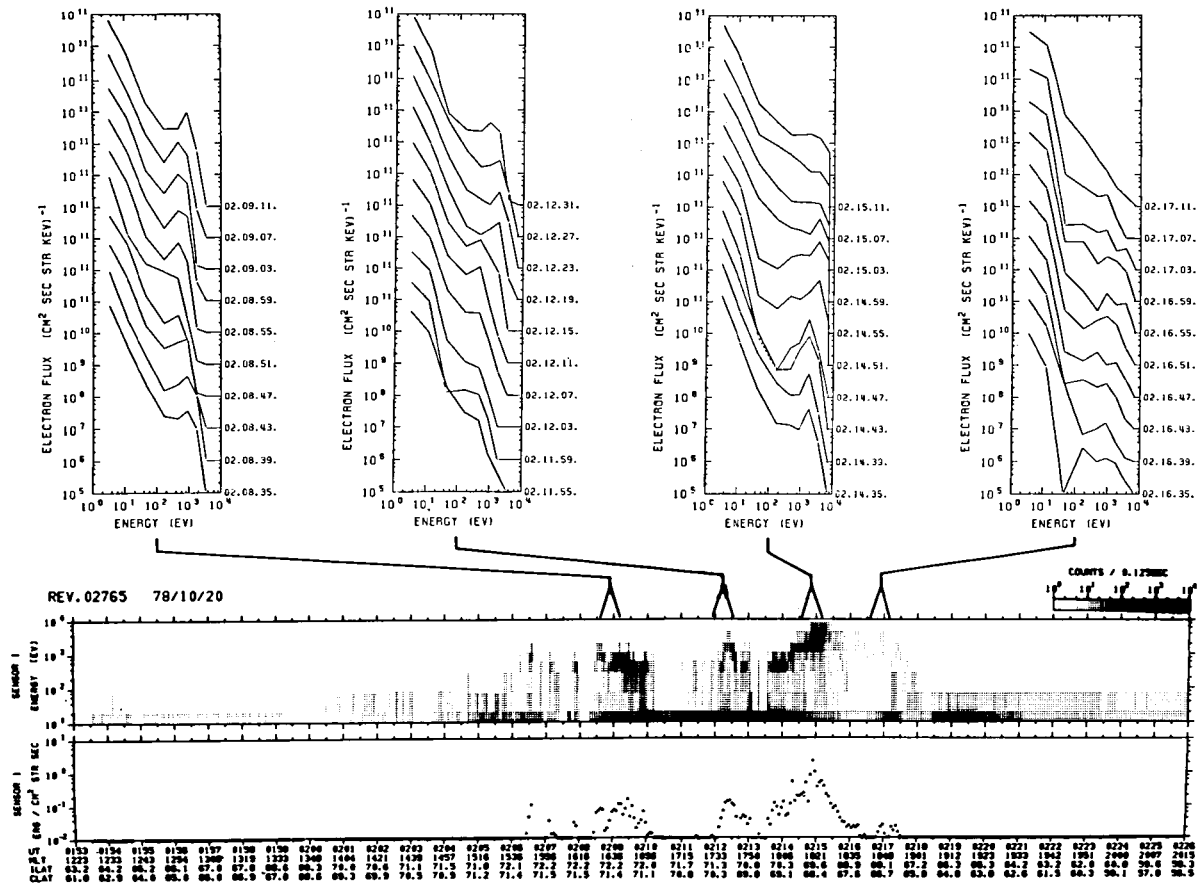
Fig. 5.8   Electron precipitation pattern in the evening hours.

noted above are first observed, and then the satellite encountered the evening inverted-V event. The peak energy is higher in the evening than in the early afternoon.

The precipitation features mentioned above are typical at moderate geomagnetic conditions, but have significant variations depending on the substorm phase especially on the nightside, as shown in the following subsection.

2.4 Relationship of the Precipitation Pattern with the Substorm Phase on the Nightside

Figures 5.9 and 5.10, respectively, show the precipitation patterns of four successive orbit passes, the data of which were acquired in Churchill, Manitoba, Canada. In Panel (a) of each figure, magnetic midnight is adjusted to coincide roughly among four successive passes, although the invariant latitudes in each pass are different. The satellite paths in the polar coordinate of magnetic local time and invariant latitude, and the magnetic records in the Churchill meridian are given in Panels (b) and (c), respectively, of each figure. The numbered vertical-line interval in the magnetic records in Figs. 5.9(c) and 5.10(c) corresponds to the numbered precipitation pattern. These four passes are suitable for study of the substorm, since those were obtained during various phases of the substorm.

April 24, 1978 (Fig. 5.9 (a), (b) and (c))

It was a very disturbed day (ΣK_p = 39), on which many onsets of substorms were listed in Boulder Geomagnetic Substorm Log
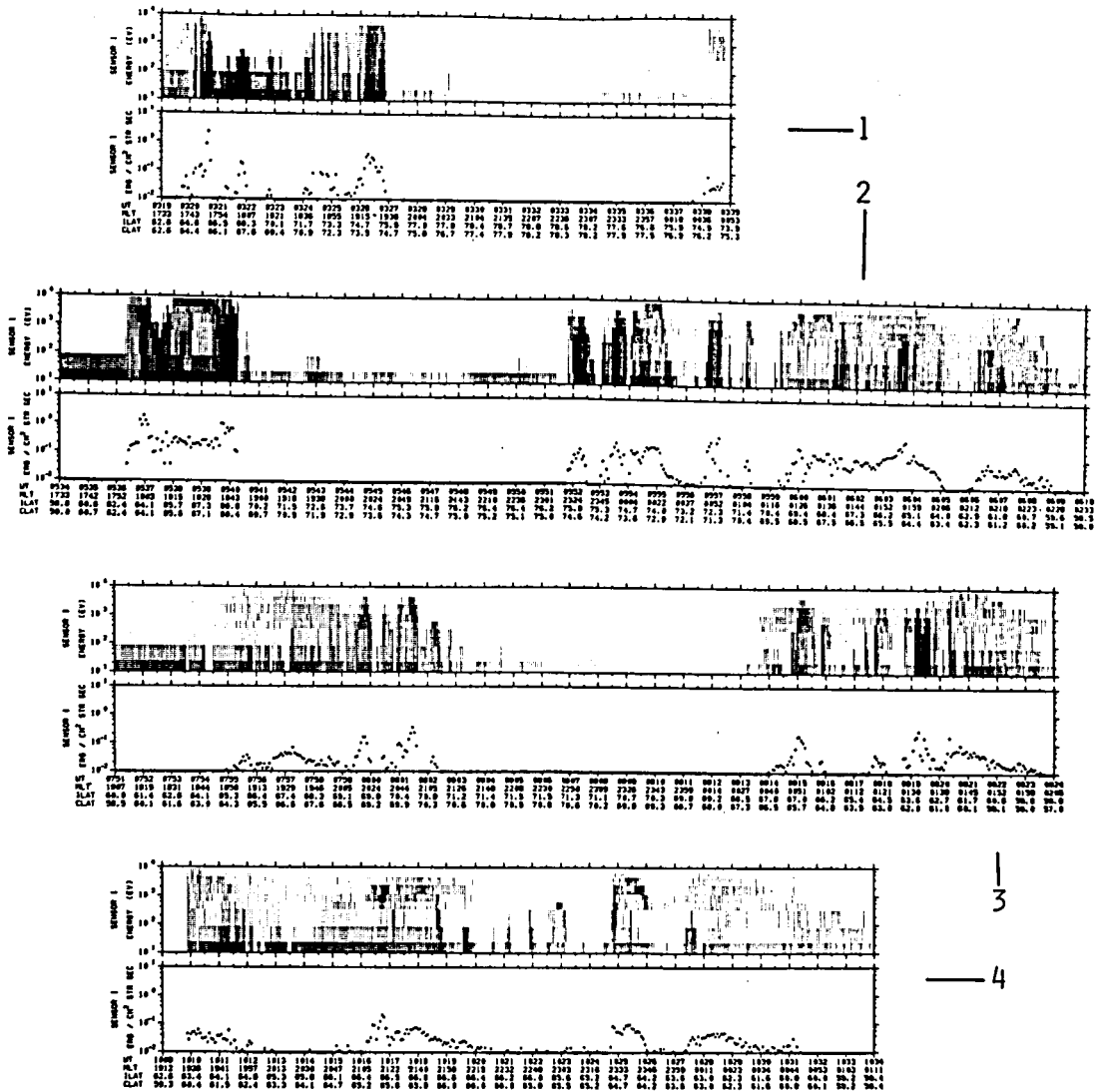
Fig. 5.9(a) Energy-time spectrograms of precipitating electrons for four
successive orbits of Revs. 846, 847, 848 and 849 from top
panel to bottom.   See also Figs. 5.9 (b) and (c).
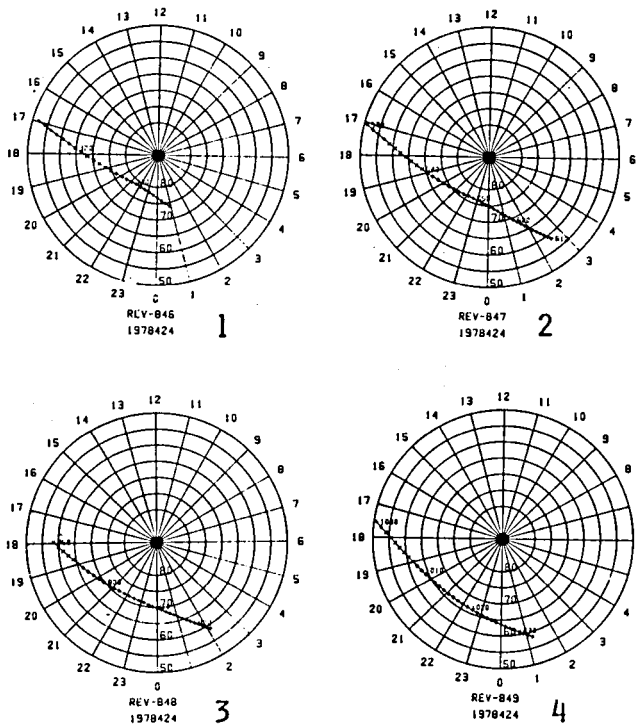
Fig. 5.9(b)

Orbits for the above
four revolutions.
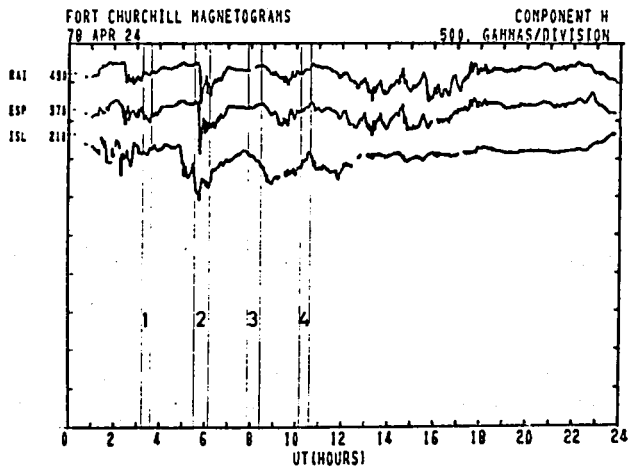
Fig. 5.9(c) Magnetic records of Fort Churchill meridian chain.
The numbered vertical line interval corresponds to
the number shown in Fig. 5.9(a) and (b).

[Solar Geophysical Data, No. 405]. The data No. 1 in Fig. 5.9(a)
were obtained in the course of seven multiple-onset substorms,
0125, 0220, 0230, 0250, 0325, 0355 and 0450 UT. The precipita-
tion pattern shows diffuse and subsequently discrete ones (low
energy bursts) with increasing latitudes. Enhancement of precip-
itation occurred around 0325, just corresponding to the onset.
The data No. 2 was also obtained in the course of three multiple-
onset substorms; 0505, 0550 and 0610 UT. The precipitation
pattern shows clearly the difference between evening and morning.
On the evening side the pattern is characterized by discrete
precipitation of the inverted-V, whereas on the morning side it is
by diffuse precipitation. Several structured bands are seen
around local midnight just after the substorm onset (0550UT),
probably indicating the presence of the poleward expanding auroral
bulge. The data No. 3 and No. 4 show relatively weaker precip-
itation compared to those in No. 1 and No. 2, reflecting the
recovery phase. The data No. 3 show diffuse and structured
precipitation at lower and higher latitudes, respectively, in both
the evening and morning sides, suggesting the continuity of the
auroral oval.

April 25, 1978 (Fig. 5.10 (a), (b) and (c))

The value of ΣK_p was 25- on this day. The data No.1 was
obtained during ∿30 minutes just after the substorm onset (0130
UT). As the satellite traversed from lower to higher latitudes
around 1800 MLT, it suddenly encountered the intense discrete
precipitation, whereas in the morning side the precipitation shows
diffuse precipitation with some low-energy burst embeded in it.
The data No. 2 show the precipitation pattern similar to the
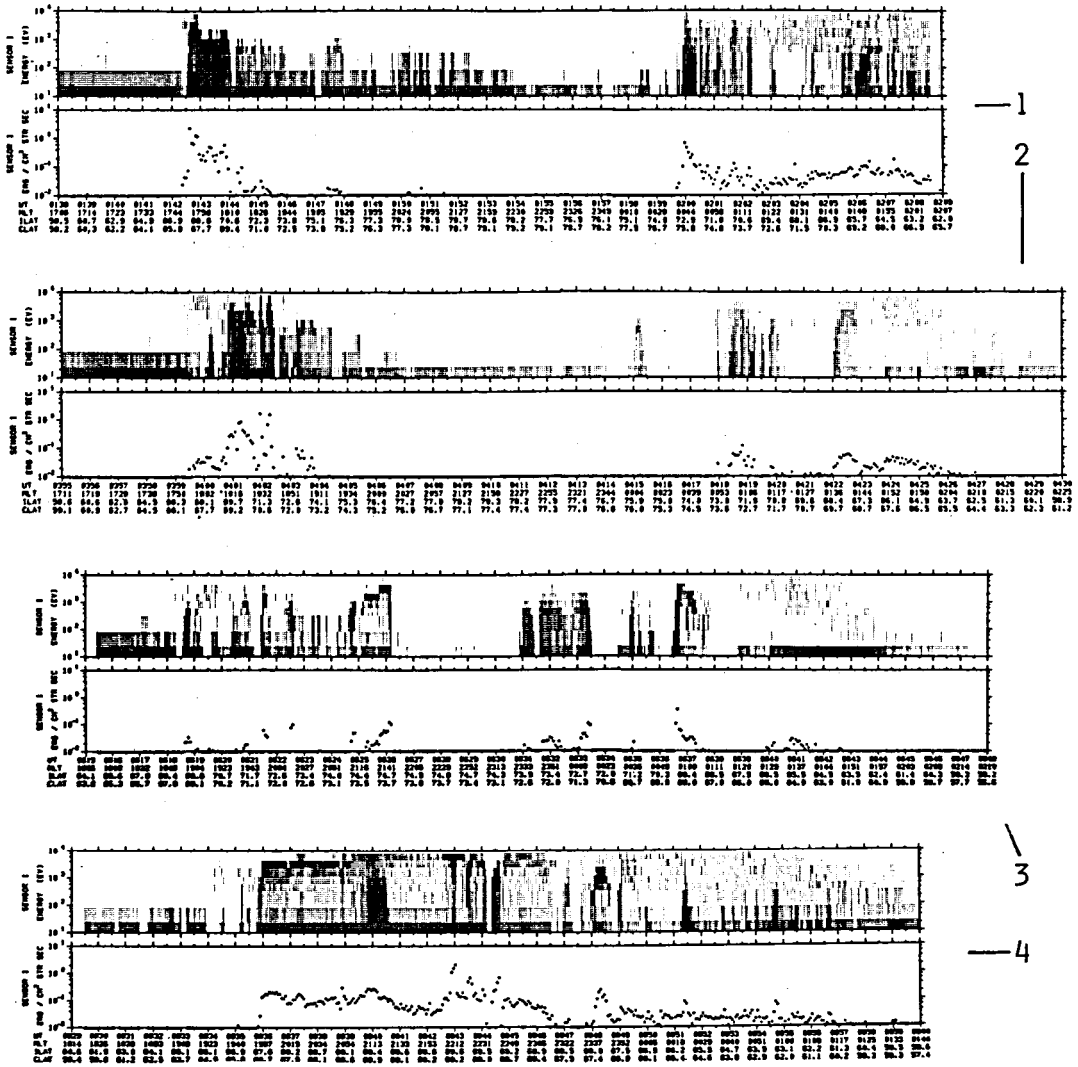
Fig. 5.10(a) same as Fig. 5.9(a).   Rev. Nos. are 856, 857, 858 and 859
from top to bottom.   See also Figs. 5.10 (b) and (c).
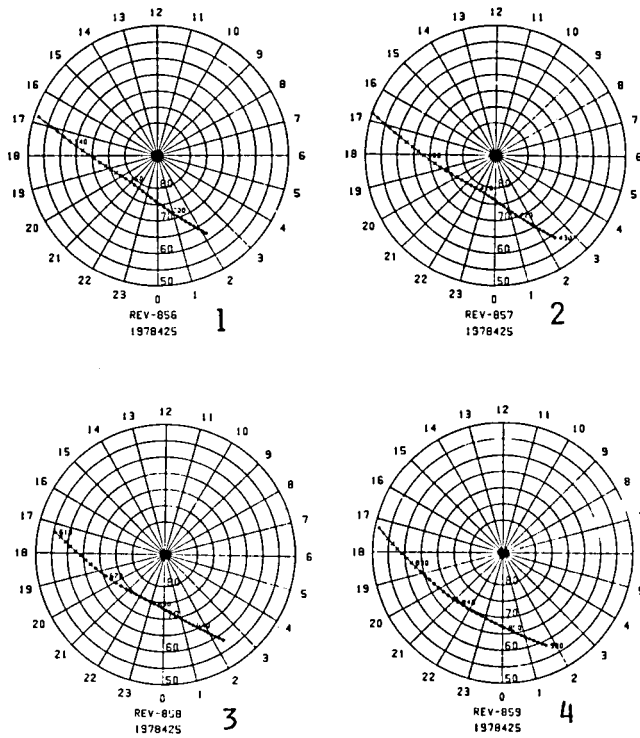
Fig. 5.10(b)

Orbits for the above
four revolutions.
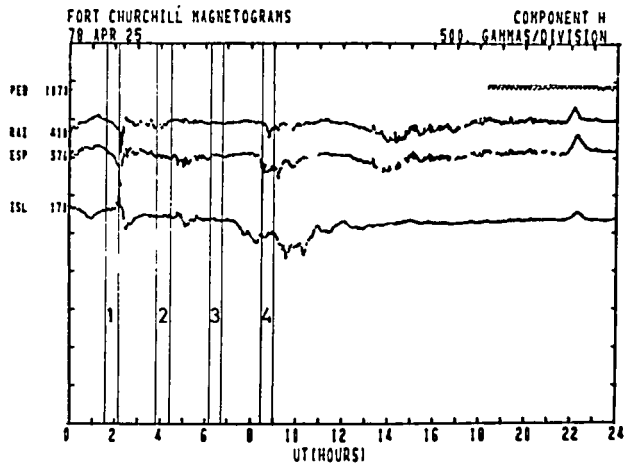
Fig. 5.10(c) Magnetic records of Fort Churchill meridian chain.
The numbered vertical line interval corresponds to
the number shown in Fig. 5.10(a) and (b).

pattern of No. 1.   The data No.3 show a faint discrete precipi-
tation on the evening side and around midnight.   The similar
pattern is seen also in No.4 of the previous figure.   The data
No.4, obtained just after the substorm onset (0825 UT), show the
precipitation pattern similar to the pattern of No.1, although the
energy distribution is much harder.

　　All of these passes were obtained in magnetic local times
from the evening hours to the post midnight through midnight.
The precipitation characteristics deduced from the above obser-
vations are summarized below.

 (a) The general picture that polar auroras are characterized by
the diffuse precipitation and the structured discrete one at
lower and higher latitudes, respectively, is only an average
morphology and cannot be applied to the individual case, although
the precipitation pattern in the recovery phase has such a feature
with no marked difference between evening and morning, indicating
the continuity of the auroral oval.

 (b) At the expansion and early recovery phase, the precipitation
pattern on the evening side is not necessarily the same as the
pattern on the morning side.   The structured discrete precipi-
tation is predominant on the evening side, whereas the diffuse
precipitation is so on the morning side.   The satellite often
detected the intense discrete precipitation suddenly, probably a
travelling surge, when the satellite traversed obliquely from low
to high latitudes in the evening side.   The satellite also
observed the burst-like precipitations, probably poleward bulges
around midnight.

 (c) At quiet times, faint discrete precipitations are seen on the
evening side.

2.5 Spatial Structure of the Inverted-V Event

As described above, the precipitation pattern of auroral electrons can be classified generally into the diffuse and discrete precipitation. The 'so-called' inverted-V event, which is typical of the discrete precipitation, has attracted attention of most auroral and magnetospheric researchers, since the peaked spectrum is considered to manifest electron acceleration due to the DC electric field aligned along the magnetic field. Because of the semi-polar orbit, the KYOKKO observations have provided us with interesting precipitation patterns which show longitudinal as well as latitudinal variation in contrast with the earlier observations by polar orbiting satellites; see Section 2.2 in Chapter I, and therefore are suitable for investigation of the spatial structure of the inverted-V event.

The inverted-V events in various shapes have already been shown in Figs. 5.3 and 5.6 — 5.10. Those are recognized sometimes as inverted-"U" (long-duration inverted-V) events, when the satellite was skimming along the auroral oval. Figure 5.11 shows purely a latitudinal profile of auroral electrons which is similar to the earlier observations by the polar-orbiting satellites [e.g., Frank and Ackerson, 1971]. The inverted-V event occurred around 1950 MLT at an invariant latitude of about 69° when the satellite traversed the auroral oval toward higher latitudes with a small change of magnetic local time (1930-2000 MLT). The monoenergetic peak seen in the sensor-1 energy-time spectrogram as a narrow black band at higher latitudes than the diffuse precipitation region is a typical characteristic of the inverted-V event. The spatial extent of this inverted-V event
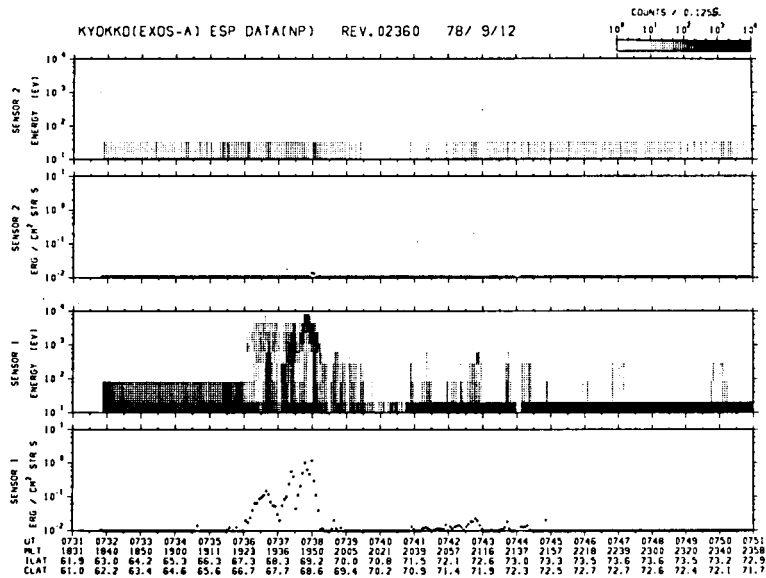
Fig. 5.11 A typical inverted-V precipitation observed when the satellite traversed the auroral region toward higher latitudes with a small change of magnetic local time.

is about 200 km.

Figure 5.12 shows a summary of the inverted-V precipitation observed by the KYOKKO satellite. Only the part of the precipitation pattern which shows an inverted-V event is displayed in each panel. The panels from (a) to (e) are ordered so that the duration, i.e., the spatial extent, becomes longer. The width of the structure in panel (d) extends over 2.5 hours in magnetic local times, while the change of the invariant latitude is only $2°$. It is also interesting to note that the peak energy remains nearly constant in the long-duration inverted-V event. Some fluctuation of the peak energy can be seen in panel (e), but this is because the satellite passed along the multiple arcs which
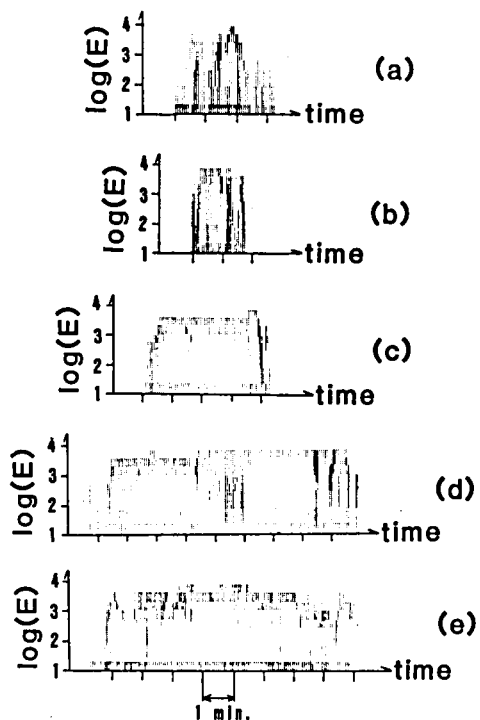
Fig. 5.12   A summary of the inverted-V events with various
            periods of duration observed by KYOKKO.

were also moving, just after a substorm onset at Rev. 2595,

October 4, 1978 [Kaneda et al. 1980].

The existence of long-duration inverted-V events indicates

that this structure is stable rather than transient.   The

inverted-V structure is generally interpreted as due to precipi-

tating electrons accelerated by a quasi-static electric field

parallel to the magnetic field.   The mono-energetic peak energy

is suggestive of the electrostatic potential difference along the

magnetic field line between the observation point and the source region. The durations of inverted-V events provide us with information on the configuration of the DC electric field, if the duration shows spatial extent rather than temporal variation. Inverted-V events observed by the KYOKKO satellite have various durations because of the semipolar orbit of the satellite, while the change of invariant latitudes is only a few degrees at most during one event. That is, an inverted-V event with shorter duration shows a latitudinal profile while a longer duration one shows a longitudinal profile. The monoenergetic peak energy is nearly constant for a long duration event, in contrast to the shorter event which really shows an inverted-V shape. This may suggest that the equipotential contours of the DC electric field are extensive in longitude (i.e., nearly constant potential for a constant L-value) and have a meridional cross-section that is V-shaped. In addition, most of the parallel electric field must exist above altitudes of 4000 km, since the mono-energetic peak energies observed by the KYOKKO satellite at altitudes of 2500-4000 km are comparable to those observed previously by lower-altitude rockets and satellites [e.g., Arnoldy et al., 1974; Frank and Ackerson, 1971]. This is consistent with recent ion and electron observations from the S3-3 satellite [Mizera and Fennel, 1977; Cladis and Sharp, 1979; Ghielmetti et al., 1978].

Frank and Ackerson [1971] and Frank and Gurnett [1972] have suggested that the inverted-V events occur on open field lines and that the source region is the magnetosheath. On the other hand, Burch et al. [1976] and Lin and Hoffman [1979] have suggested that these events occur on the closed field lines as well as on the open field lines and also that the source region is not only

the magnetosheath but also the plasma sheet. Our observations
seem to support the latter argument, because the inverted-V
events occur at the poleward detached region of the precipitation
zone (probably on the open field lines) as well as even in the
midst of the diffuse precipitation region (on the closed field
lines); e.g., Fig. 5.3.

Figure 5.13 shows spatial occurrence maps of inverted-V
events for the geomagnetic conditions of $K_p \geq 3_-$ and $K_p \leq 2_+$,
respectively. It is noticed here again that the KYOKKO satellite
could not attain an invariant latitude higher than about 79°.
The observation times for these data are almost equally distributed
in magnetic local time. The occurrence map shown in Fig. 5.13 is

KYOKKO
Inverted-V Event Occurrence Map
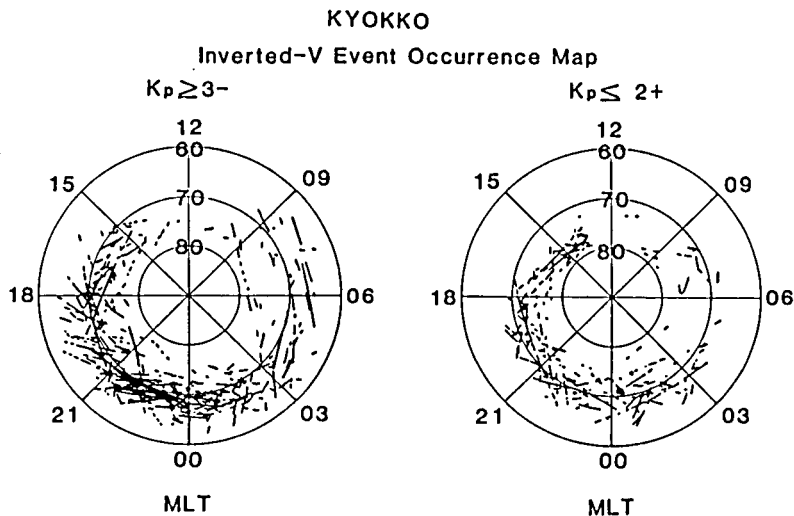
Fig. 5.13 Spatial occurrence maps of inverted-V events for the geomagnetic
conditions of $K_p \geq 3_-$ and $K_p \leq 2_+$. Magnetic local
time (MLT) and circles of constant invariant latitudes are shown
for reference.

consistent with the earlier statistical study of inverted-V

events [Lin and Hoffman, 1979], and also is similar to the

occurrence of the optical aurora [Feldstein, 1966; Lui et al.,

1975] and of the larger-scale field-aligned current [Iijima and

Potemra, 1978]. The region of inverted-V events roughly coincides

with the upward current region obtained by Iijima and Potemra

[1978]. Inverted-V events occur at all local times and at higher

latitudes in the dayside hemisphere, although the frequency of

occurrence is least in the morning of 0300-1200 MLT. They are

detected more frequently as the K_p-index is higher. The average

latitudinal width of inverted-V events is about 1°. The longi-

tudinal extent varies from a narrow one of several tens of km up

to about several thousands of km. Under disturbed conditions

$(K_p \geq 3_-)$, inverted-V events occur most frequently at invariant

latitudes of 65°-70° in the pre-midnight sector: They were

detected in about 80 % of the orbital passes traversing this

region. Under relatively quiet conditions $(K_p \leq 2_+)$, inverted-V

events occur at higher latitudes than under disturbed conditions,

while the frequency of occurrence is nearly constant in the MLT

range of 1300-0200 through midnight. A further notable feature

is that inverted-V events do not occur around noon. A clear

asymmetry in the frequency of occurrence can be seen between

morning and afternoon, especially under relatively quiet conditions.

2.6 New Finding of the Localized Intense Flux of Upgoing

     Electrons

     In this section we are concerned with characteristics of the

electron fluxes escaping upward from the polar ionosphere to the magnetosphere. Generally the upward electrons observed by the KYOKKO satellite comprise four components; (a) ionospheric photo-electrons, (b) secondary electrons and/or degraded primaries caused by the auroral electron precipitation, (c) secondary electrons produced by the high energy particles precipitating from the outer radiation belt, and (d) localized upward electrons which do not correspond simultaneously to the electron precipitation.

The first three components can be seen in the sensor-2 data in Figs. 5.3 and 5.11. Rather stable electron fluxes below several tens of eV show the photoelectrons escaping from the sunlit ionosphere. The disappearance of them near the center time interval in Fig. 5.11 corresponded to the sun set of the ionosphere. The similar feature found in the precipitation pattern (sensor-1 data) may suggest that they are conjugate photoelectrons, being transported through the magnetosphere, and thus that those regions are connected to the conjugate points by the closed magnetic field lines. The second (b)-component can be seen in conjunction with the sensor-1 data. Intensification in the stable photoelectron flux is correlated well with the precipitation. Precipitating electrons with high energy, e.g. ≥ 1 keV, may go deep into the ionosphere (E-region) and produce many secondary electrons there. Only a limited part of degraded primaries can escape upward from there, and hence most of the item-(b) component have usually an energy below several tens of eV, although small number of upward electrons have sometimes an energy comparable to that of the precipitating electrons. The third (c)-component have often been observed at lower latitudes than the auroral region. They may also include the degraded

primaries.   Small contribution of the radiation belt particles

to the sensor-1 data would be because most of the radiation belt

particles have a pancake distribution in pitch angles especially

at low altitude and cannot make a large effect on the data of

sensor-1 which measures precipitating electrons along the magnetic

field line.   On the other hand the high energy particles may be

degraded and/or scattered by the neutral atmosphere, changing the

pitch angles, and be detected by the sensor 2.

The last (d) component is a unique phenomenon observed by

the KYOKKO satellite, and we call it a LUE (localized upward

electron) event.   Figure 5.14 shows such an example.   The LUE

event can be seen soon after 0928 UT, just corresponding to the

valley between two inverted-V events, when the satellite was

moving around the highest latitude with only a small change of

latitude.   Energy spectra of the upward and downward electron

fluxes during this event are shown in Fig. 5.15, in which energy

spectra obtained during the inverted-V event are also shown for

comparison.   In the inverted-V event, the precipitating electrons

have a large peak at an energy of $\sim$ 4 keV together with the

power-law spectrum in lower energies.   These low energy electrons,

which have nearly the same flux and same spectrum as those of the

upward electrons, may arise from reflection of upward electrons

by the potential barrier which accelerate the precipitating

electrons.   On the other hand, the upward electrons in the LUE

event have much higher energy and intensity than the precipitating

electrons.   Their spectrum has no peak, but become only broadened

up to a few hundreds of eV.   Another example is shown in Fig.

5.16, in which the LUE event can be seen just in the equatorward

of the precipitation region.   In this example, the energies of
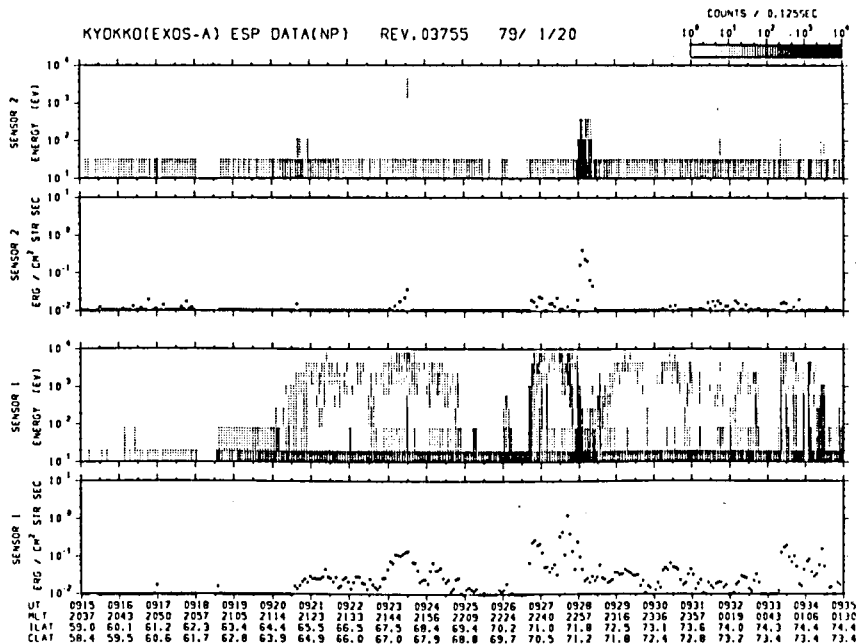
Fig. 5.14 Energy-time spectrogram and the energy flux on Rev. 3755.
The LUE event can be seen in the sensor-2 data (upper two
panels) soon after 0928 UT, just corresponding to the valley
between two inverted-V precipitation (lower two panels).
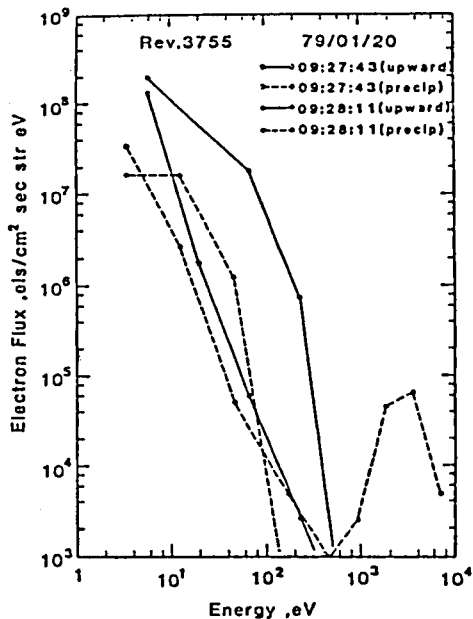
Fig. 5.15

Energy spectra of the
upward (solid lines)
and downward (dashed
lines) electron fluxes
in the inverted-V and
LUE events, respective-
ly, at Rev. 3755.
See also Fig. 5.14.

upward electrons extend over about 1 keV, but this example belongs to an exceptional case. The energy of about 100 eV is generally the uppermost. This example is displayed in order to show a prominent case of the localized upward electron fluxes. These localized upward electron fluxes can carry the downward flowing current, though the charge carriers for the current are electrons below 10 eV in most cases. The regions of localized upward electron fluxes can be classified into two; equatorward and poleward of precipitation regions. Figure 5.17 shows a spatial occurrence map of these regions. It is interesting to note that these regions roughly coincide with those of large-scale downward field-aligned currents obtained by Iijima and Potemra [1978]; see Fig 1.7. The probability of detecting these events is not so high, but it may be because localized upward electrons below several ten eV are obscure by the presence of photoelectrons, if it be the case. Even so, particular explanations are necessary for the localized upward electrons with 100 eV in absence of significant electron precipitation. Hultqvist and Borg [1978] have proposed a model with two oppositely directed field-aligned electrostatic potential drops for interpretation of ESRO-1A data. Mozer et al. [1980b] also reported a S3-3 observation of the parallel electric field, the direction of which is consistent with our LUE event, in the cusp region accompanied by the low frequency turbulence, intense fluxes of upward field-aligned low-energy electrons and conical ions. However, the results reported here cannot be simply explained by acceleration due to the parallel electric field, since the upward electron fluxes have not a peak in the energy spectra. Those electrons seem to be heated rather than monoenergetic acceleration, probably by

KYOKKO(EXOS-A) ESP DATA(NP)   REV.03878   79/ 1/31

COUNTS / 0.125SEC

UT	2021 2022 2023 2024 2025 2026 2027 2028 2029 2030 2031 2032 2033 2034 2035 2036 2037 2038 2039 2040 2041
MLT	1826 1834 1842 1851 1900 1910 1920 1931 1943 1955 2008 2021 2035 2050 2105 2121 2137 2153 2210 2226 2243
ILAT	58.0 58.9 59.8 60.7 61.6 62.4 63.2 63.9 64.6 65.3 65.9 66.5 67.0 67.5 67.8 68.2 68.4 68.6 68.6 68.6 68.5
CLAT	60.9 61.9 62.9 63.9 64.9 65.9 66.7 67.5 68.2 68.8 69.4 69.9 70.3 70.6 70.8 70.9 70.8 70.6 70.4 70.0 69.4

Fig. 5.16   Energy-time spectrograms on Rev. 3878.   The LUE event in the
            sensor-2 data (upper panel) can be seen in the equatorward of
            the precipitation (lower panel).
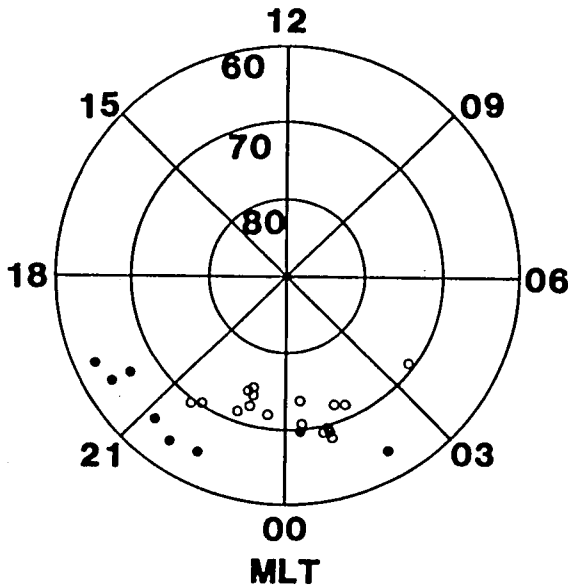
Fig. 5.17
   Spatial distribution of
   the LUE event. See text.

o **poleward of precipitation**

• **equatorward of precipitation**

the electrostatic turbulence, although we have had no simultaneous
wave measurement during the LUE events.   One of the reasons for
no other observation of the LUE event would be because most of
the satellites have been spin-stabilized and therefore have had
little chance of detecting this low-probability event, if the LUE
event could be seen only along the magnetic field line.

2.7   Conclusion

The electron spectrometer on board the KYOKKO satellite was
designed to measure simultaneously both the upward and downward
electron fluxes along the geomagnetic field line in the energy
range from several eV up to $\sim$ 10 keV.   The instrument was
designed and constructed so as to get as more results as possible
for investigation of auroral electrons under the severe boundary
(weight, power, telemetry) and environmental (vibration, shock,
temperature) conditions.   Instrumental performance was excellent
and revealed various interesting characteristics of the auroral
electrons with respect to (a) local-time dependence of the
pricipitation pattern, (b) substorm-phase variation of the
night-side precipitation, (c) spatial structure of the inverted-V
events and (d) characteristics of the upgoing electrons including
the LUE event.   Most of these results are generally consistent
with earlier observations by other researchers and supplementary
to them.   In particular, we believe the items (c) and (d) will
contribute to progress of the auroral and magnetospheric physics.
The future experiment should be simultaneous observations between
the auroral and distant magnetosphere along the geomagnetic field

line, which will be essential to solve the mechanisms of plasma injection and transport.

§3. Observations of Hot Electrons in the Inner Magnetosphere
    by JIKIKEN Satellite and Their Correlations with
    VLF Wave Activities

The scientific satellite EXOS-B (JIKIKEN) was launched on September 16, 1978 into the elliptic orbit of inclination 31°, the initial apogee and perigee being 30,055 km and 227 km, respectively.   JIKIKEN could explore the inner magnetosphere at middle and low magnetic latitudes.   The purposes of the charged particle measurements on board JIKIKEN were as follows:

(1) To investigate the dynamics of electrons and ions in the
    inner magnetosphere.

(2) To investigate wave-particle interactions in the inner
    magnetosphere with the aid of wave measurements.

(3) To observe the response of magnetospheric plasma when
    the active experiment; i.e., SPW (high power radio wave
    emission) or CBE (controlled electron beam emission)
    is performed.

We are here concerned only with the electron measurements, focusing on the correlative study with VLF wave activities.

3.1 Instrumentation

Charged particle detectors (ESP) on board JIKIKEN consisted
of an electron sensor, an ion sensor and electronic circuits.
The electron and ion sensors measured electrons and ions in the
energy ranges from a few eV to 10 keV and from 10 eV to 30 keV,
respectively.   The characteristics of the sensors are summarized
in Table 5.1.   A schematic view of the ESP instrument installed
on the satellite is shown in Fig. 5.18.   The structure of the
electron sensor is better understood in Fig. 5.19; a schematic
drawing of the vertical cross section of Fig. 5.18.   The electron
sensor was composed of a front collimator, a hemispherical
electrostatic energy analyzer with the inner and outer radii of

Table 5.1 Characteristics of the ESP sensors on board JIKIKEN

	Electron	Ion
Type of analyzer	hemispherical	cylindrical (60° sector)
Energy range	3 eV $\sim$ 10 keV	10 eV $\sim$ 30 keV
Energy resolution	3 % (*)	5 % (*)
Geomtric factor	1.217×10^{-3} cm^2 sr	1.0×10^{-3} cm^2 sr
Detection efficiency	0.5 (assumed)	1.0 (assumed)
View direction	perpendicular to the spin axis of the satellite	same as the left
Field of view	$4^{o} \times 13^{o}$	$3^{o} \times 3^{o}$

(*) These energy resolutions are those of sensors only.
    Refer to Table 5.2 concerning the energy width of the data.

28 mm and 32 mm, respectively, and a channeltron as a detector.
The ion sensor was composed of a collimator, a 60°-cylindrical
electrostatic analyzer with the inner and outer radii of 58.5 mm
and 61.5 mm, respectively, and a channeltron.   View directions
of both the electron sensor and the ion sensor were perpendicular
to the satellite main axis.   Both collimators extruded from the
satellite surface by about 15 mm.

Figure 5.20 shows a block diagram of the instrument.   The
methods of energy scanning, data sampling and data compress were
same as those used in the electron spectrometer on board the
KYOKKO satellite (see Fig. 5.2), although allocation of the PCM
telemetry words was different.   Rather sufficient words were
allocated to the ESP instrument on board JIKIKEN, and therefore
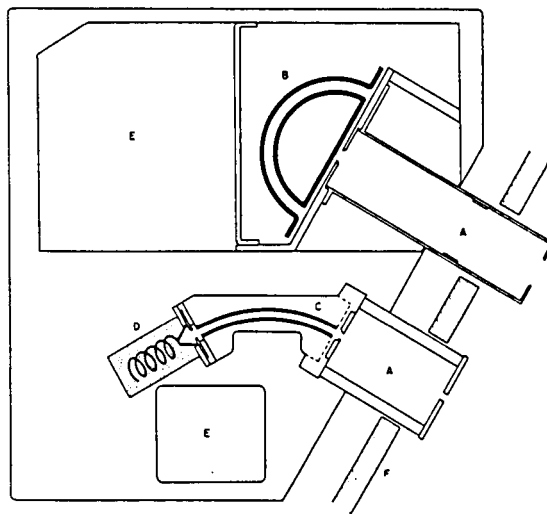
Fig. 5.18   Schematic diagram of charged particle detectors.
   A: Collimators
   B: Hemispherical electrostatic electron analyzer (see Fig. 5.19)
   C: Cylindrical electrostatic ion analyzer
   D: Channeltron and its support for the ion sensor
   E: Sweep voltage power supply, high voltage power supplies for
    channeltrons, charge amplifiers, and pulse discriminating
    and shaping circuits.
   F: Surface of the satellite.

the data were sampled continuously every 62.5 msec, which yielded 16 channels of count data in one energy sweep for electrons and ions, respectively. Allocation of the ESP data in the PCM telemetry is shown in Fig. 5.21. However, only the data of 13 channels were physically meaningful to obtain the energy distribution, since the data during the rise time and also the background data were included in 16 channels of count data. Correspondence of the channel No. to the measured energy is shown in Table 5.2, together with the conversion factor which is a reciprocal of the energy-geometric factor multiplied by the detection efficiency.
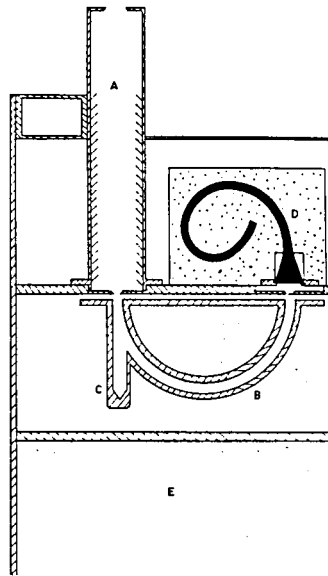
Fig. 5.19 Schematic diagram of the electron sensor; vertical cross
section of Fig. 1.
A: Collimator   B: Hemispherical electrostatic analyzer
C: Trap for high energy particles and solar radiation
D: Channeltron and its support.
E: Sweep voltage power supply, high voltage power supplies
for channeltrons, charge amplifiers, and pulse
discriminating and shaping circuits.
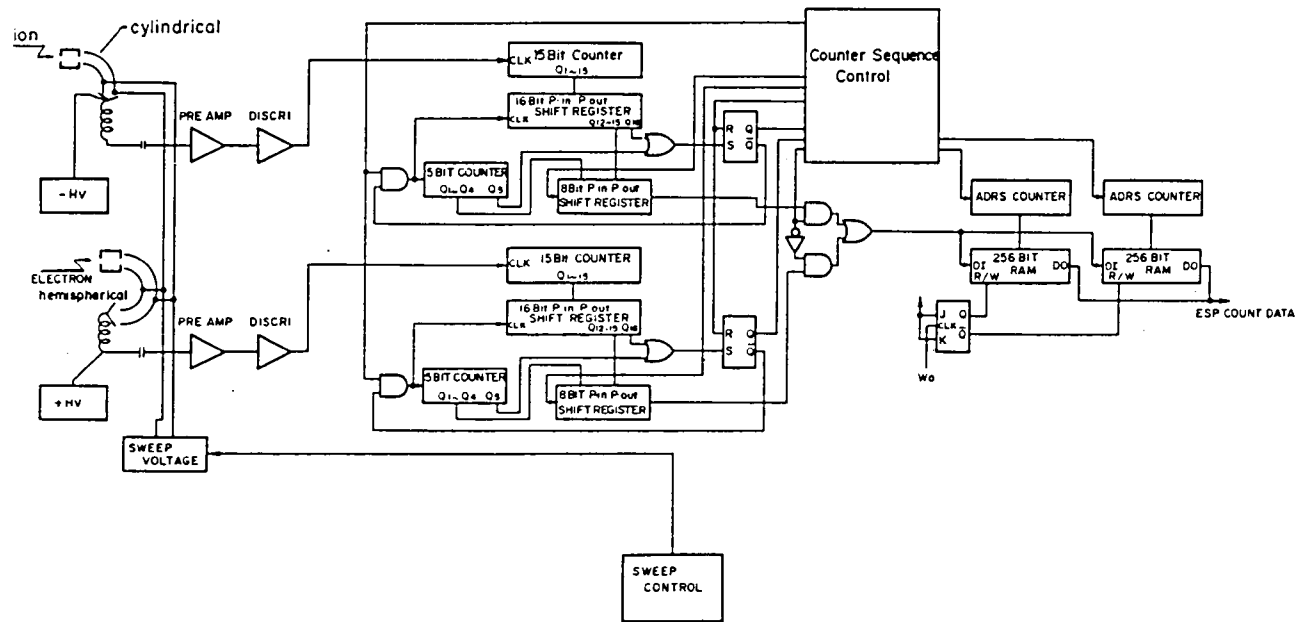
Fig. 5.20   Block diagram of the ESP instrument on board JIKIKEN satellite.

ion count data

electron count data

W92	W93	W94 – W106	W107	W108	W109	W110 – W122	W123	W124	W125	W126	W127

(rising period) (meaningful data) (b.g.) (rising period) (meaningful data) (b.g.) (status) (monitors of analyzer voltages)

(ch. 1 ch. 13)   (ch. 1 ch. 13)
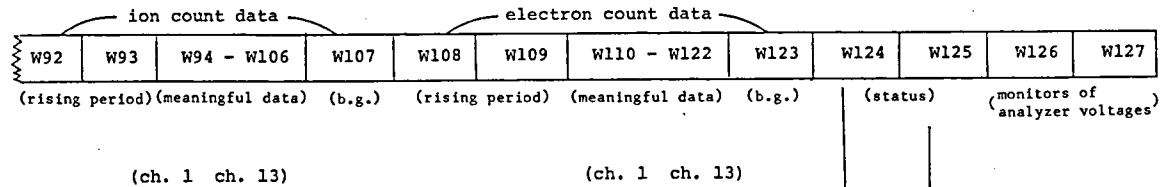
$W_{No.}$	$B_{No.}$	Signal Name	$W_{No.}$	$B_{No.}$	Signal Name
W124	B_0	Analyzer on/off	W125	B_0	Electron HV B_0
	B_1	Electron HV on/off		B_1	Electron HV B_1
	B_2	Ion HV on/off		B_2	Electron discri level B_0
	B_3	Cal on/off		B_3	Electron discri level B_1
	B_4	Sweep Start		B_4	Ion HV B_0
	B_5	Sweep monitor gain		B_5	Ion HV B_1
	B_6	Ion counter overflow		B_6	Ion discri level B_0
	B_7	Electron counter overflow		B_7	Ion discri level B_1

Fig. 5.21 ESP data in the PCM format on JIKIKEN.

Table 5.2 Correspondence of the channel number to the measured energy and the conversion factor.

Channel No.	Electron Boundary energy (eV)	Mean energy (eV)	Conversion factor $(cm^2 \, str \, eV)^{-1}$	Ion Boundary energy (eV)	Mean energy (eV)	Conversion factor $(cm^2 \, str \, eV)^{-1}$
1	$5.04\times10^3\sim9.47\times10^3$	6.91×10^3	8.48	$1.54\times10^4\sim2.89\times10^4$	2.11×10^4	9.47×10^{-1}
2	$2.68\times10^3\sim5.04\times10^3$	3.68×10^3	1.59×10^1	$8.26\times10^3\sim1.54\times10^4$	1.13×10^4	1.77
3	$1.43\times10^3\sim2.68\times10^3$	1.96×10^3	2.99×10^1	$4.42\times10^3\sim8.26\times10^3$	6.04×10^3	3.31
4	$7.62\times10^2\sim1.43\times10^3$	1.04×10^3	5.61×10^1	$2.37\times10^3\sim4.42\times10^3$	3.24×10^3	6.18
5	$4.07\times10^2\sim7.62\times10^2$	5.57×10^2	1.05×10^2	$1.27\times10^3\sim2.37\times10^3$	1.74×10^3	1.15×10^1
6	$2.17\times10^2\sim4.07\times10^2$	2.97×10^2	1.97×10^2	$6.83\times10^2\sim1.27\times10^3$	9.32×10^2	2.15×10^1
7	$1.16\times10^2\sim2.17\times10^2$	1.59×10^2	3.68×10^2	$3.67\times10^2\sim6.83\times10^2$	5.01×10^2	4.00×10^1
8	$6.23\times10^1\sim1.16\times10^2$	8.51×10^1	6.88×10^2	$1.98\times10^2\sim3.67\times10^2$	2.69×10^2	7.43×10^1
9	$3.34\times10^1\sim6.23\times10^1$	4.56×10^1	1.28×10^3	$1.06\times10^2\sim1.98\times10^2$	1.45×10^2	1.38×10^2
10	$1.79\times10^1\sim3.34\times10^1$	2.45×10^1	2.39×10^3	$5.74\times10^1\sim1.06\times10^2$	7.81×10^2	2.56×10^2
11	$9.63 \quad \sim1.79\times10^1$	1.31×10^1	4.46×10^3	$3.10\times10^1\sim5.74\times10^1$	4.21×10^1	4.75×10^2
12	$5.18 \quad \sim9.63$	7.06	8.30×10^3	$1.67\times10^1\sim3.10\times10^1$	2.27×10^1	8.79×10^2
13	$2.79 \quad \sim5.18$	3.80	1.54×10^4	$9.04 \quad \sim1.67\times10^1$	1.23×10^1	1.63×10^3

3.2 Method of Data Reduction

An example of the obtained data at Rev. 143 is shown in Fig.
5.22.   The energy-time spectrograms for electrons and ions,
respectively, are presented together with the sun angle and the
pitch angle.   At first glance of Fig. 5.22 there may be seen a
remarkable spin modulation of the electron and ion counts, the
maxima of which are detectd around zero degree of the sun angle.
Therefore, this spin modulation is caused by the solar radiation;
i.e., photoelectrons produced at the inner surface of the sensor
and at the satellite surface, and also the solar EUV radiation
itself that impinges onto the channeltrons by random reflection.
The magnitude of this contamination depends on the sun angle and
also the measured energy for the electron data; more contaminated
in lower energies.   In this figure, the background counts are
found to be negligibly small except around zero degree of the sun
angle.   The day, November 6, 1978, was a very quiet day; there
occurred no substorm and $\Sigma K_p = 4_+$.   Figure 5.22 shows no
significant electron flux above a few keV, though there can be
moderate flux of high-energy ions which would be the outer radia-
tion belt ions on such a quiet day.   Electrons with the energy of
several hundred eV to 1 keV appear around 1118 UT (L $\simeq$ 6.3, 2137
MLT, -40.4° geomagnetic latitude).   These electrons show a weak
pitch angle anisotropy, though it may not be recognized clearly in
Fig. 5.22.   Various data presentation formats will be presented
in subsequent sections, but the data processing procedure is
essentially same as that used for the KYOKKO observation.

In the early phase of satellite operation as shown in Fig.
5.22, the particle pitch angle could be obtained easily by using

EXOS-B ESP DATA   REV.0143   78/11/ 6
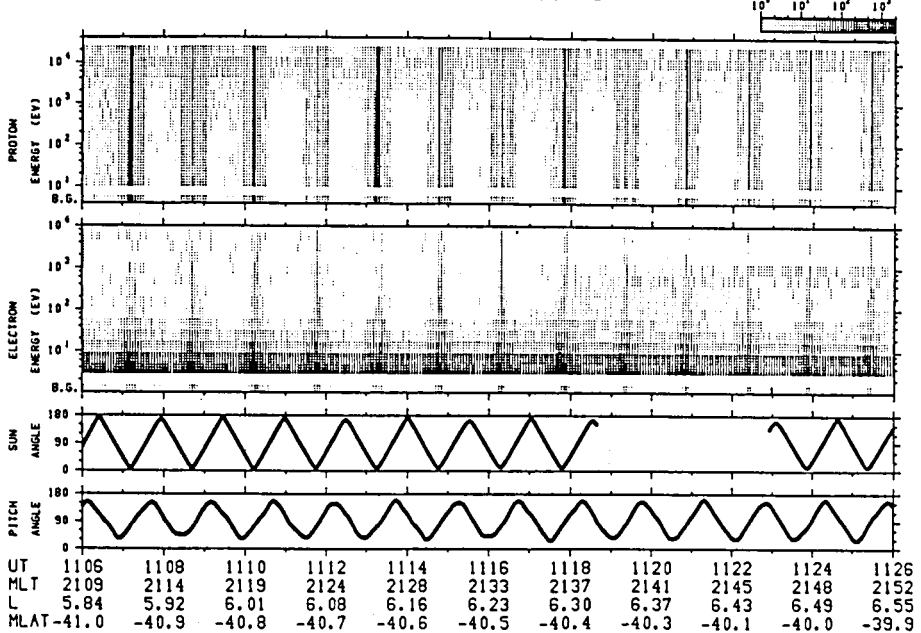
Fig. 5.22   An example of energy-time spectrogram. The sun angle and the
            particle pitch angle are also shown. Bottom four rows are
            universal time (UT) and the corresponding orbital position of
            the satellite; magnetic local time (MLT), L-value (L) and
            magnetic latitude (MLAT).

the magnetometer data measured simultaneously.   Unfortunately,

however, the function of the on-board magnetometer has become

degraded around the end of November, 1978.   Thereafter, we have

tried to deduce the pitch angles from the absolute direction of

the satellite spin axis which was determined from the sun sensor

data, in conjunction with certain symmetry properties of particle

flux.   The method is described below.

     Figure 5.23 shows a satellite coordinate system, in which

the z-axis is the satellite spin axis, "**C**" is a unit vector of

the view direction of the ESP instrument which is in the x'-y'
plane, and "**S**" and "**B$_o$**" are unit vectors of the solar direction
and the magnetic field vector, respectively. Then, the pitch
angle β_p of the measured particles is given by

$$\beta_p = \cos^{-1}(\sin\alpha_B \cos[\omega(t-T_o)-\psi]) , \tag{5.10}$$

where ω is an angular velocity of the spin, T_o is the time when
the view direction of the instrument is in the z'-x' plane, and
α_B and ψ are shown in Fig. 5.23. The quantities ω and T_o can be
obtained from the data of low-energy electrons which has a spin
modulation as shown in Fig. 5.22. However, the relationship
between the satellite spin axis and the magnetic field vector
cannot be obtained explicitly from the measured data. Thus, the
problem is to obtain α_B and ψ. Now, we consider the inertial
coordinate system, because the magnetic field vector at a given
time can be deduced from the IGRF (International Geomagnetic
Reference Field) model 1975, and also because the solar direction
at that time also can be expressed analytically in its coordinate.
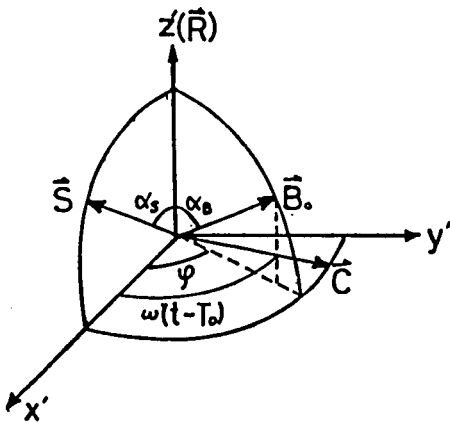
Fig. 5.23

Satellite coordinate system.

If the spin axis vector $\mathbf{R}$ is given in the inertial coordinate system, then α_B can be given by $\alpha_B = \cos^{-1}(\mathbf{B_o} \cdot \mathbf{R})$, and also ψ can be given by the solution of the following equations.

$$\cos\psi = (\cos\gamma - \cos\alpha_S \cos\alpha_B) \, / \, (\sin\alpha_B \sin\alpha_S)$$

and

$$\sin\psi = \mathbf{R} \cdot (\mathbf{S} \times \mathbf{B}) \, / \, (\sin\alpha_B \sin\alpha_S) \quad . \tag{5.11}$$

where γ is the angle between the vectors of $\mathbf{S}$ and $\mathbf{B_o}$, and α_S is the angle between the spin axis and the solar direction (see Fig. 5.23) which can be obtained from the sun sensor data. Therefore, the problem is reduced to obtain the spin axis vector $\mathbf{R}$ in the inertial coordinate system, which however cannot be determined uniquely by the sun sensor data only. Since α_S is known, $\mathbf{R}$ is on the cone as shown in Fig. 5.24, in which the z-axis is the solar direction and Ω is the phase angle parameter.

Thus the first step starts from assuming Ω. Then, the spin axis vector $\mathbf{R}$ in the inertial coordinate system can be determined,
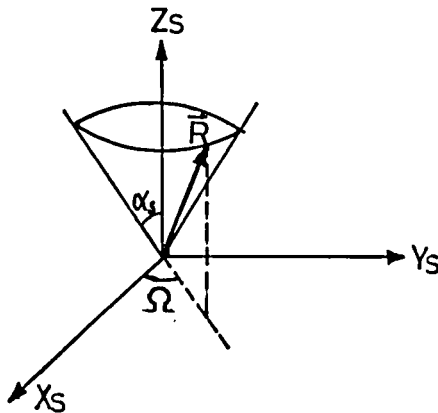
Fig. 5.24

Relationships between the solar direction and the satellite spin axis.

so that it can give rise to the observed pitch angle distribution, as mentioned above. The obtained pitch angle distribution for a given Ω could be classified, generally, into three types in shape, as shown in Fig. 5.25. Among them, types (a) or (c) are acceptable, since it is reasonable to assume that the angular distribution of electrons is symmetric about the local magnetic field line. In fact, the observed fluxes of high-energy electrons showed a spin modulation, especially around a local time of noon near the magnetic equator; the maximum appeared every half-spin period. It is quite reasonable that this maximum is assumed to occur at the pitch angle of 90°, because those electrons can be considered to have reached the noon sector by an adiabatic motion due to the gradient-B and curvature drift, and also because the earlier observations by the Explorer-45 and GEOS-2 satellites showed a similar feature [e.g., Anderson and Meda, 1977; Wrenn et al., 1979]. Therefore, the type (a) in Fig. 5.25 is most plausible, and thus the pitch angle distribution can be determined in a self-consistent manner. Even if a marked pitch angle anisotropy
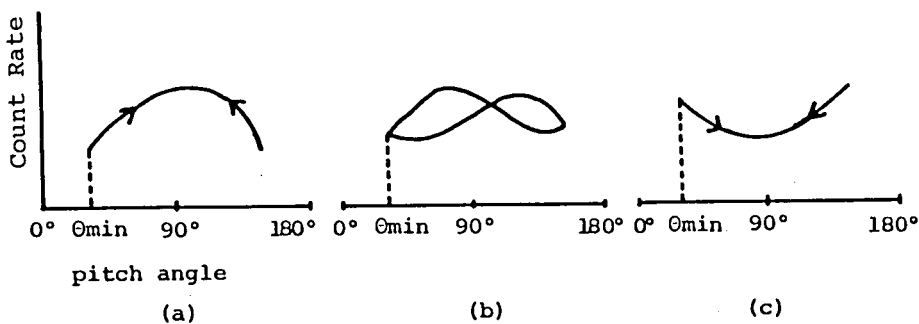
Fig. 5.25 Three types of the calculated pitch angle distribution. Type (a) is most plausible; see text.

could not be observed, the further condition that the spin axis

must be directed in nearly the same direction for at least several

days, allowed a unique determination of the spin axis direction,

because the satellite precession angle was sufficiently small.

As shown in Fig. 5.25 (a), the pitch angle distribution thus

determined does not always cover the whole pitch angle range from

0° to 180°, but rather a limited range (e.g., from 40 to 140°),

although it always covers a range around 90°.   The lowest and

highest measurable pitch angles depend on the spin axis direction

of the satellite in reference to the geomagnetic field line.

Figure 5.26 shows the direction of the satellite spin axis in the

inertial coordinate system during the Siple experiment which will

be described in Section 3.4.
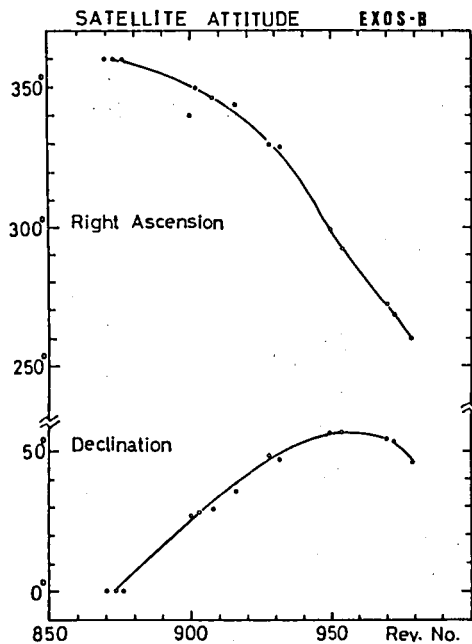
Fig. 5.26   Direction of the satellite spin axis in the inertial
coordinate system during the Siple experiment.

The VLF wave data to be presented in subsequent sections were provided by H. Matsumoto and I. Kimura (Kyoto University). Instrumentation of the VLF wave detector is described by Matsumoto et al. [1981].

3.3 Correlation of Hot Electrons with Natural Plasma Waves in a
    VLF Range —— Case Study

A continuous observation of both VLF waves and energetic electrons was made over more than 5 hours on Rev. 284.   The orbit for Rev. 284 is shown in Fig. 5.27.   As seen in Fig. 5.27, local time and geomagnetic latitude of the satellite are from 1820 LT to 2300 LT and from 35°S to 5°N, respectively.   Plasmapause crossings were detected twice on the orbit; outbound crossing at

REV. NO. = 284
DEC. 26,'78
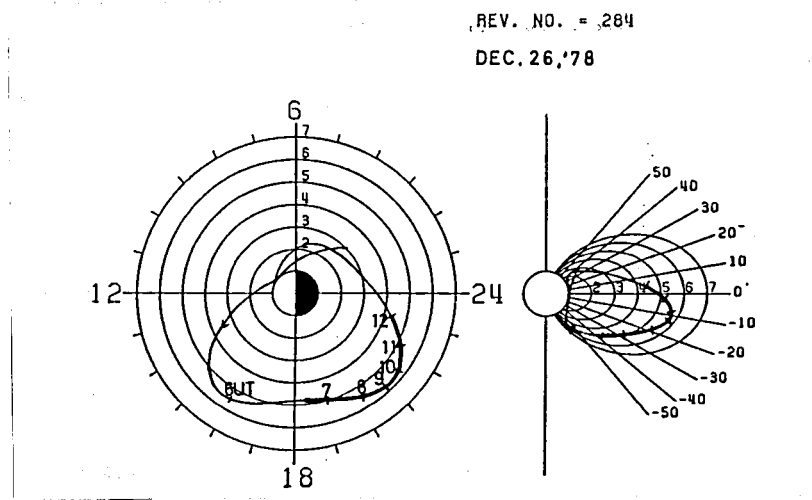
Fig. 5.27   Satellite orbit for Rev. 284.   Left and right panels show an
            equatorial projection and L-shells and a meridian projection
            on the orbit, respectively.   Thickened portions along the orbit
            indicate time intervals when the observations were made.

0815 UT and inbound crossing around 1100 UT, by a change of antenna impedance monitored by a VLF Doppler (DPL) measurement [Kimura and Hashimoto, 1980]. Therefore the L shell of the plasmapause lay around 5.5 to 5.2 in the evening to midnight sector on that day. Figure 5.28 shows a global pattern of the charged particle distribution on that pass which was reproduced from "EXOS-B WAVE / PARTICLE SUMMARY" (produced by A. Nishida and K. Maezawa at ISAS). In this figure, the counts were averaged in 10 PCM frames during 64 sec (i.e., 64 frames at 1024 bps or 16 frames at 256 bps) so as to eliminate the data contaminated by the solar radiation. The geomagnetic condition was moderate on the day, December 26: The magnetic storm took place on the previous day and a substorm occurred at 0730 UT on this day (ΣK_p = 17). Hot electrons appeared first around 0800 UT (L $\simeq$ 5.40, 2045 MLT, -17.36° geomagnetic latitude), but the energy was rather soft (several hundreds of eV). The electron energy and also flux increased with time, and at last, intense (burst-like) keV-electrons were detected for 30 minutes around 1030 UT (L $\simeq$ 5.42, 2215 MLT, -5.08° geomagnetic latitude). Those keV-electrons would be injected into the inner magnetosphere from the distant plasmasheet, probably due to the enhanced convection. Then, the keV-electrons decreased with time (with decreasing of L-value). Significant high-energy ions were detected throughout the orbit. Lower-energy ions were observed after 1130 UT (L $\simeq$ 4.76, 2252 MLT, 0.78° geomagnetic latitude), corresponding to the decrease of the keV-electrons.

Figure 5.29 shows a simultaneous presentation of both wave and electron spectra. The top panel shows a frequency spectrum of the VLF waves together with L-value, local cyclotron frequency and geomagnetic latitude. As seen in the figure, outside the
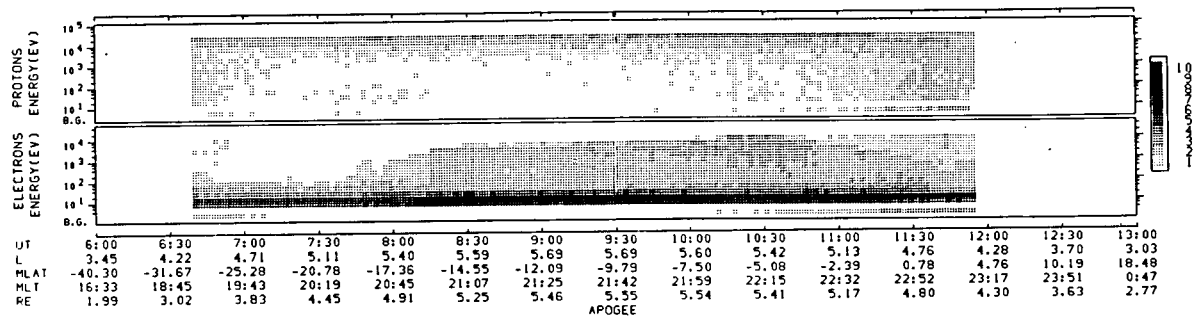
Fig. 5.28 Global pattern of the charged particle distribution on Rev. 284
(December 26, 1978; $\Sigma K_p = 17$).
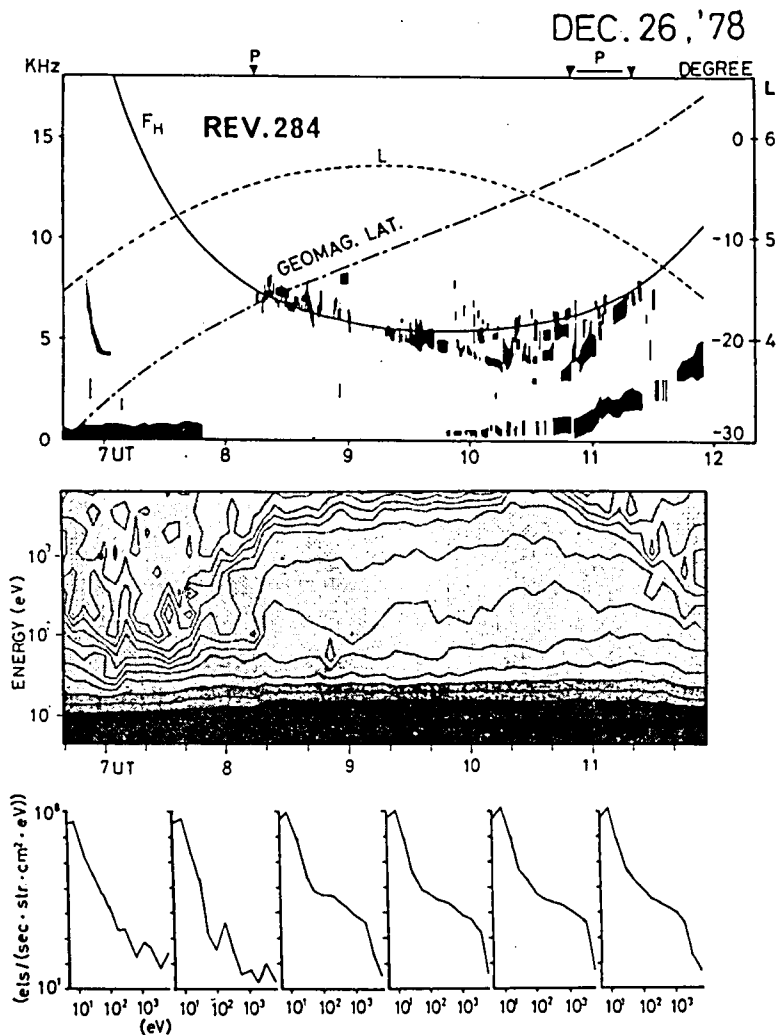
Fig. 5.29 A comparative display of VLF ave spectra and energetic
electron fluxes.   The top panel includes observed wave
spectra (blackened marks), local cyclotron frequency
(solid line), L-values (dashed line) and geomagnetic
latitude (chained line) of the satellite position.   The
middle panel is a contour map display of the observed
energetic electrons.   Darker area corresponds to higher
flux.   The lowest panel shows sampled energy spectra at
times corresponding to the vertical axes of the spectra.

plasmapause, waves whose frequency is almost equal or a little below the local cyclotron frequency are dominating. In the middle panel, the observed electron fluxes are shown by a contour map in which darker area represents higher electron fluxes. The bottom panel shows sampled energy spectra at times corresponding to the vertical axes for the energy spectra. A comparison between the wave and particle data shows a clear positive correlation of the VLF emissions appearing after 0815 UT with an increase of high energy fluxes in a range above 100 eV.

In order to see more detailed one-to-one correspondence between the VLF waves and electron fluxes, three sets of five minute data of both wave dynamic spectra and time variation of flux at each channel of the electron energy analyzer are given in Fig. 5.30. Panel (a) shows that no VLF wave activity is seen when the electron fluxes at higher channels (1 keV - 7 keV) are almost zero. Panels (b) and (c) show that the VLF emissions around or below the local cyclotron frequency (4 to 7 kHz) are well correlated with electrons with energy from 4 to 7 keV.

For a detailed correlation study between waves and particles, a great amount of data of simultaneous observations of waves and particles to be accumulated, though not many simultaneous observations have been performed. However, it is interesting to note that the case study presented here has revealed a clear positive correlation between VLF emissions around or below the local cyclotron frequency and several-keV electrons, especially in the plasmatrough.
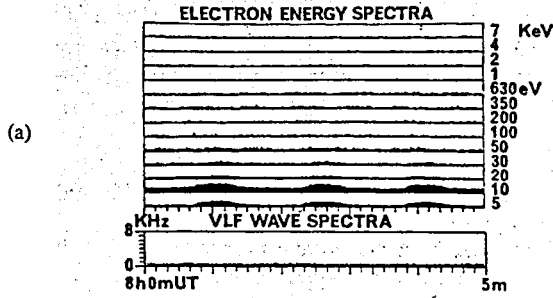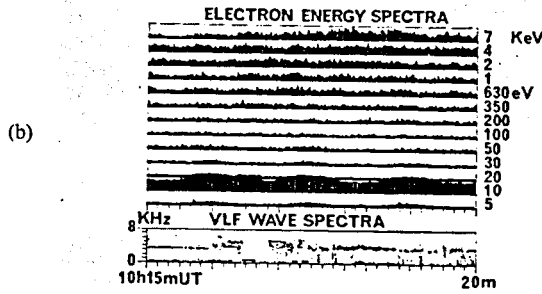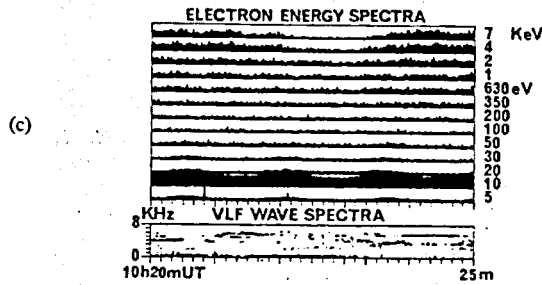
Fig. 5.30   A detailed comparison between wave dynamic spectra and electron fluxes at each channel of electron analyzer.

3.4 Characteristics of the Highly Anisotropic Electron Distributions Observed in the EXOS-B/Siple Experiment

3.4.1 Outline of the EXOS-B/Siple Experiment

VLF emissions triggered by manmade VLF signals transmitted from the ground have been observed for more than 20 years [Helliwell et al., 1964], but their generation mechanisms are still in question, even though there is a fairly general agreement among researchers that they are caused by nonlinear wave particle interactions in the magnetosphere; see Matsumoto [1979] for review. In order to study these interactions under controlled conditions, a high-power VLF transmitter connected to a 21 km dipole antenna was installed by Stanford University at Siple Station, Antarctica [Helliwell and Katsufrakis, 1974].

The EXOS-B/Siple Station joint experiments were carried out in two different periods, one in summer (July, August, and September 1979) and the other in winter (December 1979 - January 1980). The telemetry signal from EXOS-B was tracked at the NASA station in Rosman, North Carolina, in the summer campaign. The telemetry signals received at Rosman were sent to Stanford University in real-time by means of a telephone line. Workers at Stanford University then communicated with Siple Station by using a real time ATS-3 satellite link. This communication system thus enabled us to perform a closed loop active experiment, i.e., EXOS-B → Rosman → Stanford → Siple → EXOS-B. Therefore, we could change, for example, transmitter power and frequency format on a real-time basis while monitoring the wave and particle activities. In the winter campaign, the telemetry data acquisi-

tion was made at the NASA stations·in Quito and Santiago.

Siple Station is located at 84°W and 76°S geographic ($^{\circ}$5W geomagnetic; L $\sim$ 4.2). Since the Siple signals are expected to propagate primarily in the vicinity of the Siple meridian, the experiments were performed only for satellite passes which lay within $\pm$ 60° of the Siple longitude, on L shells in the range 2 < L < 5, and at latitudes near the geomagnetic equator, for the period from July 15 to August 12. Beginning on August 14, high geomagnetic latitude passes as well as the equatorial passes were selected. This change was made because the equatorial passes were all located in the afternoon sector, whereas on the ground, the rate of occurrence of Siple triggered emissions peaks in the early morning hours [Carpenter and Miller, 1976].

Summaries of the tracked orbits in the summer experiments are illustrated in Fig. 5.31, where the satellite local time (SAT-LT), geomagnetic longitude (GM-LONG) and latitudes (GMLAT), and L values are plotted. The passes on which Siple signals were observed are marked by open circles in the longitude column and those on which VLF emissions were observed are marked by solid triangles in the local time column. Siple signals were detected on about 50 % of the passes, and VLF emissions triggered by Siple signals were observed on August 14, 15, 17, 18, and 19, these passes being marked by an asterisk in Fig. 5.31 in the latitude column.

As to the geomagnetic activity in relation to the observed passes,.Figure 5.32 indicates the K_p indices during the experimental period. It is very interesting that four passes out of the five passes on which Siple triggered emissions were detected are concentrated in a geomagnetically very quiet period, just after a
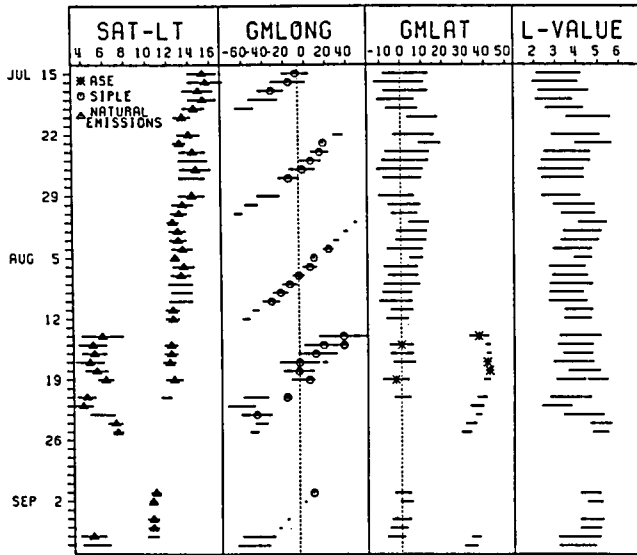
Fig. 5.31 Summary of the orbits during the EXOS-B/Siple Station joint
experiments made in the period from July 15 to September 7, 1979.
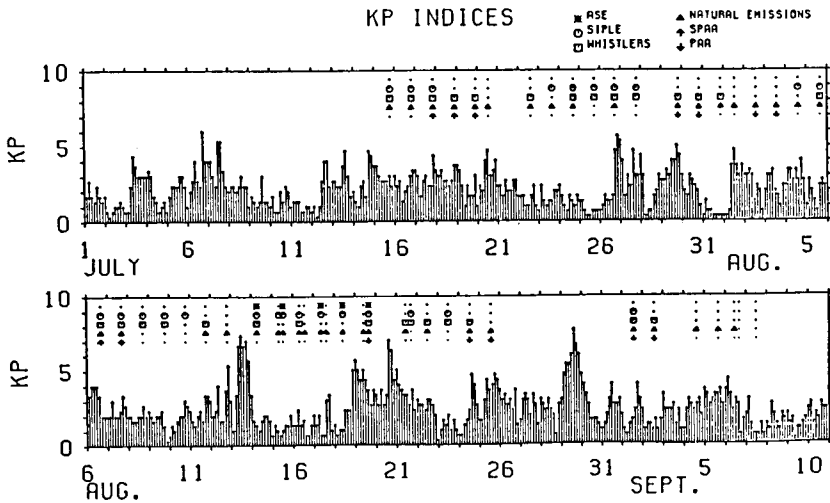
Fig. 5.32 Geomagnetic activity represented by K$_p$ indices and summary
results during the experiments. Detection of the Siple signal
(open circles), whistlers (squares), natural VLF emissions
(triangles), high pitch angle anisotropy or SPAA (upward-
pointing arrows), and medium pitch angle anisotropy or PAA
(downward-pointing arrows) at the satellite are marked for
each pass.

large magnetic storm on August 13.·

Electron pitch angle distributions during the Siple trigger-
ing events were generally not highly anisotropic with rather high
fluxes for a wide range of energy, whereas intense Siple signals
not associated with triggered emissions were accompanied by high
pitch anisotropy (HPAA) of the electron fluxes. Characteristics
of this HPAA event are described below.

3.4.2   HPAA Event

Siple signals were detected by EXOS-B mostly when the
satellite was located within ± 25° in geomagnetic longitude from
the Siple geomagnetic meridian plane.   Data from two days,
August 6 and 7, on which the satellite passes were quite close to
the Siple meridian, are shown in Figs. 5.33 and 5.34.   These
figures give simultaneous presentation of electron fluxes and
corresponding wave dynamic spectra on a compressed time scale.
In each figure, the VLF dynamic spectrum is shown in the upper
panel in an f-t format with a frequency scale from 0 to 10 kHz.
The electron flux in 8 energy channels is illustrated as a
function of time below. On the left of each row, average energies
of each channel are given, while on the right the maximum flux
(top of the scale) in els./(cm² s sr eV) is given.   The scale for
the electron flux is linear. On the horizontal axes are given
UT, L value, geomagnetic latitude, local time, and local cyclotron
frequency.

These figures reveal an interesting feature of the energetic
electron flux.   In almost all energy channels, the electron flux
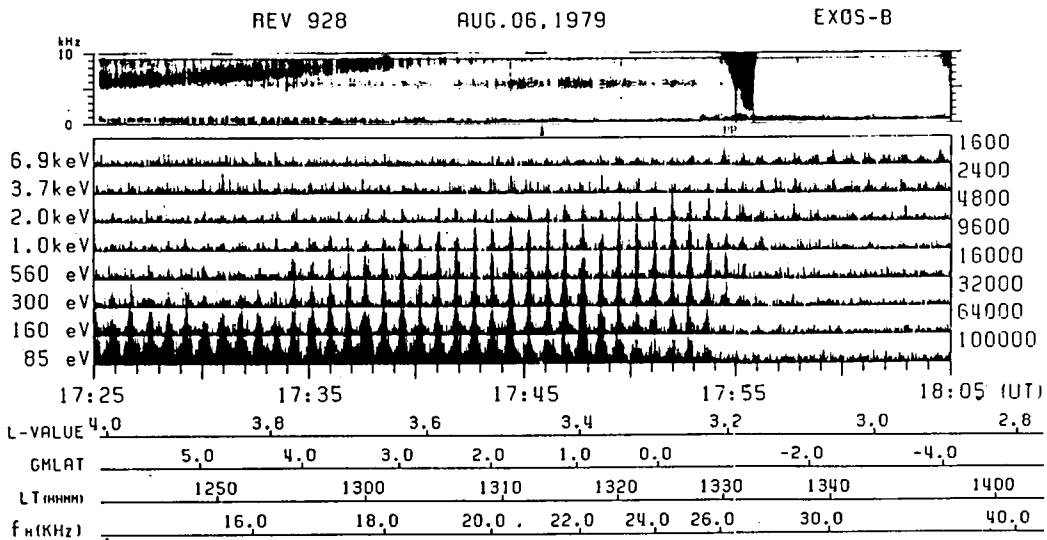
Fig. 5.33   Electron fluxes and corresponding VLF wave spectra on August 6,
High pitch angle anisotropy (HAPP) is seen.   Strong Siple
signals are observed from 1732 to 1753 UT.
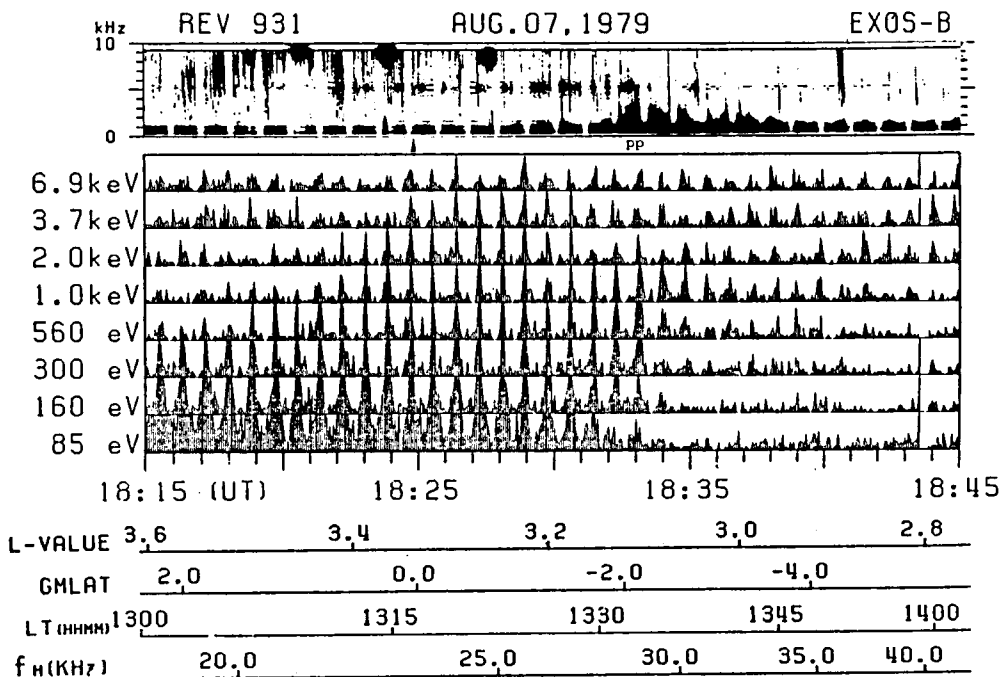
Fig. 5.34   Electron fluxes and corresponding VLF wave spectra on August 7.
High pitch angle anisotropy (HAPP) is seen.   Strong Siple signals
are observed from 1821 to 1852 UT.

is strongly modulated with a period of about 50 s, which is half
of the spin period of the satellite.   This means that the
electron pitch angle distribution is highly anisotropic with
respect to the geomagnetic field.   Detailed analysis of the
pitch angle distribution taking into account the satellite
attitude with respect to the geomagnetic field shows that the
peaks in each flux variation correspond to the flux in the
direction of $90°$ pitch angle, as noted in Section 3.2.   Such a
pitch angle distribution is usually called a 'pancake type'
[Lyons et al., 1972; Lyons and Williams, 1975a, b].   In Fig. 5.35
the observed pitch angle distributions for the August 6 case are
shown for several different energies.   In Fig. 5.35 (b) are
shown the corresponding pitch angle distributions smoothed by a
curve fitting technique.   The fitting was made by assuming a
form, $f(\alpha) = a_1 \sin m_1 \alpha + a_2 \sin m_2 \alpha$, where α is the pitch angle
and a_1, a_2, m_1, and m_2 are the constants obtained by the fitting.
Some sample values of these constants at two different time slots
for the August 6 event are tabulated in Table 5.3.   Sharper
peaks show higher pitch angle anisotropy.   As seen in these
figures, the energy at which the anisotropy is maximum, shifts
upward from the lowest (85 eV) to the highest (6.9 keV) energy
channel as the satellite moves into the plasmasphere.   The
location of the plasmapause is marked by 'pp' in the upper panel
of Figures 5.33 and 5.34 and was identified by a measurement of
the antenna impedance at 22.3 kHz [Kimura and Hashimoto, 1981].
The phenomenon of the smooth upward shift in energy of the
maximum pitch angle anisotropy was observed on five passes out of
50 passes during the summer campaign.   These events are marked
by upward pointing arrows in the K_p chart in Fig. 5.32, which
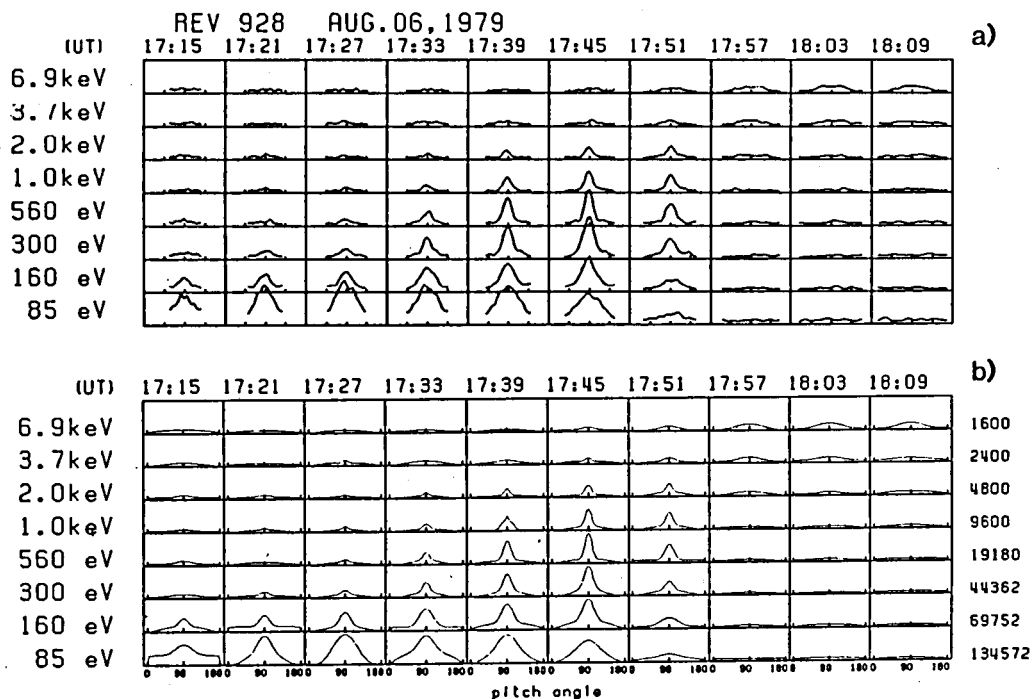
Fig. 5.35 Pitch angle distribution on August 6.
(a) Observed and (b) corresponding smoothed distribution.

Table 5.3 Characteristic constants of smoothed pitch angle distributions
for two different time slots in the August 6 event.

Time UT	Energy channel keV	a_1	m_1	a_2	m_2
1733	6.9	0.8469E+02	0.02994	0.8627E+02	5.69389
1733	3.7	0.1748E+03	1.32910	0.1678E+03	1.76025
1733	2.0	0.4574E+03	2.22496	0.4031E+03	124.85388
1733	1.0	0.8300E+03	1.61497	0.1329E+04	52.17932
1733	0.56	0.3031E+04	3.12465	0.3956E+04	60.95978
1733	0.30	0.7386E+04	2.60124	0.1393E+05	54.93289
1733	0.16	0.7856E+04	0.01476	0.3839E+05	11.79574
1733	0.085	0.5581E+05	0.76236	0.6063E+05	11.02113
1751	6.9	0.7895E+02	1.32888	0.1592E+03	5.63798
1751	3.7	0.1804E+03	0.91673	0.2496E+03	17.39874
1751	2.0	0.6938E+03	1.82838	0.1202E+04	71.54156
1751	1.0	0.1313E+04	1.82857	0.3715E+04	48.47136
1751	0.56	0.1688E+04	0.01102	0.8949E+04	27.61678
1751	0.30	0.7043E+04	1.67847	0.1249E+05	34.52147
1751	0.16	0.5236E+04	0.09222	0.1791E+05	7.05275
1751	0.085	0.1799E+05	0.31065	0.1469E+05	6.96307

stands for 'high pitch angle anisotropy (HPAA)'. In cases in
which the pitch angle distribution has no sharp pancake shape but
has a clear spin modulation effect in the observed flux that
peaks at 90°, downward pointing arrows or 'PAA' is used in Fig.
5.32.

Anderson and Maeda [1977] observed flux enhancements of a
similar nature in the pitch angle distributions in the same
energy range by the S3-A satellite just outside the plasmasphere,
which coincided with natural VLF emission events. From Figure 8
in their paper, it appears that the higher energy electrons are
found on the outer side of the plasmapause. There are, however,
some differences between theirs and ours. The first is that the
local time of their observation was mostly in the dusk to midnight
hours, whereas our observations were mostly in the afternoon
sector. The other point is that in our inbound observation, the
peak of the flux appears first at lower energy and eventually
moves toward higher energy, while vice versa in their observation.

Although transmissions lasted until 1809 UT on August 6,
Siple signals disappeared suddenly at 1753:10 UT, a time which is
almost coincident with the disappearance of the HPAA distribution
and with the plasmapause crossing time of the satellite. On
August 7, as shown in Figure 5.34, a similar weakening of Siple
signals was seen around 1835 UT in association with the dis-
appearance of the pancake distribution.

It is interesting to note that on these two events, strong
Siple signals were observed, but were not accompanied by any form
of artificially stimulated emissions (ASEs). In general, due to
the divergence of the ray paths, Siple signals propagating in a
nonducted mode just outside the plasmapause should be about 6 dB

lower in intensity than those propagating just inside the plasma-pause, where a strong focusing of the ray paths by the influence of the plasmapause intensifies the signal strength [Inan and Bell, 1977].   In spite of this general tendency, on both days strong signals were observed only for the region outside the plasmapause.   Judging from these facts, we conclude that the Siple signals were most likely amplified by the pitch angle distribution with high anisotropy.   In fact, calculation of the wave growth rate using the observed pitch angle distribution [Kimura et al., 1983] has shown that the Siple signal intensity is high only when the growth rate is positive and large.

There were a total of 5 HPAA events; on July 17, 18, 19, August 6 and 7, and one medium PAA on July 30 and 4 other PAA on July 29, August 19, and September 1 and 2.   Among these events, strong Siple signals were observed only on August 6, 7, and 19, and September 1.   A weak Siple signal was observed on July 17, and for other events no Siple signal was observed.   It is, however, evident from Fig. 5.31 that for all events except August 6, 7, and 19, September 1 and 2, the satellite location was more than 20° away from the Siple meridian, and hence the injected signal strength observed on the satellite meridian should have been quite low.   In this case, amplification may not have been sufficient to raise the signal to the observable level.

3.5 Conclusion

The charged-particle instrument on board the JIKIKEN satellite was designed and constructed to measure electrons and ions in the

energy ranges from a few eV to ∿ 10 keV and from 10 eV to 30 keV, respectively. Since the satellite is spin-stabilized, the instrument was installed on the satellite so that the view direction was perpendicular to the spin axis of the satellite in order to cover as wide pitch angles as possible by using the satellite spin. The electron sensor was essentially the same as that installed on the KYOKKO satellite, and the methods of energy scanning and data sampling also were identically designed. Therefore, the method of data reduction was the same as that used for the KYOKKO observation, except for the estimate of particle pitch angles. After malfunction of the on-board magnetometer, we have established a self consistent method for obtaining the pitch angle distribution by using the sun sensor data in conjunction with certain symmetry properties of the particle flux.

Although the data of simultaneous observations of both wave spectra and energetic electrons have been very few because of the various operational conditions of the satellite, case study has revealed interesting properties of correlation between VLF waves and energetic electrons in the plasma trough. When the electron fluxes in keV-energy range were negligibly low in the plasmasphere, no VLF wave activity was seen, whereas the VLF emissions around or a little below the local cyclotron frequency (4 to 7 kHz) in the plasma trough were well correlated with the burst-like injection of electrons with energy from 1 to 7 keV. Theoretical estimate of the resonant electron energy in a cyclotron interaction of the whistler-mode wave has shown just the same energy as the observation [Morikura, 1981]. Therefore it can be concluded that these VLF emissions were produced near the observation point by a resonant cyclotron interaction in the whistler-mode wave

with energetic electrons.   However, such a one-to-one correlation
between the wave and particle data was generally very few because
of the propagating property of waves.   A great amount of data of
the simultaneous observations of both wave and particle spectra
is necessary to be accumulated for detailed analysis.

The high pitch angle anisotropy (HPAA) of energetic electrons
with a maximum at 90° was found out in the EXOS-B/Siple joint
experiment.   One of the interesting features is that the energy
of the electrons which showed a HPAA sifted upward as the satellite
moved into the plasmasphere, crossing the plasmapause in the
equatorial region around a local time of noon.   The source of
this feature is not well understood now, but one possibility is
that the pancake pitch angle distributions are the evidence of a
past history of scattering by ELF plasmaspheric hiss, as argued
by Lyons et al. [1972].   Another feature related with the HPAA
event is that, when the satellite was located within ± 20° in
geomagnetic longitude from the Siple meridian, strong Siple
signals were observed in the geomagnetic equatorial region just
outside the plasmapause, in association with the HPAA electron
distribution.   The Siple signals were most likely amplified by
the cyclotron instability due to the HPAA, although the flux of
resonant electrons was relatively small.

In summary, the charged particle instrument on board the
JIKIKEN satellite has provided us with interesting characteristics
of energetic electrons which have a good correlation with the VLF
wave activities. However, since the wave characteristics general-
ly change from time to time in a rather short time scale, it will
be necessary in future to make a high time resolution measurement
of particles, although it may need much higher telemetry rate.

The time resolution of measurement of the pitch angle distribution
is limited by a spin period of the satellite in such an instrument
as used here, but a multi-detector instrument (e.g., a quadri-
spherical electrostatic analyzer) will be available for high time
resolution measurement of the pitch angle distribution, if the
telemetry capability will be sufficient.

§4. Observations of Low-Energy Charged Particles by OHZORA
    Satellite

The EXOS-C (OHZORA) satellite was successfully launched on
February 14, 1984 into a semi-polar orbit with an inclination of
$\sim 75^{\circ}$ and with the initial apogee and perigee of 865 km and 353
km, respectively. A low-energy particle experiment, named ESP,
was installed on the satellite to study global characteristics of
charged-particle distributions and interactions of particles with
ambient plasma and waves.

The ESP instrument was designed to measure energy and pitch-
angle distributions of electrons over the energy range from 6 eV
to 16 keV and positive ions from 200 eV to 16 keV, respectively.
This instrument has been successfully operated and obtained the
intensity and energy spectra of ionospheric photoelectrons in
addition to the energetic particles over a wide range of latitude,
longitude, altitude(350-865 km) and local time. It has been
well recognized that particle observations in this energy range
are essential for the understanding of the ionospheric and
magnetospheric physics, and extensive measurements have been made,
as described in Chapter I. Most of the data obtained by the

EXOS-C satellite are generally consistent with those obtained
hitherto by others, but some peculiar phenomena have also been
found out.

4.1   Instrumentation

     The instrument ESP was designed to measure energy and pitch-
angle distributions of electrons over the energy range from 6 eV
to 16 keV and positive ions from 200 eV to 16 keV, respectively.
Figure 5.36 shows a schematic drawing of the instrument viewed from
three orthogonal directions.   It comprises three sensors (LE, HE
and HI) and a common electronics for control and processing of the
data.   The LE sensor measures an energy distribution of low-energy
electrons over the energy range from 6 eV to 300 eV, while the HE
and HI sensors measure higher-energy electrons and ions,
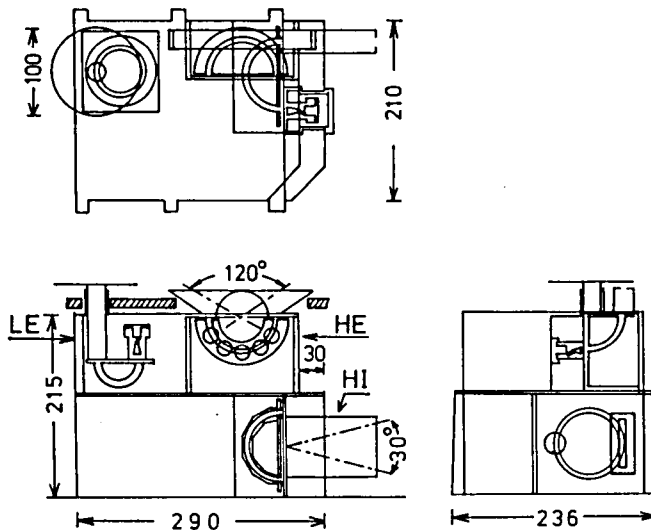
Fig. 5.36   Schematic drawing of the ESP instrument viewed from three
            orthogonal directions.

respectively, from 200 eV to 16 keV.   Characteristics of each
sensor are summarized in Table 5.4.

All three sensors have similar configurations in principle;
each sensor consists of an inlet collimator, a spherical electro-
static analyzer and channeltron(s) (Galileo CEM 4039).   Charged
particles entering the analyzer through the collimator are
deflected by the electric field ($E \propto 1/r^2$), and only those
particles which have an appropriate energy can pass through the
analyzer and impinge onto the channeltron.   All channeltrons are
shielded by aluminium of ~ 1 gr/cm^2 in order to reduce background
count rate due to penetrating high-energy particles.   The unique
features of each sensor are described below.

(a) LE sensor

The main part of the LE sensor is surrounded by a high-μ
metal in order to shield the sensor from the external magnetic
field.   The collimator has a cylindrical shape with a circular
electrode around the inlet part and is extruded from the satellite
surface by 20 mm.   Its electric potential can be controlled by
command to be 0, +1, +2, +5, or +10 volts relative to the satellite

Table 5.4 Characteristics of the ESP sensors on board OHZORA satellite.

	Sensors		
	LE	HE	HI
Analyzer	Hemispherical	Quadrispherical	Hemispherical
Energy range	6–300 eV	0.2–16 keV	0.2–16 keV
	electron	electron	ion
Energy resolution $\Delta E/E$	5%	13%	5%
Geometric factor[*] cm^2 str eV/eV	2.0×10^{-5}	1.3×10^{-4}	2.3×10^{-4}
Field of view	6.2°	10° × 10°	10° × 30°

[*] Per each channeltron.

in order to compensate the potential difference between ambient

plasma and the satellite. The energy analyzer is hemispherical

with inner and outer radii of 21.5 mm and 28.5 mm, respectively,

and has inlet and exit apertures of 3 mm ϕ. The potentials of

inner and outer hemispheres are set to satisfy $R_i V_i + R_o V_o = 0$ in

order to minimize the fringing-field effect, where R_i and R_o are

the radii of inner and outer hemispheres and V_i and V_o are the

corresponding potentials relative to the collimator, respectively,

($V_i > 0$ for electron measurement). A mesh with the potential of

5 volts below that of the outer hemisphere is inserted between

the exit slit of the analyzer and the channeltron in order to

suppress instrumental secondaries. Thus, although the energy is

scanned from 4 eV up to 300 eV (see Table 5.5), the count data

below 6 eV provide background information (see Appendix). In

order to measure more definitely the background count rate due to

penetrating high-energy particles, the mesh potential is set at

-80 volts for the step numbers 1 and 2.

(b) HE sensor

The energy analyzer of the HE sensor is quadrispherical with

inner and outer radii of 37.5 mm and 42.5 mm, respectively,

followed by five channeltrons. The analyzer is operated at

usual balanced potentials; i.e., equal voltages of opposite

polarity ($V_i > 0$) are applied to the inner and outer spherical

plates, respectively. The dispersion in the polar angle of the

beam incidence results in the maximum spatial dispersion of the

beam at the 90° deflection in spherical electrostatic analyzers,

so that the exit position of the beam in a quadrispherical

analyzer can be related directly to the polar angle of incidence.

The channeltrons in the HE sensor are placed at the positions corresponding to the incident polar angles of $0°$, $±30°$ and $±60°$, respectively. Thus the HE sensor can measure electron fluxes at five different pitch angles simultaneously. In addition, although the sensitivity of a usual quadrispherical analyzer has a dependence on the incident polar angle θ as $G \sim \cos \theta$ and hence decreases when $\theta \rightarrow ±90°$, we have developed a sophisticated shaping collimator which gives identical view fields and geometric factors for five channeltrons without sacrificing sensitivities. Our quadrispherical analyzer has no slit at the entrance plane of the analyzer for defining the entrance area, and instead, the shaping collimator defines the entrance area of the analyzer as well as the field of view. The geometric factor for each channeltron is defined by the geometry of the collimator and the exit slit of the analyzer.

(c) HI sensor

The energy analyzer is a hemispherical one with the same inner and outer radii as those of the HE sensor, and it is operated also at the balanced potentials with $V_i < 0$. The field of view of the collimator is enlarged to $5° \times 30°$ in order to obtain a large geometric factor.

Figure 5.37 shows a schematic view of the EXOS-C satellite, where the LE and HE sensors are at the location designated ESP. The satellite has four solar-cell paddles, and the bottom side of the spacecraft as illustrated in Fig. 5.37 is controlled to face the sun. Therefore, the LE and HE sensors view the anti-solar direction and are completely free from the EUV background due to
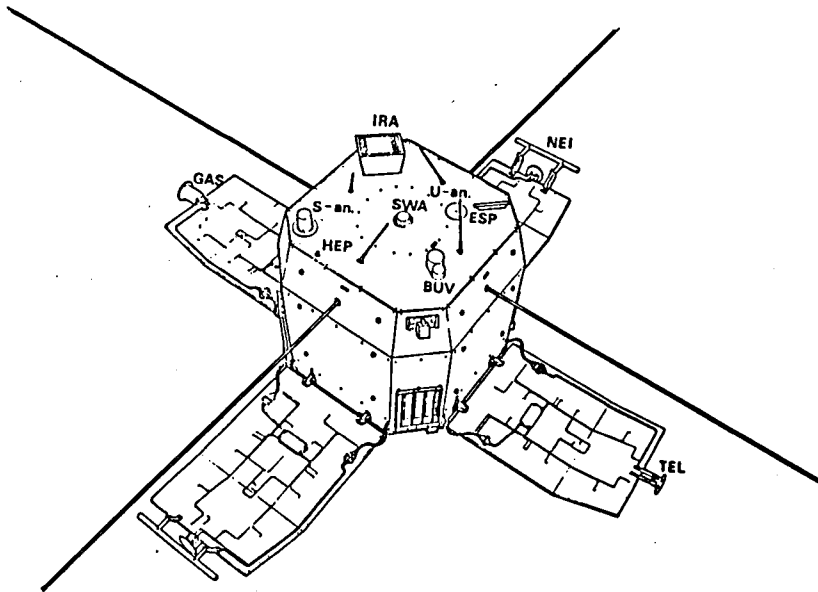
Fig. 5.37 Schematic view of OHZORA satellite.
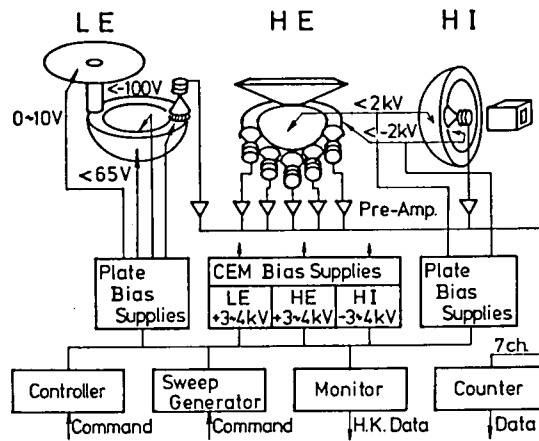
Fig. 5.38 Block diagram of the ESP instrument on board OHZORA.

the solar radiation. The HI sensor is also free from such background, since its view direction is perpendicular to the main axis of the satellite though it cannot be seen in Fig. 5.37.

Figure 5.38 shows a block diagram of the instrument. As noted above, the instrument includes total of seven channeltrons; one for LE, five for HE and one for HI. Each sensor has a high-voltage power supply for the channeltron(s) independently. The level of the high voltage can be selected by command in three steps of 3, 3.5 and 4 kV. Output charge pulses of each channeltron are amplified, discriminated, shaped and are counted by a 19-bit counter. Eight levels of pulse discrimination are prepared independently for each sensor in order to obtain pulse height distributions. The count data are compressed into 8-bit data and transmitted to the ground in the allocated PCM-telemetry words. The conversion of the compressed 8-bit word to the original counting can be made by the following relation.

$$
\left.\begin{array}{l}
C = D \text{ for } S = 15 \\
\text{or} \\
C = 2^{14-S} \times (D+16) \text{ for } S \neq 15,
\end{array}\right\} \quad (5.12)
$$

where C is the original sample counts, and D and S are the decimal values of the upper and lower 4 bits of the 8-bit word, respectively.

Energy of measurement is scanned stepwise by applying stepped voltages (SV) to the analyzer plates. As shown in Fig. 5.38, the instrument includes two SV power supplies for energy scanning; one is common for both HE and HI, and another is for LE. Figure 5.39 shows energy-scanning modes for LE and HEI (HE
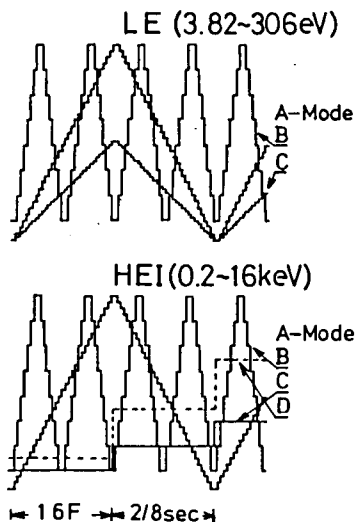
Fig. 5.39   Energy scanning modes of ESP on board OHZORA.

and HI), respectively.   Tables 5.5 and 5.6 show the relationships
among step numbers, measurement energies and scanning modes.   It
should be noted that the A-mode is a basic 32-step mode for both
of LE and HEI, and that all results presented in subsequent
sections have been obtained in the A-mode.   The B-mode is a high
time resolution mode which sacrifices the energy resolution, and
the C and D modes for HEI are prepared for detecting modulated
fluxes.

The differential particle flux f(E) can be obtained from the
observed counts C by

$$f(E) = C / (\langle G \cdot \Delta E \rangle \ \tau \ \eta), \tag{5.13}$$

where $\langle G \cdot \Delta E \rangle$ is an energy-geometric factor of the analyzer,
τ is a sampling time and η is the detection efficiency.   For an

Table 5.5 Measurement energies and observation modes in the LE sensor.

Step	Energy (eV)	A-mode	B-mode	C-mode	Step	Energy (eV)	A-mode	B-mode	C-mode
1	(3.56)*			o	33	34.2			
2	(3.82)*	o		o	34	36.7	o		
3	(4.10)*			o	35	39.4			
4	(4.40)*	o		o	36	42.3	o		
5	(4.72)*			o	37	45.4			
6	(5.07)*	o		o	38	48.7	o		
7	(5.44)*			o	39	52.3			
8	(5.84)*	o	o	o	40	56.1	o	o	
9	6.27			o	41	60.2			
10	6.73	o		o	42	64.6	o		
11	7.22			o	43	69.3			
12	7.75	o		o	44	74.4	o		
13	8.32			o	45	79.9			
14	8.92	o		o	46	85.7	o		
15	9.58			o	47	92.0			
16	10.3	o	o	o	48	98.7	o	o	
17	11.0			o	49	106.			
18	11.8	o		o	50	114.	o		
19	12.7			o	51	122.			
20	13.6	o		o	52	131.	o		
21	14.6			o	53	141.			
22	15.7	o		o	54	151.	o		
23	16.9			o	55	162.			
24	18.1	o	o	o	56	174.	o	o	
25	19.4			o	57	187.			
26	20.8	o		o	58	200.	o		
27	22.4			o	59	215.			
28	24.0	o		o	60	231.	o		
29	25.8			o	61	248.			
30	27.7	o		o	62	266.	o		
31	29.7			o	63	285.			
32	31.9	o	o	o	64	306.	o	o	

*For background information.

analyzer of the type used in this instrument, the energy resolution ΔE/E is constant over the energy range of measurement, where E is the center energy of transmitted particles and ΔE is the energy bandwidth, respectively.   To estimate ⟨G·ΔE⟩ it is necessary to know the transmission function of the analyzer which is a complex function of the inlet position, two-dimensional incidence angle and energy of incident particles.   Characteristics of each sensor were derived by numerical fitting of the transmission function obtained experimentally in the pre-flight calibration test and are summarized in Table 5.4.   Figure 5.40

Table 5.6 Measurement energies and observation modes in the HE and HI sensors.

Step	Energy (keV)	A-mode	B-mode	C-mode	D-mode
1	(0.20)*	o			
2	(0.23)*	o			
3	(0.27)*	o			
4	(0.31)*	o	o	o	
5	0.35	o			
6	0.41	o			o
7	0.47	o			
8	0.54	o	o	o	
9	0.62	o			
10	0.71	o			
11	0.82	o			
12	0.95	o	o	o	
13	1.09	o			
14	1.26	o			o
15	1.45	o			
16	1.67	o	o	o	
17	1.92	o			
18	2.21	o			
19	2.55	o			
20	2.93	o	o	o	
21	3.38	o			
22	3.89	o			o
23	4.48	o			
24	5.16	o	o	o	
25	5.95	o			
26	6.85	o			
27	7.89	o			
28	9.09	o	o	o	
29	10.5	o			
30	12.1	o			o
31	13.9	o			
32	16.0	o	o	o	

*: Overlapped with the LE measurement.

shows an example of transmission curves for the HE sensor. It can be seen that the fitted curves agree well with experimental results.

4.2 Instrument Performance in Orbit

Operation of the ESP experiment commenced about 4 weeks after the launch, at which time all high-voltage power supplies were turned on successfully, and it was confirmed that the whole
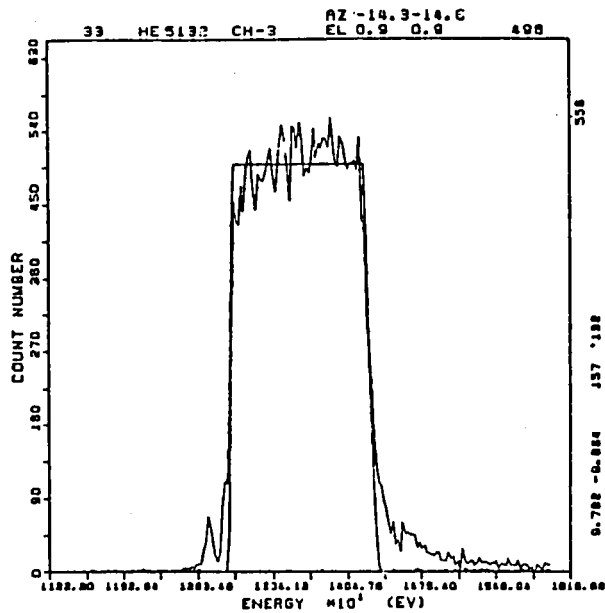
(a)
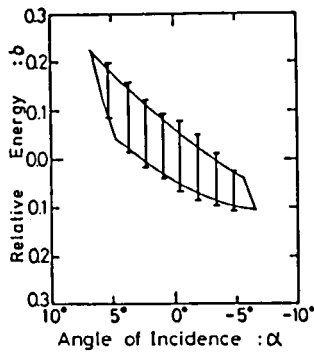
(b)

Fig. 5.40 Examples of transmission curves for HE-3.
    (a) Energy response. The zig-zag line shows an experimental
    result, and the smooth rectangular response is numerical fitting.
    (b) Energy-angle response. The bars how responses obtained
    experimentally, and the contour curve shows a numerical result,
    respectively.

instrument of ESP operated normally. In this section we describe the performance of the instrument in orbit for better understanding of the observational results.

4.2.1 Channeltron Performance

A pulse height distribution of each channeltron output was examined by inter-comparison among the data obtained at different levels of pulse discrimination. The result indicated that all channeltrons had sufficient gains so that they were operating in the well-saturated range at the lowest level of the high voltage. It was also decided that the discrimination level of the fifth level was suitable for all channeltrons. No significant degradation in the channeltron gain has been detected in 5 months after the launch.

4.2.2 LE Bias

As noted in section 4.1, the potential (LE bias) of the inlet collimator of the LE sensor can be selected by command to be one of 0, +1, +2, +5 and +10 volts relative to the satellite. It has been determined by examination of the obtained data that the LE bias of 1-volt level is most suitable. The measured energies of the LE data are relative to this LE bias.

4.2.3 Background Count Rate and Its Subtraction

As noted in section 4.1, the LE sensor has background channels (steps) in the energy scanning. Therefore, the background count

rate has been subtracted easily from the signal count rate, although the background has been negligibly small except in the South-Atlantic anomaly region.   Other two sensors have no specified channels for background information, but the data have indicated that the background count rate is negligibly small also in the HI sensor except in the South-Atlantic anomaly region. Therefore, no background correction has been made in the HI data. The dark counts in the HE data, however, have been found to be greater than expected, and the count rate corresponding to 2 x 10^6 els./cm^2 sec str keV at 1 keV have been subtracted from HE data in normal circumstances.   We believe that this does not produce a problem for investigation on the auroral electron precipitation.   Validity of the background subtraction from the HE data has been examined by comparing the result with the LE data in the overlapping energy range of 200 - 300 eV.   Figure 5.41 shows an example of comparison between the LE data and the HE data which were obtained during stable precipitation in the dayside auroral zone at Rev. 00974.   It is seen that both data show a good agreement.

4.3 Observational Results and Discussion

    The ESP experiment has yielded global characteristics of low energy charged-particle distributions over a wide range of latitude, longitude, altitude(350-865 km) and local time.   In this section some typical examples of data are presented and discussed.   Here the term "typical" means that similar features are observed·frequently on many orbits other than the ones
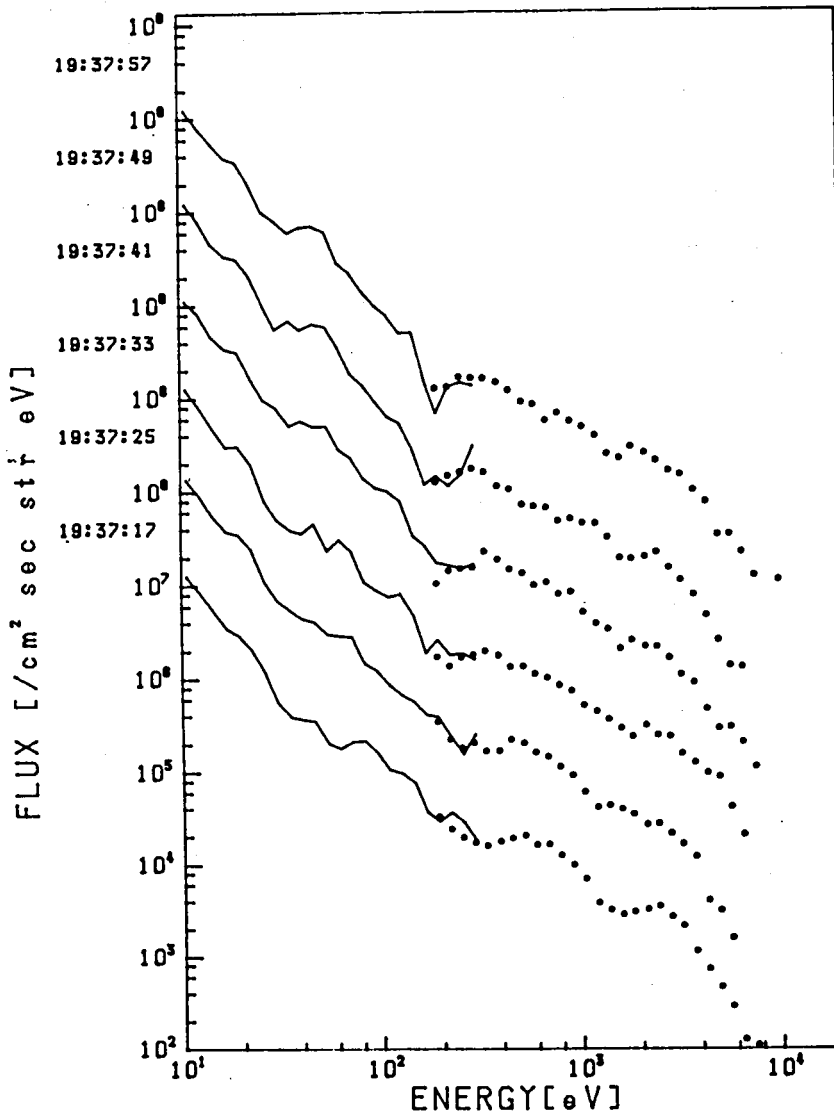
Fig. 5.41 Intercomparison between the LE and HE results.

presented here.

Figures 5.42, 5.43 and 5.44 show global patterns of charged-particle distributions obtained from the ESP and HEP (high energy particle) experiments at Revs. 00835, 00944 and 00953, respectively, in moderate geomagnetic activity; K_p indices were 2-, 3- and 2 at Revs. 00835, 00944 and 00953, respectively. In each figure, the upper five panels show the energy-time spectrograms of the LE, HE-3, HE-5, HE-1 and HI data from ESP, while the lower two panels show the integrated flux obtained from the S-1 sensor of HEP. The pitch angle of each sensor is also shown below each energy-time spectrogram. Note that the 0°-pitch angle means precipitation in the northern hemisphere, whereas the 180°-pitch angle does so in the southern hemisphere. The satellite location is given in the bottom rows.

The HE and HI data show several characteristic zones of energetic particle distributions; auroral zones in the southern and northern hemispheres, the region of the South-Atlantic geomagnetic anomaly, and the equator zone.

At first, let us discuss characteristics of auroral particles. It should be noted that in each figure the southern auroral region is on the dayside while the northern one is on the nightside, and that the highest invariant latitudes are $(72.5^{\circ}, 73.7^{\circ})$ at Rev. 00835, $(70.0^{\circ}, 71.3^{\circ})$ at Rev. 00944 and $(72.5^{\circ}, 78.2^{\circ})$ at Rev. 00953, respectively, where the first and second values in the parenthesis are for the southern and northern hemispheres, respectively. Characteristics of auroral particles observed in these orbits are described below.

 (a) The electron precipitation regions are observed at latitudes
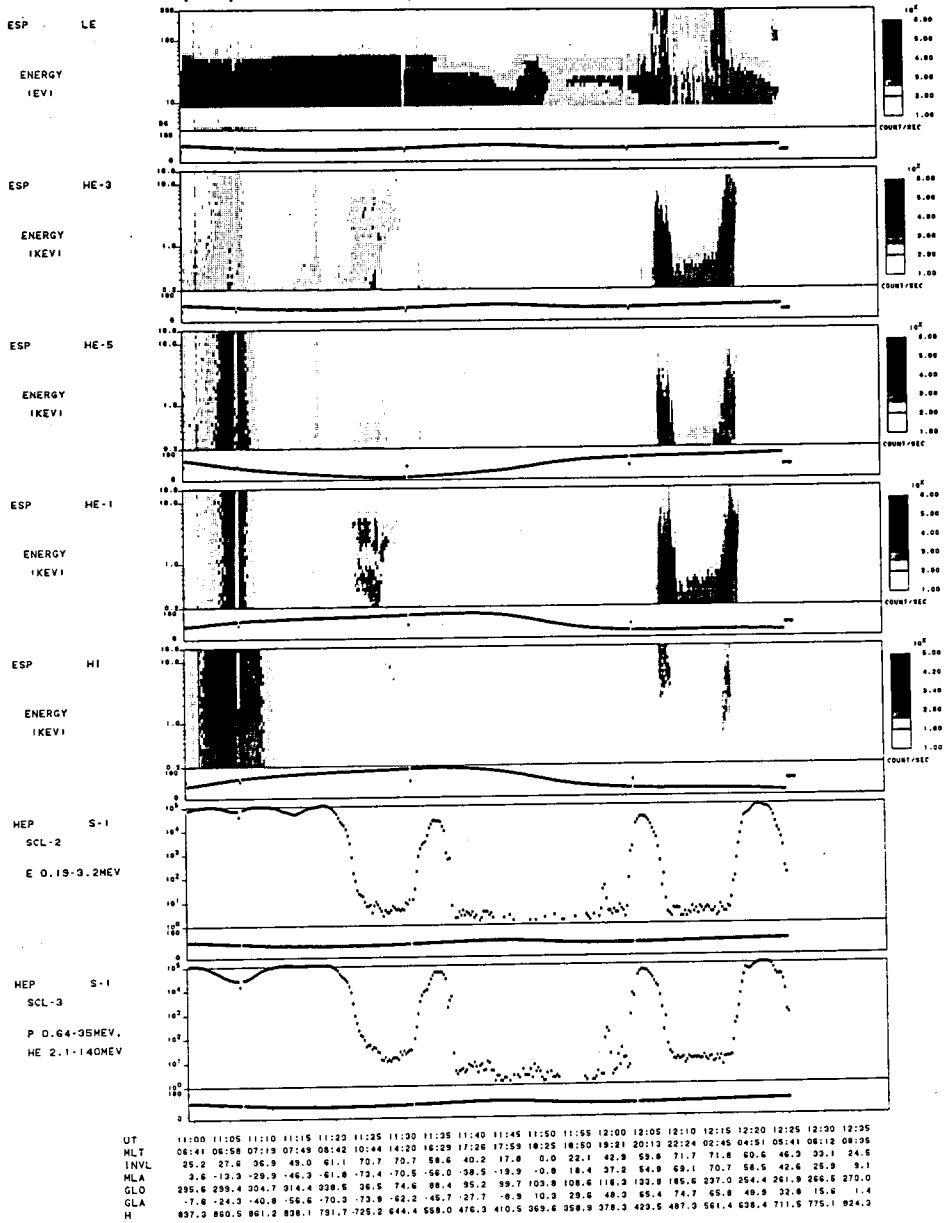
Fig. 5.42 Global patterns of charged particle distribution obtained
on Rev. 00835.
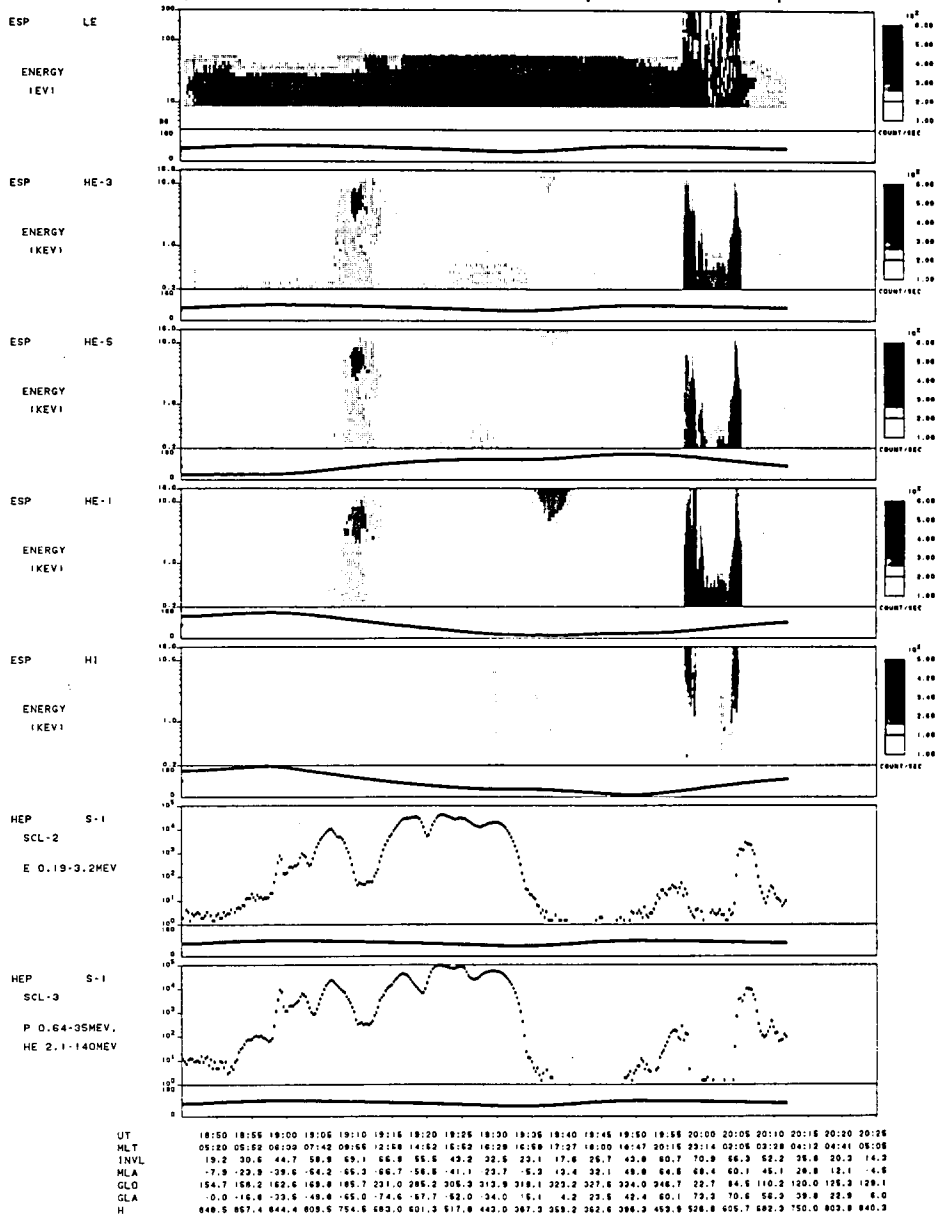
Fig. 5.43   Same as Fig. 5.42.   Rev. No. is 00944.
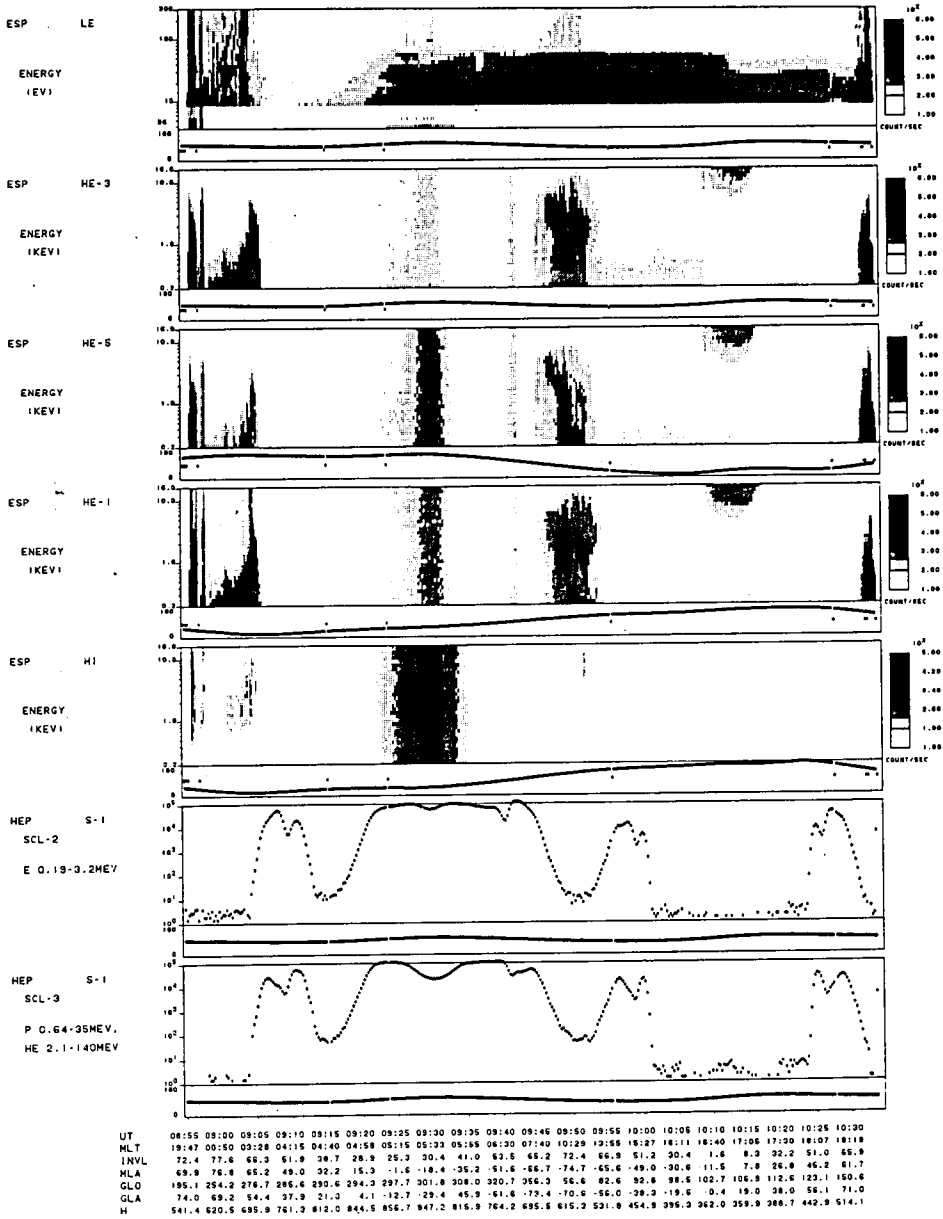
Fig. 5.44 Same as Fig. 5.42. Rev. No. is 00953.

higher than the trapping boundary of higher-energy particles in both dayside and nightside regions. On Rev. 00835 (Fig. 5.42), the HE-1 data show the precipitation of energetic electrons into the dayside auroral region from 1123 UT to 1131 UT, just corresponding to a valley of the HEP data (lower two panels), and into the nightside auroral region at ∿1208 UT and ∿1217 UT, both of which just correspond to the high-latitude boundary of the HEP data. Similar features can also be seen on Rev. 009444 (Fig. 5.43) and Rev. 00953 (Fig.5.44).

(b) The electron precipitation pattern is diffuse in the dayside auroral region (1123-1131 UT on Rev. 00835; 1907-1913 UT on Rev. 00944; 0946-0954 UT on Rev. 00953), whereas on the nightside it is quite discrete and the polar cap region is located between two discrete precipitation regions (∿1208 UT and ∿1217 UT on REv. 00835; ∿1957 UT and ∿2004 UT on Rev.00944; ∿0957 UT and ∿0904 UT on Rev. 00953). The discrete precipitation on the nightside shows an inverted-V feature.

(c) In both the northern and southern high-latitude parts of the orbits shown in Figs. 5.42-5.44, the HE-1 data and the HE-5 data represent precipitating and upward electrons, respectively, while the HE-3 data show electrons with a pitch angle of ∿90°. The pitch angle distribution of auroral electrons, which can be obtained by a comparison among HE-1 ∿ 5 data, is found to be widely spread in both discrete and diffuse precipitations (see item (b) for time bands), although the precipitating component is much more intense than the upward flux.

(d) It can be seen that the energy spectrum of ions precipitating into the auroral region is harder than the corresponding electrons, especially on the nightside; see item (b) for time bands.

The above characteristics are generally consistent with earlier satellite observations [e.g., Frank and Ackerson, 1971; Frank and Gurnett, 1971,; Meng, 1978; Mukai and Hirao, 1982 and Section 2 in this chapter], but the feature (c) and (d) cannot be explained by a simple acceleration mechanism such as the electric double-layer.

Next, the observations of the South-Atlantic anomaly region are described. It can be seen in Fig. 5.44 that in the midst of this region both HE and HI data from 0923 UT to 0935 UT have been contaminated by high-energy particles penetrating through the satellite and instrument structures, and the HEP instrument observed intense fluxes of high-energy particles simultaneously. Therefore, it seems difficult at present to obtain a meaningful value of the flux from the HE and HI data in this region. However, it can be seen in different satellite locations that similarly high levels of high-energy particle fluxes do not necessarily produce similar count rates in the HE and HI data. Spectral difference of high-energy particles may produce different background count rates in the ESP instrument. Future works through cooperative study with the HEP investigator group would make it possible to subtract reasonable background count rates from the HE and HI data in the South-Atlantic anomaly region. In other regions, there is no serious problem in subtraction of background count rate.

The HE data also show a peculiar feature that energetic electrons are observed at dusk hours near the equator in Figs. 5.43 and 5.44; 1935-1941 UT on Rev. 00944 and 1010-1017 UT on Rev. 00953. These electrons are energetic, but since the HEP instrument have not detected these electrons, they may have

energies of 10 - 100 keV. Voss and Smith [1980] have surveyed
global zones of energetic particle precipitation and found an
equatorial zone of ions and neutrals with energies of 10 - 100
keV. Further work is required to delineate the above feature
observed by OHZORA (EXOS-C) satellite.

Now we proceed to discuss characteristics of the LE data.
The LE data show photoelectrons escaping from the topside iono-
shere and also secondary electrons due to precipitation of
auroral particles at high latitudes.   The data below 6 eV
provide the background count rate as noted in section 4.1 and are
indicated in Figs. 5.42-5.44, and the data in the energy range
from 6 to 8.3 eV are not shown to avoid confusion (See Appendix).
It can be seen that the photoelectron energy distribution is
characterized by a sharp cutoff near 60 eV and also some structure
in the energy range from 20 to 30 eV.   This feature is shown
more clearly in Fig. 5.45, in which the energy spectra are
presented every 56 seconds in the time interval from 1101 UT to
1203 UT on Rev. 00835.   The solar zenith angle (χ) at the
satellite location has varied as 80°(1101 UT) - 79°(1109 UT)
94°(1140 UT) - 101°(1157 UT) - 100° (1203 UT).   Note that the
photoelectron flux decreased after $\sim$1140 UT and also that the
energy spectra include secondary electrons due to diffuse precipi-
tation of auroral particles around 1125 UT.
   As described in Chapter 1V, we first found the existence of
several peaks in the energy range from 20 to 30 eV at lower
altitudes, which could be attributed to photoelectrons emitted
from N_2 and O by the intense solar He II(304 $\overset{o}{A}$) radiation, and
which were smeared out due to Coulomb collisions with ambient
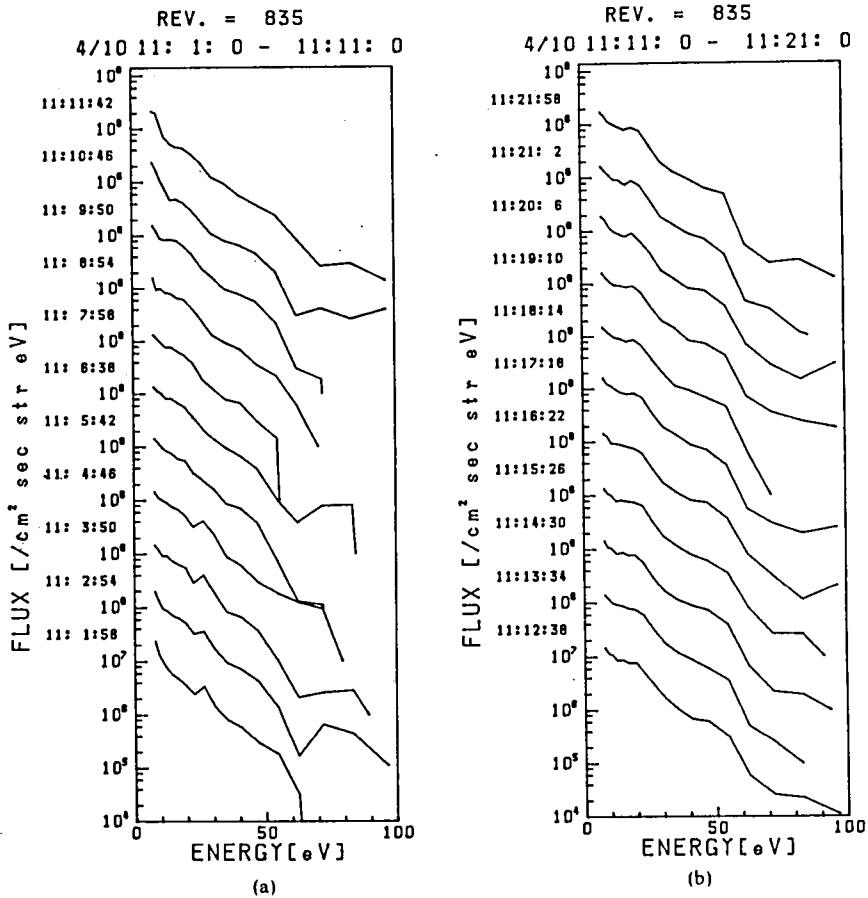
Fig. 5.45 Energy spectra of low-energy electrons observed on Rev. 00835.
The data at every 56 seconds are presented. Successive record
is shifted up by an order of magnitude.

thermal electrons at higher altitudes.   Thereafter, these peaks

have been identified clearly also by satellite observations

[Doering et al., 1975, 1976; Lee et al., 1980a].   The drop in

the spectrum above 60 eV which is due to the absence of significant

solar radiation at energies higher than 70-80 eV has also been

identified previously [see Chapter 1V; also Doering et al., 1975,

1976; Lee et al., 1980a].   Therefore, the features of the

photoelectron energy distribution observed from the EXOS-C

REV. = 835   REV. = 835
4/10 11:21: 0 - 11:32: 0   4/10 11:32: 0 - 11:42: 0

(c)   (d)
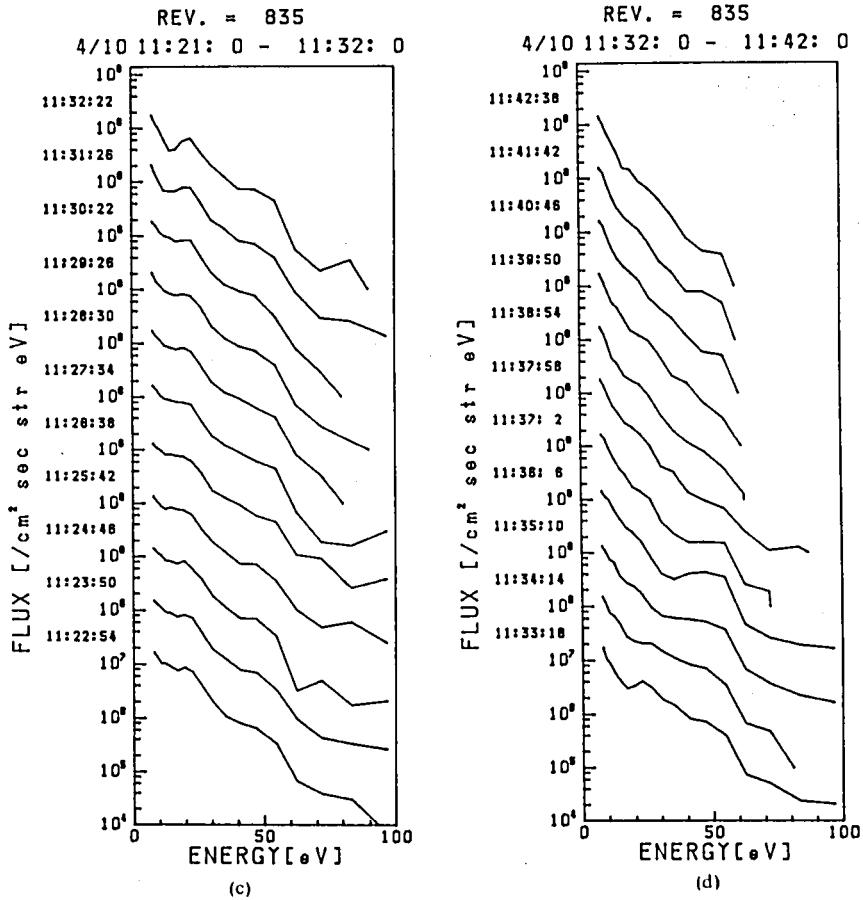
Fig. 5.45 (continued)

satellite are generally consistent with the previous ones.

However, the structure in the energy range from 20 to 30 eV
looks highly variable.   For example, a peak can be seen at the
energy of 27 eV in the first four spectra (1101:58 ∿ 1104:46
UT; χ ≃ 80°).   A plateau-like structure with a shoulder at ∿20
eV can be seen in most spectra in Panel (b) and (c), and the
shoulder sometimes changes into a broad peak.   The spectra have
no characteristic features during some periods of time after

REV. = 835
4/10 11:42: 0 - 11:52: 0

REV. = 835
4/10 11:53: 0 - 12: 3: 0
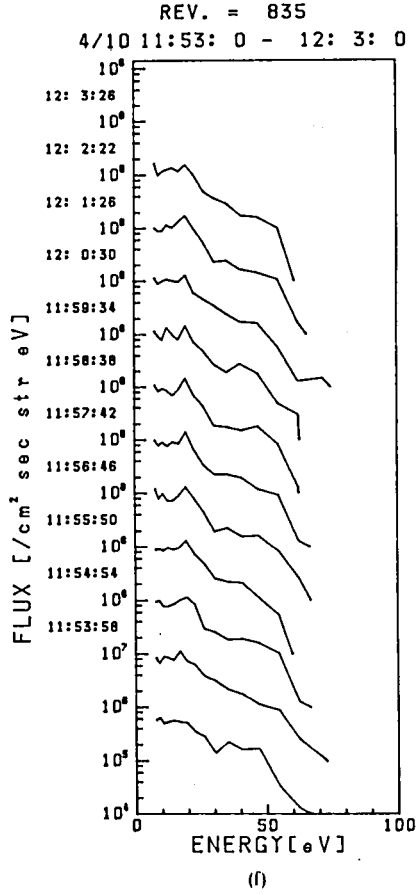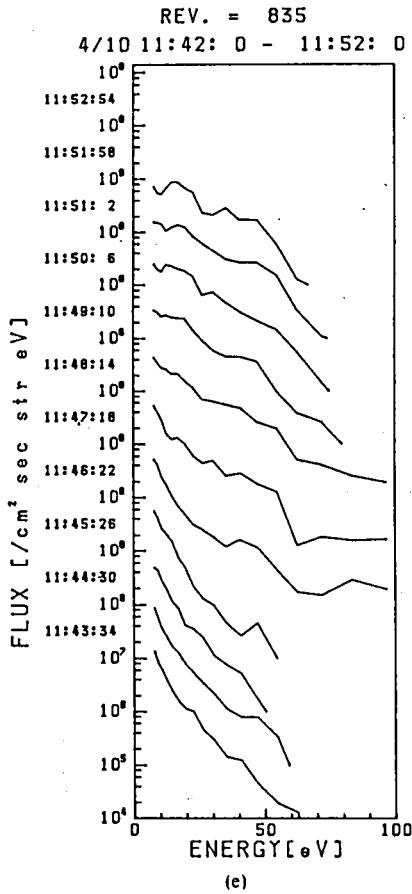
Fig. 5.45 (continued)

∿1140 UT (χ ≃ 94°), but a peak at ∿20 eV can be seen again at
the largest solar zenith angle (χ ≃ 101°) during 1155 ∿ 1203 UT,
though the electron flux has decreased about one order of magnitude
below the daytime flux. Lee et al. [1980b] also have found that
both the flux and spectral structure of photoelectrons in the
energy range of 20 to 30 eV are extremely variable at altitudes
higher than 300 km and have a good correlation with the density
of the ambient plasma. Unfortunately we have not obtained the

REV. = 953
4/18 9:16: 0 -   9:26: 0

REV. = 953
4/18 9:26: 0 -   9:36: 0
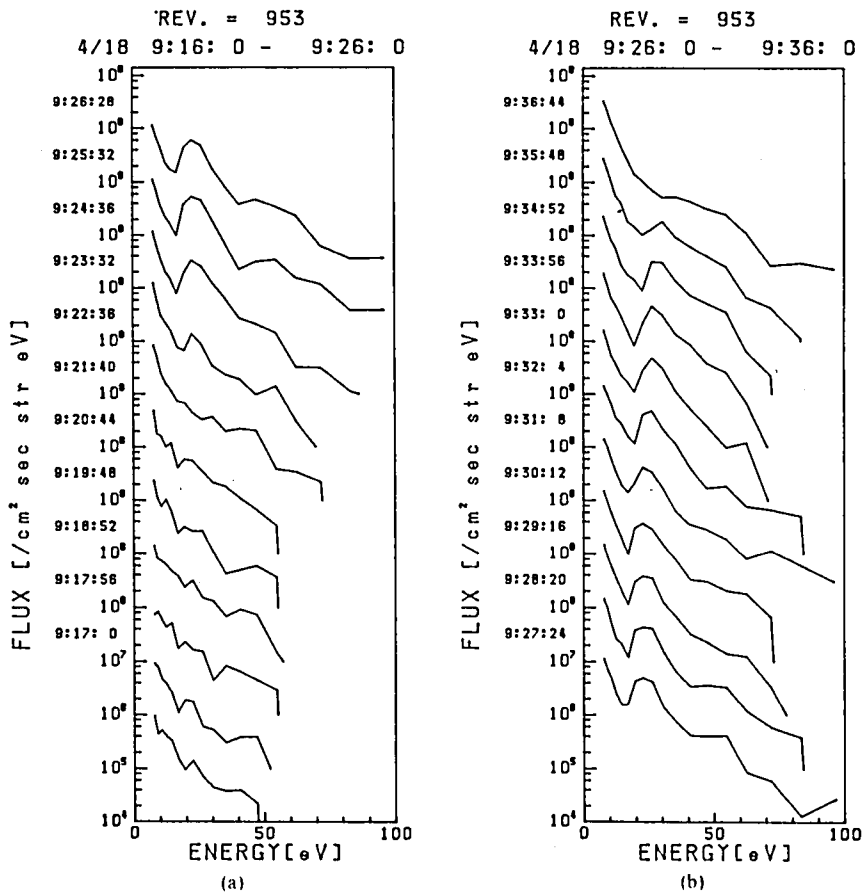
Fig. 5.46 Same as Fig. 5.44. Rev. No. is 00953.

electron density data on this particular orbit.

At Rev. 00953, the structure in the energy range of 20 -30 eV has some peculiar feature. Figure 5.46 shows energy spectra during the period of 0917(χ = 105°) - 0947(χ = 86°) UT. The energy spectra after $\sim$0940 UT(χ = 93°) are similar to those in the previous figures, but the peak observed during 0923(χ = 104°) - 0934(χ = 98°) UT over the South-Atlantic anomaly region is too prominent to be identified purely as ionospheric photoelectrons

REV. = 953

4/18 9:36: 0 -   9:47: 0

Fig. 5.46   (continued)

(c)
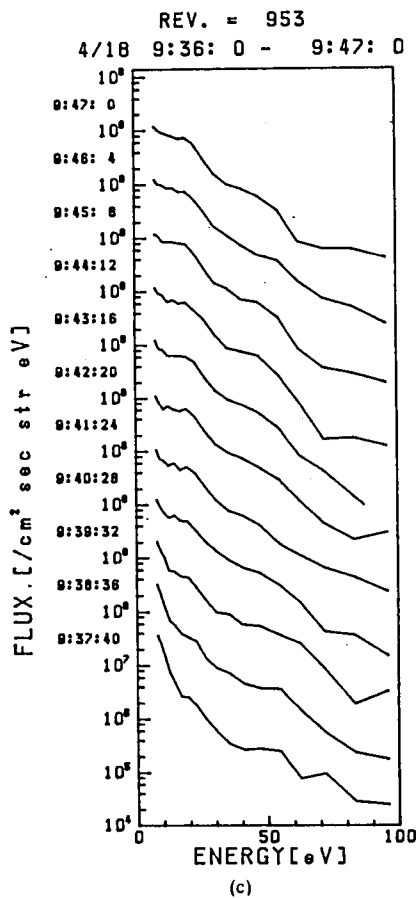
at these large solar zenith angles.   The source of these
electrons is not identified at present.

4.4 Conclusion

    This section has described characteristics of the ESP
instruments on board OHZORA (EXOS-C) satellite, the technical

performance in orbit, and a preliminary analysis of results which
were obtained during the initial phase of satellite operation.

The ESP instrument consists of three sensors (LE, HE and HI)
and a common electronics for control and processing of the data. The
LE sensor measures an energy spectrum of low-energy electrons
in an energy range from 6 eV to 300 eV, while the HE and HI
sensors measure higher-energy electrons and positive ions,
respectively, from 200 eV to 16 keV.   The LE sensor consists of
an inlet collimator, a hemispherical electrostatic analyzer and a
channeltron.   Several considerations were made in instrumental
design for reliable measurement of low-energy electrons.   The HI
sensor has a similar configuration to the LE sensor but with
different geometrical dimension.   The HE sensor consists of a
sophisticated collimator, a quadrispherical electrostatic analyzer
and five channeltrons in order to measure energy distributions of
electrons at five pitch angles simultaneously.   Characteristics
of each sensor were calibrated in the pre-flight test by using
the calibration facility at ISAS.

The technical performance of the instrument in orbit has
been excellent.   The ESP experiment has provided us with global
characteristics of low-energy charged particle distribution over
a wide range of latitude, longitude, altitude (350-865 km) and
local time.   The main scientific results are summarized as
follows.

The HE and HI sensors have observed auroral particles.
The precipitation of auroral particles are observed at latitudes
higher than the trapping boundary of higher-energy particles.
The electron precipitation pattern is diffuse in the dayside
auroral region, whereas it is quite discrete on the nightside.

The pitch angle distribution of precipitating auroral electrons
is found to be rather widely spread in pitch angles in both
discrete and diffuse precipitations.   The energy spectrum of
ions precipitating into the auroral region is found to be harder
than the corresponding electrons, especially in the nightside
auroral region.

Energetic electrons with energies of 10 - 100 keV have been
newly detected at dusk hours near the equator.   However, the
nature of these electrons is not yet known.

The photoelectron energy distribution is shown to have a peak
in an energy range of 20 to 30 eV and also a sharp cutoff near 60
eV.   These featurs are quite consistent with our rocket observa-
tions (see Chapter IV).   However, the spectral structure in the
energy range of 20 to 30 eV is found to make a significant
variation depending on latitude, longitude and local time.   A
large peak at 20 - 30 eV, which is too prominent to be identified
purely as photoelectrons escaping from the ionosphere, is observed
occasionally over the South-Atlantic anomaly region.

Most of the above characteristics are generally consistent
with earlier observations, and supplementary to them.   A further
study in future will delineate more detailed characteristics of
charged particles in space.

Chapter VI. Concluding Remarks

In this thesis, basic transmission properties of a hemi-
spherical electrostatic energy analyzer and the relevant electron
optical system have been studied.   Then we have applied them to
the in-situ measurement of low-energy electrons by rockets and
satellites.   The scientific results obtained have revealed inter-
esting characteristics of ionospheric photoelectrons, auroral
electrons and magnetospheric electrons.   These will contribute to
progress of the ionospheric and magnetospheric physics.

We have adopted a hemispherical electrostatic energy analyzer,
based upon the reviews of observations of those electrons by other
researchers and of various existing methods in Chapter I.   The
primary attraction of this instrument is high energy resolution
over a wide energy range from a few eV to several tens of keV.
It has inherently a double focusing feature due to the spherical
symmetry and therefore has a good transmission.   In addition,
there is less chance of unwanted particles reaching the detector
compared with other types of energy analyzers, because the particle
trajectories are long and curved.   This feature is especially
important for the measurement of low energy electrons, since most
instrumental secondaries are produced at low energies and become a
cause for background noise.   Moreover, for measurements of ionos-
pheric photoelectrons in the low energy, we have developed a
sophisticated inlet collimator that can constitute a three-
electrode electron lens.

In Chapter II, transmission properties of analyzing elements
used in the low energy electron spectrometer have been investigated,

taking into account the application for space use. After a
general consideration for space use of a particle detector,
properties of hemispherical electrostatic analyzers have been
studied, and design parameters have been derived. Although the
energy-angle response of the analyzer has generally a skewing
property, a suitable design of the inlet collimator can lead to
the approximation of the ideal response, for which the energy-
geometric factor can be obtained by the crude estimate of the
analyzer energy width multiplied by the geometric factor of the
inlet collimator. A simple method for obtaining the geometric
factors of the collimating electron lens have been developed by
using a paraxial-ray approximation. The calculated results have
been summarized in contour lines for convenience of design. We
have also calculated the geometric factors by ray tracing with
least approximation and obtained a good agreement in comparison
with those estimated by a paraxial-ray approximation for use in
practical cases.

In Chapter III, the rocket-borne electron spectrometers for
measurement of the ionospheric photoelectrons have been developed,
based upon the results obtained in the Chapter II. In design
principle, emphasis has been laid on the high energy resolution
and flexible operation which enables to measure very low energy
electrons. We have discussed several auxiliary items such as
magnetic shielding, potential difference between the rocket and
the ambient plasma, shadowing effect, instrumental photoelectrons
and secondaries, and vacuum sealing. Most of these items arise
from basic natures of low energy electrons; magnetic susceptibility
and co-existence possibility of spurious electrons. Though
auxiliary, it is essential for a reliable measurement of low

energy electrons from rockets to take these items into account in design and construction of the spectrometer. Several flight experiences have led to refinement of instrumental performances. Characteristics of the instrument have also been calibrated by the pre-flight experiments in the laboratory, studying the nature of a low energy electron beam.

The scientific results obtained by means of the rocket-borne electron spectrometer have been discussed in Chapter IV. Data reduction has been made by conversion of the raw data into the physical quantities, using the instrumental characteristics. It should be emphasized here again that rejection of spurious data is essential for obtaining reliable results. Correction of potential difference between the rocket and the ambient plasma has been necessary for precise determination of the measured energy. The daytime observations have revealed various prominent features in the energy spectra of ionospheric photoelectrons and their altitudinal variations. Those results have been discussed in terms of comparison with the calculated spectra. It has been found that the spectral features above 20 eV are related with production of the primary photoelectrons, while those in lower energies are with the energy-loss processes. A remarkable coincidence between observation and theory has been obtained, which indicates the high-resolution capability and high reliability of our electron spectrometer. The predawn experiments have revealed interesting characteristics of the conjugate photo-electrons, which are different from those of the daytime photo-electrons.

In Chapter V, the electron spectrometers have been applied to the satellite payloads in order to measure energetic electrons

in the ionosphere and magnetosphere; auroral electrons by KYOKKO, inner-magnetosheric electrons by JIKIKEN, and ionospheric photo-electrons and auroral particles by OHZORA.

The KYOKKO observation has revealed interesting characteristics of auroral electrons with respect to (a) local-time dependence of the precipitation pattern, (b) substorm phase variation of the night-side precipitation, (c) spatial structure of the inverted-V event and (d) characteristics of the upgoing electrons including the LUE (localized upgoing electron) event. In particular, items (c) and (d) are regarded as new findings which could be obtained from the adequate design of the instrument matched with the orbit and the attitude control system of the satellite.

The JIKIKEN observation has revealed interesting characteristics of energetic electrons with a good correlation with the VLF wave activities. A high pitch angle anisotropy (HPAA) with a maximum at 90 degrees was observed in the equatorial region around a local time of noon. The energy of these electrons with the HPAA shifted upward as the satellite moved into the plasma-sphere, crossing the plasmapause. It was found that strong Siple signals were observed just outside the plasmapause in association with the HPAA electron distribution, when the satel-lite was within 20° apart from the Siple meridian in geomagnetic longitude.

The OHZORA observation has yielded global distribution of low energy charged particles including auroral particles, energetic electrons around the equator and ionospheric photoelectrons. Most of the observed results are consistent with previous observa-tions, but some peculiar phenomena have also been found out. Among them, the spectral shape of low energy electrons in an energy

range from 20 to 30 eV is found to make a significant variation depending on latitude, longitude and local time. These electrons may be regarded as the ionospheric photoelectrons in most cases, but a large peak which is too prominent to be identified purely as the photoelectrons is observed occasionally over the South-Atlantic anomaly region. The source may be related with precipitation of high energy particles from the radiation belt, though the details have not been understood yet.

In satellite instrumentation, the limitations of weight, size, power consumption and bit rate, and other environmental conditions are much severer than in the rocket payloads. On the other hand, energy coverage and time resolution of the charged-particle observation must meet the scientific objectives. Our electron spectrometers have been designed to obtain as more scientific results as possible under such allowed resources. In future, simultaneous measurements of energy and pitch angle distributions of charged particles with high time resolution will be essential for detailed study of dynamical behaviors of particles in the various transport processes including wave-particle interactions. Spherical electrostatic analyzers with bending angles of 90° or 270° can be applicable to such a purpose and have been partly used in the OHZORA satellite. Future instrumentation will require more channels for high resolution measurements, in which the on-board processing of data compression will be essential, although, to some extent, we have already made compression of the count data from 19 bits to 8 bits.

The LE analyzer on board the EXOS-C satellite is operated under the condition that Eq. (2.20) is satisfied (see p. 232), so that the fringing-field effect is minimum. From Eqs. (2.19) and (2.20),

$$V_O = (E_0/q) \ (R_O - R_i) \ / \ R_O. \tag{A.1}$$

In our LE analyzer (Ro = 28.5 mm, Ri = 21.5 mm)

$$V_O = 0.2456 \times (E_0/q). \tag{A.2}$$

If E_0 and V_O are expressed in units of eV and volt, respectively,

$$V_O = -0.2456 \times E_0. \tag{A.3}$$

We have inserted a mesh between the exit slit and the channeltron. The particle energy must overcome the electric potential V_M of this mesh for being detected by the channeltron; i.e.,

$$E_0 + V_M > 0. \tag{A.4}$$

$$\text{If} \quad V_M = V_O - 5, \tag{A.5}$$

then the electron energy should be greater than 6.6 eV, combining (A.3), (A.4) and (A.5). In practice this cutoff energy is not so clear because of the effect of the channeltron inlet potential

($\sim$200 volts) penetrating through the rough mesh. Thus, the data

obtained at energies which are marked by asterisks in Table 5.5

provide background information. In addition, the mesh potential

is set at -80 volts at the step numbers 1 and 2 (see Table 5.5)

in order to measure the background count rate more definitely.

If V_M = -80 volts, the electron energy which satisfies the above

conditions does not exist at all.

Electron trajectories, the energy of which is from 6 eV to 8

eV may be affected more or less by this mesh potential. There-

fore, correction must be made for count rates obtained from 6 eV

to 8.3 eV, but it has not been made in Section 4 of Chapter V

yet. The data in the above energy range are not presented in

that section to avoid confusion.

References

Afanas'ev, V. P. and S. Ya, Yavor: Electrostatic energy analyzers, Sov. Phys. Tech. Phys., $\underline{20}$, 715-733, 1976.

Akasofu, S. -I.: The development of the auroral substorm, Planet. Space Sci., $\underline{12}$, 273-282, 1964.

Akasofu, S.-I.: Physics of Magnetospheric Substorms, D. Reidel Pub. Co., Dordrecht, Holland, 1977.

Akasofu. S. -I., and Y. Kamide: Recent progress in studies of magnetospheric storms and substorms, J. Geomag. Geoelectr., $\underline{32}$, 585-615, 1980.

Anderson, P. R., and K. Maeda: VLF emissions associated with enhanced magnetospheric electrons, J. Geophys. Res., $\underline{82}$, 135-146, 1977.

Arnoldy, R. L., P. B. Lewis and P. O. Isaacson: Field aligned auroral electron fluxes, J. Geohpys. Res., $\underline{79}$, 4208-4221, 1974.

Ashihara, O. and K. Takayanagi: Velocity distribution of ionospheric low-energy electrons, Planet. Space Sci., $\underline{22}$, 1201-1217, 1974.

Banks, P. M. and A. F. Nagy: Concerning the influence of elastic scattering upon photoelectron transport and escape, J. Geophys. Res., $\underline{75}$, 1902-1910, 1970.

Baumgartner, W. E. and W. K. Huber: Secondary electron emission multipliers as particle detectors, J. Phys. E, $\underline{9}$, 321-330, 1976.

Block, L. P.: Potential double layers in the ionosphere, Cosmic Electrodynamics, $\underline{3}$, 349-376, 1972.

Block, L. P.: Double layers, in Physics of the Hot Plasma in the Magnetosphere, edited by B. Hultqvist and L. Stenflö, Plenum, New York, USA, 1975.

Bloomberg, H. W.: Effect of plasma instability on F region photoelectron distributions, J. Geophys. Res., $\underline{80}$, 2851-2853, 1975.

Burch, J. L., S. A. Fields, W. B. Hanson, R. A. Heelis, R. A. Hoffman and R. W. Janetzke: Characteristics of auroral electron acceleration regions observed by Atmosphere Explorer C. T. Geophys. Res., $\underline{81}$, 2223-2230, 1976.

Carlson, H. C.: Ionospheric heating by magnetic conjugate-point photoelectrons, J. Geophys. Res., $\underline{71}$, 195-199, 1966.

Carpenter, D. L., and T. R. Miller: Ducted magnetospheric propagation of signals from the Siple, Antarctica, VLF transmitter, J. Geophys. Res., $\underline{81}$, 2692-2700, 1976.

Chappell, C. R., K. K. Haris, and G. W. Sharp: A study of
the influence of magnetic activity on the location of the
plasma pause as measured by OGO 5, J. Geophys. Res., 75,
50-56, 1970.

Chase, L. M.: The geometrical factor of large aperture
hemispherical electrostatic analyzers, Rev. Sci. Instr., 44,
998-1002, 1973.

Cicerone, R. J. and S. A. Bowhill: Photoelectron fluxes in
the ionosphere computed by a Monte Carlo method, J. Geophys.
Res., 76, 8299-8316, 1971.

Cicerone, R. J., W. E. Swartz, R. S. Stolarski, A. F. Nagy
and J. S. Nisbet: Thermalization and transport of
photoelectrons: a comparison of theoretical approaches, J.
Geophys. Res., 78, 6709-6728, 1973.

Cladis, J. B. and R. D. Sharp: Scale of electric field
along magnetic field in an inverted-V event. J. Geophys.
Res., 84, 6564-6572, 1979.

Dalgarno, A., M. B. McElroy, and A. I. Stewart: Electron
impact excitation of the dayglow, J. Atmos. Sci., 26, 753-762,
1969.

Doering, J. P., W. G. Fastie and P. D. Feldman: Photoelectron
excitation of N_2 in the Day Airglow, J. Geophhys. Res.,
75, 4787-4802, 1970.

Doering, J. P., W. K. Peterson, C. O. Bostrom and J. C.
Armstrong: Measurement of low-energy electrons in the day
airglow and dayside auroral zone from atmosphere Explorer-C,
J. Geophys. Res., 80, 3934-3944, 1975.

Doering, L. P., W. K. Peterson, C. O. Bostrom and T. A. Potemra:
High resolution daytime photoelectron energy spectra from
AE-E, Geophys. Res. Lett., 3, 129-131, 1976.

Duboin, M. L., G. Lejuene, M. Petit and G. Weill: Excitation
of oxygen lines and ionospheric heating by conjugate
photoelectrons, J. Atmos. Terr. Phys., 30, 299-304, 1968.

Ejiri, M., R. A. Hoffman, and P. H. Smith: Energetic particle
penetrations into the inner magnetosphere, NASA/GSFC
X-625-77-254, 1979.

Engelhard, A. G., A.V. Phelps and C. G. Risk: Determination of
momentum transfer and inelastic collision cross sections for
electrons in nitrogen using transport coefficients,
Phys. Rev., 135, A1566-A1574, 1964.

Evans, J. V. and I. J. Gastman: Detection of conjugate
photoelectrons at Millstone Hill, J. Geophys. Res., 75,
807-815, 1970.

Feldstein, Y. I.: Peculiarities in the auroral distribution
and magnetic disturbance distribution in high latitudes

caused by the asymmetrical form of the magnetosphere,
Planet. Space Sci., 14, 121-130, 1966.

Frank, L. A.: Initial observations of low-energy electrons in
the earth's magnetosphere with OGO-3, J. Geophys. Res., 72,
185-195, 1967.

Frank, L. A.: Plasma in the earth's polar magnetosphere, J.
Geophys. Res., 76, 5202-5219, 1971.

Frank, L. A. and K. L. Ackerson: Observations of charged
particle precipitation into the auroral zone. J. Geophys.
Res., 76, 3612-3643, 1971.

Frank, L. A. and D. A. Gurnett: Distribution of plasmas and
electric fields over the auroral zones and polar caps. J.
Geophys. Res., 76, 6829-6846, 1971.

Green, A. E. S. and T. Sawada: Ionization cross sections and
secondary electron distributions, J. Atmos. Terr. Res., 34,
1719-1728, 1972.

Green, A. E. S. and R. S. Stolaroki: Analytic models of electron
impact excitation cross sections, J. Atmos. Terr. Phys., 34,
1703-1717, 1972.

Ghielmetti, A. G., R. G. Johnson, R. D. Sharp and E. G.
Shelley: The latitudinal diurnal, and altitudinal
distributions of upward flowing energetic ions of ionospheric
origin. Geophys. Res. Lett., 5, 59-62, 1978.

Goldstein, H.: Classical Mechanics, Addison-Wesley Press Inc.,
Cambridge, 1951.

Gosling, J. T., J. R. Asbridge, S. J. Bame, and W. C. Feldman:
Effects of a long entrance aperture upon the azimuthal response
of spherical section electrostatic analyzers, Rev. Sci. Instr.,
49, 1260-1268, 1978.

Grivet, P.: Electron Optics, Pergamon Press Ltd., London, 1965.

Hanson, W. B.: Structure of the Ionosphere, Satellite Environment
Handbook, edited by F. S. Johnson, Stanford Univ. Press,
Stanford, California, USA, p.24, 1965.

Hanson, W. B.: Electron temperatures in the upper atmosphere,
Space Res., 3, 282, 1963.

Hays, P. B., and W. E. Sharp: Twilight airglow 1,
photoelectrons and [OI] 5577 Angstrom radiation, J. Geophys.
Res., 78, 1153-1166, 1973.

Heikilla, W. J., J. B. Smith, J. Tarstrup and J. D. Winningham:
The soft particle spectrometer in the ISIS-I satellite, Rev. Sci.
Instr., 41, 1393-1402, 1970.

Helliwell, R. A., and J. P. Katsufrakis: VLF wave injection
into the magnetosphere from Siple Station, Antarctica, J.

Geophys. Res., <u>79</u>, 2511-2518, 1974.

Henry, R. J. W.: Photoionization cross sections for atomic oxygen,
    Planet. Space Sci., <u>15</u>, 1747-1755, 1967.

Heristchi, Dj: Taux de compotage d'un telescope cosmique
    compose de deux disques circularires, Nucl. Instr. Meth.,
    <u>47</u>, 39-44, 1967.

Hinteregger, H. E.: The extreme ultraviolet solar spectrum and
    its variation during a solar cycle, Ann. Géophys., <u>26</u>,
    547-554, 1970.

Hoegy, W. R., J.-P. Fournier, and E. G. Fontheim: Photoelectron
    energy distribution in the F region, J. Geophys. Res.,
    <u>70</u>, 5464-5468, 1965.

Hughes, A. Ll., and V. Rojanski: On the analysis of electronic
    velocities by electrostatic means, Phys. Rev., <u>34</u>, 284-290,
    1929.

Hultqvist, B., and H. Borg: Observations of energetic ions
    in the inverted-V events, Planet Space Sci., <u>26</u>, 673-689,
    1978.

Iijima, T. and T. A. Potemra: Large-scale characteristics
    of field-aligned currents associated with substorms. J.
    Geophys. Res., <u>83</u>, 599-615, 1978.

Inan, U. S., and T. F. Bell: The plasmapause as a VLF wave
    guide, J. Geophys. Res., <u>82</u>, 2819-2827, 1977.

Jacchia, L. G.: Revised static models of the thermosphere and
    exosphere with empirical temperature profiles, <u>Spec. Rep. 332</u>,
    Smithon. Astrophys. Observ., Cambridge, Mass., <u>1971.</u>

Kan, J. R.: Toward a unified theory of discrete auroras,
    Space Sci. Rev., <u>31</u>, 71-117, 1982.

Kaneda, E., T. Mukai and K. Hirao: Some features of auroral
    substorms observed by KYOKKO. <u>Highlights of the Japanese</u>
    <u>IMS program</u>, Tokyo, ISAS, Univ. Tokyo, 1980.

Kaneda, E., T. Mukai and K. Hirao: Synoptic features of auroral
    system and corresponding electron precipitation observed by
    KYOKKO, Physics of Auroral Arc Formation: Geophysical
    Monograph Series, <u>25</u>, 24-30, 1981.

Kaya, N., T. Mukai, H. Matsumoto and T. Itoh: Characteristics of
    auroral particles observed by EXOS-C, J. Geomag. Geoelectr.,
    <u>37</u>, 347-363, 1985.

Kimura, I., and K. Hashimoto: VLF doppler shift measurement
    for ionization duct monitoring by EXOS-B satellite (JIKIKEN),
    J. Geomag. Geoelectr., <u>33</u>, 89-99, 1981.

Kimura, I., H. Matsumoto, T. Mukai, K. Hashimoto, T. F. Bell,
    U.S. Inan, R. A. Helliwell, and J. P. Katsufrakis: EXOS-B/SIPLE

station VLF wave-particle interaction experiments: 1.
general description and wave-particle correlations, J. Geophys.
Res., 88, 282-294, 1983.

Kondo, Y. and T. Ogawa:Odd nitrogen in the lower thermoshere
under auroral perturbations., J. Geomag. Geoelectr.,
28, 253-282, 1976.

Koons, H. C., and J. F. Fennell: Particle and wave dynamics
during plasma injections, J. Geophys. Res., 88, 6221-6229,
1983.

Knudsen, W. C.: Latitudinal variation of differential photo-
electron flux at 560-km altitude, J. Geophys. Res., 77,
1233-1241, 1972.

Knudsen, W. C., and G. W. Sharp: Eclipse and non-eclipse
differential photoelectron flux, J. Geophys. Res., 77,
1221-1232, 1972.

Kubo, H., T. Mukai and N. Kawashima: Observation of charged
particles on board the scientific satellite "JIKIKEN", Bull.
Inst. Space Aeronaut. Sci., 15, 751-765, 1979. (in Japanese)

Kubo, H., T. Mukai and N. Kawashima: Observation of charged
particles aboard the scientific satellite JIKIKEN (EXOS-B),
J. Geomag. Geoelectr., 33, 125-143, 1981.

Kuyatt, C. E. and J. A. Simpson: Electron monochromator design,
Rev. Sci. Instr., 38, 103-111, 1967.

Kuyatt, C. E.: Measurement of electron scattering from a static
gas target, in Methods of Experimental Physics 7A, edited
by B. Berderson and W. L. Fite (Academic Press, New York),
1-42, 1968.

Lee, J. S., J. P. Doering, T. A. Potemra and L. H. Brace:
Measurements of the ambient photoelectron spectrum from
atmosphere Explorer: I. AE-E measurements below 300 km during
solar minimum conditions, Planet Space Sci., 28,
947-971, 1980a.

Lee, J. S., J. P. Doering, T. A. Potemra and L. H. Brace:
Measurements of the ambient photoelectron spectrum from
Atmosphere Explorer: II. AE-E measurements from 300 to 1000
km during solar minimum conditions, Planet Space Sci., 28,
973-996, 1980b.

Lejeune G. and G. Wormer: Diffusion of photoelectrons along
a field line inside the plasmasphere, J. Geophys. Res., 81,
2900-21916, 1976.

Lin, C. S., J. N. Barfield, J. L. Burch and J. D. Winningham:
Near-conjugate of inverted-V electron precipitation using DE
1 and DE 2, J. Geophys. Res., 90, 1669-1681, 1985.

Lin, C. S. and R. A. Hoffman: Characteristics of the
inverted-V event. J. Geophys. Res., 84, 1514-1524, 1979.

Lui, A. T. Y., C. D. Anger, D. Venkatesan, and W. Sawchunk: The topology of the auroral oval as seen by the Isis 2 scanning auroral photometer. J. Geophys. Res., 80, 1795-1804, 1975.

Lui, A. T. Y., D. Venkatesan, C. D. Anger, S. -I. Akasofu, W. J. Heikkila, J. D. Winningham and J. R. Burrows: Simultaneous observations of particle precipitations and auroral emissions by the ISIS 2 satellite in the 19-24 MLT sector. J. Geophys. Res., 82, 2210-2226, 1977.

Lyons, L. R., R. M. Thorne and C. F. Kennel: Pitch angle diffusion of radiation belt electrons within the plasmasphere, J. Geophys. Res., 77, 3455-3474, 1972.

Lyons L. R. and D. J. Williams: The quiet time structure of energetic (35-560 KeV) radiation belt electrons, J. Geophys. Res., 80, 943-950, 1975a.

Lyons L. R. and D. J. Williams: Storm and post-storm evolution of energetic (35-560 KeV) radiation belt electron distributions, J. Geophys. Res., 80, 3985-3994, 1975b.

Mantas, G. P.: Theory of photoelectron thermalization and transport in the ionosphere, Planet. Space Sci., 23, 337-354, 1975.

Mantas, G. P. and S. A. Bowhill: Calculated photoelectron pitch angle and energy spectra, Planet. Space Sci., 23, 355-375, 1975.

Matsumoto, H.: Nonlinear whistler-mode interaction and triggered emission in the magnetosphere, in Wave Instabilities in Space Plasmas, edited by P. J. Papadopoulous, D. Reidel, Hingham, Mass., 1979.

Matsumoto, H., S. Miyatake, T.Tsuruda, A. Morioka, J. Ohtsu, H. Oya and I. Kimura: VLF wave observation by satellite JIKIKEN (EXOS-B), J. Geomag. Geoelectr., 33, 63-72, 1981.

Matsumoto, H., K. Hashimoto, M. Morikura, I. Kimura and T. Mukai: Correlation between VLF plasma waves and energetic electrons simultaneously observed by satellite JIKIKEN (EXOS-B), J. Geomag. Geoelectr., 33, 73-87, 1981.

Matsumoto, H., M. Morikura, K. Hashimoto, I. Kimura and T. Mukai: Observation and comparative study of VLF emissions and high energy electron flux by EXOS-B satellite, Bull. Inst. Space Aeronaut. Sci., 15, 725-738, 1979. (in Japanese)

Matsumoto, H., K. Hashimoto, M. Morikura, I. Kimura and T. Mukai: Correlation between VLF plasma waves and energetic electrons simultaneously observed by satellite JIKIKEN (EXOS-B), J. Geomag. Geoelectr., 33, 73-87, 1981.

McMahon, W. J., and L. Heroux: Rocket measurement of thermospheric photoelectron energy spectra, J. Geophys. Res., 83, 1390-1394, 1978.

Meng, C. I.: Electron precipitation and polar aurora, Space
    Sci. Rev., 22, 223-300, 1978.

Mizera, P. F. and J. F. Fennell: Signatures of electric fields
    from high and low altitude particles distributions, Geophys.
    Res. Lett., 4, 311-314, 1977.

Morikura, M.: Experimental study of VLF wave-particle interaction
    by the scientific satellite EXOS-B, Master Thesis,
    Kyoto Univ., 1981. (in Japanese)

Mozer, F. S., C. A. Cattell, M. K. Hudson, R. L. Lysak, M.
    Temerin, and R. B. Torbert: Satellite measurements and
    theories of low altitude auroral particle acceleration. Space
    Sci. Rev., 27, 155-213, 1980.

Mozer, F. S.: On the lowest altitude S3-3 observations of
    electrostatic shocks and parallel electric fields, Geophys.
    Res. Lett., 7, 1097-1098, 1980b.

Mukai, T. and K. Hirao: Rocket measurement of photoelectrons in
    the ionosphere by K-9M-40, Bull. Inst. Space Aeronaut. Sci.,
    9, 394-405, 1973a. (in Japanese)

Mukai, T. and K. Hirao: Rocket measurement of the differential
    energy spectrum of the photoelectrons, J. Geophys. Res., 78,
    8395-8398, 1973b.

Mukai, T. and K. Hirao: Rocket measurement of the photoelectrons
    in the ionosphere by K-9M-45, Bull. Inst. Space Aeronaut. Sci.,
    10, 703-714, 1974. (in Japanese)

Mukai, T. and K. Hirao: Rocket measurement of the photoelectrons
    in the ionosphere by K-9M-47, Bull. Inst. Space Aeronaut. Sci.,
    11, 593-603, 1975. (in Japanese)

Mukai, T. and K. Hirao: Characteristics of Auroral electrons
    observed in the morning-side from "KYOKKO", Bull. Inst. Space
    Aeronaut. Sci., 14, 1179-1194, 1978. (in Japanese)

Mukai, T., Y. Kondo and K. Hirao: Rocket observation of conjugate
    photoelectrons in the predawn ionosphere, Planet Space Sci.,
    27, 31-38, 1979.

Mukai, T. and K. Hirao: Observations of precipitating electrons
    by Kyokko, Proceedings of International Workshop on
    Selected Topics of Magnetospheric Physics held in Tokyo,
    pp. 20-24, 1979a.

Mukai, T. and K. Hirao; Characteristics of auroral electrons
    observed by KYOKKO, paper presented at First International
    Symposium on IMS Results held at La Trobe University,
    Melbourne, Australia, as part of the XVII General Assembly
    of the IUGG, 1979b.

Mukai, T., H. Kubo, and N. Kawashima; Observation of energetic
    particles by JIKIKEN, ibid., 1979.

Mukai, T. and K. Hirao; Characteristics of the auroral electrons observed by the KYOKKO satellite, US-Japan Seminar on Wave-Particle Interactions in Space Plasmas held at Kyoto Kaikan, Okazaki, Kyoto, pp. 49-53 (extended abstracts), 1981.

Mukai, T. and K. Hirao: Characteristics of the inverted-V events observed by the KYOKKO satellite, Mem. Nat. Inst. Polar Res., Special Issue No. 22, 116-124, 1982.

Mukai, T., N. Kaya, H. Matsumoto, T. Itoh and K. Hirao; Initial observation of low-energy charged particles by satellite OHZORA (EXOS-C), J. Geomag. Geoelectr., 37, 365-387, 1985.

Myers, B. F., D. A. Hamlin and M. R. Schoonover: Calculated and observed photoelectron-flux spectra at dawn, J. Atmos. Terr. Phys., 37, 387-406, 1975.

Nagy, A. F. and P. M. Banks: Photoelectron fluxes in the ionosphere, J. Geophys. Res., 75, 6260-6270, 1970.

Nagy, A. F., J. D. Winningham and P. M. Banks: The effect of conjugate photoelectron impact ionization on the predawn ionosphere, J. Atmos. Terr. Phys., 35, 2289-2291, 1973.

Nisbet, J. S.: Photoelectron escape from the ionosphere, J. Atmos. Terr. Phys., 30, 1257-1278 , 1968.

Noxon, M. F. and A. E. Johanson: Effect of magnetically conjugate photoelectrons on OI(6300 Å), Planet. Space Sci., 18, 1367-1379, 1970.

Ogawa, T.: Photoelectron elementary processes, Proceedings of Ionospheric Research Symposium held at ISAS, pp. 39-58, 1971. (in Japanese)

Oyama, K.-I: Characteristics of the contaminated Langmuir probe and countermoves for its application to the space observations, ISAS Report No. 525, 1975.

Oyama, K. -I., and K. Hirao: Evidences of a distorted electron energy distribution in ionospheric plasma, Planet. Space Sci., 24, 900-904, 1976.

Oyama, K. -I., and K. Hirao: Energy gain of supra-thermal electrons from the excitated neutral gases, J. Geomag. Geoelectr., 37, 913-926, 1985.

Paolini, F. R., and G. C. Theodoridis: Charged particle transmission through spherical plate electrostatic analyzers, Rev. Sci. Instr., 38, 579-588, 1967.

Paradopoules, K.: A review of anomalous resistivity for the ionosphere, Rev. Geophys. Space Phys., 15, 113-127, 1977.

Paszkowski, B., Electron Optics, Iliffe Books Ltd., London, 1968.

Peterson, L. R., S. S. Prasad and A. E. S. Green: Semi-empirical electron impact cross sections for atmospheric gases,

Can. J. Chem., <u>47</u>, 1774-1780, 1969.

Peterson, W. K., J. P. Doering, T. A. Potemra, R. W. McEntire and
    C. O. Bostrom: Conjugate photoelectron fluxes observed on
    Atmosphere Explorer C, Geophys. Res. Lett., <u>4</u>, 373-376, 1977.

Prather, M. J., M. B. McElroy and J. Rodriguez: Photoelectrons
    in the upper atmosphere: A formulation incorporating effect
    of transport, Planet. Space Sci., <u>26</u>, 131-138, 1978.

Purcell, E. M.: The focussing of charged particles by a spherical
    condenser, Phys. Rev., <u>54</u>, 818-826, 1938.

Rao, B.C.N., and J. L. Donley: Photoelectron flux in the
    topside ionosphere measured by retarding potential analyzers,
    J. Geophys. Res., <u>74</u>, 1715-1719, 1969.

Roble R. G. and R. E. Dickinson: Is there enough solar extreme
    ultraviolet radiation to maintain the global mean thermospheric
    temperature ?, J. Geophys. Res., <u>78</u>, 249-257, 1973.

Rogers, F. T., Jr: On the theory of the electrostatic beta-
    particle analyzer. V, Rev. Sci. Instr., <u>22</u>, 723-726, 1951.

Rosenbauer, H., H. Grunwaldt, M. D. Montgomery, G. Paschmann,
    and N. Sckopke: Heos 2 plasma observations in the distant
    polar magnetosphere: the plasma mantle, J. Geophys. Res.,
    <u>80</u>, 2723-2737, 1975.

Roy, D., and J. -D. Carette: Improvement of the resolving power
    and transmission of electrostatic spectrometers,
    J. Appl. Phys., <u>42</u>, 3601-3615, 1971.

Saflekos, N. A., T. A. Potemra, W. K. Peterson and J. P.
    Doering: Simultaneous observations of transverse magnetic
    disturbances and auroral electron precipitation from TRIAD
    and AE-C spacecraft/ EOS (abstract only), <u>58</u>, 720, 1977.

Schlegel, K., Monte Carlo simulation of a model ionosphere-III.
    photoelectron and escape electron spectra, J. Atmos. Terr.
    Phys., <u>36</u>, 183-187, 1974.

Schulz, G. J.: Vibratinal excitation of N_2, CO, and H_2 by
    electron impact, Phys. Rev., <u>135</u>, A988-A994, 1964.

Shepherd, G. G., J. F. Pieau, T. Ogawa, T. Tohmatsu, K. Oyama
    and Y. Watanabe: Direct measurement of conjugate photo-
    electrons and predawn 630 nm airglow, Planet. Space Sci.,
    <u>26</u>, 211-217, 1978.

Sharp, R. D., R. G. Johnson and E. G. Shelley: Energetic
    particle measurements from within ionospheric structures
    responsible for auroral acceleration processes,
    J. Geophys. Res., <u>84</u>, 480-488, 1979.

Shea, M. F., R. D. Sharp, and M. B. McElroy: Measurement
    and interpretation of low-energy photoelectrons,
    J. Geophys. Res., <u>73</u>, 4199-4212, 1968.

Shoen, R. I.: Laboratory measurements of photoionization, photoexcitation, and photodetachment, Can. J. Chem., <u>47</u>, 1879, 1969.

Steckelmacher, W.: Energy analyzers for charged particles, J. Phys. E, <u>6</u>, 1061-1071, 1973.

Stolarski, R. S.: Energetic of the midlatitude thermosphere, J. Atmos. Terr. Phys., <u>38</u>, 863-868, 1976.

Stolarski, R. S.: Analytic approach to photoelectron transport, J. Geophys. Res., <u>77</u>, 2862-2870, 1972.

Stolarski, R. S. and N. P. Johnson: Photoionization and photo-absorption cross sections for ionospheric calculations, J. Atmos. Terr. Phys., <u>34</u>, 1691-1701, 1972.

Stone, E. J., and E. C. Zipf: Electron-impact excitation of $^3S^0$ and $^5S^0$ states of atomic oxygen, J. Chem. Phys., <u>60</u>, 4237, 1974.

Swartz, W. E., J. S. Nisbet and A. E. S. Green: Analytic expression for the energy transfer rate from photoelectrons to thermal electrons, J. Geophys. Res., <u>76</u>, 8425-8426, 1971.

Swaltz, W. E. and J. S. Nisbet: Incompatibility of solar EUV fluxes and incoherent scatter measurements at Arecibo, J. Geophys. Res., <u>78</u>, 5640-5656, 1973.

Swarts, W. E., G. J. Bailey and R. J. Moffett: Electron heating resulting from interhemispherical transport of photoelectrons, Planet. Space Sci., <u>23</u>, 589-598, 1975.

Swarts, W. E. and J. S. Nisbet: Revised calculations of F region ambient electron heating by photoelectrons, J. Geophys. Res., <u>77</u>, 6259-6261, 1972.

Swift, D. W.: Mechanism for the discrete aurora── a review, Space Sci., Rev., <u>22</u>, 35-75, 1978.

Takayanagi, K., and Y. Itikawa: Elementary processes involving electrons in the ionosphere, Space Sci. Rev., <u>11</u>, 380-450, 1970.

Thomas G. R., and D. M. Willis: Analytical deviation of the geometric factor of a particle detector having circular or rectangular geometry, J. Phys. E, <u>5</u>, 260-263, 1972.

Thuillier, G., G. Lejeune and J. E. Blamont: Altitude profiles of the photoelectron induced O $^1D(\lambda\ 6300\ \text{Å})$ predawn enhancement by observation and theory, Planet. Space Sci., <u>24</u>, 1141-1150, 1976.

Timothy: Use of open-structure channel electron multipliers in sounding rocket experiments, Rev. Sci. Instr., <u>44</u>, 207-211, 1973.

Tohmatsu, T., T. Ogawa, H. Tsuruta: Photo-electron processes

in the upper atmosphere, I energy spectrum of the primary
photoelectrons, Rept. Ionos. Space Res. Japan,
19, 482-508, 1965.

Victor, G. A., K. Kirby-Docken and A. Dalgarno: Calculations
    of the equilibrium photoelectron flux in the thermosphere,
    Planet. Space Sci., 24, 679, 1976.

Voss, H. D., and L. G. Smith: Global zones of energetic
    particle precipitation, J. Atmos. Terr. Phys., 42, 227-239,
    1980.

Vasyliunas, M.: Deep space plasma measurement, in Methods of
    Experimental Physics, edited by R. H. Roberg and H. R. Gream,
    Academic Press, New York, 9B, 49-88, 1971.

Winningham, J. D., F. Yasuhara, S. -I., Akasofu, W. J.
    Heikilla: The latitudinal morphology of 10-eV to 10-keV
    electron fluxes during magnetically quiet and disturbed
    times in the 2100-0300 MLT sector, J. Geophys. Res., 80,
    3148-3171, 1975.

Wrenn, G. L., and G. G. Shepherd: A conjugates point effect
    observed for electron temperatures in the 1000-2500 km height
    range, J. Atmos. Terr. Phys., 31, 1383-1389, 1969.

Wrenn, G. L.: Satellite measurements of photoelectron fluxes,
    Ann. de Geophys., 30, 49-57, 1974.

Wrenn, G. L., J. F. E. Johnson and J. I. Sojka: Stable
    'pancake' distributions of low energy electrons in the plasma
    trough, Nature, 279, 512-514, 1979.

Yngvesson, K. O. and F. W. Perkins: Radar Thomson scatter
    studies of photoelectrons in the ionosphere and Landau damping,
    J. Geophys. Res., 73, 97-110, 1968.